

THÈSE

En vue de l'obtention du

DOCTORAT DE L'UNIVERSITÉ DE TOULOUSE

Délivré par :

Institut National Polytechnique de Toulouse (INP Toulouse)

Discipline ou spécialité :

Dynamique des fluides

Présentée et soutenue par :

Mme FRANCHINE NI

le lundi 24 avril 2017

Titre :

Accounting for complex flow-acoustic interactions in a 3D thermo-acoustic Helmholtz solver

---

Ecole doctorale :

Mécanique, Energétique, Génie civil, Procédés (MEGeP)

Unité de recherche :

Centre Européen de Recherche et Formation Avancées en Calcul Scientifique (CERFACS)

Directeurs de Thèse :

M. THIERRY POINSOT

M. FRANCK NICOUD

Rapporteurs :

M. JONAS MOECK, TECHNISCHE UNIVERSITAT BERLIN

M. YVES AUREGAN, UNIVERSITE DU MANS

Membres du jury :

Mme AIMEE MORGANS, IMPERIAL COLLEGE OF SCIENCE LONDRES, Présidente

M. FRANCK NICOUD, UNIVERSITE DE MONTPELLIER, Membre

M. THIERRY POINSOT, INP TOULOUSE, Membre

M. YOANN MERY, GROUPE SAFRAN, Membre

Accounting for complex flow-acoustic interactions in a 3D thermo-acoustic Helmholtz solver

by

Abstract in English

Environmental concerns have motivated turbine engine manufacturers to create new combustor designs with reduced fuel consumption and pollutant emissions. These designs are however more sensitive to a mechanism known as combustion instabilities, a coupling between flame and acoustics that can generate dangerous levels of heat release and pressure fluctuations. Combustion instabilities can be predicted at an attractive cost by Helmholtz solvers. These solvers describe the acoustic behavior of an inviscid fluid at rest with a thermoacoustic Helmholtz equation, that can be solved in the frequency domain as an eigenvalue problem. The flame/acoustics coupling is modeled, often with a first order transfer function relating heat release fluctuations to the acoustic velocity at a reference point. One limitation of Helmholtz solvers is that they cannot account for the interaction between acoustics and vorticity at sharp edges. Indeed, this interaction relies on viscous processes at the tip of the edge and is suspected to play a strong damping role in a combustor. Neglecting it results in overly pessimistic stability predictions but can also affect the spatial structure of the unstable modes. In this thesis, a methodology was developed to include the effect of complex flow-acoustic interactions into a Helmholtz solver. It takes advantage of the compactness of these interactions and models them as 2-port matrices, introduced in the Helmholtz solver as a pair of coupled boundary conditions: the Matrix Boundary Conditions. This methodology correctly predicts the frequencies and mode shapes of a non-reactive academic configuration with either an orifice or a swirler, two elements where flow-acoustic interactions are important. For industrial combustors, the matrix methodology must be extended for two reasons. First, industrial geometries are complex, and the Matrix Boundary Conditions must be applied to non-plane surfaces. This limitation is overcome thanks to an adjustment procedure. The matrix data on non-plane surfaces is obtained from the well-defined data on plane surfaces, by applying non-dissipative transformations determined either analytically or from an acoustics propagation solver. Second, the reference point of the flame/acoustics model is often chosen inside the injector and a new reference location must be defined if the injector is removed and replaced by its equivalent matrix. In this work, the reference point is replaced by a reference surface, chosen as the upstream matrix surface of the injector. The extended matrix methodology is successfully validated on academic configurations. It is then applied to study the stability of an annular combustor from Safran. Compared to standard Helmholtz computations, it is found that complex flow-acoustic features at dilution holes and injectors play an important role on the combustor stability and mode shapes. First encouraging results are obtained with surface-based flame models.

Résumé en français

Afin de répondre aux enjeux environnementaux, les fabricants de turbine à gaz ont mis au point de nouveaux concepts de chambre de combustion plus propres et moins consommateurs. Ces technologies sont cependant plus sensibles aux instabilités de combustion, un couplage entre acoustique et flamme pouvant conduire à des niveaux dangereux de fluctuations de pression et de dégagement de chaleur. Les solveurs de Helmholtz sont une méthode numérique efficace pour prédire ces instabilités de combustion. Ils reposent sur la description d'un fluide non visqueux au repos, dont le comportement acoustique est régi par une équation d'Helmholtz thermoacoustique, résolue dans le domaine fréquentiel comme un problème aux valeurs propres. Le couplage flamme/acoustique est modélisé

par une fonction de transfert du premier ordre entre les perturbations de dégagement de chaleur et la vitesse acoustique en un point de référence. Bien que performants, les solveurs de Helmholtz négligent l'interaction entre acoustique et vorticité aux coins, car celle-ci dépend d'effets visqueux. Cette interaction pourrait fortement amortir l'acoustique d'une chambre de combustion et la négliger revient à faire des prédictions trop pessimistes voire erronées. Par conséquent, une méthodologie a été mise au point afin d'inclure dans un solveur de Helmholtz l'effet d'interactions complexes entre acoustique et écoulement. Ces interactions étant compactes, elles sont modélisées par des matrices 2×2 et ajoutées au solveur comme des paires de conditions limites : les conditions limites de matrice. Grâce à cette méthodologie, les fréquences et modes d'une configuration académique non-réactive sont correctement calculées en présence de deux éléments où une telle interaction est forte: un orifice et un tourbilloneur. Afin d'être applicable aux chambres industrielles, deux extensions sont nécessaires. Premièrement, les surfaces de matrices doivent pouvoir être non-planes, afin de s'adapter aux géométries industrielles complexes. Pour cela, une procédure d'ajustement a été mise en place. La matrice est mesurée sur des surfaces planes et des transformations non-dissipatives lui sont appliquées afin de la déplacer sur les surfaces non planes. Ces transformations peuvent être déterminées analytiquement ou calculées avec un solveur de propagation acoustique. Le deuxième point concerne le point de référence du modèle de flamme. En effet, celui-ci est souvent choisi à l'intérieur de l'injecteur ce qui pose problème si celui-ci est retiré du domaine de calcul et remplacé par sa matrice. Dans cette thèse, le point de référence est remplacé par une surface de référence. La méthodologie étendue est validée sur des configurations académiques puis appliquée à une chambre annulaire de Safran. Cette nouvelle méthodologie permet de constater que l'interaction écoulement/acoustique au niveau des trous de dilution et des injecteurs joue un effet important sur la stabilité de la chambre mais aussi sur la structure des modes. Les premiers résultats avec une surface de référence pour la flamme sont encourageants.

Acknowledgements

Il y a maintenant un peu plus de trois ans, je terminais mes études en école d'ingénieur et j'avais le choix entre deux projets différents pour la suite : trouver un emploi d'ingénieur, ce à quoi me prédestinait mon parcours, ou bien découvrir le monde de la recherche en faisant une thèse. J'avais gardé de bons contacts avec le CERFACS, où j'avais déjà effectué un petit stage de deux mois. Je n'avais pas non plus du leur laisser un trop mauvais souvenir puisqu'ils m'ont trouvé un beau sujet de thèse sur les instabilités de combustion. A l'époque, je ne savais pas du tout ce que c'était, mais j'avais compris que c'était mal et qu'il fallait l'éviter. La première réunion avec l'équipe travaillant sur cette thématique fut rude. J'en suis repartie en me demandant si je n'aurais pas du faire "sigles incompréhensibles" comme seconde langue vivante au lieu du chinois...

Trois ans plus tard, j'en sais un peu plus sur les instabilités. Je peux suivre une réunion en restant impassible devant les mots "FTF", "N-tau", "omega i", "stabilité linéaire", même si j'ai finalement fait bien plus d'acoustique à froid qu'avec flamme. J'ai même réussi à écrire le manuscrit que vous tenez actuellement entre les mains, et ce ne fut pas sans peine ! Je suis vraiment soulagée d'avoir réussi à arriver au bout du chemin et à apporter ma brique aux travaux sur les instabilités de combustion.

Je voudrais commencer par remercier mon jury de thèse, pour avoir accepté de relire ce travail et pour la pertinence de leurs remarques et conseils. Bien sûr, ce travail n'aurait pas pu voir le jour sans l'aide de mes encadrants, Franck et Thierry au laboratoire, Juan, Sébastien, Alain et Yoann en entreprise. Merci de m'avoir donné l'opportunité de travailler sur ce sujet, d'avoir supporté avec patience mes questions "bêtes et naïves". Merci également pour votre disponibilité et l'accueil chaleureux dont je bénéficie encore. Je remercie aussi les chercheurs seniors qui m'ont souvent fait économiser des semaines voire des mois de travail grâce à leur expérience : Gabriel, Antoine, Olivier, Jérôme, Eleonore, Bénédicte, Marc, Guillaume.

Merci également à mes camarades de promo du CERFACS, qui m'ont aidé dans le travail mais aussi en dehors. Sans vous, ce séjour au CERFACS aurait été bien différent: César pour les sandwichs du péché mignon et les balades en roller, Mélissa pour toujours m'aider à entamer/terminer les pots de thèse et autres buffets, Majd et Romain pour leurs histoires de légumes bios et de co-voiturages dignes des feux de l'amour, Luis et Francis à qui j'ai toujours posé mes questions les plus pourries (schéma num et modèles de combustion turbulente, woohoo !), et enfin bien sûr mon double maléfique Aicha, avec qui on a partagé tellement de choses (le même sujet de thèse initial, la mauvaise LV2, les galères, les heures de sommeil en moins, l'angoisse du "mais que vais-je raconter à Franck ce mois-ci", les visites fréquentes aux salons de thé et aux restos à fondue chinoise). Je voudrais aussi remercier d'anciens thésards du CERFACS qui m'ont bien aidé au début de la thèse: Abdullette, Corentin, Michaël, David, Thomas J. et L., Basti, Greg, Damien, Sandrine, Lucas, Anthony, Manqi, Mélanie (j'espère n'oublier personne !). Merci aussi aux nouveaux thésards pour les bons moments passés ensemble, je vous souhaite au moins autant de succès et de plaisir que pour moi : Dario, Omar (la vedette !), Pierre (machine), Thomas G., Romain Bizzari (je te dois encore une boîte de biscuits...), Lucien, Félix, Maxime (et ta divine madeleine à la crème pâtissière, j'en bave encore), Luc, Fabien et Charlélie. Enfin dans la catégorie thésards, je remercie aussi l'équipe PSC de l'IMFT avec qui j'ai eu l'occasion de travailler : Maxence, Tom, Emilien, Pradip, Christian, Daniel, Laurent, Quentin.

Je voudrais également remercier les membres des autres équipes du CERFACS. L'équipe

CSG, toujours au top pour résoudre nos problèmes informatiques. L'équipe administration, pour faire le plein de bonne humeur et de gentillesse. Et les amis des équipes autres que CFD : Hélène, Géraldine, Oliver, Mélanie, Sophie.

Je remercie de tout coeur ma famille et ma belle-famille, qui m'ont encouragé tout au long de ces trois années parfois difficiles. Il y a eu ceux qui m'ont encouragé à me reposer et qui ont contribué à m'éviter le burn-out. Et ceux qui m'ont encouragé à travailler toujours plus et ont très certainement aidé à ce que je ne finisse pas trop en retard ! Quelque soit la philosophie, le plus important est que nous nous aimons et que nous serons toujours là les uns pour les autres.

Enfin, merci à vous lecteur, qui démarrez ce manuscrit. J'espère que vous le trouverez compréhensible et que vous me pardonnerez les coquilles ou erreurs que vous y démasquerez. Certaines pages auraient probablement gagné à être écrites avec plus d'heures de sommeil...

Bonne lecture !

Contents

Abstract **v**

Acknowledgements **vii**

List of Figures **xi**

List of Tables **xix**

1 Introduction **1**
1.1 New challenges for turbine engines 1
1.2 Combustion instabilities 3
1.3 Numerical prediction of combustion instabilities 5
1.4 The choice of the Helmholtz solver 21
1.5 Hydro-acoustic interactions in thermo-acoustic studies 23
1.6 Thesis objectives and outline 33

2 A methodology to account for hydro-acoustic interaction in a Helmholtz solver **35**
2.1 Matrix representation for hydro-acoustic coupling 35
2.2 Matrix measurement methods 36
2.3 Including a network matrix in a Helmholtz solver : the Matrix Boundary Condition 39
2.4 Code validation of the Matrix Boundary Condition 41

3 Application of the HMBC approach to an academic test rig. **45**
3.1 Target setup: the PRELINTRIG experiment 45
3.2 Description of the validation strategy 47
3.3 Measurement methods 47
3.4 Setup for standard and MBC Helmoltz computations 55
3.5 Application to a diaphragm 56
3.6 Application to a helicopter swirler 62

4 Extending the Matrix Boundary Condition to industrial configurations 65
4.1 Introduction 65
4.2 The validity of complex MBC surfaces 67
4.3 Adjusting plane-wave matrices to complex MBC surfaces 72
4.4 The case of dilution holes 83
4.5 An FTF formulation based on a reference surface 99

5 Application of the MBC methodology to an industrial combustor **107**
5.1 Description of the configuration of interest 107
5.2 Helmholtz computations 109
5.3 Multiperforated plates 114
5.4 Dilution holes 117

5.5 Swirler . . . 122
5.6 Flame representation . . . 131
5.7 Summary of acoustic contributions - Energy balance . . . 139

6 Conclusion **145**

A Navier-Stokes Equations **149**

B Transition expressions between acoustic matrix formulations **153**
B.1 Scattering matrix $\mathbf{S}$ and wave transfer matrix $\mathbf{T_w}$ . . . 154
B.2 Wave transfer matrix $\mathbf{T_w}$ and acoustic transfer matrix $\mathbf{T_a}$ . . . 154
B.3 Acoustic transfer matrix $\mathbf{T_a}$ and mobility matrix $\mathbf{M}$ . . . 154

C Resolution of the Helmholtz equation with the AVSP solver **157**
C.1 The Helmholtz problem . . . 157
C.2 Discretization of $\nabla \cdot \left(\frac{1}{\rho_o(\mathbf{x})}\nabla p\right)\hat{}\,(\mathbf{x})$ for interior nodes . . . 157
C.3 Discretization of $\nabla \cdot \left(\frac{1}{\rho_o(\mathbf{x})}\nabla p\right)\hat{}\,(\mathbf{x})$ for boundary nodes . . . 159
C.4 Discretized Helmholtz equation and fixed point iteration . . . 160

D Analytical models for the acoustic behaviour of an orifice with bias flow **163**
D.1 The model of Howe . . . 164
D.2 The model of Bellucci . . . 165

E Analytical expressions of α for disks and half-spheres **169**

F Analytical models and correlations for the correction length l_{eq} **171**
F.1 Existing models and correlations . . . 171
F.2 Determination of a new correlation for l_{eq} . . . 172

G Acoustic flux balance criterion for the SAFRAN swirler **175**
G.1 Acoustic flux balance for matrix jump conditions . . . 175
G.2 Eigenvalues of $\mathbb{I} - \mathbf{S}^{\dagger\tilde{}}\mathbf{S}$ for the SAFRAN swirler . . . 176

H Helmholtz computations of the SAFRAN combustor with active flames only **179**

I Separation of the acoustic flux contributions in the Helmholtz computation of the SAFRAN combustor **183**

List of Figures

1.1 Air traffic volume from 1950 to 2015. Source : IATA. 2
1.2 Typical NO, HC and CO trends with equivalence ratio in a spark-ignition engine, adapted from [1] 2
1.3 General behavior as the equivalence ratio is reduced near the lean blowout limit (T. Rosfjord, UTRC; published in AGARD Report 820, Schadow et al. 1997). 3
1.4 Combustion instabilities are based on a coupling between heat release and acoustics. When a mean flow is present, hydrodynamic effects also play a role in this coupling. 4
1.5 Typical pressure signal when a combustion instability grows and reaches a limit cycle (from [3]). 4
1.6 Rocket engines of the Apollo Space Program damaged by combustion instabilities 5
1.7 The injector of an LPP design jet combustor, after a combustion instability. 5
1.8 Some numerical approaches for combustion instabilities. The illustrations on top are from (from left to right): [10],[11],[12],[13],[14],[15] 6
1.9 Examples of LES visualizations of combustion instabilities in a) a scaled industrial single burner [21], b) an annular helicopter combustor [24] c) an academic burner [20] 9
1.10 Eigenfrequencies of a 3D burner with swirled injector from [35]. Experiments: o. LNSE: x. 11
1.11 From [36]. Evolution of eigenfrequencies with increasing mean flow (indicated by thick dashed arrows) predicted by an LEE solver (white circles) for a 1D tube with flame. 13
1.12 Example of Helmholtz solver application from [24]. Left: Mode structure predicted by the Helmholtz solver and amplification rate as a function of the FTF time delay. Right, pressure fluctuations from the LES for two time delays, leading to an unstable (solid lines) and stable (dotted lines) combustor. 15
1.13 Acoustic quantities involved in the definition of the impedance. 15
1.14 A compact acoustic element can be represented as a pair of jump conditions. If the jump conditions are linear, they are equivalent to a matrix. 17
1.15 Example of acoustic network representation for a realistic combustor (adapted from [57]). 18
1.16 Flame Transfer Function model. 19
1.17 Flame Transfer Matrix model. 20
1.18 A typical turbojet combustor design. The zero Mach number assumption is valid in between the dashed lines. Non-acoustic effects are expected at the perforated plates, dilution holes, swirler, due to the presence of a shear layer. Spray droplets, heat transfer at walls and structural vibrations also interact with acoustics, but are not studied here. 22

1.19 Three types of hydro-acoustic interactions: 1) Vortex sound in unbounded flows, 2) Vortex sound at rigid boundaries, 3) Conversion of acoustics into vorticity at trailing edges. 23
1.20 Comparison of the growth of the maximum fluctuating velocity u' for a cylinder shear layer, without and with acoustic perturbation at 410 Hz and 490 Hz. From [91] 24
1.21 From [102]: flow field near the sharp edge of a pulsed tube. The pictures (a) - (f) are at $t/T = 0, 0.25, 0.41, 0.53, 0.65$ and 0.90. 25
1.22 Acoustic u'_{ac} (squares) and convective (circles) velocity fluctuations u'_{cv} along the centerline of a diaphragm with mean flow, forced acoustically at 400 Hz, 600 Hz and 1000 Hz. 25
1.23 General damping system in a plane-wave test rig 26
1.24 Vortex sound models are divided into two categories depending on the vorticity representation: vortex sheet (bottom) or discrete vortices (top) 29
1.25 Experimental visualization of vorticity vs vorticity field computed with discrete vortex model. From [116] 29
1.26 Example of damping properties retrieved with vortex sound theory assuming a) a vortex sheet, b) a discrete vortex field. 30
1.27 Quasi-steady jet models 31
1.28 Left: Modulus of scattering matrix coefficients from experiments and the quasi-steady model of [120] at M=0.045. Right: Overview of the test rig and damping element of interest. 31
1.29 Black box matrix models 32

2.1 Illustration of the direct matrix inversion with discrete harmonic forcing method. At least two acoustic states are required and obtained here by changing the forcing location. 37
2.2 Illustration of the system identification with white noise forcing method. . . 39
2.3 Helmholtz computation with Matrix Boundary Condition approach. 40
2.4 Quarter-wave tube configuration for validation of the MBC code 41
2.5 Mesh for the standard Helmholtz computation of the quarter-wave tube. . . 42
2.6 Mesh for the Helmholtz computation with MBC of the quarter-wave tube. . 43
2.7 Mode structure (modulus and phase of complex pressure amplitude) along the axis of the quarter-wave tube, for the first two modes. 43

3.1 Sketch of the experimental setup. The junction may contain either a diaphragm or a swirler. Three microphones are placed upstream and downstream of the element. The loudspeaker position changes depending on the type of measurement (top figure: matrices, bottom figure: acoustic modes). 46
3.2 Acoustic elements: (a) Diaphragm, (b) Swirler. 46
3.3 MBC validation strategy with the four axes of comparison. Annotated blocks are detailed in the indicated sections. 48
3.4 $\mathcal{E}(\omega)$ spectra for the diaphragm at $U = 0.17$ m/s, normalized by the fitted value at ω_0. Two modes are displayed with the best fit for f_0 indicated in the title, and the uncertainty estimated with a 95% confidence interval. . . 50
3.5 Description of the four configurations used in this study. For example, the second configuration is composed of the 3 ducts while the acoustic element is located in the junction between ducts 2 and 3 ; the outlet is open. 50
3.6 Geometry for the pulsed computations of the diaphragm, and zoom of the mesh near the diaphragm aperture. 52

3.7 Geometry for the pulsed computations of the swirler, and zoom of the mesh near the swirler. 52
3.8 Modulus (left) and phase (right) of the AMT outlet reflection coefficient. A cut-off frequency can be defined as $f_c = \frac{K}{4\pi}$ at which the phase is equal to $\pi + \phi$ with $\phi = \tan^{-1}(\frac{1-R_K}{1+R_K})$. 54
3.9 Typical LES temporal signals and DMD reconstruction for pressure (left) and axial velocity (right) (swirler mode at f = (284.9 - 13.2i) Hz and U = 0.34 m/s). 54
3.10 Acoustic mode with a swirler as acoustic element, f = (284.9 - 13.2i) Hz, at $U = 0.34$ m/s. Fit of a DMD complex pressure field as a sum of plane waves. 55
3.11 Boundary conditions for (a) the AVSP complete runs, where the acoustic element is meshed and wall boundary conditions are applied and (b) MBC runs, where the acoustic element is replaced by its 2-port representation. . . 56
3.12 Diaphragm case - Comparison C1 in Fig. 3.3. Scattering matrix coefficients for $U = 0.34$ m/s. Experimental coefficients (from IMFT) are plotted as white circles with error bars and LES data is denoted by black squares. Howe's model [111] coefficients are also shown for reference (dashed lines). . 58
3.13 Diaphragm case - Comparison C1 in Fig. 3.3. Acoustic flux balance criterion based on the eigenvalues of $\mathbb{I} - \mathbf{S}^\dagger\mathbf{S}$ where $\mathbf{S}$ is the scattering matrix. When both eigenvalues are positive, $\mathbf{S}$ dissipates acoustic energy. 59
3.14 Diaphragm case. Comparison of standard and MBC AVSP eigenfrequencies with the experimental (C2-EXP, left) and LES (C2-LES, right) results, at $U = 0.34$ m/s. The experimental frequencies are plotted with error bars, obtained in Section 3.3.1 59
3.15 Diaphragm case. Comparison C2-EXP, C2-LES and C3. Evolution of the eigenfrequencies of mode 1 and mode 2 with the bulk velocity U. Each column corresponds to a mode. Real parts of the eigenfrequency are featured on the top row, imaginary parts are on the bottom row. 60
3.16 Diaphragm case. Comparison C2-EXP, C2-LES and C3. Evolution of the eigenfrequencies of mode 3 and mode 4 with the bulk velocity U. Each column corresponds to a mode. Real parts of the eigenfrequency are featured on the top row, imaginary parts are on the bottom row. 60
3.17 Diaphragm case. Comparison of the second eigenmode experimental structures at $U = 0.34$ m/s with the mode structures obtained from a standard Helmholtz computation and with the MBC approach (C2-EXP in Fig. 3.3). 61
3.18 Diaphragm case. Comparison of the second eigenmode LES structures at $U = 0.34$m/s with the mode structures obtained from a standard Helmholtz computation and with the MBC approach (C2-LES in Fig. 3.3). 61
3.19 Swirler case. Structure of mode A at $U = 0.34$ m/s: Standard Helmholtz (black circles), Helmholtz solver with MBC (white squares) and LES results (grey triangles). 63
3.20 Swirler case. Structure of mode B at $U = 0.34$ m/s: Standard Helmholtz (black circles), Helmholtz solver with MBC (white squares) and LES results (grey triangles). 63
3.21 Swirler case, mode A. Frequencies obtained from 50 additional Helmholtz computations where the coefficients were "randomly" varied (see body text). The nominal result is recalled as a white square. 64
3.22 Swirler case. Structure of mode A when varying the scattering matrix coefficients (grey curves). The nominal result of Fig. 3.19 is recalled in black. The modified matrix coefficient is indicated for the outermost curves. 64

4.1 Extensions of the HMBC methodology required for an industrial combustor. 65
4.2 MBC surfaces chosen in this thesis for a complex combustor geometry . . . 66
4.3 Validation of complex MBC surfaces on the swirler in a tube configuration. Two HMBC computations are performed : one with plane coincident MBC surfaces (top) and one with complex MBC surfaces (bottom). Both are compared to a reference standard Helmholtz computation where the complete geometry is discretized. 68
4.4 Matrix 1 and Matrix 2 coefficients. 69
4.5 Overview of the meshes used in the Helmholtz computations of Tab. 4.1. From top to bottom : runs 1, 2, 3, and 4. 70
4.6 First four eigenmodes for the computations of Tab. 4.1. The modulus and argument of pressure is plotted as a function of the axial coordinate. 70
4.7 Modulus of axial acoustic velocity amplitude for the first mode of run 2 and run 3. 71
4.8 How can the matrix measured at plane transverse cuts in LES be used in a Helmholtz computation with complex MBC surfaces ? 72
4.9 The matrix data measured at surfaces S_m cannot be applied directly to the surfaces S_a and provide the correct results. For this, the matrix needs to be adjusted from S_m to S_a. 72
4.10 Geometries used for the error assessment of MBC surface averaged quantities. From top to bottom : geometry 1, 2 and 3. MBC surfaces are represented in red and blue. 74
4.11 Matrix linking surface averaged value of $\hat{p}$ and $\rho_o c_o \hat{u}$ on MBC patches. Geometry 1 with mesh size dx_1. (Top: modulus, Bottom: phase). 75
4.12 1D velocity discontinuity : theory versus AVSP discretization. 75
4.13 Absolute value of axial velocity at the downstream MBC surface (black lines) and surrounding wall. Geometry 1 with dx_1. 76
4.14 Real MBC surface $\mathcal{S}$ (in dark grey) versus effective MBC surface, approximately extended by $\mathcal{C}dx$ (in light grey). 76
4.15 Measurement method for $\mathcal{T}_u$ and $\mathcal{T}_d$ without error on T_{22}. 77
4.16 Coefficient T_{22} for $\mathcal{T}_d$ measured on geometry 1 with mesh size dx_1, using surface averages (crosses) or an intermediate MBC surface as presented in the main text (circles). The expected value is recalled in solid lines. 78
4.17 $\mathcal{T}_u$ and $\mathcal{T}_d$ coefficients as a function of frequency (top: absolute value, bottom: argument), linking the complex MBC surfaces of Fig. 4.3, top, to the plane coincident surfaces of Fig. 4.3, bottom. 79
4.18 Mesh for the measure of $\mathcal{T}_u$ (top) and $\mathcal{T}_d$ (bottom) for the IMFT swirler (complex MBC in red, plane MBC in blue). 80
4.19 Coefficients of the adjusted matrix $\mathbb{T}_a$ (top: absolute value, bottom: argument), compared to the original matrix $\mathbb{T}_m$. (For absolute values, the left y-scale corresponds to $\mathbb{T}_m$ and the right one to $\mathbb{T}_a$.) 81
4.20 Third and fourth eigenmode structures from HMBC computations with $\mathbb{T}_m$, $\mathbb{T}_a$ and from a standard Helmholtz computation. 82
4.21 Orifice matrix measured at plane surfaces (dashed lines) and at orifice surfaces (dotted lines). 83
4.22 1D acoustic network decomposition of domains (a) between S_{mu} and S_{au}, (b) between S_{md} and S_{ad} 84
4.23 Measurement of l_{eq} for the adjustment procedure of orifices. 85
4.24 Overview of the meshes for the numerical computation of $\mathcal{T}_u$ and $\mathcal{T}_d$ for the IMFT orifice (top: coarse, botom: fine). MBC surfaces linked by an identity matrix are displayed in red and blue. 87

4.25 Numerical and analytical values of $\mathcal{T}_d^{-1}$ on coarse mesh 88
4.26 Numerical and analytical values of $\mathcal{T}_d^{-1}$ on fine mesh 89
4.27 Eigenfrequencies of a 3D-HMBC computation of the orifice of Chapter 3 with numerical $\mathcal{T}_u$ and $\mathcal{T}_d$ (black triangles). The frequencies found with a 1D-HMBC computation are recalled as black crosses. 90
4.28 Influence of the model for l_{eq} on the eigenfrequencies of the 3D-HMBC computation (see Tab. 4.6). 90
4.29 Correction length l_{eq} from various models. 91
4.30 Influence of the model for l_{eq} on the eigenfrequencies of the 3D-HMBC computation (see Tab. 4.6). 91
4.31 Third and fifth mode for the 3D-HMBC computations on the coarse mesh (see Tab. 4.6). 92
4.32 Third and fifth mode for the 3D-HMBC computations on the fine mesh (see Tab. 4.6). 92
4.33 Outer casing of a real annular combustor (courtesy of Safran Helicopter Engines) showing the difficulty to define the confinement of a dilution hole in a real geometry. 93
4.34 Comparison of R_a and X_a with LES and experiments, for $\sigma = 0.048$ and $\sigma = 0.012$. 95
4.35 $\ell - l_{eq}$ against Strouhal number, for $\eta = 0.0, 0.4, 1.0$ and $\sigma = 0.0, 0.0625, 0.2$. 95
4.36 R_a and X_a against Strouhal number, for $\eta = 0.0, 0.4, 1.0$ and $\sigma = 0.0, 0.0625, 0.2$. 96
4.37 Orifice geometry on which the effect of σ on the HMBC solution is assessed. The 3D-HMBC surface is displayed in red. 97
4.38 Eigenfrequencies of the HMBC computations with Bellucci model. The Strouhal numbers are indicated in the top horizontal axis. 97
4.39 Eigenmodes of the HMBC computation with the Bellucci model. 98
4.40 Reference point vs reference surface in the FTF definition. 99
4.41 Reference setup of the Rijke tube (top: mesh, bottom: flame zone in grey with reference point and reference vector). 100
4.42 MBC setup of the Rijke tube (top: mesh, bottom: flame zone in grey with reference surface visualized with surface normals). 100
4.43 Eigenmodes of the Rijke tube with point-based FTF and surface-based FTF 101
4.44 Annular PBC geometry with four burners. 102
4.45 Transverse representation of the PBC configuration with reference point (left) and reference surface (right). 102
4.46 One sector of configuration 1 (left) and configuration 2 (right). The reference point / surface is highlighted in red. 103
4.47 Structure of mode P1 with no FTF (top: configuration 1, bottom: configuration 2). The color field and lines correspond to $|\hat{p}| \cos[arg(\hat{p})]$. 104
4.48 Modulus of axial and transverse velocity along a burner centerline, close to the reference location (red vertical line) for configuration 1 (solid lines) and configuration 2 (dotted lines). 105
4.49 Structure of mode P1 with point-wise FTF (top) and surface FTF (bottom). The color field and lines correspond to $|\hat{p}| \cos[arg(\hat{p})]$. 106

5.1 Annular combustor of interest. Front (left), side (middle) and rear (right) views. 108
5.2 Design of the combustor of interest. The high-pressure distributor is replaced by a converging nozzle. For confidentiality reasons, this image is rescaled and some geometrical details are hidden. 108

5.3 Top: Time samples of the global heat release (black) and velocity in the injector (grey) from a mono-sector reactive LES. Both signals are normalized by their time average. Bottom: FFT amplitudes of the normalized heat release (black) and velocity (grey). The amplitude corresponding to 0 Hz was removed to improve clarity. 109
5.4 Standard and HMBC geometries for the Helmholtz computations. 110
5.5 Mean flow fields for the Helmholtz computations of the industrial combustor. 112
5.6 First azimuthal mode at $f = 292.7 - 0.0i$ Hz for R0. 113
5.7 A tilted perforation, with a streamwise angle α_1 and a compound angle α_2. 115
5.8 Straightened perforate used for the analysis of perforated plates 115
5.9 First azimuthal mode at $f = 293.0 - 0.90i$ Hz for R1. 116
5.10 Density and speed of sound in the transverse cut of a dilution hole (from an average LES solution). The color scale is the same as in Fig. 5.5. 118
5.11 Matrix of one dilution hole in R2a, R2b, R2c and R2d. 119
5.12 First azimuthal mode at $f = 292.5 - 1.01i$ Hz for R1. 120
5.13 First azimuthal mode at $f = 291.7 - 9.83i$ Hz for R2a. 121
5.14 Geometry and boundary conditions for the LES computation of the industrial swirler matrix. 122
5.15 Overview of the mesh for the LES of the swirler in a tube (12 millions of nodes). 123
5.16 Lengths used to define the size of the tube cross-section in Fig. 5.14.The combustor miniatures indicate the location of the cut. In each cut, the average of the two lengths displayed is used to define the matrix configuration. 123
5.17 Reference plane from which the target pressure at the outlet of Fig. 5.14 is extracted. The color scale corresponds to the pressure field (blue : low, red : high). 124
5.18 Flow fields of the non-reactive swirler computation without acoustic forcing. All variables except for the axial Mach number are normalized by their spatial average. 125
5.19 Pressure and velocity signals up- and downstream of the swirler. Each signal is normalized by the time average and plotted with the fit from the DMD (sum of the carrier at 0 Hz and fluctuation at 290 Hz). 126
5.20 Pressure amplitude and phase from DMD (points) and plane-wave fit (lines). The grey zone represents the swirler location. 126
5.21 Left: example of matrix surfaces for the swirler. The upstream surface is a portion of cylinder enclosing the swirler. The downstream surface is a disk. Right: Three sets of matrix surfaces S1, S2 and S3, shown in the transverse cut of one sector. The downstream surface is common to S1, S2 and S3. . . 127
5.22 Swirler of the industrial combustor: non-dissipative plane matrix measured with AVSP-f (lines) and dissipative plane matrix from the LES (crosses). Top: modules. Bottom: phases. 128
5.23 Procedure to readjust the speed of sound and density when using the matrix of a non-reactive LES with a mean flow field from a reactive LES. 129
5.24 First azimuthal mode at $f = 281.7 - 14.4i$ Hz for R3b computation. The mode structure for R3a is similar. 130
5.25 Flame zone in red (with non zero FTF parameters) for R4x and R5x computations. 132
5.26 Transverse cut of the mesh used in the reactive LES of the industrial combustor. 132
5.27 Points (each set of probe is represented with only one probe) 134

5.28 Reference velocities from probes (top) and surface averaging (bottom). All signals are normalized by their time average. 134
5.29 Heat release and surface averaged velocity signals with the DMD and FFT reconstructions. All quantities are normalized by an arbitrary constant U_o. 136
5.30 Heat release fluctuations $\dot{Q}'(t)$ against transformed velocity fluctuations $Nu'(t-\tau)$ for surface S1, with the FTF parameters obtained from Fourier analysis (R=0.54). 136
5.31 First azimuthal mode at $f = 272.6 + 2.01i$ Hz for R5 computation. 139
5.32 Complex frequencies of the first azimuthal mode for the Helmholtz computations of Tab. 5.1 140
5.33 Contributions to the acoustic energy balance as defined in Eq. (5.31). The sum of the three first columns (acoustic flux $-\frac{\int_T F dt}{E(0)}$, heat release $\frac{\int_T S dt}{E(0)}$, and error ϵ defined in Eq. (5.29)) is equal to the last one (total energy change $\frac{E(T)}{E(0)} - 1$). 143

B.1 Inward normal convention in the Helmholtz solver, compared with usual choice made in acoustic network analysis. 153

C.1 Triangle cell element in 2D 158
C.2 2D interior node j with its dual cell in grey. 158
C.3 2D boundary node with its dual cell in grey. The boundary edge is represented by hatched lines. 159
C.4 Fixed point iteration in AVSP. For clarity, the limiter Δ is not represented. 161

D.1 Quantities of interest for the acoustic behavior of an orifice in bias flow. . . 163
D.2 Evolution of Γ_{St} and Δ_{St} with the Strouhal number. 165
D.3 Reactance of an orifice with Howe's model and Bellucci's model. 166
D.4 LES transfer matrix vs Howe's model and Bellucci's model for the orifice of Chapter 3 ($U = 0.34$ m/s). Top: real part. Bottom: imaginary parts. In grey crosses, the result for the modified Bellucci model of Chapter 4 is also indicated. 167
D.5 LES transfer matrix vs Howe's model and Bellucci's model for the orifice of Chapter 3 in a larger confinement tube ($U = 0.34$ m/s). Top: real part. Bottom: imaginary parts. In grey crosses, the result for the modified Bellucci model of Chapter 4 is also indicated. 168

F.1 Typical orifice geometry. 171
F.2 Matrix of configuration A0 (crosses) and fits for l_{eq} and σ (solid lines). . . . 173
F.3 Evolution of l_{eq} with $\sqrt{\sigma}$ for different mesh resolutions (crosses) and associated linear fit (solid lines). 174
F.4 Evolution of A and B with η. 174

G.1 Acoustic two-port with different up- and downstrea thermodynamic properties and sections. 175
G.2 Eigenvalues of $\mathbb{I} - \tilde{\mathbf{S}}^\dagger \tilde{\mathbf{S}}$ for the plane matrices (left), adjusted matrices (middle) and adjusted matrices with temperature jump (right). On each plot, the eigenvalues of the adjustment matrices are also recalled. 177

H.1 Modulus of pressure in a transverse cut and phase of pressure seen from the back of the combustor for R4a, R4c, R4d and R4e. 181

I.1 Energy balance for the most amplified mode of R5a, with (left) and without (right) correction. 185

List of Tables

2.1 Examples of acoustic 2-ports formulation [126]. 36
2.2 First five eigenfrequencies (in Hz) of the quarter-wave tube with $Ls + L_1 + L_2 = 1.0$ m. 42

3.1 Reflection coefficient R_{LES} effectively measured in the diaphragm AMT computations, vs theoretical values with radiation losses R_{rad} 53
3.2 Eigenfrequencies (in Hz) for the $U = 0$ m/s, in the experiments and the AVSP computation of the complete geometry with no matrix dissipation. The inlet and outlet impedances are given in Eq. (3.10) and Eq. (3.11) and include the end corrections plus radiation losses if $\alpha = 1$. 57
3.3 Swirler case. Scattering matrix coefficients from LES for $U = 0.34$ m/s and eigenvalues of $\mathbb{I} - \mathbf{S}^\dagger\mathbf{S}$ 62
3.4 Complex frequencies (in Hz) of mode A and mode B with the swirler at $U = 0.34$ m/s, from LES, Helmholtz solver with LES matrix and standard Helmholtz solver. The relative difference between Helmholtz and LES results is also displayed. 64

4.1 Helmholtz computations for the validation of complex MBC surfaces. 68
4.2 Eigenfrequencies (in Hz) of the Helmholtz computations of Tab. 4.1 69
4.3 Error on T_{22} in $\mathbb{T}_{\text{surface}}$. The effectively measured value can be predicted with Eqs. E.1 and E.2 76
4.4 Eigenfrequencies of the HMBC computations with $\mathbb{T}_m$ and the adjusted matrix $\mathbb{T}_a$. The solutions of a standard Helmholtz computation are also recalled 78
4.5 Properties of the meshes used for the numerical computation of $\mathcal{T}_u$ and $\mathcal{T}_d$. 86
4.6 List of HMBC computations with different values of l_{eq}. 91
4.7 Eigenfrequencies of the Rijke tube with a point-based FTF (reference geometry) and surface-based FTF (MBC geometry). 101
4.8 Dimensions, mean flow fields and flame parameters for the 4 burners PBC configuration. 103
4.9 Complex eigenfrequencies for the first azimuthal mode of the chamber with FTF. The relative difference is normalized using the values of configuration 1.105

5.1 Helmholtz computations performed on the industrial setup and their characteristics. Elements can be either "resolved" elements, i.e. discretized in the geometry and computed by the Helmholtz solver, or modeled with a matrix model. For the swirler, two matrices are measured: a "passive" one, representing the acoustic behaviour in the absence of mean flow and viscosity, and an "active" one, containing the flow-acoustic interaction. . . . 111
5.2 List of R2x computations. 117
5.3 Frequencies of the first azimuthal mode for R2x computations. The result of R1 is also recalled. 120

5.4 Scattering matrix coefficients and eigenvalues of $\mathbb{I}-\mathbf{S}\dagger\mathbf{S}$ of the swirler of the industrial configuration at 290 Hz. The notation is the same as for Tab. 3.3. 127
5.5 List of R3x computations 127
5.6 First azimuthal mode frequency for R3x computations. The result of R2a is also recalled. 129
5.7 FTF gain and delay, from an FFT filtering at 290 Hz and from the DMD mode at 298 Hz. The FTF parameters N and τ are defined in Eq. (5.9). The correlation coefficient CC is defined in Eq. (5.11). 135
5.8 R5x computations with flame, dilution holes and swirlers models. 137
5.9 Frequencies of the first order azimuthal modes of R5x and R6 computations. 138

F.1 Configurations used for the determination of a new correlation for l_{eq} 172
F.2 Discretized orifice radius a for each mesh size. 173

H.1 List of R4x computations (active flame in a simplified geometry without dissipative elements). 179
H.2 Frequency of the first azimuthal mode in R4x computations. 180

Chapter 1

Introduction

This thesis revolves around a central question:

What is the impact of acoustic-mean flow interactions on combustion instabilities ?

In acoustic analysis indeed, these interactions are often neglected because the fluid is assumed inviscid and at rest. However, the interaction between the mean flow can be the source of important acoustic damping, especially at section changes. From this point of view, a combustor is full of potential dampers as will be shown in this chapter. The impact of these elements on the structure of combustion instabilities can be important but is usually not assessed.

Before starting to answer the central question, it is important to understand the motivations behind this topic and the state of the art. This first chapter will therefore explain:

- What combustion instabilities are and why the industry is interested in them (Sections 1.1 and 1.2),
- How combustion instabilities can be predicted numerically and the limitations of the numerical solvers available in the litterature (Sections 1.3 and 1.4),
- What kind of acoustic-flow interaction is examined in this work and why it is important for the numerical prediction of combustion instabilities (Section 1.5)

This chapter ends with the presentation of the thesis objectives and the outline of this manuscript, where the strategy followed to answer the central question is detailed (Section 1.6).

1.1 New challenges for turbine engines

Air transportation has experienced a high growth rate since the 1970s, (Fig. 1.1). This raises a number of issues, in particular regarding the impact of the ever-increasing traffic on people and climate. For this reason, strict environmental objectives have been set for civil aviation. In Europe for example, the Advisory Council for Aeronautics Research (ACARE) requires that by 2020:

- Fuel consumption and CO_2 emissions per passenger kilometer are reduced by 50%,
- Nitrogen oxides (NOx) emissions are reduced by 80%,
- Perceived noise is reduced by 50%.

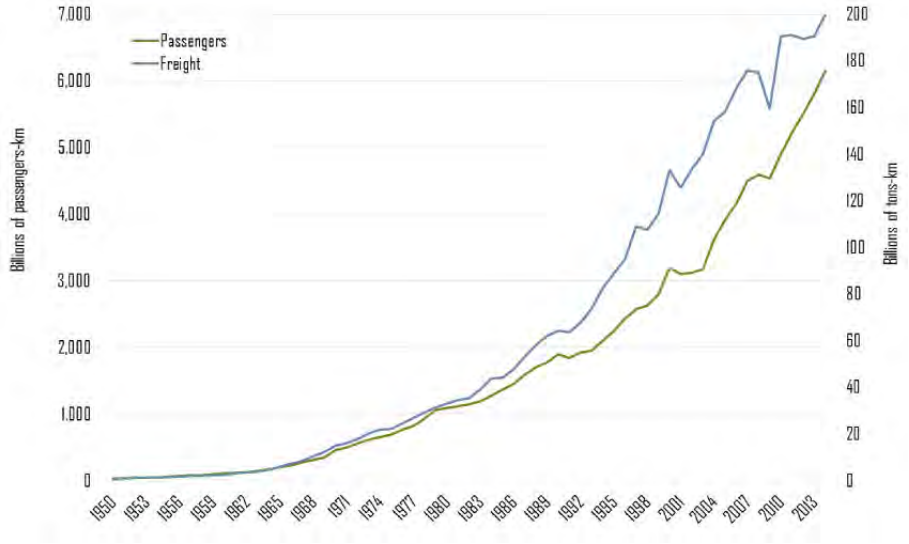


FIGURE 1.1: Air traffic volume from 1950 to 2015. Source : IATA.

These targets can be met mainly by improving the engines, and especially the combustion process in the case of pollutants. A key parameter in the formation of NOx and CO is the flame temperature. Indeed, different chemical mechanisms are active for different flame temperatures, and produce more or less pollutants. At first order, the flame temperature, and consequently NOx and CO emissions, is driven by the equivalence ratio (Fig. 1.2). As Fig. 1.2 shows, the equivalence ratio shoud be located in a lean range in order to reduce both NOx and CO emissions.

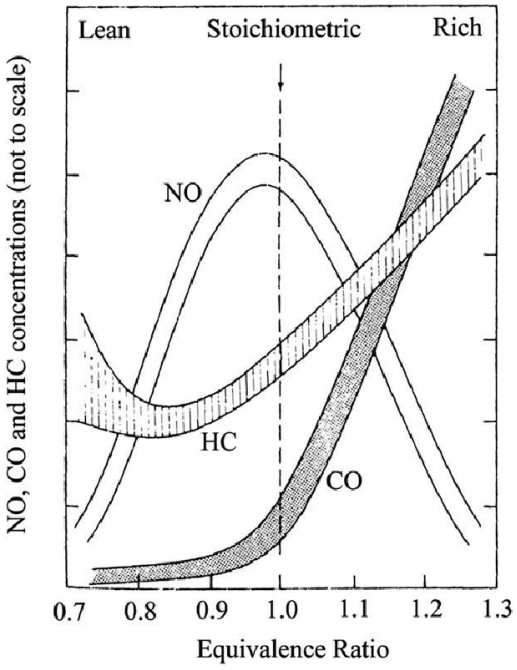


FIGURE 1.2: Typical NO, HC and CO trends with equivalence ratio in a spark-ignition engine, adapted from [1]

In modern turbine engines, this is achieved by using Lean Premixed Prevaporized (LPP) technologies, which rely on enhanced fuel injection and mixing to achieve efficient and clean combustion. Examples can be found in [2]. However, such combustors operate close

to the Lean Blow Out (LBO) limit and are prone to a phenomenon known as combustion instabilities (Fig. 1.3).

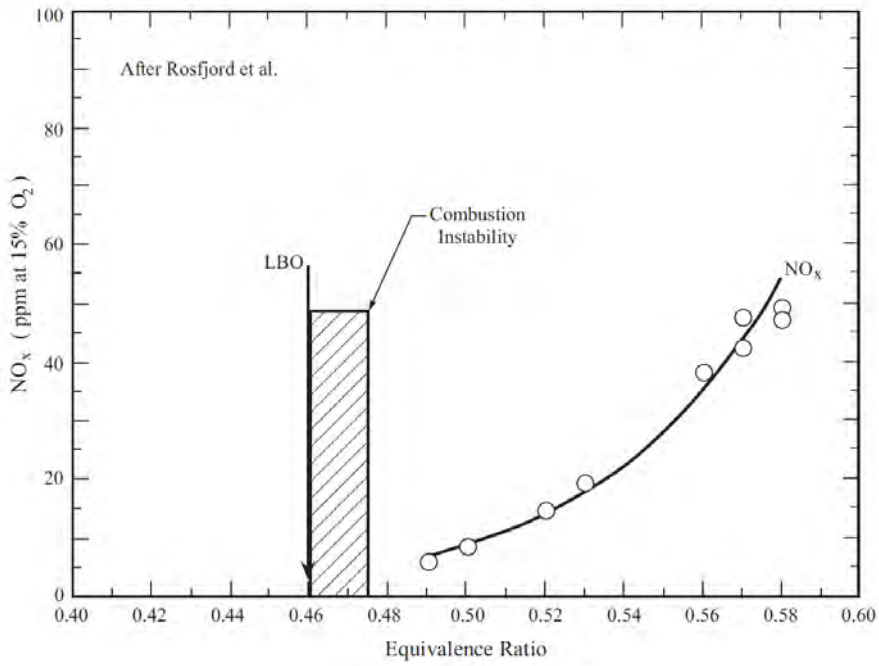


FIGURE 1.3: General behavior as the equivalence ratio is reduced near the lean blowout limit (T. Rosfjord, UTRC; published in AGARD Report 820, Schadow et al. 1997).

1.2 Combustion instabilities

A flame is characterized by an important heat release, leading to a gradient of temperature and density across the flame front. If the heat release starts to fluctuate (due to air or fuel flow rate variations for example), perturbations of density are created, and act as a source of sound. When the flame is enclosed, this sound is reflected back and generates new heat release fluctuations by modulating the air mass flow rate, and new sound waves, initiating a new cycle. This is the thermoacoustic coupling as illustrated in Fig. 1.4. When acoustic perturbations are in phase with heat release fluctuations, an instability, called combustion or thermoacoustic instability, is created [3, 4, 5, 6].

The phenomenon is not new and was observed experimentally since the 19th century [7]. Lord Rayleigh was one of the first to provide a detailed analysis of the coupling mechanism [6], which can be condensed into a simple criterion:

$$\int_V \overline{p'q'} dV > 0 \tag{1.1}$$

where p' and q' are the fluctuations of pressure and heat release. The Rayleigh criterion indicates that an instability can exist only if pressure and heat release fluctuations are in phase. When such an instability is triggered, the acoustic signals, for example the pressure (Fig. 1.5), follow a typical evolution with three phases:

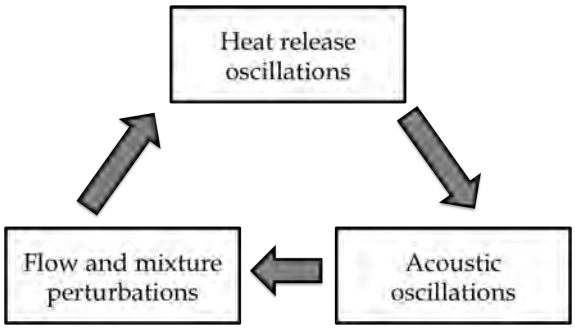


FIGURE 1.4: Combustion instabilities are based on a coupling between heat release and acoustics. When a mean flow is present, hydrodynamic effects also play a role in this coupling.

1. Linear regime : In the first instants of the instability, acoustic and heat release fluctuations are related to each other by a constant proportionality factor, and increase at an exponential rate.
2. Non-linear transition : At some point, saturation effects come into play and slow down the growth rate. An over-shoot is often observed at this stage.
3. Limit cycle : When the growth rate becomes equal to the global damping rate of the combustor, the amplitude of the fluctuations reaches a constant value.

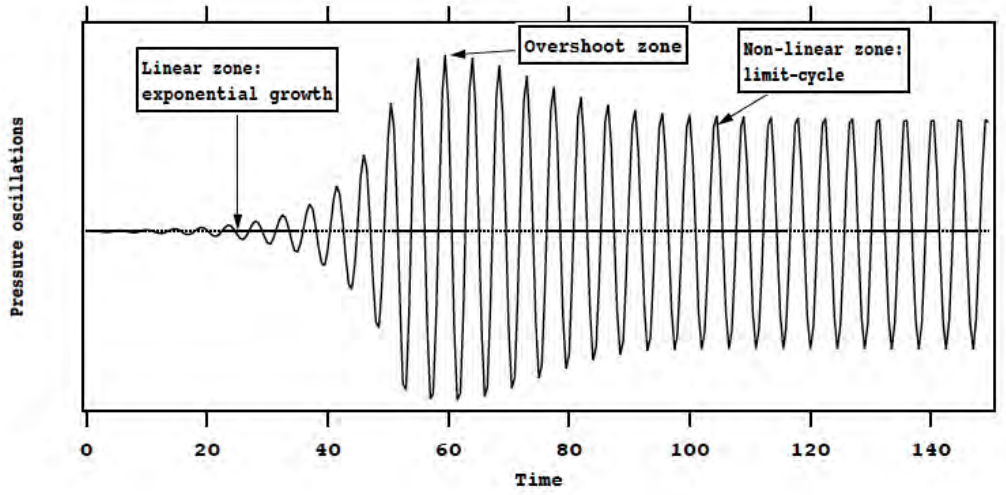


FIGURE 1.5: Typical pressure signal when a combustion instability grows and reaches a limit cycle (from [3]).

From an industrial perspective, combustion instabilities should be avoided since the large pressure and heat release fluctuations associated can cause great damage to the engine (Figs 1.6 - 1.7). First observed in rocket engines [5], combustion instabilities are now also a problem for turbine engines, since the low equivalence ratio of LPP technologies makes the flame more sensitive to flow fluctuations [5, 8].

Control of combustion instabilities *a priori* is possible although difficult. Some solutions include the use of fuel staging, acoustic dampers, improvement of the mixing system, a modification of the injector and/or chamber design, and even the introduction of active control devices [2, 9]. However, none of the above solutions ensures an absolute absence of instabilities at all operating points. Each specific configuration should ultimately be tested

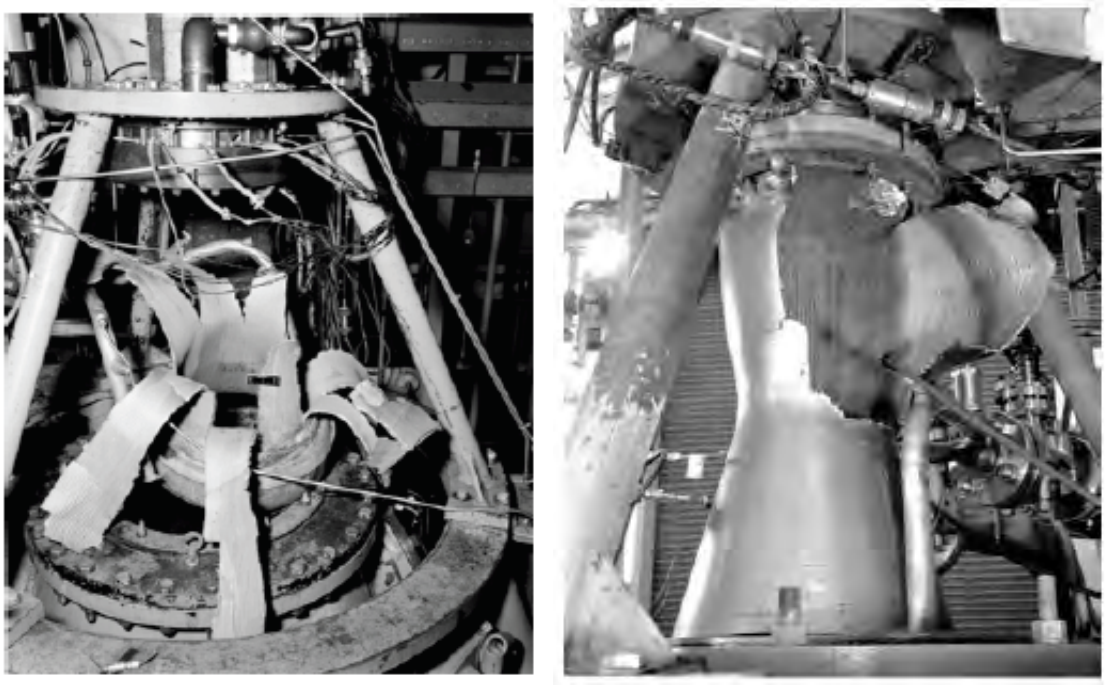


FIGURE 1.6: Rocket engines of the Apollo Space Program damaged by combustion instabilities

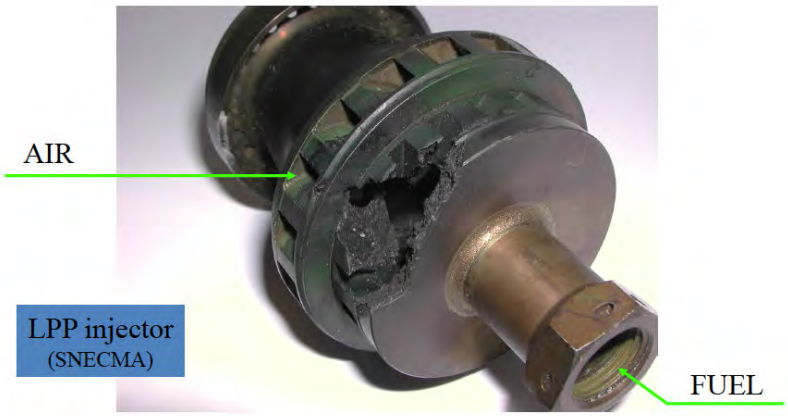


FIGURE 1.7: The injector of an LPP design jet combustor, after a combustion instability.

experimentally but this can be difficult and very expensive. An alternative or complement is to check the stability of the combustor at the design stage, with the use of cost-effective numerical tools.

1.3 Numerical prediction of combustion instabilities

In the field of combustion instabilities (and in general), numerical solvers can complement experiments in two ways:

Detailed measurements Measurements in a combustor are generally difficult and costly,

because of the high temperature (and pressure), not to mention the destructive effects of the instability itself. Therefore, the experimenter only has access to global quantities and a few local probes, while a numerical computation easily provides the structure of the instability at any point in the chamber, at any time. This additional data is of great help in the understanding and analysis of combustion instabilities. However, meaningful data is obtained only if the numerical computation is performed with accurate models and schemes, and for long computational times. Accuracy takes precedence over CPU cost in this case.

Fast and cheap results In the highly competitive energy and transport industries, being able to predict the stability of a combustor in the shortest time and at the lowest cost is critical. If so, CPU cost must be reduced by retaining only the key parameters and physics in the numerical tool. Thanks to the gain of CPU time, this type of tool can be used for sensitivity analysis for example, where a baseline setup is run several times while varying the input parameters, or even the geometry.

At one end of the spectrum lies Large Eddy Simulation. It is a high-fidelity representation of thermoacoustic instabilities, but requires heavy computational capacities. At the other end, analytical models based on a drastically simplified representation of flame and acoustics are able to provide stability results on a regular laptop within minutes. In between, there is a wide range of descriptions of intermediate accuracy and CPU cost (Fig. 1.8). The 3D Helmholtz approach is one of them and is favored in this thesis. This section explains why, by reviewing some of the most important numerical tools of Fig. 1.8.

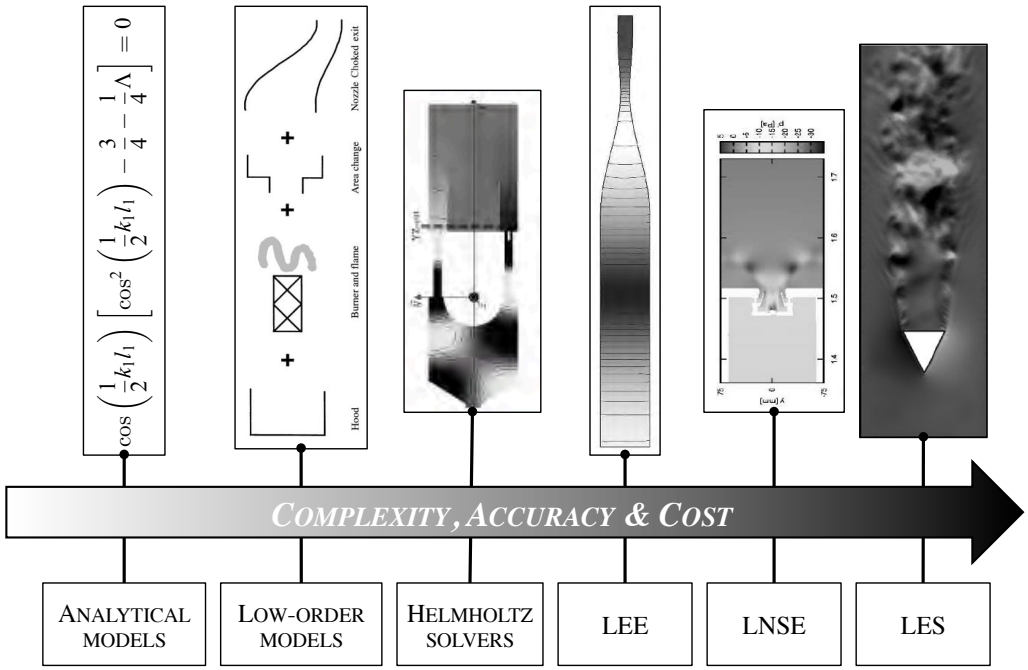


FIGURE 1.8: Some numerical approaches for combustion instabilities. The illustrations on top are from (from left to right): [10],[11],[12],[13],[14],[15]

Among these tools, time domain and frequency domain methods are distinguished. Time domain simulations attempt to reproduce the instability chronologically, from triggering to limit cycle. These solvers have the advantages of providing an intuitive "what you see is what you get" type of solution, and are well suited to describe all phases of the instability, from the linear regime to the limit cycle. However, they provide a partial description of instabilities. Only the most amplified mode for the chosen operating point is visible.

Latent unstable modes (i.e. modes that could be unstable for other operating conditions) are dominated and may not appear at all [16].

In order to have information on all modes, frequency-domain tools can be used. Assuming that all fluctuations are periodic, these tools provide the frequency, shape and amplification rate of all unstable modes compatible with the combustor configuration. In addition, acoustic boundary conditions are easier to take into account in the frequency domain [17]. On the other hand, frequency-domain tools are often limited to the linear regime, although extensions to the non-linear regime have been developed [18].

1.3.1 Large Eddy Simulation

Of all the numerical tools presented in Fig. 1.8 Large Eddy Simulation methods are the most accurate. LES methods rely on the Navier-Stokes equations of mass, momentum and energy, describing a compressible, viscous, reactive flow in time domain. The Navier-Stokes equations are the starting point of all the models presented here and are provided in Appendix A. They constitute an excellent model of turbulent fluids. However, they cannot be solved analytically, because of the nonlinear term $u_i u_j$[1]. Even the numerical resolution of Navier-Stokes equations, also known as *Direct Numerical Simulation* (DNS) involves heavy computational capacities as it requires very small mesh sizes and time steps in order to solve for the finest scales of the flow.

The mesh and time step requirements can be greatly decreased if all quantities f are decomposed into an average (steady) part $\bar{f}$ and a turbulent fluctuation f'. Instead of looking at f as in DNS, the behaviour of the smoother, large-scale averaged quantities $\bar{f}$ is analyzed by solving the averaged Navier-Stokes equations. This is the approach followed in *Reynolds Averaged Navier-Stokes* (RANS) techniques. RANS techniques have a few drawbacks though. First, unclosed quantities, linked to the unresolved components f', appear during the averaging procedure and must be closed. This is done using empirical models that are often case dependent. Second, fully unsteady flows such as combustion instabilities cannot be studied with RANS because only averaged quantities are resolved.

An intermediate approach consists in filtering the Navier-Stokes equations. All quantities are now decomposed into a filtered and an unfiltered component, $f = \breve{f} + f''$.

$$\breve{f}(\mathbf{x}) = \int f(\mathbf{x}') F_\Delta(\mathbf{x} - \mathbf{x}') d\mathbf{x}' \tag{1.2}$$

where F_Δ is the LES filter. The filter can be defined in space, time or spectral domain, with different shapes (box, gaussian, etc.) but it always has a cut-off nature, aimed at removing the smallest scales of the flow. If defined in space for example, F discards all scales smaller than a threshold Δ, the mesh size in practical computations.

The filtered quantities are therefore smoother than the original ones, but retain the characteristics of the largest structures. This filtering operation is not as simple as it may seem. For example, the filtered value of an LES perturbation is not zero $\breve{f''} \neq 0$. Similarly, the filtering operator is not idempotent $\breve{\breve{f}} \neq \breve{f}$. Moreover, filtering and derivative operators do not commute if the filter size varies in space or in time. Assuming commutativity can be the source of errors as discussed by [19]. This is an issue to keep in mind but most LES rely on the commutativity assumption nonetheless. The filtered equations presented

[1] This is actually one of the seven most important open problems in mathematics of the Clay Institute and any significant progress towards an analytical resolution is rewarded a US$1,000,000 prize.

below in the mass, momentum and energy form are no exception. In these equations, Favre filtering is introduced as:

$$\tilde{f} = \frac{\overline{(\rho f)}}{\breve{f}} \tag{1.3}$$

Conservation of mass

$$\frac{\partial}{\partial t}\breve{\rho} + \frac{\partial}{\partial x_i}\breve{\rho}\tilde{u}_i = 0 \tag{1.4}$$

Conservation of species

$$\frac{\partial}{\partial t}(\breve{\rho}\tilde{Y_k}) + \frac{\partial}{\partial x_j}(\breve{\rho}\tilde{Y_k}\tilde{u_j}) = -\frac{\partial}{\partial x_j}[\breve{J}_{j,k} + \breve{J}^t_{j,k}] + \breve{\dot{\omega}}_k \tag{1.5}$$

Conservation of momentum

$$\frac{\partial}{\partial t}(\breve{\rho}\tilde{u_i}) + \frac{\partial}{\partial x_i}(\breve{\rho}\tilde{u_i}\tilde{u_j}) = -\frac{\partial}{\partial x_j}[\breve{p}\delta_{ij} - \breve{\tau}_{ij} - \breve{\tau_{ij}}^t] \tag{1.6}$$

Conservation of energy

$$\frac{\partial}{\partial t}(\breve{\rho}\tilde{E}) + \frac{\partial}{\partial x_j}(\breve{\rho}\tilde{E}\tilde{u_j}) = -\frac{\partial}{\partial x_j}[\overline{u_i(p\delta_{ij} - \tau_{ij})} + \breve{q}_j + \breve{q_j}^t] + \overline{\dot{\omega}_T} \tag{1.7}$$

In equations (1.4) to (1.7), many unclosed terms appear due to the filtering process. Some terms are directly related to unfiltered quantities such as the subgrid scale stress tensor $\breve{\tau}^t_{ij}$, diffusion flux $\breve{J}^t_{j,k}$ and heat flux $\breve{q}^t_i$ (their expression is not given here but can be found in [3] for example). But even some filtered quantities must be closed, the most important one being the resolved reaction rates $\breve{\dot{\omega}}_k$.

As with RANS, closure is provided by models and a large variety is available (some of them are listed in [3]). Their choice has an impact on the final LES result. For example, Bauerheim et al. [12] showed that the flame response to acoustic forcing is modified when changing the model for the subgrid stress tensor. Compared to RANS however, closure models in LES can rely on the information about the resolved scales and be formulated so as to be completely solution dependent.

While there is room for improvement, LES has shown its capability to correctly predict thermo-acoustic instabilities, in academic setups [20, 21, 22, 23, 15] and industrial gas turbine burners [24, 25]. The interaction between the flame and the flow can be analyzed in great detail with unrivaled visualizations (Fig. 1.9), for longitudinal instabilities [20], but also transverse ones [15] and even in a complete industrial annular chamber [24]. LES can be used to study the impact of imperfect fuel mixing [25] or heat transfer [26] on the flame dynamics or conversely the effect of combustion instability on the production of pollutants [21].

However, LES is still an expensive tool that requires fine meshes and long computational times and is not suited for sensitivity analysis for example. For this purpose, simpler tools are derived by progressively simplifying the Navier-Stokes equations. These simplifications are indicated in the text by sentences in bold font starting with a star symbol ★.

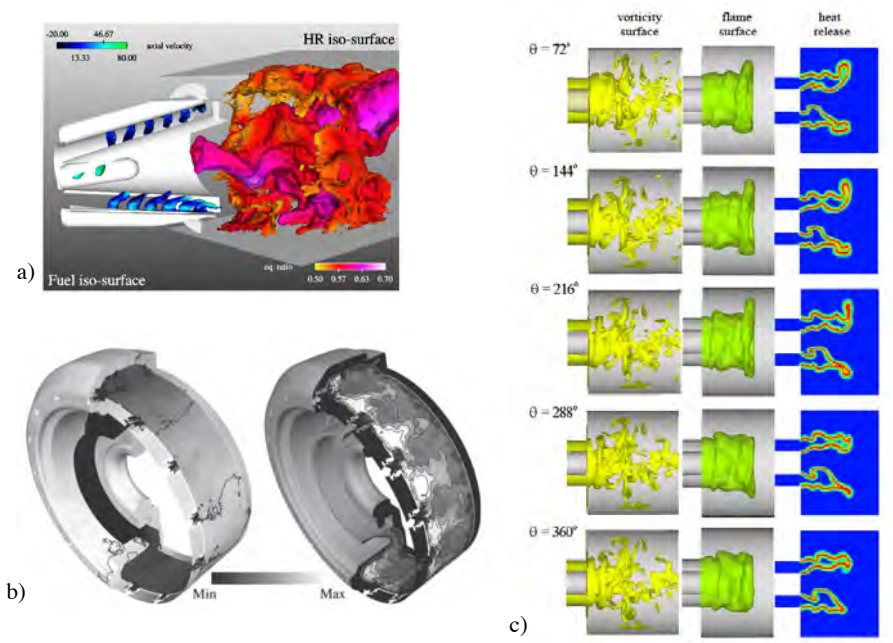


FIGURE 1.9: Examples of LES visualizations of combustion instabilities in a) a scaled industrial single burner [21], b) an annular helicopter combustor [24] c) an academic burner [20]

1.3.2 Linearized Navier-Stokes Equations

Another way to reduce the complexity of the Navier-Stokes equations is to examine them from an acoustical perspective. The details of the flame chemistry are completely ignored. All species are assumed to have the same molecular weight and heat capacities. The heat release $\dot{\omega_T}$ is modeled with simple acoustic models presented in Section 1.3.7. Heat diffusion is also neglected as it usually has little impact on acoustics. This already greatly simplifies the expressions of Eq. (1.4) to (1.7).

Further simplification is obtained by performing first order linearization around a steady state. For this, all variables are decomposed into an average and a fluctuating component. This fluctuating component is different from the turbulent one defined in RANS. It is linked to acoustics and since acoustics are periodic, it can be written as harmonic.

$$f(x_i, t) = f_o(x_i) + \Re[\hat{f}(x_i)\exp(-i\omega t)] \tag{1.8}$$

with $\omega = 2\pi f$ the angular frequency. In order to avoid confusion with the angular frequency, the heat release $\dot{\omega}_T$ is from now on refered to as $\dot{q}$. Heat diffusion is discarded from all the following models and $\dot{q}$ should not be mistaken with q the heat flux.

$\hat{f}$ is the complex amplitude of the fluctuation and its module is assumed small compared to $\bar{f}$. Another good property of $\hat{f}$ is that its characteristic scale (the acoustic wavelength) is generally much larger than that of the flow. This means that $\hat{f}$ can be solved on much coarser grids, with a reduced computational cost.

The final set of assumptions is the following.

★ **Simplification 0: All species have the same molecular weight and heat capacities.**

★ **Simplification 1: The flame is modeled as an acoustic element.**

★ **Simplification 2: No heat diffusion.**

★ **Simplification 3: Acoustic perturbations are small enough to linearize the equations at first order.**

With these assumptions, the *Linearized Navier-Stokes Equations* can be derived and are given below in the frequency domain. In order to avoid confusion with the angular frequency ω, the notation for the heat release is switched from $\dot{\omega}_T$ to $\dot{q}$ in all frequency formulations. Also note that ω is a complex quantity. Its real part determine the period of the oscillation while the imaginary part corresponds to an amplification rate. With the convention of Eq. (1.8), a positive imaginary part leads a growing fluctuation and a negative imaginary part damps the oscillation.

Conservation of mass

$$-i\omega\hat{\rho} + \frac{\partial}{\partial x_i}(u_{o,i}\hat{\rho} + \rho_o\hat{u}_i) = 0 \tag{1.9}$$

Conservation of momentum

$$-i\omega\rho_o\hat{u}_i + \frac{\partial}{\partial x_j}(\rho_o u_{o,j}\hat{u}_i) + (\rho_o\hat{u}_j + u_{o,j}\hat{\rho})\frac{\partial u_{o,i}}{\partial x_j} = -\frac{\partial\hat{p}}{\partial x_i} + \frac{\partial\hat{\tau}_{ij}}{\partial x_j} \tag{1.10}$$

With $\hat{\tau}_{ij} = -\frac{2}{3}\mu\frac{\partial\hat{u}_k}{\partial x_k}\delta_{ij} + \mu\left(\frac{\partial\hat{u}_i}{\partial x_j} + \frac{\partial\hat{u}_j}{\partial x_i}\right)$

Conservation of energy

Non reactive, low Mach number flows can be assumed isentropic [27, 28]. In this case, the energy equation is decoupled from the mass and momentum equations and can be replaced by the isentropic relationship:

$$\hat{p} = \hat{\rho}c_o^2 \tag{1.11}$$

This is often used in aeroacoustics. In the field of combustion instabilities, the flow is reactive and the isentropic assumption is not valid anymore. An equation for the conservation of energy or entropy must be included. Traditionally, the equation of entropy is preferred. Both are equivalent and can be derived from one another using thermodynamic relationships.

$$-i\omega\hat{s} + u_{o,i}\frac{\partial\hat{s}}{\partial x_i} + \hat{u}_i\frac{\partial s_o}{\partial x_i} = \frac{r}{p_o}\left[\left(\hat{\dot{q}} - \frac{\hat{p}}{p_o}\bar{\dot{q}}_T\right) + \left(\tau_{o,ij}\left(\frac{\partial\hat{u}_i}{\partial x_j} - \frac{\hat{p}}{p_o}\frac{\partial u_{o,i}}{\partial x_j}\right) + \hat{\tau}_{ij}\frac{\partial u_{o,i}}{\partial x_j}\right)\right] \tag{1.12}$$

The entropy is related to the fluctuations of pressure and density thanks to the linearized equation of state for an ideal gas.

$$\hat{s} = c_v\frac{\hat{p}}{p_o} - c_p\frac{\hat{\rho}}{\rho_o} \tag{1.13}$$

In equations (1.9) to (1.13), the average quantities (index o) are inputs, extracted for example from a RANS or LES computation. There are seven unknowns (in three dimensions), $\hat{\rho}$, $\hat{u}_i$, $\hat{p}$, $\hat{s}$ and $\hat{\omega}_T$, but only six equations. The seventh relationship is obtained as an acoustic model for the unsteady heat release $\hat{\omega}_T$ and is presented in Section 1.3.7.

The solution of equations (1.9) to (1.13) describes the propagation of three modes of fluctuations: acoustics, vorticity and entropy, in the presence of a heat release source term and a turbulent mean flow. In particular, it accounts for mean flow effects such as

- the generation of acoustics due to the acceleration of entropy waves [29], a key mechanism for "convective-type" instabilities [5]
- the conversion of acoustics into vorticity at sharp edges [30], known to be an important source of acoustic damping in gas turbine combustors.

As noted by [31, 32], the LNSE equations presented in this manuscript do not account for the impact of turbulent fluctuations on acoustic ones. In the studies of [31, 32], the authors derived a new set of LNSE equations for non reactive flows by performing a triple decomposition. All variables are separated into an average steady part, a coherent fluctuation corresponding to acoustics, and a non-coherent fluctuation associated to turbulence. The three contributions can be isolated by combining phase averaging (to remove turbulence) and time averaging (which removes all fluctuations). Phase averaging is applied to the Navier-Stokes equations before linearizing the result around the steady state up to first order. With this procedure, an unclosed stress tensor representing the effect of turbulent fluctuations on acoustics appears and is modeled with an eddy viscosity approach. The main effect of this tensor is to damp some spurious hydrodynamic instabilities not observed in experiments.

The analysis for reactive flows is much less advanced, and applications to combustion instabilities are still rare but LNSE appear as a promising tool. Successful results were obtained in two academic configurations: a 2D Rijke tube [33, 34], and more interestingly, a 3D academic burner composed of two cylindrical tubes joined by a swirled injector [35]. For this last case, the eigenfrequencies were measured experimentally and LNSE results compare well with them (Fig. 1.10).

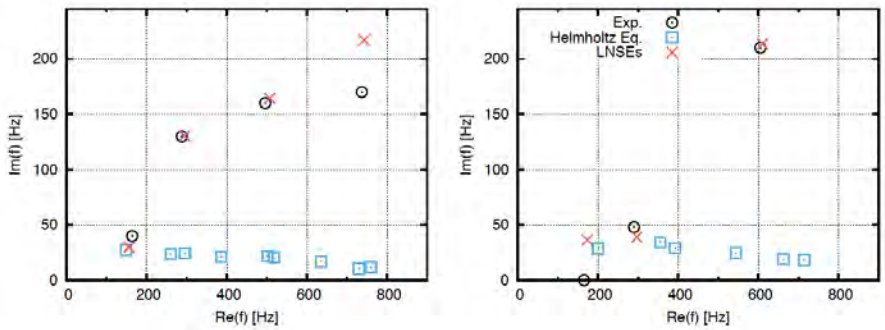


FIGURE 1.10: Eigenfrequencies of a 3D burner with swirled injector from [35]. Experiments: o. LNSE: x.

1.3.3 Linearized Euler Equations

Viscous effects can usually by neglected in the description of an acoustic problem, especially at low frequencies. In this case, the Linearized Euler Equations (LEE) can be used

instead of the Linearized Navier-Stokes. Only the equation of momentum and entropy are different and provided here. The conservation of mass (1.9) and the equation of state (1.13) are still applicable.

★ **Simplification 3: Inviscid fluid.**

Conservation of momentum

$$-i\omega\rho_o\hat{u}_i + \frac{\partial}{\partial x_j}(\rho_o u_{o,j}\hat{u}_i) + (\rho_o\hat{u}_j + u_{o,j}\hat{\rho})\frac{\partial u_{o,i}}{\partial x_j} = -\frac{\partial\hat{p}}{\partial x_i} \tag{1.14}$$

Conservation of entropy

$$-i\omega\hat{s} + u_{o,i}\frac{\partial\hat{s}}{\partial x_i} + \hat{u}_i\frac{\partial s_o}{\partial x_i} = \frac{r}{p_o}\left(\hat{\dot{q}} - \frac{\hat{p}}{p_o}\dot{q}_o\right) \tag{1.15}$$

Because they account for mean flow fields, LEE equations can capture the effect of the steady shear layer on acoustics, and the associated damping at sharp edges. However, the damping mechanism in LEE is not complete as the retroaction of acoustics on the mean flow is neglected (unless the unsteady vorticity is reintroduced in the equations and computed by applying a Kutta condition on the edge for example, see section 1.5.3). From an hydro-acoustic damping point of view, LEE methods are part of the quasi-steady approaches discussed in Section 1.5.3. In situations where the retroaction is not important, LEE methods provide the same results as LNSE, as was shown for orifices and area expansions in the thesis of Gikadi [35].

Other mechanisms well simulated by LEE solvers include:

- the impact of mean flow on acoustic propagation (refraction),
- the acoustic flux at boundaries due to a non-zero mean flow,
- the generation of acoustics due to the acceleration of entropy waves (convective effects).

As in the case of LNSE, thermo-acoustic applications with LEE solvers are quite rare. The main studies of [36, 37] are rather theoretical and focus on the impact of a non-zero mean flow on the stability of simple quasi 1D geometries (Fig. 1.11). In particular, it is shown in [36] that in the presence of a nozzle, even a small mean flow ($M < 0.1$) can greatly modify the stability of a combustor compared to the zero Mach number situation.

Despite these good results, solving the LEE system requires a careful treatment to avoid numerical instabilities, for example with the use of artificial viscosity [13]. This limits the practicality of LEE for industrial combustors.

1.3.4 Helmholtz solvers

The mean flow velocity in most gas turbine combustors is relatively low ($M \lesssim 0.1$) and has little impact on acoustic modes, for which entropy conversion is not involved. In this case, Linearized Euler Equations can be simplified by setting $M = 0$ to obtain the classical acoustics equations.

★ **Simplification 4: Zero mean flow.**

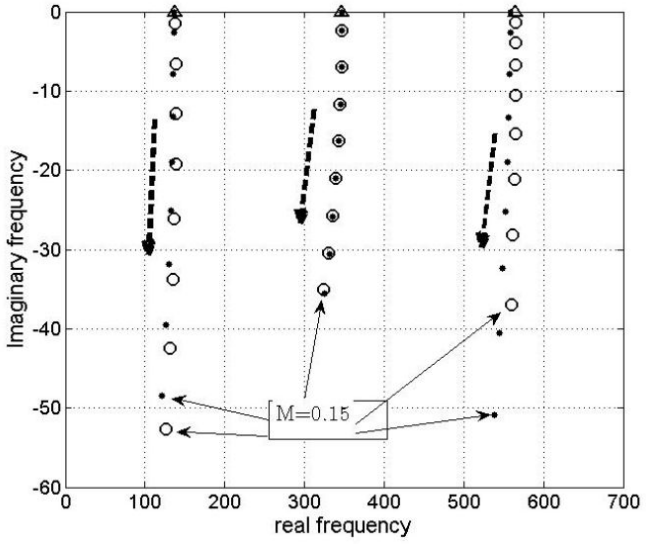


FIGURE 1.11: From [36]. Evolution of eigenfrequencies with increasing mean flow (indicated by thick dashed arrows) predicted by an LEE solver (white circles) for a 1D tube with flame.

Conservation of mass

$$-i\omega\hat{\rho} + \hat{u}_i \frac{\partial \rho_o}{\partial x_i} + \rho_o \frac{\partial \hat{u}_i}{\partial x_i} = 0 \tag{1.16}$$

Conservation of momentum

$$-i\omega\hat{u}_i = -\frac{1}{\rho_o}\frac{\partial \hat{p}}{\partial x_i} \tag{1.17}$$

Conservation of energy

When $\bar{M} = 0$, the momentum and entropy conservation equation for stationary quantities show that

$$\bar{\rho}\frac{\partial u_{o,i}}{\partial t} = -\frac{\partial p_o}{\partial x_i} = 0 \tag{1.18}$$

$$\frac{\partial s_o}{\partial t} = \frac{r\dot{q}_o}{p_o} = 0 \tag{1.19}$$

Equation (1.19) is inserted into the conservation of entropy (1.15) that is now expressed as:

$$-i\omega\hat{s} + \hat{u}_i \frac{\partial s_o}{\partial x_i} = \frac{r\hat{\dot{q}}}{p_o} \tag{1.20}$$

The fluctuation of entropy $\hat{s}$ can be obtained from the fluctuation of pressure $\hat{p}$ and density $\hat{\rho}$ with Eq. (1.13). For an ideal gas, the gradient of mean entropy can be related to the gradient of mean density, by combining the equation of state of an ideal gas with Eq. (1.18).

$$\frac{\partial s_o}{\partial x_i} = \frac{c_v}{p_o}\frac{\partial p_o}{\partial x_i} - \frac{c_p}{\rho_o}\frac{\partial \rho_o}{\partial x_i} = -\frac{c_p}{\rho_o}\frac{\partial \rho_o}{\partial x_i} \tag{1.21}$$

With Eqs. (1.13) and (1.21), the conservation of entropy is reformulated as:

$$\hat{u}_i \frac{\partial \rho_o}{\partial x_i} = -\hat{\dot{q}} \frac{\rho_o(\gamma - 1)}{p_o \gamma} - i\omega \left(\frac{\hat{p}}{c_o^2} - \hat{\rho} \right) \tag{1.22}$$

Helmholtz equation

The conservation of mass (1.16), momentum (1.17) and entropy (1.22) can be combined into a non-homogeneous Helmholtz equation (i.e. wave equation in frequency domain) describing the propagation of acoustics in the presence of a flame. For this, (1.22) is first injected into (1.16).

$$-i\omega \frac{\hat{p}}{\gamma \bar{p}} + \frac{\partial \hat{u}_i}{\partial x_i} = \frac{\gamma - 1}{\gamma p_o} \hat{\dot{q}} \tag{1.23}$$

The time derivative of Eq. (1.23) (i.e. multiplication by $-i\omega$) is then substracted from the space derivative of Eq. (1.17) to provide a Helmholtz equation for pressure.

$$\frac{\partial}{\partial x_i} \left(\frac{1}{\rho_o} \frac{\partial \hat{p}}{\partial x_i} \right) + \omega^2 \frac{\hat{p}}{\gamma p_o} = i\omega \frac{\gamma - 1}{\gamma p_o} \hat{\dot{q}} \tag{1.24}$$

In the absence of flame or complex impedance boundary conditions, the discretization of the Helmholtz equation leads to a linear sparse eigenvalue problem that can be solved by efficient, well-known algorithms (for example: [38, 39, 40]). If a flame or a complex impedance boundary is present, the eigenproblem becomes nonlinear with respect to frequency. This issue can be treated with the use of a fixed point [17] which increases a bit the cost of the computation (see Appendix C). Even in this case, the Helmholtz problem is much simpler to solve than the LEE system and was used successfully on many 3D industrial configurations [41, 17, 24, 42]. A very successful example is the work of Wolf [24] where the stability of an helicopter annular combustor computed with an LES is correctly retrieved by the AVSP Helmholtz solver (Fig. 1.12).

Helmholtz solvers are usually used for linear stability prediction. But combined to a non-linear description of the flame, they can also provide information about nonlinear thermoacoustic coupling. In the work of Silva et al. [18] for example, the AVSP Helmholtz solver combined to an experimental Flame Describing Function (defined in Section 1.3.7) is able to retrieve the amplitude of limit cycles.

A feature of Helmholtz solvers (and frequency-domain solvers in general) is their ability to manage complex impedances. The complex impedance Z defines the ratio of pressure over normal velocity at a boundary (Fig. 1.13).

$$Z = \frac{\hat{p}}{\rho_o c_o \hat{\mathbf{u}} \cdot \mathbf{n}} \tag{1.25}$$

with $\mathbf{n}$ the local boundary normal.

Therefore, even if the baseline equation of Helmholtz solvers is simple and relies on many simplifications, it is possible to reincorporate some of the neglected mechanisms into the solver with adequate boundary conditions. Mechanisms modeled with this strategy include:

- the acoustic damping due to vorticity shedding at perforated plates [43],

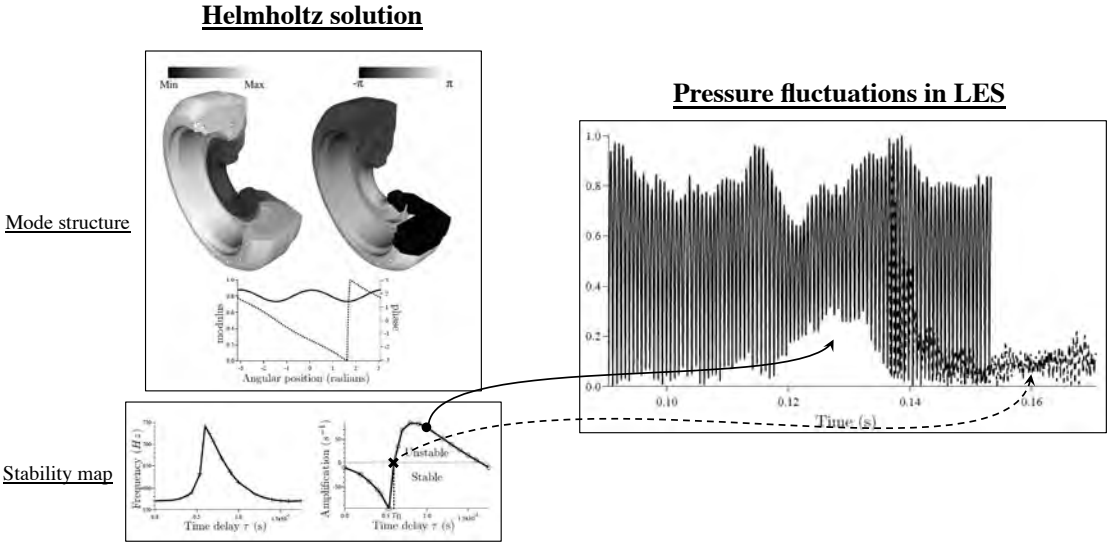


FIGURE 1.12: Example of Helmholtz solver application from [24]. Left: Mode structure predicted by the Helmholtz solver and amplification rate as a function of the FTF time delay. Right, pressure fluctuations from the LES for two time delays, leading to an unstable (solid lines) and stable (dotted lines) combustor.

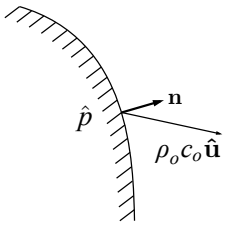


FIGURE 1.13: Acoustic quantities involved in the definition of the impedance.

- the convective effects due to the propagation of acoustic and entropy waves in a nozzle with mean flow [44]

The present work fits into this type of strategy as will be explained later.

1.3.5 Galerkin methods

Just as Helmholtz solvers, Galerkin methods start with a wave equation featuring a source term h and a set of complex boundary conditions symbolized by the function f.

$$\nabla^2 p' - \frac{1}{c_o^2}\frac{\partial^2 p'}{\partial t^2} = h \tag{1.26}$$

$$\nabla p' \cdot \mathbf{n} = -f \tag{1.27}$$

The expressions of h and f can be obtained from the analysis of the Linearized Navier-Stokes Equations in the most general case, and contains all the complexity of the flow / flame / acoustics interaction, including the effect of fluid or solid particles if the equations of a multi-phase fluid are used. The principle of Galerkin method is to project the solution

of Eqs. (1.26)-(1.27) on a family of simpler orthogonal modes $\psi_m(\mathbf{x})$ [45, 46], solution of the homogeneous problem with solid walls ($h = f = 0$).

$$p'(\mathbf{x}, t) \approx \sum_{m=1}^{M} \eta_m(t)\psi_m(\mathbf{x}) \tag{1.28}$$

Each mode is associated to its angular eigenfrequency ω_n. The coefficients of the projection $\eta_m(t)$ are time-dependent and contain the amplification rate. When inserted in (1.26) and (1.27), and after spatial averaging over the combustor domain, expression (1.28) transforms the wave problem (1.26) into a collection of oscillator equations.

$$\ddot{\eta}_m(t) + \omega_m^2 \eta_m(t) = F_m \quad m = 1, \ldots, M \tag{1.29}$$

The effect of h and m is included in the term F_m. System (1.29) can be further simplified into a system of first order differential equations by assuming that the amplitude of the unstable oscillations changes slowly during one period. This last system, not shown here, is fairly easy to solve. It can be found in [5]

Galerkin methods provide linear stability results [45, 47] but they are especially powerful for the study of non-linear flame-acoustics mechanisms in time domain, such as:

Limit cycles The transition from the linear regime to the limit cycle, as well as the amplitude of the limit cycle fluctuations can be computed with this type of approach [48, 49].

Nonlinear stability and triggering When nonlinear flame dynamics are considered, a linearly stable system can become unstable if the amplitude of the initial disturbance is larger than a certain threshold. This mechanism, known as a subcritical Hopf bifurcation can be explored with Galerkin methods [50].

Transient growth Thermoacoustic eigenmodes are known to be non-orthogonal [17]. The non-orthogonality can have unexpected consequences. An initial state of low acoustic amplitude (or the order of the background noise), composed solely of linearly stable modes, can actually lead to temporarily growing fluctuations that eventually transition to nonlinear instability if the triggering threshold is reached. This issue is examined in [51, 52].

One drawback of Galerkin method lies in the projection procedure. Indeed, artificial constraints are imposed on the solution of Eq. (1.26) and (1.27) through the choice of the basis function. For example, the Galerkin solution of a burner with $f \neq 0$ will not reproduce the mode structure correctly at the boundaries. The error can be minimized in practice by projecting onto a sufficiently large family. If truncation is performed after too few terms however, significant errors can be observed [53, 54, 55].

1.3.6 Network models

For low frequency modes, where the acoustic waves propagate only in the duct axial direction, one-dimensional network approaches can be used. Network models start from the solution of the convective wave equation, recalled below. This wave equation is able to capture the effect of a uniform mean flow $\mathbf{u_o}$ on the speed of acoustic propagation.

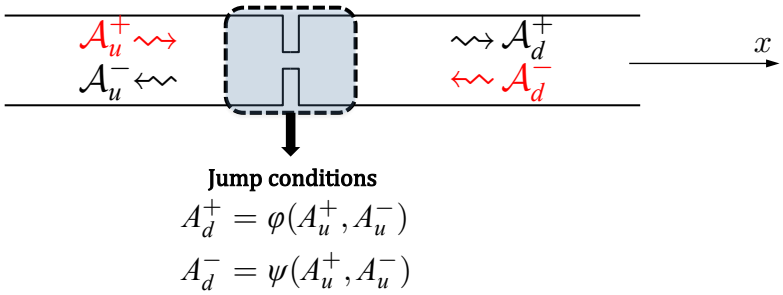


FIGURE 1.14: A compact acoustic element can be represented as a pair of jump conditions. If the jump conditions are linear, they are equivalent to a matrix.

$$\left(\frac{\partial}{\partial t} + \mathbf{u_o} \cdot \nabla\right)^2 p' - c_o^2 \nabla^2 p' = 0 \tag{1.30}$$

In a 1D configuration and for a uniform flow (constant mean velocity u_o, density ρ_o and speed of sound c_o), the solution of Eq. (1.30) is the sum of two plane waves g^+ and g^- traveling in opposite directions, at $c_o + u_o$ and $c_o - u_o$ respectively. In thermoacoustic applications, the low Mach number assumption is often applied to obtain the following expressions of g^+ and g^-:

$$g^+(x,t) = A^+ \exp\left[-i\omega\left(t - \frac{x}{c_o}\right)\right] \tag{1.31}$$

$$g^-(x,t) = A^- \exp\left[-i\omega\left(t + \frac{x}{c_o}\right)\right] \tag{1.32}$$

The pressure and velocity fluctuations in the 1D pipe are:

$$p'(x,t) = \Re[\hat{p}(x)\exp(-i\omega t)] \quad \text{with} \quad \hat{p}(x) = A^+\exp(ikx) + A^-\exp(-ikx) \tag{1.33}$$

$$u'(x,t) = \Re[\hat{u}(x)\exp(-i\omega t)] \quad \text{with} \quad \hat{u}(x) = \frac{1}{\rho_o c_o}[A^+\exp(ikx) - A^-\exp(-ikx)] \tag{1.34}$$

Of course, in a real configuration, the geometry is not 1D, nor are ρ_o and c_o uniform. However, if these changes are compact with respect to the acoustic wavelength, they can be modeled as a set of jump conditions (Fig. 1.14). For example, the connection between two tubes can be represented by a set of two jump conditions, also called acoustic 2-port.

$$A_d^+ = \phi(A_u^+, A_u^-) \tag{1.35}$$

$$A_d^- = \psi(A_u^+, A_u^-) \tag{1.36}$$

The configuration of interest can therefore be described as a series of 1D uniform pipes, linked by jump conditions. When boundary conditions are supplemented, the complete system is described by a matrix including the impedances and the jump conditions. The resonances of the system are determined by solving the dispersion relation, i.e. finding the complex frequencies for which the determinant of the matrix is null.

Acoustic network models usually belong to one of the following two categories. They either work in frequency domain and assume a linear flame regime [56, 57, 58], or in time domain with non-linear flame dynamics [59, 60, 61]. The transition from frequency to time domain is possible thanks to a Laplace transform.

This approach is very efficient and provides good estimations of the eigenfrequencies and eigenmodes on simple longitudinal [57, 61] and annular combustors [59, 60, 58]. An interesting application on an industrial annular combustor was also performed by Kruger et al. [56]. However, the choice of the 1D representation in this case is probably not unique and is part of the art of applying the method, as illustrated in Fig. 1.15. In the work of Kruger et al. [56] for example, a 3D FEM solver was used to tune the parameters of the acoustic network.

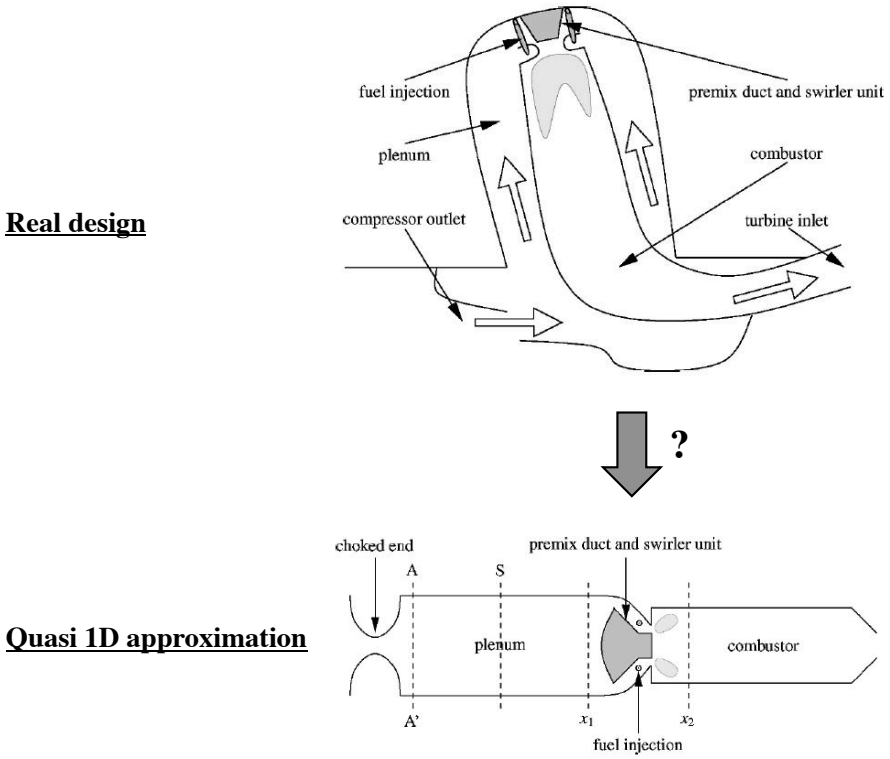


FIGURE 1.15: Example of acoustic network representation for a realistic combustor (adapted from [57]).

1.3.7 Flame models

In LES, the flame is described as accurately as possible, by including the information from a chemical scheme in the unsteady Navier-Stokes equations. In acoustic models (LNSE, LEE, Helmholtz, Galerkin and network approaches), a model is still required for the perturbation of heat release $\hat{q}$ in equations (1.12), (1.15), (1.24) and (1.26) but the complexity of the true chemical mechanism is not kept.

Instead, the flame is described as a simple acoustic element. In the linear regime, the total heat release fluctuation $\hat{\dot{Q}} = \int \hat{q} dV$ can be related to the velocity fluctuation $\hat{u}$ upstream of the flame through a first order *Flame Transfer Function* (FTF), characterized by a gain N and a delay τ. In frequency domain, it is expressed as:

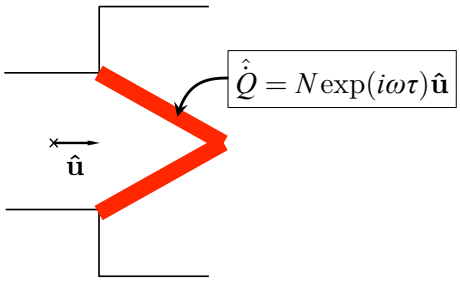


FIGURE 1.16: Flame Transfer Function model.

$$FTF(\omega) = \frac{\hat{\dot{Q}}}{\hat{u}} = N(\omega)\exp(i\omega\tau(\omega)) \tag{1.37}$$

with $\hat{\dot{Q}}$ and $\hat{u}$ the complex amplitudes of the total heat release fluctuations and velocity fluctuations (Fig. 1.16). The analytical prediction of N and τ is a difficult task because it requires an adequate knowledge of the flame/acoustics interaction, achievable only in simple academic configurations [62, 63, 64]. They can however be measured experimentally or numerically [10, 65, 66, 67].

The FTF formalism was extended by [68] to nonlinear regimes with the *Flame Describing Function* (FDF). The FDF is in fact a collection of FTF obtained for different acoustic amplitudes, quantified by $|\hat{u}|$ for example.

$$FDF(\omega, |\hat{u}|) = \frac{\hat{Q}}{\hat{u}} = N(\omega, |\hat{u}|)\exp(i\omega\tau(\omega, |\hat{u}|)) \tag{1.38}$$

Another popular model, especially for acoustic network models, is the *Flame Transfer Matrix* (FTM). With the FTM approach, the flame is considered as a compact interface, characterized by a set of linear jump conditions, i.e. an acoustic matrix (Fig. 1.17). Due to the linearity assumption, this formalism is reserved for linear stability prediction. It could be extended to nonlinear analysis with an approach similar to the FDF.

$$\begin{pmatrix} \hat{p}_d \\ \rho_{o,d} c_{o,d} \hat{u}_d \end{pmatrix} = \mathbb{T}_{\text{flame}} \begin{pmatrix} \hat{p}_u \\ \rho_{o,u} c_{o,u} \hat{u}_u \end{pmatrix} \tag{1.39}$$

Just as n and τ, the coefficients of $\mathbb{T}_{\text{flame}}$ can be derived from first principles only for academic flames and are usually measured experimentally or numerically [69, 11, 70, 71]. FTF and FTM models are equivalent provided that the acoustic velocity used in the FTF is measured close enough to the flame compared to the acoustic wavelength [72]. In this case, it is possible to construct matrix $\mathbb{T}_{\text{flame}}$ in (1.39), from Eq. (1.37) and vice versa [72].

1.3.8 Dissipation models

In thermo-acoustic instabilities, the flame acts as the main source term of acoustic energy. It is therefore an important contribution when assessing the stability of a combustor *but it is not the only one*. The total stability of the combustor is governed by the balance between the flame source term and mechanisms leading to a dissipation of the acoustic

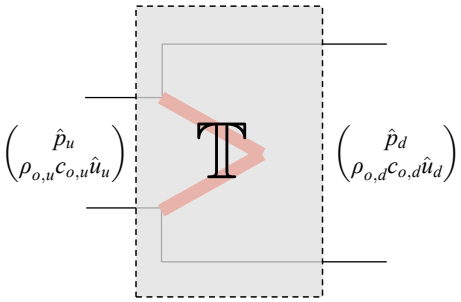


FIGURE 1.17: Flame Transfer Matrix model.

energy. The nature of these mechanisms is quite varied but can be divided into two categories. Acoustic energy can be dissipated either in the bulk of the flow, by volumic processes, or for a closed system, at boundaries. Some of these mechanisms are now briefly reviewed.

For a viscous fluid, acoustic energy can be lost through shear stress and heat losses at walls [73, 74, 75]. Indeed, acoustic waves can be viewed as velocity and enthalpy fluctuations. If the velocity and enthalpy are set to a constant value at walls, momentum and thermal diffusion will act so as to minimize these fluctuations, which translates into a dissipation of acoustic energy. This thermo-viscous damping term scales as the square root of the frequency and is usually very small for the low frequencies observed in gas turbines [76]. If necessary, the damping rate associated to thermo-viscous dissipation can be recovered for any solution of an inviscid Helmholtz computation following the method of Searby et al. [76].

For an inviscid fluid, acoustic energy can still be lost at boundaries if these are not perfectly reflecting (i.e. more energy is going out of the system than into it). This type of dissipation is easy to include in an acoustic solver (such as the Helmholtz solver) when the associated boundary impedance is known. Boundaries can be non-perfectly reflecting for a number of reasons.

- Some absorbent material can be installed there (the nature of these materials is not discussed here). This is often used in experiments when an anechoic termination is required for example.
- If the system is open to the atmosphere, acoustic energy can be lost through radiation [77]. The associated impedance was derived by Levine [77] and can easily be plugged in an acoustic solver.
- If the mean flow at a boundary is non zero, acoustic energy can be convected in/away of the system. Notably, this mechanism leads to dissipation when a nozzle is connected to the domain [78, 79, 80, 36, 44]. The dissipating effect of nozzles has been explored in Helmholtz studies by [36, 44].

Acoustic energy can also be dissipated directly in the bulk of the fluid.

By homogeneous diffusive processes. Dissipation by thermal and viscous diffusion also acts in the fluid volume. This term is however extremely small and can usually be neglected [81, 82].

By fluid/structure coupling. If walls are allowed to vibrate, the coupling between fluid and structural acoustics must be considered as it can lead to a dissipation of acoustic

energy [82, 83]. The coupling problem is quite complex and the associated damping is therefore neglected in this study.

By particles Acoustic energy can be dissipated through drag and heat exchange with particles [84, 82]. For linear flow instabilities, the effect of particles depends on their Stokes number (the ratio between the kinetic energy of the particle and the energy dissipated by friction with the fluid). Particles with a large Stokes number tend to stabilize the flow (due to drag), while particles with a small Stokes number destabilize the flow by increasing the inertia of the fluid-particles mixture [85]. This mechanism is important in rocket engines because of the strong interaction between acoustics and flow instabilities [5]. The effect on pure acoustic fluctuations is however not well documented, to the author's knowledge. In this study, particles are neglected based on the fact that the spray volume is small compared to the combustor volume in most gas turbines.

By vorticity shedding This is the main source of dissipation examined in this work and is examined in details in Section 1.5. At sharp edges, acoustics can be converted into vorticity. Acoustic energy is therefore transferred to the mean flow in the form of vortices. This energy is ultimately lost as the vortices are destroyed by viscosity. It is suspected that this mechanism is a great source of dissipation in modern gas turbines.

The important point of this quick review is that while dissipation at boundaries is quite easy to include in an acoustic solver (provided the associated impedance is known), dissipation in the fluid bulk is based on mechanisms that cannot be described by simple linear acoustics. This probably explains why the latter is neglected in most thermo-acoustic studies. However, as already mentioned in the beginning of this section, dissipation terms should be considered more carefully as they too contribute to the global stability of a combustor. Out of the four bulk dissipation mechanisms listed above, this work will focus on the one relying on vorticity shedding. Indeed, as will be explained in Section 1.5), the latter is compact enough to be considered as a boundary process and represented by an impedance-type model.

1.4 The choice of the Helmholtz solver

For gas turbine applications, a Helmholtz solver complemented with FTF (Section 1.3.7) is a good trade-off betweeen physical accuracy and computational cost. It is the numerical approach favored in this thesis because:

- It is adapted to complex 3D geometries [41, 17, 24, 42], and the real combustor geometry can be solved directly contrary to acoustic network models.
- It solves a much easier equation than LNSE and LEE thanks to the zero Mach number assumption, which is justified in most cases.
- It is much faster than LES and thus appropriate for sensitivity analysis at the design stage.
- It can easily account for complex impedance boundaries.
- It can be coupled to an FTF/FTM or an FDF to predict respectively linear amplification [17, 42], or limit cycle amplitude [18].

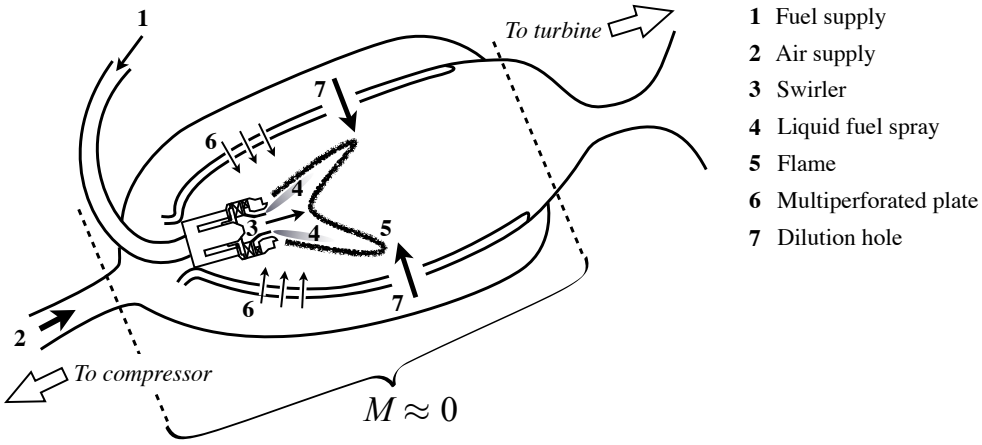


FIGURE 1.18: A typical turbojet combustor design. The zero Mach number assumption is valid in between the dashed lines. Non-acoustic effects are expected at the perforated plates, dilution holes, swirler, due to the presence of a shear layer. Spray droplets, heat transfer at walls and structural vibrations also interact with acoustics, but are not studied here.

Helmholtz solvers are consequently of great interest for jet engine manufacturers and Safran Aircraft Engines, who funded this thesis, is no exception. However, the simplicity of Helmholtz solvers relies on a set of assumptions that restrict the domain of validity of the tool. While the assumption of inviscid fluid at zero Mach number is acceptable in most of the combustor domain (with a Mach number of $M \lesssim 0.1$ and Reynolds number of $Re \gtrsim 10^4$), it discards many local mechanisms that have an important impact on the global combustor acoustics.

An inviscid mean flow can modify the propagation speed of acoustic waves and hence the structure and frequencies of acoustic modes. In the absence of a flame, this effect scales as the square of the Mach number and is therefore minor in jet engine combustors (but it is not for rocket engines !). In the presence of an acoustically active flame however, even a small mean flow can have an important impact on the combustor stability [36, 33], due to convective effects. This problem can be tackled with the Delayed Entropy-Coupled Boundary Condition developed by [44].

Conversely, the presence of viscosity (without mean flow) leads to acoustic dissipation at solid walls (and to a much lesser extent in the bulk), due to the creation of an acoustic boundary layer (the Stokes layer). However, the associated dissipation effects are usually negligible in jet engine combustors. If necessary, they can be assessed by post-processing Helmholtz solutions, following the method described in [76].

Another mechanism depends on both the presence of a small mean flow and of viscosity: the interaction between acoustics and vorticity. As will be explained in the next section, this phenomenon can appear at trailing edges and is suspected to play an important role in the acoustics of a combustor. Indeed, an industrial combustor is full of trailing-edge like geometrical details (Fig. 1.18).

1.5 Hydro-acoustic interactions in thermo-acoustic studies

1.5.1 Hydro-acoustic interactions

The interaction between vorticity and acoustic fields, grouped here under the term "hydro-acoustic interactions", is complex and is the flow-acoustic interaction of interest in this study. Indeed, it is suspected to be an important counterpart to the flame/acoustics coupling but has not been often studied in the field of combustion instabilities. Three types of hydro-acoustic interaction are often encountered (Fig. 1.19). The first two can lead to an increase of acoustic energy while the third one can only dissipate this energy and is the major topic studied here.

Case 1 In unbounded flows, vorticity acts as quadrupole source of sound. In a low Mach number flow, this source of sound is usually small enough to be neglected [86, 87].

Case 2 When a vortex hits a rigid boundary, it emits sound as a dipole, a much more efficient source of sound than a quadrupole. Whistling effects, often encountered in corrugated pipes, are based on this mechanism [88, 89, 90].

Case 3 At a sudden expansion, or any trailing edge in the presence of mean flow, a shear layer is created. When subject to an acoustic forcing, a hydrodynamic instability can develop in the shear layer [91, 92], visible in the form of shed vortices (Fig. 1.21). The vortex shedding process extracts acoustic energy and therefore acts as an acoustic damping term [93], as was observed experimentally [94, 95, 96, 97] and numerically [98, 99]. This damping term might be important in jet engine combustors, since the combustor geometry is full of "trailing-edge" like details [94]. For example, perforated plates sometimes exploit this hydro-acoustic damping for the passive control of combustion instabilities [100, 43, 101]

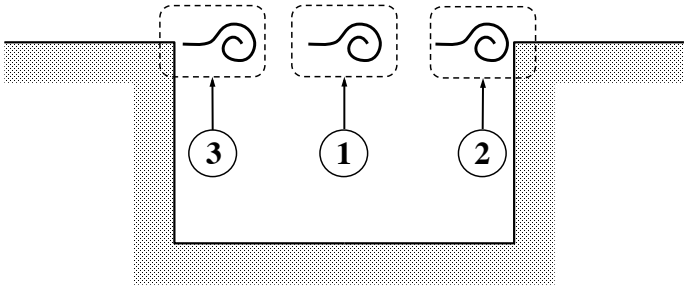


FIGURE 1.19: Three types of hydro-acoustic interactions: 1) Vortex sound in unbounded flows, 2) Vortex sound at rigid boundaries, 3) Conversion of acoustics into vorticity at trailing edges.

Case 3, the interaction between acoustics and shear layer at a sharp edge, is the case of interest in this thesis. Figure 1.21 shows an experimental visualisation of the vortex shedding process at the exit of a pipe with sharp edges in the presence of mean flow [102]. When the acoustic velocity flows inward, the associated velocity perturbation causes the shear layer to roll up into a vortex. After half a period, the acoustic velocity changes sign. The vortex detaches from the edge and is convected downstream by the mean flow, where it can no longer interact efficiently with acoustics. As Fig. 1.20 shows for the shear layer of a cylinder, the interaction between acoustics and vorticity definitely leads to some energy transfer in favor of the vorticity field. Fig. 1.20 also shows that this energy transfer is not simple and depends on the frequency of the acoustic forcing.

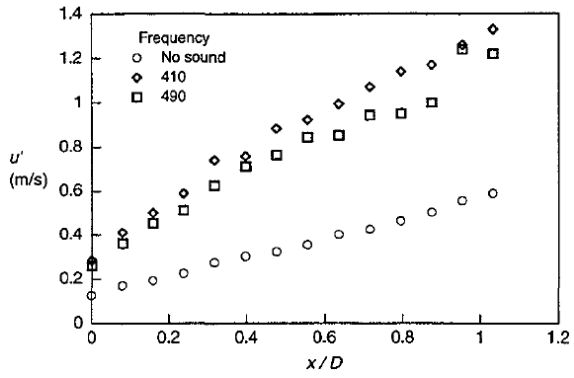


FIGURE 1.20: Comparison of the growth of the maximum fluctuating velocity u' for a cylinder shear layer, without and with acoustic perturbation at 410 Hz and 490 Hz. From [91]

An interesting feature of this process is that it is independent of the acoustic amplitude as long as the latter is "small enough"[2]. In this case, the damping regime is qualified as linear because acoustic quantities on both sides are connected by linear relationships. At higher acoustic amplitudes (or for a low mean flow), the shear layer is created mainly by the acoustic velocity and is not related to the mean flow anymore. In this case, the acoustic damping is proportional to the acoustic amplitude and the damping regime is qualified as nonlinear. In this thesis, only the linear damping regime is examined.

No matter linear or nonlinear, the interaction between shear layers and acoustic waves is governed by viscous effects close to the trailing edge [105]. Therefore this effect can be reproduced by LES or LNSE codes, but is discarded from simple models without viscosity, such as Helmholtz solvers. Fortunately, models are available to compensate this, by taking advantage of the fact that viscous effects are important only in a very limited region of space. This will be developed in Section 1.5.3 but an interesting visualization from Noiray et al. [106] is provided in Fig. 1.22. In this experiment, Noiray et al. examine the acoustics-vorticity mode conversion at a diaphragm. They decomposed the centerline velocity fluctuation into a convective component (vorticity) and an acoustic part. At the location of the diaphragm $z/D = 0$, mode conversion happens and is visible by a simultaneous increase of the convective velocity and drop of the acoustic velocity. The change is sudden and confirms that conversion takes place very close to the diaphragm.

1.5.2 Characteristic quantities for hydro-acoustic damping

Before introducing the models, some usual quantities used in the estimation of hydro-acoustic damping are presented here, for the general damping system of Fig. 1.23. The damping properties are usually measured by imposing an acoustic forcing in a plane-wave configuration as shown in Fig. 1.23. The acoustics of the test rig can be characterized by:

- Upstream and downstream wave amplitudes (A_u^+, A_u^-) and (A_d^+, A_d^-) respectively. Equivalently, acoustic pressure and velocities can be reconstructed from Eq. (1.33) and (1.34).

[2]This has been quantified differently depending on authors. Some compare the unsteady pressure loading to the same steady quantity [103]. Others prefer to examine the ratio of acoustic velocity over mean flow velocity [104].

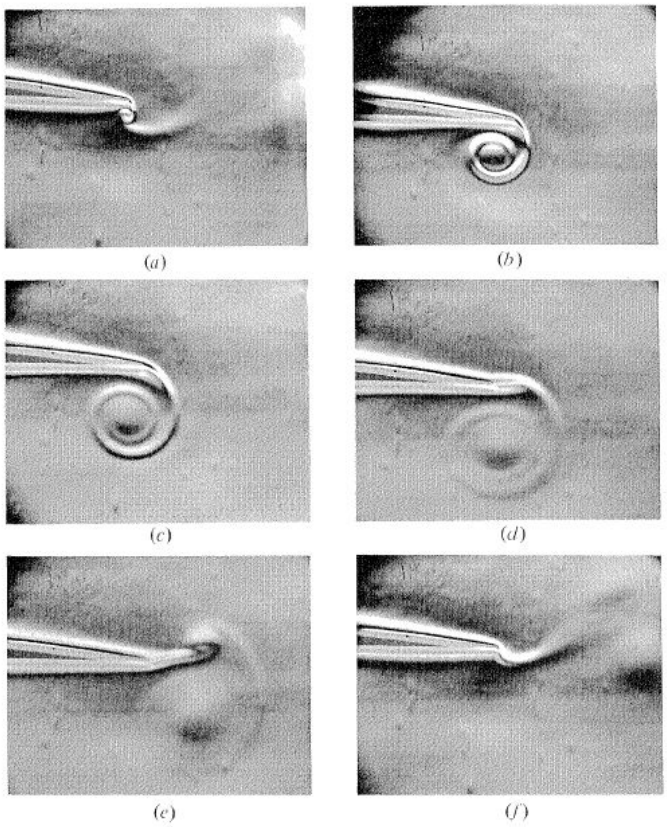


FIGURE 1.21: From [102]: flow field near the sharp edge of a pulsed tube. The pictures (a) - (f) are at $t/T = 0, 0.25, 0.41, 0.53, 0.65$ and 0.90.

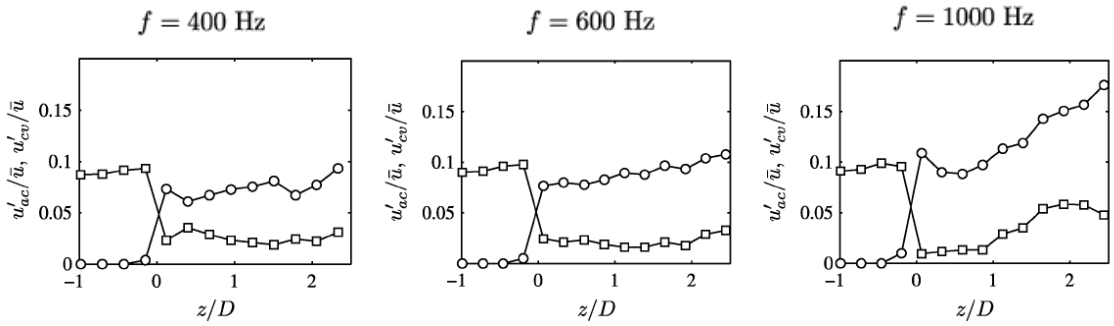


FIGURE 1.22: Acoustic u'_{ac} (squares) and convective (circles) velocity fluctuations u'_{cv} along the centerline of a diaphragm with mean flow, forced acoustically at 400 Hz, 600 Hz and 1000 Hz.

- Upstream W_u and downstream W_d acoustic fluxes defined as (for $M = 0$):

$$W_u = \frac{1}{2}\Re(\hat{p}_u \hat{u}_u^*) = \frac{1}{2}(|A_u^+|^2 - |A_u^-|^2) \tag{1.40}$$

$$W_d = \frac{1}{2}\Re(\hat{p}_d \hat{u}_d^*) = \frac{1}{2}(|A_d^+|^2 - |A_d^-|^2) \tag{1.41}$$

If the outlet is anechoic ($A_d^- = 0$), the acoustic fluxes can be decomposed into an incident W_i, reflected W_r and transmitted W_t contribution.

$$W_i = \frac{1}{2}|A_u^+|^2 \tag{1.42}$$

$$W_r = \frac{1}{2}|A_u^-|^2 \tag{1.43}$$

$$W_t = \frac{1}{2}|A_d^+|^2 \tag{1.44}$$

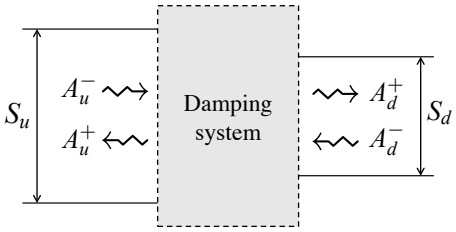


FIGURE 1.23: General damping system in a plane-wave test rig

The damping properties can be divided into two categories: configuration-dependent quantities and intrinsic quantities.

Configuration-dependent quantities

Configuration-dependent quantities refer to quantities that, as the name indicates, depend not only on the damping system of interest, but also on the surrounding measurement rig. For the analysis of mufflers for example, it is common to assume that the downstream reflection coefficient is zero (i.e. anechoic outlet) [107]. The Transmission Loss (TL) and its variants follow this convention. The Transmission Loss shown below quantifies how much acoustic energy is transmitted through the system, compared to what was injected.

$$\textbf{Transmission Loss:} \quad TL = 10\log\left(\frac{W_i S_u}{W_t S_d}\right) \tag{1.45}$$

Another quantity frequently used to qualify the damping properties of a system is the absorption coefficient. It describes the acoustic flux lost in the system.

$$\textbf{Absorption coefficient:} \quad \Delta = \frac{W_{in}S_u - W_{out}S_d}{W_{in}S_u} \tag{1.46}$$

where the ingoing flux W_{in} and outgoing flux W_{out} are defined as:

$$W_{in} = \frac{1}{2}(|A_u^+|^2 + |A_d^-|^2) \tag{1.47}$$

$$W_{out} = \frac{1}{2}(|A_d^+|^2 + |A_u^-|^2) \tag{1.48}$$

Definition (1.46) depends on the downstream boundary condition through the wave amplitude A_d^-. Of course, the transmission loss and absorption coefficient are not the

only configuration-dependent quantities used for the measurement of damping properties. Many variants can be derived, usually based on acoustic fluxes.

Intrinsic quantities

Configuration-dependent quantities have one issue: they cannot be reused in another configuration. In this case, intrinsic quantities should be derived. For orifices for example, the Rayleigh conductivity K_R is such a quantity. It is based on the fact that the acoustic velocity is conserved through the orifice, but not the acoustic pressure. The Rayleigh conductivity provides the ratio between the jump of acoustic pressure and the acoustic velocity (more precisely the acoustic volume flow rate) through the orifice.

$$\textbf{Rayleigh conductivity:} \quad K_R = \frac{i\rho_o\omega\hat{G}}{[\hat{p}_u - \hat{p}_d]} \quad \text{with} \quad \hat{G} = S_u\hat{u}_u = S_d\hat{u}_d \tag{1.49}$$

The jump of acoustic impedance of the orifice is directly related to the Rayleigh conductivity and is expressed as:

$$\textbf{Jump of impedance:} \quad Z = \frac{\hat{p}_u - \hat{p}_d}{\rho_o c_o \hat{u}_u} = \frac{i\omega S_u}{c_o K_R} \tag{1.50}$$

The Rayleigh conductivity is a particularly interesting property of simple damping elements such as orifices, slits and sudden area expansions, that can be computed analytically. For general elements with more complex geometries (a swirler say), the Rayleigh conductivity or the jump impedance can be measured experimentally or computed numerically, provided the acoustic volume flux is conserved through the system of interest.

If this assumption is not verified, the complete **matrix** of the system must be determined, as described in Chapter 2. The matrix formalism is the most general and can also be applied when the acoustic volume flux is conserved. In this case, the expression of the matrix can be derived from the knowledge of K_R or Z (see Appendix D).

The three intrinsic quantities described here all have an important quality. They are easy to transcribe into an impedance boundary condition and can consequently be implemented in a Helmholtz solver.

1.5.3 Models for hydro-acoustic interactions

Vortex sound theory

Hydro-acoustic interactions in a low Mach number confined flow are best described by the vortex sound analogy developed by Powell [30] and later extended by Howe [108].

The key idea of the vortex sound approach is to describe the acoustic field in terms of total enthalpy. For a homentropic, non conductive, frictionless fluid at low Mach number, a non-homogeneous wave equation for the fluctuation of total enthalpy $B' = p'/\rho_o + \mathbf{u}_o \cdot \mathbf{u}'$ can be derived [108, 88]:

$$\frac{1}{c_o^2}\frac{D_o^2 B'}{Dt^2} - \nabla^2 B' = \nabla \cdot (\mathbf{\Omega} \times \mathbf{u}) \tag{1.51}$$

with c_o the speed of sound, $\mathbf{u} = \mathbf{u}_o + \mathbf{u}'$ the velocity decomposed into an average part $\bar{\mathbf{u}}$ and a fluctuating part $\mathbf{u}'$. The material derivative is defined as $\frac{D_o}{Dt} = \frac{\partial}{\partial t} + \mathbf{u}_o \cdot \nabla$ and $\mathbf{\Omega} = \nabla \times \mathbf{u}$ the total vorticity. In equation (1.51), the RHS explicitly shows that the vorticity $\mathbf{\Omega}$ is responsible for the generation / damping of sound. Alternatively, Howe also obtained an expression for the rate of dissipation of acoustic energy due to the interaction with vorticity.

$$\mathcal{P} = -\frac{1}{T}\int_T \int_V \rho_o[\mathbf{\Omega} \times \mathbf{u}) \cdot \mathbf{u}']dV dt \tag{1.52}$$

where T is the characteristic time of interest, a period of the acoustic signal for example. With the knowledge of the vorticity distribution $\mathbf{\Omega}$, expression (1.52) can be used to evaluate *a posteriori* the dissipation / amplification of sound due to vorticity in experiments or LES computations [109]. For *a priori* predictions of hydro-acoustic damping, eq. (1.51) should be solved. To do this, the dependency of vorticity to the acoustic field must be known. As said earlier, the conversion of acoustic waves into vorticity shedding is ruled by viscous effects near the trailing edge. The role of viscosity is to "smooth" the acoustic field, which is otherwise singular close to the trailing edge [105]. To approximate this, an unsteady Kutta condition is often applied at the trailing edge [94, 93, 110]. This condition provides the strength of the vorticity field required to keep pressure and velocity bounded.

The last step required to solve equation (1.51) is to assume a shape for the vorticity distribution. In the literature, two types of models are often found:

Vortex sheet Shed vortices are represented by an infinitely thin sheet where vorticity of constant strength is convected at the velocity of the mean flow in the jet [111, 106]. The strength of the vortex sheet is determined by application of the Kutta condition. Due to its simplicity, the vortex sheet model has enjoyed a great popularity and was used to derive the impedance of orifices, perforated plates, slits or sudden area expansions in the linear regime [111, 95, 86, 112, 96, 110]. For simple elements, the impedance can be expressed analytically and this is a strong point of the vortex sheet model. As an example, the expression of the Rayleigh conductivity derived by Howe [111] for an orifice with bias flow can be found in Appendix D.

Discrete vortex model In this refinement, the sheet is decomposed into discrete vortices of varying strengths. The trajectory of the vortices is obtained by applying Kelvin theorem and their strength is determined by the Kutta condition. This model provides more accurate results than the vortex sheet model, in particular for high amplitude regimes, but requires to solve numerically the vortices [102, 113, 114, 115]. The vorticity field obtained with this method is very close to the real one, at least in the proximity of the dissipating edge (Fig. 1.25).

Both vorticity distributions lead to good predictions of the damping properties, as the examples of Fig. 1.26 show. The good agreement is another proof that the role of viscosity in hydro-acoustic damping is confined to a very small region, since a Kutta condition is able to capture it so well.

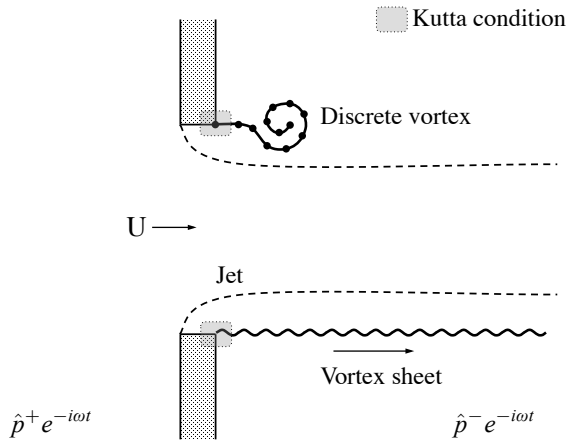


FIGURE 1.24: Vortex sound models are divided into two categories depending on the vorticity representation: vortex sheet (bottom) or discrete vortices (top)

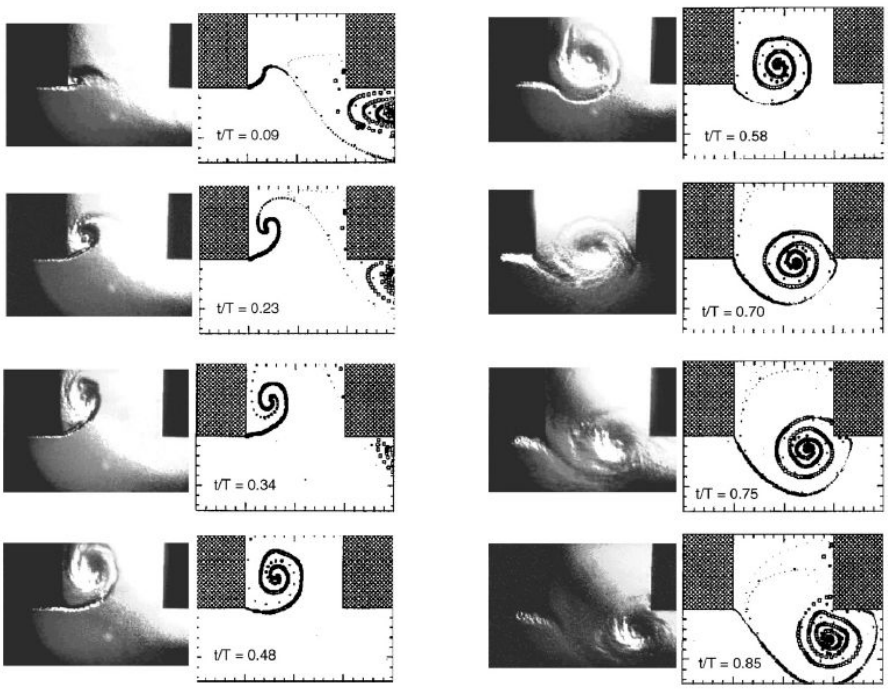
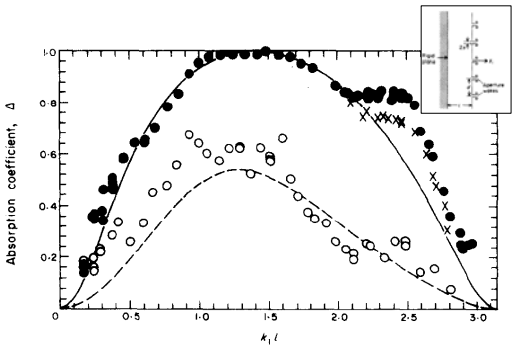
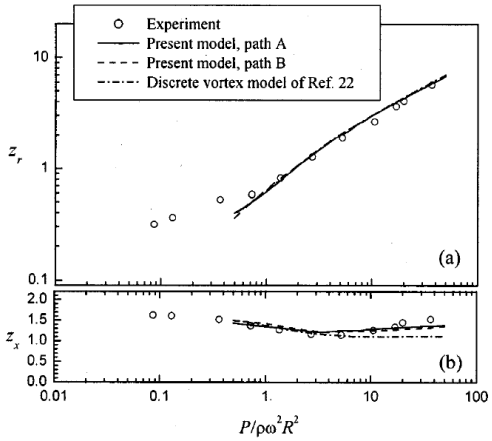


FIGURE 1.25: Experimental visualization of vorticity vs vorticity field computed with discrete vortex model. From [116]



(A) Absorption coefficient of an array of slit, predicted with an analytical expression (lines) and measured experimentally (symbols) at two Mach numbers. From [86].



(B) Normalized acoustic impedance of a diaphragm with sound pressure amplitude. From [117].

FIGURE 1.26: Example of damping properties retrieved with vortex sound theory assuming a) a vortex sheet, b) a discrete vortex field.

Quasi-steady models

Models derived from the vortex sound analogy have the advantage of representing the feedback of acoustics on hydrodynamics. In cases where this feedback is not important (at low frequencies), another class of models assumes that the shear layer is steady. In this case, the damping properties of sharp edges (e.g. orifices and sudden section changes) in mean flow is due to the absence of pressure recovery in the downstream jet and can be derived from the Bernoulli equation for linear and nonlinear regimes [118, 119, 120, 103, 121].

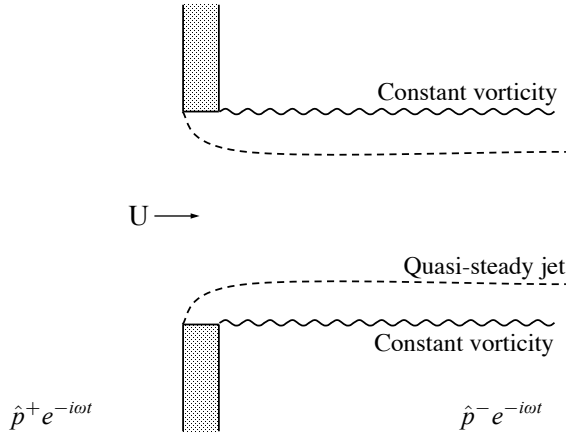


FIGURE 1.27: Quasi-steady jet models

With this approach, Durrieu et al. [120] was able to predict correctly the evolution of the matrix of confined Borda tube with the mean flow velocity, from simple conservation equations. The model compares well with experiments, even for non vanishing frequencies (Fig. 1.28).

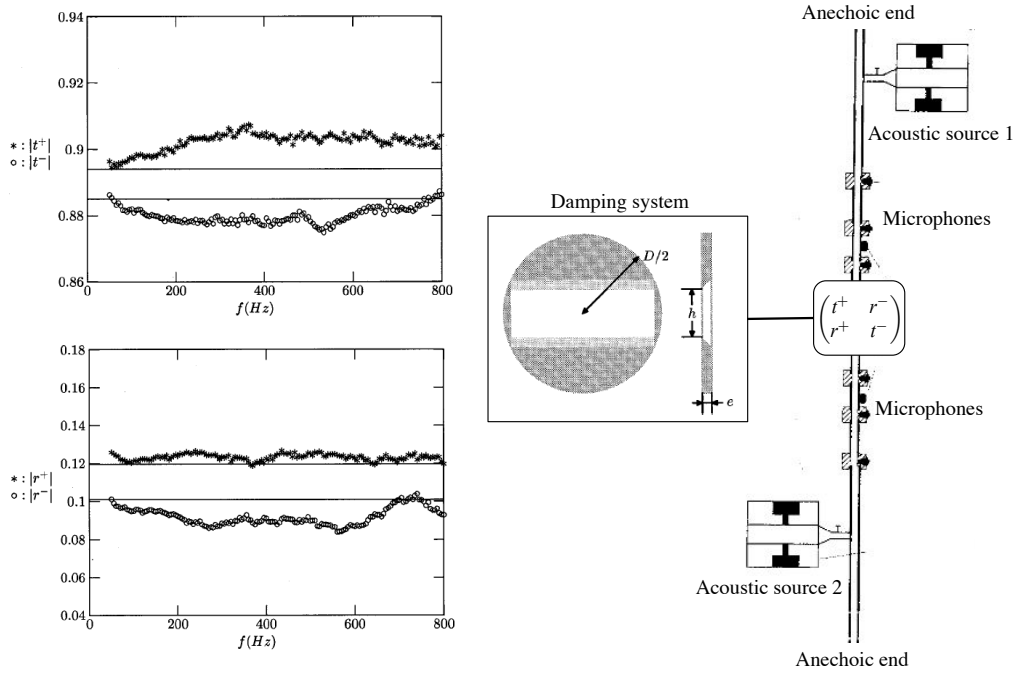


FIGURE 1.28: Left: Modulus of scattering matrix coefficients from experiments and the quasi-steady model of [120] at M=0.045. Right: Overview of the test rig and damping element of interest.

Black-box approach

Quasi-steady and vortex sound models provide excellent results for simple configurations, easily solved analytically or with simple numerical tools. However, they are not suited to predict the hydro-acoustic behaviour of complex geometries such as swirlers. In this case, a black-box approach can be used. Again, this is possible because hydro-acoustic damping is a local, compact mechanism that is well represented by acoustic jump conditions. The element of interest is computed with a solver of high accuracy (LES for example) and modeled as an acoustic n-port. It was shown that this acoustic n-port correctly captures the hydro-acoustic coupling for a number of configurations, with LES, LNSE or even Lattice-Boltzmann solvers [122, 123, 14, 90, 99, 32]. This black-box approach is in fact similar to the Flame Transfer Matrix method. The acoustic n-port can be plugged into a simpler acoustic tool, so as to combine the accuracy of an LES-type solver with the simplicity of an acoustic solver. First results were obtained for a Helmholtz computation with an analytical matrix model of the flame and the injector [42]. Because the matrix parameters are very easy to change, Laera et al. [42] were able to analyse the effect of a change in the flame and injector parameters. To the authors' knowledge, similar results have not yet been performed with a matrix containing the hydro-acoustic losses from experiments or LES.

1.5.4 Hydro-acoustic damping in thermo-acoustic studies

The key points of the quick review on hydro-acoustic conversion can be summarized as follows:

- Energy can be transferred from acoustics to the mean flow via vorticity shedding, at any kind of trailing edge (orifice, sudden section change, obstacle...).

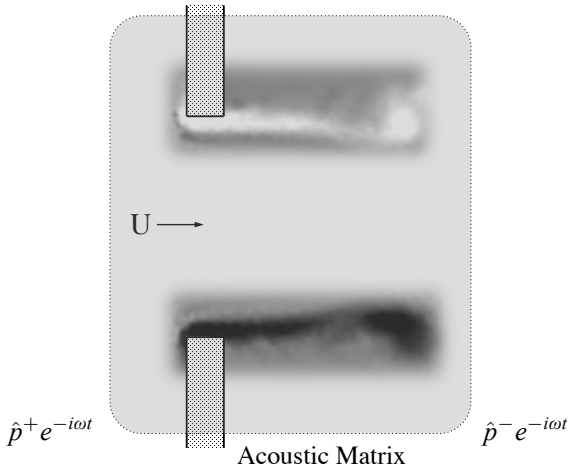


FIGURE 1.29: Black box matrix models

- This process depends on viscosity but only in a very limited region of space. The flow can be considered inviscid everywhere and the viscous effects represented by a Kutta condition at the edge.
- Based on this assumption, models with different levels of complexity have been developed. They rely either on a vortex sound analogy or a quasi-steady assumption.
- From these models, the damping behavior of simple elements such as orifices or sudden section change can be studied analytically or semi-analytically.
- More complex geometries are not tractable analytically, but can be analyzed with a black-box, matrix approach.

For the numerical prediction of combustion instabilities with acoustic tools, these points have several implications.

1. A combustor contains many potentially damping elements as Fig. 1.18 shows. Dilution holes, perforated plates and the swirled injector are all good candidates for hydro-acoustic damping.
2. These sources of damping have an important impact on combustion instabilities but have rarely been addressed by numerical prediction tools. Either an LES or LNSE solver is used and the hydro-acoustic damping is naturally included in the prediction, or an acoustic tool is used and hydro-acoustic damping is assumed negligible. Some exceptions are the work of Gullaud [43] who implemented a model based on vortex sound theory to account for the damping of perforated plates in a Helmholtz solver, and the work of Yang and Morgans who studied the impact of Helmholtz resonators on thermoacoustic instabilities by implementing a nonlinear quasi-steady model in an acoustic network code [124].

One reason behind this lack of studies is that the damping behaviour of complex geometries is not easy to evaluate. It can be assessed nonetheless with a black-box matrix approach which is compatible with many acoustic solvers, in particular Helmholtz solvers.

1.6 Thesis objectives and outline

Going back to the central question,

What is the impact of acoustic-mean flow interactions on combustion instabilities ?

The majority of studies on thermoacoustics focus on the source term (the Rayleigh term) of the acoustic energy, linked to the RHS of Eq. (1.24), but very few are dedicated to the loss term (the acoustic dissipation, mainly due to hydro-acoustic interaction), forgetting that it is the difference between the two terms which control stability. In many cases, for example in zero Mach number solvers, this dissipation term is even simply set to zero. Analytical models for the hydro-acoustic behaviour of simple elements are available but only partially solve the problem. Indeed, more complicated elements such as swirlers cannot be modeled analytically.

Consequently, the objectives of the present thesis are:

- To develop a methodology that includes the hydro-acoustic damping behaviour of any type of element in a frequency-domain acoustic solver.
- To apply this methodology for the thermoacoustic analysis of an industrial combustor and assess the impact of hydro-acoustic damping on a realistic combustion instability.

Because of the industrial application, the hydroacoustic damping effects will be represented with a matrix approach combined to a Helmholtz solver as the latter provides a good trade-off between accuracy and cost for complex geometries.

The first aspect of this thesis was to implement an approach to plug acoustic matrices into a Helmholtz solver. For this purpose, a Matrix Boundary Condition was developed and presented in Chapter 2. This chapter also explains how to obtain the hydro-acoustic damping matrices.

The second part of this work is dedicated to the validation of the matrix methodology. In Chapter 3, the Matrix Boundary Condition is introduced in the Helmholtz computation of an academic test rig, with experimental and LES matrices. The comparison between Helmholtz results and measurements from experiments and LES shows an excellent agreement, confirming that combining the matrix data with the Helmholtz solver does capture hydro-acoustic conversion.

The simple methodology introduced in Chapters 2 and 3 proved to be inoperable as such for industrial geometries. The reasons are exposed in Chapter 4. Extensions are proposed and successfully applied to simple test cases.

Finally, the extended methodology is applied to a Safran industrial burner in Chapter 5. An acoustic analysis including acoustic energy balance is performed on the Helmholtz solutions with and without Matrix Boundary Condition, so as to assess the impact of hydro-acoustic damping on a realistic instability.

Chapter 2

A methodology to account for hydro-acoustic interaction in a Helmholtz solver

The first objective of this thesis is to introduce hydro-acoustic damping into a Helmholtz solver, by modeling this mechanism with an equivalent matrix. In this chapter, the basic theory behind the acoustic matrix representation is recalled (Section 2.1), as well as the methods to measure it (Section 2.2). The matrix is included in the Helmholtz solver with a new boundary condition, described in Section 2.3. Finally, a code validation of the boundary condition on a simple case is performed in Section 2.4

2.1 Matrix representation for hydro-acoustic coupling

In a 1D tube, the general solution of the acoustic wave equation consists in the superposition of two plane waves travelling in opposite directions at the speed of sound c_o. The expression of the plane waves and associated acoustic pressure and velocity has been given in Eqs. (1.31) to (1.34). In a straight uniform tube without any losses, the waves propagate unchanged and their amplitudes A^+ and A^- remain constant in the tube. However, when the flow properties change or in the presence of losses, propagation is affected and so are A^+ and A^-. The modification can be continuous. For example, the presence of a viscous boundary layer at the walls tends to damp the wave amplitudes as they travel in the tube [74, 125].

When the modification is located in a limited region of space as is the case for hydrodynamic damping, its effect on A^+ and A^- can be represented as a pair of jump conditions (Fig. 1.14), as expressed in Eq. 1.36. If the jump conditions ϕ and ψ are linear, they can be written as a 2×2 matrix, also called acoustic 2-port. This linearity assumption is important. In practice, it is verified for hydro-acoustic coupling at low acoustic level (i.e. in the linear regime). At higher acoustic levels, i.e. in the nonlinear regime, this is not true anymore and the matrix representation is not adapted.

Depending on the acoustic quantities used as inputs and outputs, different matrix formulations can be defined and some of them are listed in Tab. 2.1. All formulations are essentially equivalent and it is possible to switch from one formulation to another with the expressions of Appendix B.

As said earlier, this matrix representation is well-suited for hydro-acoustic damping because the latter is compact with respect to the acoustic wavelength. Moreover, in cases where the matrix cannot be determined analytically, its coefficients can still be measured

Name	State variables	Defining equation
Acoustic transfer matrix	p', u'	$\begin{pmatrix} p'_d \\ \rho_{o,d} c_{o,d} u'_d \end{pmatrix} \equiv T_a \begin{pmatrix} p'_u \\ \rho_{o,u} c_{o,u} u' \end{pmatrix}$
Wave transfer matrix	A^+, A^-	$\begin{pmatrix} A^+_d \\ A^-_d \end{pmatrix} \equiv T_w \begin{pmatrix} A^+_u \\ A^-_u \end{pmatrix}$
Scattering matrix	A^+, A^-	$\begin{pmatrix} A^+_d \\ A^-_u \end{pmatrix} \equiv S \begin{pmatrix} A^+_u \\ A^-_d \end{pmatrix}$
Mobility matrix	p', u'	$\begin{pmatrix} \rho_{o,u} c_{o,u} u'_u \\ \rho_{o,d} c_{o,d} u'_d \end{pmatrix} \equiv M \begin{pmatrix} p'_u \\ p'_d \end{pmatrix}$

TABLE 2.1: Examples of acoustic 2-ports formulation [126].

experimentally or numerically, with the methods detailed in the next section. The matrix formalism has been used successfully to predict the damping behavior of a variety of elements (orifices [120, 127, 128], sudden section changes [129, 122, 128], swirlers [126], T-junctions [130, 31]), with a variety of numerical solvers (LES [127, 130, 122], LNSE [128, 31] or even Lattice Boltzmann methods [99]).

In fact, the matrix formalism extends beyond hydro-acoustic damping, and can also be applied to the prediction of whistling [90], flame-acoustics coupling [131] or even to model the acoustic behaviour of a heat exchanger [132].

2.2 Matrix measurement methods

No matter whether experimental or numerical, matrix estimation methods are essentially the same and rely on measuring the response of the element of interest to an acoustical forcing. In order to easily quantify this response, the element is usually encased in a long tube in order to have plane acoustics far from the perturbating element. To the author's knowledge, only two methods are used in the litterature and differ in the type of forcing and the system inverted to obtain the matrix. These two methods are presented below.

2.2.1 Discrete harmonic forcing with direct matrix inversion

In this technique, a source of acoustic fluctuations is introduced in the test rig. In experiments, this could be a loudspeaker or a siren. Numerically, this source term can be directly introduced as a source point in the volume, or at the boundaries, using an inlet with a fluctuating velocity for example. The fluctuation is assumed to be composed of a finite, discrete set of frequencies.

The acoustic forcing creates a particular acoustic state in the test rig, characterized by a pair of plane wave amplitudes (A^+_u, A^-_u) and (A^+_d, A^-_d). These wave amplitudes are

related by the matrix coefficients of the system of interest, expressed in with the scattering formalism for example:

$$A_2^+ = S_{11}(\omega)A_1^+ + S_{12}(\omega)A_2^- \tag{2.1}$$
$$A_1^- = S_{21}(\omega)A_1^+ + S_{22}(\omega)A_2^- \tag{2.2}$$

Equations (2.1) and (2.2) contain four unknowns S_{11}, S_{12}, S_{21}, S_{22}, the matrix coefficients. In order to determine them, at least another pair of equations is required and obtained by creating a new, different acoustic state (Fig. 2.1). This can be done either by changing the location of the acoustic forcing (two-source method) or by modifying the boundary conditions (two-load method).

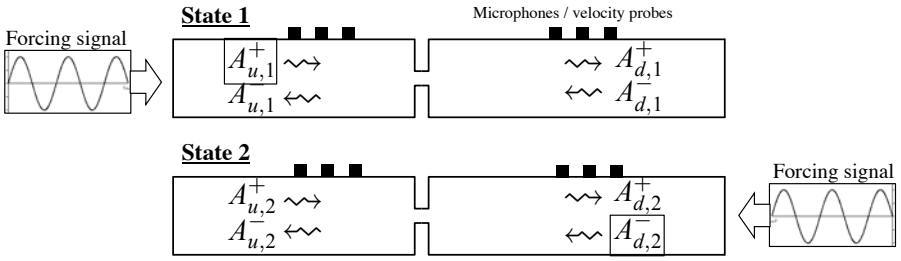


FIGURE 2.1: Illustration of the direct matrix inversion with discrete harmonic forcing method. At least two acoustic states are required and obtained here by changing the forcing location.

With $N \geq 2$ acoustic states:

$$\underbrace{\begin{pmatrix} A^+_{u,1} & A^-_{d,1} & 0 & 0 \\ 0 & 0 & A^+_{u,1} & A^-_{d,1} \\ \vdots & \vdots & \vdots & \vdots \\ A^+_{u,j} & A^-_{d,j} & 0 & 0 \\ 0 & 0 & A^+_{u,j} & A^-_{d,j} \\ \vdots & \vdots & \vdots & \vdots \\ A^+_{u,N} & A^-_{d,N} & 0 & 0 \\ 0 & 0 & A^+_{u,N} & A^-_{d,N} \end{pmatrix}}_{H} \underbrace{\begin{pmatrix} S_{11} \\ S_{12} \\ S_{21} \\ S_{22} \end{pmatrix}}_{s} = \underbrace{\begin{pmatrix} A^+_{d,1} \\ A^-_{u,1} \\ \vdots \\ A^+_{d,j} \\ A^-_{u,j} \\ \vdots \\ A^+_{d,N} \\ A^-_{u,N} \end{pmatrix}}_{a} \tag{2.3}$$

This system can be inverted with a least-square inversion, and the error on the inversion can also be estimated.

$$\tilde{s} = (H^\dagger H)^{-1} H^\dagger a \quad , \quad err_{\text{relative}} = ||H\tilde{s} - a||/||a|| \tag{2.4}$$

where † denotes the hermitian transpose. One last question is how to obtain the plane wave amplitudes. For this, the pressure and/or velocity temporal signals must be available at different locations of the test rig. These signals are first filtered in order to extract only the frequencies of interest, with a Fourier Transform, or a Dynamic Mode Decomposition [133] for example. The wave amplitudes can then be retrieved with the multi-microphone method [134, 70], privileged in this thesis, or with the Characteristics Based Filter of [135].

The discrete harmonic forcing technique is probably the simplest and the oldest one, but it is still used today [136, 70, 72]. It is easy to set up experimentally and to implement numerically in an LES code such as AVBP, where fluctuating boundary conditions are already available. Moreover, the results are straightforward to interpret and check.

2.2.2 White noise forcing with System Identification

The coefficients of the scattering matrix can be seen as transfer functions between the ingoing (A_u^+, A_d^-) and the outgoing wave amplitudes (A_d^+, A_u^-), similar to the transfer functions found in signal processing. Therefore, System Identification (SI) techniques from communication engineering can also be applied to the estimation of the matrix coefficients, as noted by [11]. The principle is only briefly recalled here. More details can be found in [11, 137].

Instead of directly computing the matrix coefficients in frequency domain, SI methods work in temporal domain. The equivalent of a transfer function in temporal domain is the Unit Impulse Response, sometimes abridged as Impulse Response (IR). For a single input single output, linear, time invariant, causal system, the discrete Impulse Response h is defined as:

$$r_i = \sum_{k=0}^{L} h_k s_{i-k} \quad \text{for } i = L, .., N \tag{2.5}$$

with

$$s_i = s(i\Delta t), \qquad i = 0, \ldots, N, \quad \text{the discrete input signal of length N,} \tag{2.6}$$

$$r_i = r(i\Delta t) \qquad i = 0, \ldots, N \quad \text{the discrete output signal of length N,} \tag{2.7}$$

$$h_k = h(k\Delta t) \qquad k = 0, \ldots, L \quad \text{the discrete IR of length L} \tag{2.8}$$

The Impulse Response h is directly related to the transfer function F:

$$F(\omega) = \sum_{k=0}^{L} h_k \exp(-i\omega\Delta t k) \tag{2.9}$$

The Impulse response (and therefore the transfer function) can be estimated by inverting the Wiener-Hopf relationship (2.10). In this equation, Γ and $\mathbf{c}$ are respectively approximations for the autocorrelation matrix of the input signal $\mathbf{s}$, and the cross-correlation matrix between $\mathbf{s}$ and $\mathbf{r}$. Their exact expression is not important here and can be found in [11]. What is important however is that Γ and $\mathbf{c}$ can be built as soon as all input and output signals for *one acoustic state* are known. In the case of a system with multiple inputs, this acoustic state is obtained by forcing all inputs simultaneously.

$$\mathbf{\Gamma h} = \mathbf{c} \tag{2.10}$$

If Γ is invertible then:

$$\mathbf{h} = \Gamma^{-1}\mathbf{c} \tag{2.11}$$

In order to have good invertibility properties for Γ, the acoustic forcing needs to satisfy a few criteria:

- all excitation signals should be uncorrelated with themselves.
- the excitation signals should have a broadband, low-pass filtered spectrum with constant amplitude in the frequency range of interest.
- the statistical independence of the different excitation signals for a multiple inputs system should be maximal.

This can be achieved with several uncorrelated white noise signals (although more optimal signals exist, see [137]), and the procedure to obtain the matrix is the following:

1. Impose a white noise acoustic forcing on all input ports of the matrix, for instance A_u^+ and A_d^- in the scattering matrix case (Fig. 2.2).
2. Measure the response signals (A_d^+ and A_u^-).
3. Compute the auto-correlation Γ and cross-correlation $\mathbf{c}$ arrays.
4. Obtain the Impulse Responses with eq. (2.11). For the matrix, four impulse responses are obtained.
5. Compute the transfer functions in frequency domain with eq. (2.9) to obtain S_{11}, S_{12}, S_{21} and S_{22}.

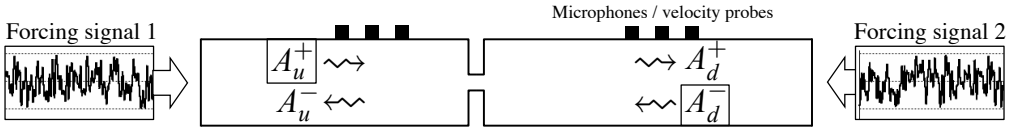


FIGURE 2.2: Illustration of the system identification with white noise forcing method.

From a numerical point of view, a great advantage of the System Identification method is that only one acoustic state and consequently only one CFD computation is required to obtain the full matrix over a large range of frequencies. On the other hand, the method raises a certain number of numerical issues that should be treated carefully. For example, the reflection at boundaries needs to be minimized in order to avoid pollution of the excitation signal by resonances. and this cannot be done over a broad frequency spectrum with conventional NSCBC boundaries. Moreover, the quality of the result is not as easy to check as with the direct matrix inversion of Sec. 2.2.1. An excellent review of these issues is given in [137].

For these reasons, discrete harmonic forcing with direct matrix inversion was preferred over System Identification with white noise forcing. A careful implementation of System Identification methods would however provide notable CPU cost reductions for future works with the matrix approach.

2.3 Including a network matrix in a Helmholtz solver : the Matrix Boundary Condition

Now, assume that the matrix of an element is known for acoustic quantities located at two planes u and d and that we want to replace this zone in the Helmholtz solver by its

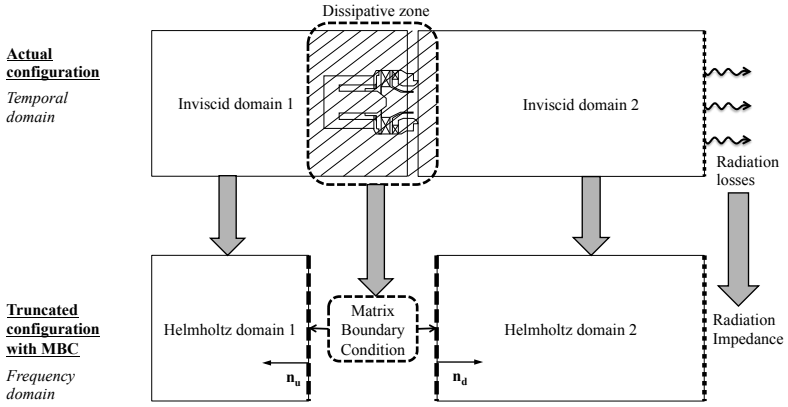


FIGURE 2.3: Helmholtz computation with Matrix Boundary Condition approach.

matrix. The simplest example is a swirler connecting two large domains. In each domain, the Helmholtz solver can be used but in the swirler the zero mean flow inviscid fluid assumption fails and it is preferable to replace it by its matrix either measured or computed with LES. How can this data be included in a Helmholtz computation ? The idea is to cut the geometry into two domains where the Helmholtz equation is solved separately. The matrix data, measured from a time domain experiment or CFD computation, is then used to link the two domains (Fig. 2.3), thanks to an adequate pair of boundary conditions, the Matrix Boundary Conditions (MBC). While acoustic losses at the boundaries are captured with regular boundary conditions, the Matrix Boundary Condition accounts for damping mechanisms located *inside* the combustor.

This boundary condition was implemented in the AVSP Helmholtz solver developed at CERFACS [17]. The AVSP solver discretizes the Helmholtz equation for pressure (1.24) into an eigenvalue problem, with a finite volume approach presented in Appendix C. The eigenfrequencies of this problem are complex and provide the oscillation frequency and growth/damping rate of the non-evanescent acoustic modes in the combustor. The pressure fields of these modes are described by the eigenvectors.

At boundaries (Fig. C.3), if a Dirichlet condition is not prescribed ($\hat{p} = 0$), information about the pressure gradient is necessary to fully solve the Helmholtz problem. For example, a Neumann boundary condition can be imposed by setting $\nabla\hat{p} \cdot \mathbf{n}$ (this is actually equivalent to setting $\hat{\mathbf{u}} \cdot \mathbf{n} = 0$). Dirichlet and Neumann boundaries provide some simple approximations to respectively walls/inlets, and outlets.

General boundaries can be represented by their acoustic impedance (2.12), which can be imposed with a Robin boundary condition (C.12). In the impedance definition (2.12), an inward convention is chosen for the surface normal $\mathbf{n}$ in AVSP.

$$Z = \frac{\hat{p}}{\rho_o c_o \hat{\mathbf{u}} \cdot \mathbf{n}} \tag{2.12}$$

$$\nabla\hat{p} \cdot \mathbf{n} = i\frac{\omega}{c_o Z}\hat{p} \tag{2.13}$$

For acoustic matrices, a pair of Robin relationships can be derived for the up and downstream gradients of pressure, thanks to the mobility matrix coefficients.

$$\begin{cases} \nabla\hat{p}_u \cdot \mathbf{n_u} = M_{11}\dfrac{i\omega}{c_{o,u}}\hat{p}_u + M_{12}\dfrac{i\omega}{c_{o,d}}\dfrac{\rho_{o,u}}{\rho_{o,d}}\hat{p}_d \\ \nabla\hat{p}_d \cdot \mathbf{n_d} = M_{22}\dfrac{i\omega}{c_{o,d}}\hat{p}_d + M_{21}\dfrac{i\omega}{c_{o,u}}\dfrac{\rho_{o,d}}{\rho_{o,u}}\hat{p}_u \end{cases} \tag{2.14}$$

For the truncated geometry of Fig. 2.3, the Matrix Boundary Conditions (MBC) defined by (2.14) is imposed on the up- and downstream surfaces of the truncation. The quantities $\hat{p}_u$ and $\hat{p}_d$ can be either computed point-wise, or spatially averaged over the corresponding patch. For point-wise computation, an interpolation step, presented in [138], is required to accommodate for non-coincident meshes between patch u and patch d. If $\hat{p}_u$ and $\hat{p}_d$ are uniform, both choices lead to the same result, but $\hat{p}_u$ and $\hat{p}_d$ are not always uniform as will be shown in Chapter 3.

The Helmholtz computation with Matrix Boundary condition (referred to as HMBC in the rest of the manuscript) corresponds to a nonlinear eigenvalue problem with respect to the eigenvalue. Indeed, the matrix coefficients depend on the frequency, an unknown of the eigenproblem, and so will the MBC operator. Since the frequency dependency is not known a priori, there is no general algorithm to solve the nonlinear eigenvalue problem at the present time. This issue is treated in AVSP with an iterative fixed point approach [17], detailed in Appendix C.

The matrix data is usually available for a set of real frequencies. At each fixed point iteration, the matrix coefficients could be updated with a simple linear interpolation at the real part of the new frequency guess. This is suitable when the eigenfrequencies of interest have a small imaginary part. When the imaginary part becomes larger however, the matrix should also be known along the imaginary axis. This can be done from the values at real frequencies, provided that the matrix coefficients are holomorphic functions of the frequency (as they usually are). In this case, each coefficient can be interpolated in the real domain with a known holomorphic function, that has the interesting property of remaining valid in the entire complex plane [139]. In AVSP, the matrix data can therefore be provided either as a table of values at real frequencies, or as a polynom valid in the complex plane.

2.4 Code validation of the Matrix Boundary Condition

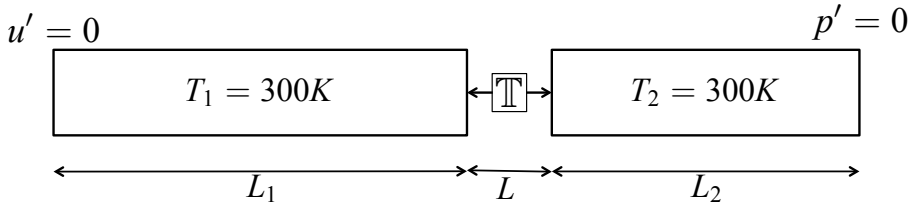


FIGURE 2.4: Quarter-wave tube configuration for validation of the MBC code

The newly developed Matrix Boundary Condition is first tested on the configuration of Fig. 2.4. It consists of a 1D tube of constant cross-section filled with air (perfect gas constant equal to $R = 287J \cdot kg^{-1} \cdot K^{-1}$), divided by a pair of Matrix Boundary Conditions. The length of the upstream portion is L_1 and the length of downstream portion is L_2. The gas is at $T_1 = T_2 = 300$ K corresponding to a speed of sound of $c_o = 347.4$ m/s.

n	Theory	Standard Helmholtz	HMBC
0	86.8 Hz	86.8 Hz	86.8 Hz
1	260.5 Hz	260.5 Hz	260.5 Hz
2	434.2 Hz	434.2 Hz	434.2 Hz
3	607.9 Hz	607.9 Hz	607.9 Hz
4	781.6 Hz	781.5 Hz	781.5 Hz

TABLE 2.2: First five eigenfrequencies (in Hz) of the quarter-wave tube with $Ls + L_1 + L_2 = 1.0$ m.

A fixed-velocity boundary condition is used at the inlet and fixed-pressure one at the outlet. For this first test, a simple propagation matrix is imposed at the Matrix Boundary Conditions:

$$\mathbb{T} = \begin{pmatrix} \cos(kL) & i\sin(kL) \\ i\sin(kL) & \cos(kL) \end{pmatrix} \tag{2.15}$$

with L an arbitrary length. This configuration corresponds to a simple quarter-wave tube and has infinite discrete eigenfrequencies given by:

$$f_n = (2n+1))\frac{c_o}{4(L_1+L_2+L)} \quad n \in \mathbb{N} \tag{2.16}$$

For $L_1 = 0.4$ m, $L_2 = 0.5$ m and $L = 0.1$ m, the eigenfrequencies of the quarter-wave tube are listed in Tab. 2.2. The corresponding eigenmodes can be reconstructed as:

$$\hat{p}_n(x) = cos(k_n x) \quad \text{with} \quad k_n = \frac{2\pi f_n}{c_o} \tag{2.17}$$

Alternatively, the eigenfrequencies and eigenmodes can be computed with a standard Helmholtz solver, on the 3D parallelepipedic mesh of Fig. 2.5. These two reference solutions are compared to an HMBC computation, on the mesh of Fig. 2.6.

As Tab. 2.2 (eigenfrequencies) and Fig. 2.7 (eigenmodes), both the standard Helmholtz computation and the HMBC one correctly reproduce the frequencies and mode structures of the quarter-wave tube. Identical results are obtained for 1 processor and for 24. These results validate the code of the Matrix Boundary Condition in the AVSP Helmholtz solver at least in a simple 1D case where the analytical solution is known. The next chapter addresses a more complex case: a non reactive swirler installed at IMFT.

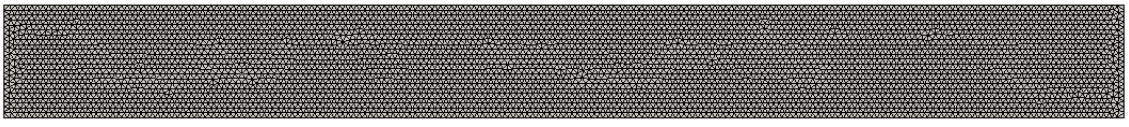


FIGURE 2.5: Mesh for the standard Helmholtz computation of the quarter-wave tube.

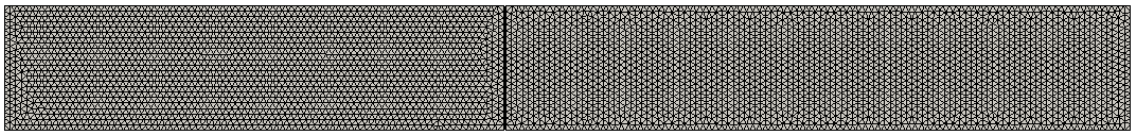


FIGURE 2.6: Mesh for the Helmholtz computation with MBC of the quarter-wave tube.

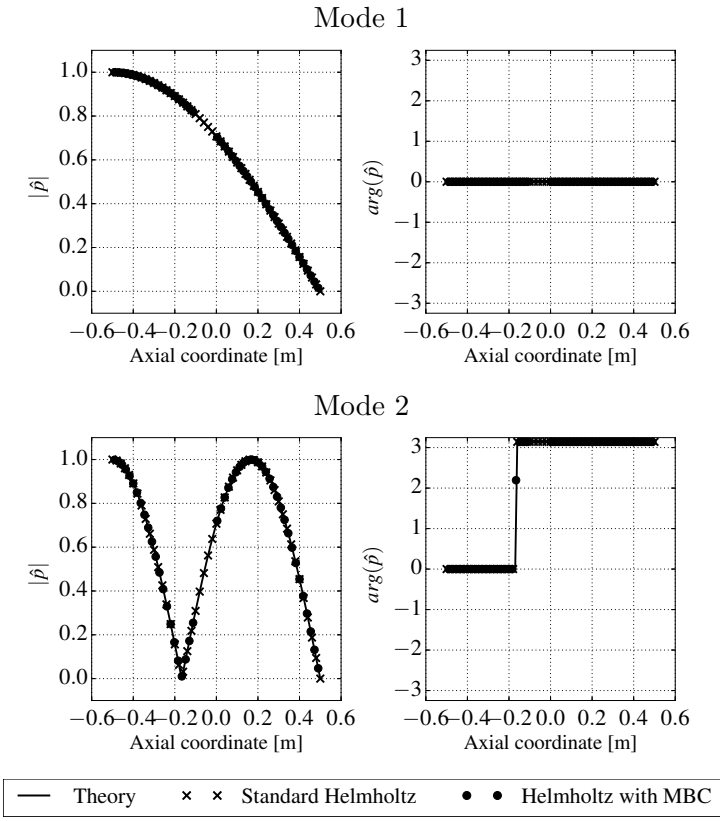


FIGURE 2.7: Mode structure (modulus and phase of complex pressure amplitude) along the axis of the quarter-wave tube, for the first two modes.

Chapter 3

Application of the HMBC approach to an academic test rig.

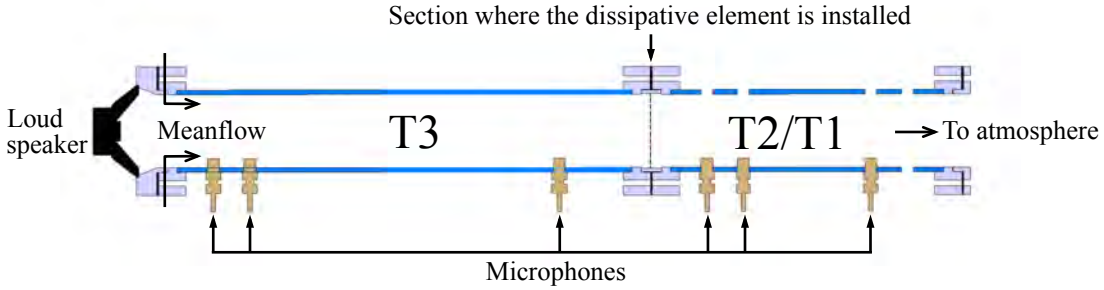
In Chapter 2, a methodology was developed to include the matrix of acoustically dissipative elements into a Helmholtz solver. In this chapter, this methodology is now tested on an academic test rig, for which numerical and experimental acoustic measurements are available. The experiment is non reacting and the goal of the chapter is to perform an HMBC computation using the matrices obtained from the acoustic measurements. The results of the HMBC computations show that the dissipative behaviour of orifices and swirlers is indeed captured by the matrices, whether numerical or experimental. Including the matrix data in an HMBC computation thus improves the estimation of the damping rates and mode structures, compared to a standard Helmholtz solution. The results presented in this chapter are adapted from an article accepted by AIAA Journal [**?**].

3.1 Target setup: the PRELINTRIG experiment

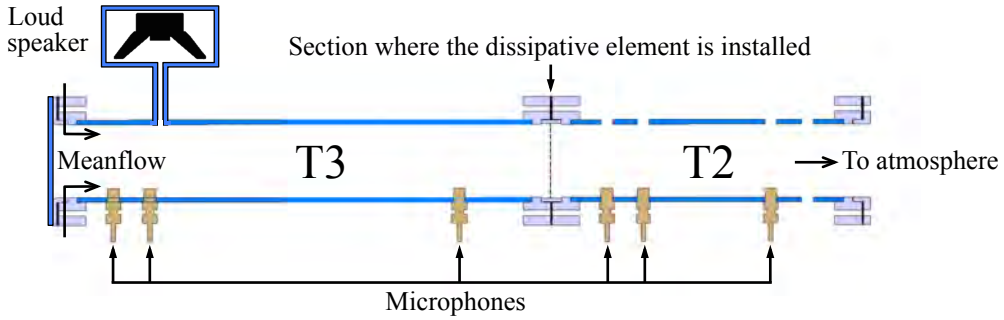
The configuration of interest is the experimental test rig PRELINTRIG from IMFT. This test rig is composed of cylindrical ducts of different lengths, that can be connected by a dissipative element (Fig. 3.1). Two dissipative elements are considered in this study: a diaphragm (Fig. 3.2a) and a swirler (Fig. 3.2b). The experiments are run at ambient temperature $T_o = 299$ K and ambient pressure $P_o = 101550$ Pa with air (specific ratio of $\gamma = 1.4$ and molecular mass of $W = 28.97$ g/mol). All measurements were performed at Institut de Mécanique des Fluides de Toulouse (IMFT) by Maxence Brebion.

Air flow is driven by eight uniformly distributed radial injectors. In order to perform acoustic measurements, the rig air flow is excited by a loudspeaker (Focal ISN 100) fixed in a PVC air tight module. Six microphones (Bruel & Kjaer 1/4" Type 4954B) measure the acoustic pressure in the rig: three upstream and three downstream of the dissipative element. Three PVC tubes (T1, T2, T3) with the same cross-section but different lengths are used in the experimental studies. Their inner radius is $R = 0.04$ m and lengths are $l_1 = 0.26$, $l_2 = 0.34$, $l_3 = 0.56$ m respectively.

End corrections of $\delta_{in} = 0.010$ m and $\delta_{out} = 0.025$ m are used to match the experimental and Helmholtz solver eigenfrequencies, in absence of mean flow. The value of the correction length at the outlet corresponds to the correlation of Levine and Schwinger [77] $\delta_{out} = 0.6R$. The inlet correction length includes the effect of the loudspeaker and injection tubes



(A) Configuration for matrix measurement. The downstream part is composed of T2 only or T2 and T1, to obtain the four configurations of Fig. 3.5.



(B) Configuration for acoustic modes measurement

FIGURE 3.1: Sketch of the experimental setup. The junction may contain either a diaphragm or a swirler. Three microphones are placed upstream and downstream of the element. The loudspeaker position changes depending on the type of measurement (top figure: matrices, bottom figure: acoustic modes).



(A) Diaphragm



(B) Swirler

FIGURE 3.2: Acoustic elements: (a) Diaphragm, (b) Swirler.

and no correlation is available for this geometry. The value of $\delta_{in} = 0.010$ m was chosen because it allows to fit the the experimental frequencies in an optimal way.

Two types of acoustic measurements can be performed on this test rig: the acquisition of 2-port matrices (Fig. 3.1a) and the acquisition of the eigenmodes and eigenfrequencies (Fig. 3.1b). For matrix measurement, T1, T2 and T3 are combined to obtain four independent configurations (Fig. 3.5), as explained in Section 3.3.1. For the measurement of acoustic modes and frequencies, only tubes T3 and T2 are used and are placed upstream and downstream of the element of interest respectively (Fig. 3.1b). In this case, the loudspeaker is placed on the side of the tube to minimize the coupling between the loudspeaker cavity and the main rig.

Acoustic matrices and modes are determined for three different flow rates characterized

by their bulk velocities: $U = 0.0$; 0.17 ; 0.34 m/s. These bulk velocities, imposed by a mass-flow meter, are controlled with a precision of 2% by using hot-wire based velocity profile measurements. In every case, the Mach number is lower than 0.001 and Mach number effects in the inviscid zones can be neglected.

The acquisition system is based on the Labview software and its associated multichannel acquisition board. Measurements are performed with harmonic excitations, for frequencies ranging from 50 up to 1000 Hz, well below the cut-off frequency of 2500 Hz. This ensures that only plane waves exist in the ducts. For each frequency and configuration, samples of 2 s are recorded at a sampling rate of 10 kHz.

3.2 Description of the validation strategy

For the PRELINTRIG test rig, matrix data and reference eigenmodes are measured experimentally (M. Brebion) and numerically, with methods detailed in Section 3.3. Standard and MBC Helmholtz computations are then performed, following the procedure described in Section 3.4.

To check the validity of the MBC methodology, four types of comparisons, called C1, C2-LES, C2-EXP and C3 in Fig. 3.3, are performed:

C1 Matrices obtained from the experiments and from the LES are compared, to check their validity and robustness to either numerical or experimental artefacts.

C2-LES The LES matrix data is used as an input of the Helmholtz solver with MBC. The resulting eigenfrequencies and eigenmodes are compared with the LES values, and with the results of the Helmholtz solver without MBC.

C2-EXP The experimental matrix data is used as an input of the Helmholtz solver with MBC. The resulting eigenfrequencies and eigenmodes are compared with the experimental values and with the results of the Helmholtz solver without MBC.

C3 The MBC Helmholtz solver results from the LES matrix and from the experimental matrix are compared to check the sensitivity of the results to the input data used to model the non-acoustic element.

3.3 Measurement methods

3.3.1 Experimental matrices and modes

In order to perform comparison C2-EXP (Fig. 3.3), the acoustic modes and acoustic matrices are measured experimentally.

Frequencies and dissipation of acoustic modes in the experiment

The first step is to measure the frequencies and damping rates of the acoustic modes in the experiment (Fig. 3.1b). To do this, the test rig is excited by a loudspeaker producing a monochromatic harmonic signal at a constant voltage, and the resulting pressure waves are measured by microphones for a discrete set of frequencies. Under the plane wave

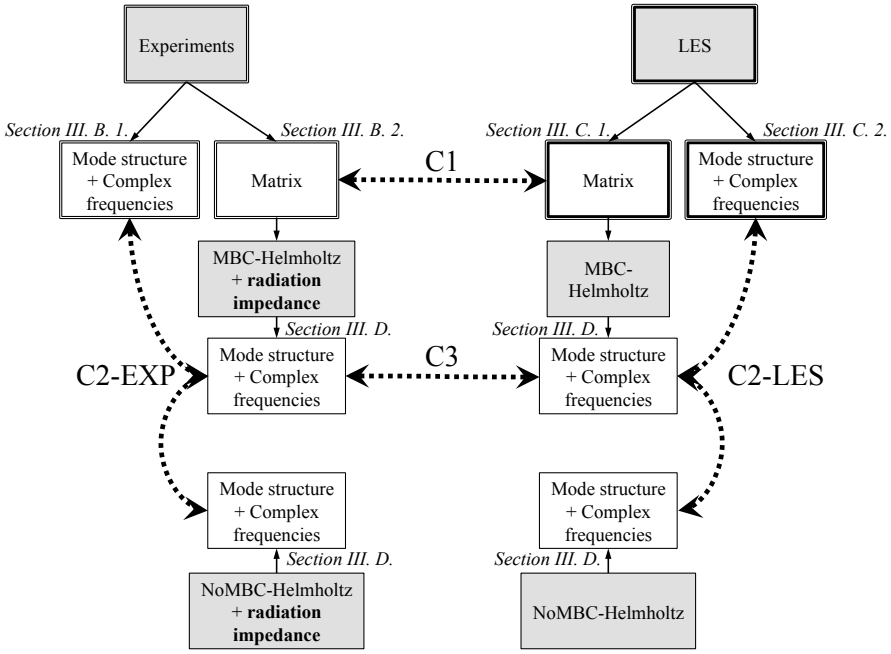


FIGURE 3.3: MBC validation strategy with the four axes of comparison. Annotated blocks are detailed in the indicated sections.

assumption, the complex acoustic pressure amplitude at location z_j can be expressed as:

$$\hat{p}(z_j) = a_j e^{i\phi_j} = \mathcal{A}^+ e^{ik^+ z_j} + \mathcal{A}^- e^{-ik^- z_j} \tag{3.1}$$

$$\rho_o c_o \, \hat{u}(z_j) = \mathcal{A}^+ e^{ik^+ z_j} - \mathcal{A}^- e^{-ik^- z_j} \tag{3.2}$$

where $\mathcal{A}^+$ and $\mathcal{A}^-$ are the amplitudes of the right and left traveling waves respectively. z_j is the axial coordinate in the duct, with the origin $z = 0$ chosen at the center of the acoustic element (diaphragm or swirler).

By measuring the complex acoustic pressure at different locations, the wave amplitudes are retrieved at each frequency thanks to the multi-microphones technique [134, 70].

$$\underbrace{\begin{pmatrix} e^{ik^+ z_1} & e^{-ik^- z_1} \\ \dots & \dots \\ e^{ik^+ z_J} & e^{-ik^- z_J} \end{pmatrix}}_{D} \underbrace{\begin{pmatrix} \mathcal{A}^+ \\ \mathcal{A}^- \end{pmatrix}}_{x} = \underbrace{\begin{pmatrix} a_1 e^{i\phi_1} \\ \dots \\ a_J e^{i\phi_J} \end{pmatrix}}_{b} \tag{3.3}$$

$$\tilde{x} = (D^\dagger D)^{-1} D^\dagger b \tag{3.4}$$

System (3.3) is overdetermined when more than two microphones are used and is inverted with a least-square approach as done in Eq. (3.4).

The wave amplitudes are combined to reconstruct $\mathcal{E}$, the period-averaged acoustic energy integrated over the volume V of the rig, as defined in Eq. (5.20).

$$\mathscr{E} = \int_V \left(\frac{1}{4\rho_o c_o^2} |\hat{p}(z)|^2 + \frac{1}{4} \rho_o |\hat{u}(z)|^2 \right) dV \tag{3.5}$$

For plane waves at low Mach number in a forced harmonic regime, the wave amplitudes are constant in each inviscid rig portion and the term in the integral of Eq. (5.20) is independent of the coordinate z. The integration can thus be performed separately over the upstream and downstream volumes V_u and V_d to obtain Eq. (3.6).

$$\mathscr{E}(\omega) = V_u \left[\frac{1}{2\rho_o c_o^2} \left(|\mathcal{A}_u^+(\omega)|^2 + |\mathcal{A}_u^-(\omega)|^2 \right) \right] + V_d \left[\frac{1}{2\rho_o c_o^2} \left(|\mathcal{A}_d^+(\omega)|^2 + |\mathcal{A}_d^-(\omega)|^2 \right) \right] \tag{3.6}$$

The spectrum of acoustic energy $\mathcal{E}(\omega)$ contains information about the eigenfrequencies of the system, in the form of resonance peaks (Fig. 3.4). A fit is performed on these peaks to retrieve the complex eigenfrequencies [140, 18], based on the idea that the complex wave amplitudes $\mathcal{A}^+$ and $\mathcal{A}^-$ in the system are solutions of a damped oscillator equation of the form:

$$\ddot{\eta}(t) - 2\,\omega_{0i}\,\dot{\eta}(t) + \omega_{0r}^2\,\eta(t) = F \tag{3.7}$$

where $F = \hat{F}\mathrm{e}^{-i\omega t}$ is the harmonic forcing term and $\eta(t)$ is to be replaced by $\mathcal{A}^+ e^{-i\omega t}$ or $\mathcal{A}^- e^{-i\omega t}$. The forcing angular frequency ω is to be distinguished from the unknown complex angular eigenfrequency $\omega_0 = 2\pi f_0 = \omega_{0r} + i\,\omega_{0i}$, whose imaginary part ω_{0i} is the growth rate. Equation (3.7) is valid only for negative values of ω_{0i}, corresponding to purely damped acoustics, as is the case here. Transposing Eq. (3.7) in the Fourier domain gives an expression for $\mathcal{A}^+$ and $\mathcal{A}^-$ as a function of ω_{0r} and ω_{0i}, which is combined with Eq. (3.6) to yield an expression for $\mathcal{E}(\omega)$:

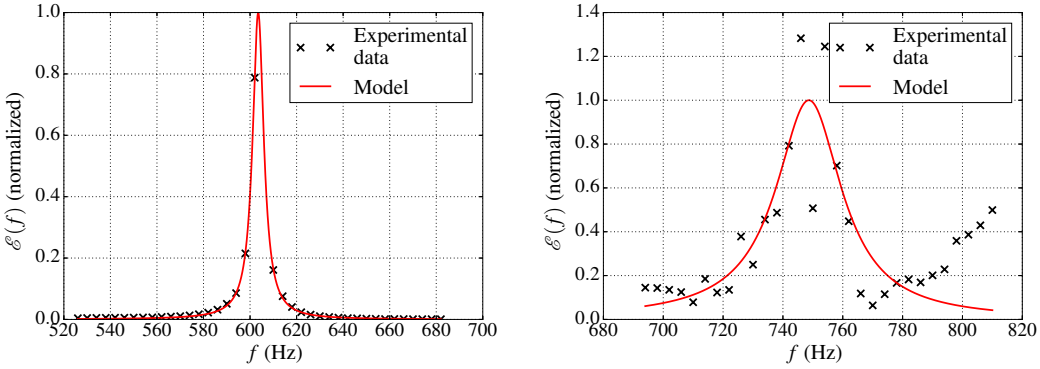
$$\mathscr{E}_{\text{theo}}(\omega) = \frac{1}{2\pi} \frac{G}{(\omega_{0r}^2 - \omega^2)^2 + 4\,\omega_{0i}^2\,\omega^2} \tag{3.8}$$

with $G = |\hat{F}|^2 \frac{V_{up}+V_{down}}{2\rho_o c_o^2}$. This is the form used to fit $\mathcal{E}(\omega)$. The three parameters G, ω_{0r}, ω_{0i} are tuned so that Eq. 3.8 produces the best possible match of the measured spectrum $\mathcal{E}(\omega)$. This method is equivalent to but more precise than measuring the width at half-height of the peaks [141, 18]. The adequation of the fit is assessed by computing the uncertainty on $f_0 = (\omega_{0r} + i\omega_{0i})/(2\pi)$ with a 95% confidence interval. This uncertainty is low when the data is well-fitted (Fig. 3.4a) and increases as soon as the quality of the fit deteriorates, when the signal is noisy for example (Fig. 3.4b).

Once the eigenfrequencies are estimated, the associated eigenmodes and acoustic fields can easily be reconstructed using Eq. 3.1 and Eq. 3.2.

Experimental 2-port matrices

The 2-port matrix is reconstructed following [142], with the scattering matrix formalism (see Tab. 2.1). This requires at least two linearly independent configurations. More robust results are obtained by using four independent configurations. In this study, this is achieved by combining the three ducts T1, T2, T3 and switching the outlet impedance from open to closed (Fig. 3.5). For each configuration, the wave amplitudes are measured upstream and downstream of the acoustic element of interest with the multi-microphone technique exposed previously. As explained in Section 2.2.1, an over-determined system



(A) (603.5 ± 0.1) - i(2.9 ± 0.1) Hz (B) (748.9 ± 3.5) - i(13.4 ± 5.0) Hz

FIGURE 3.4: $\mathcal{E}(\omega)$ spectra for the diaphragm at $U = 0.17$ m/s, normalized by the fitted value at ω_0. Two modes are displayed with the best fit for f_0 indicated in the title, and the uncertainty estimated with a 95% confidence interval.

(2.3) is defined from the four independent configurations of Fig. 3.5 with the matrix coefficients $\mathbf{S} = \begin{pmatrix} t_u & r_d \\ r_u & t_d \end{pmatrix}$ as unknowns, and inverted with a least-square approach.

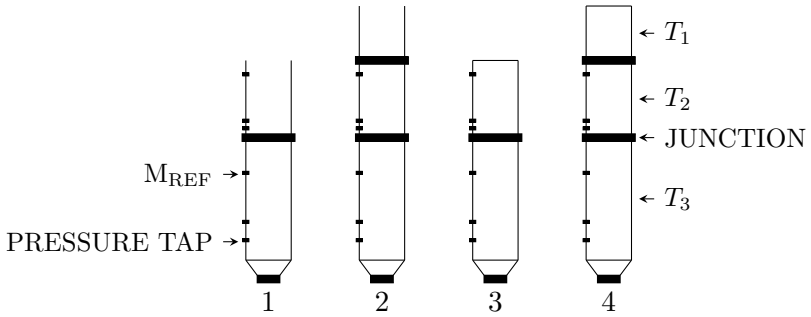


FIGURE 3.5: Description of the four configurations used in this study. For example, the second configuration is composed of the 3 ducts while the acoustic element is located in the junction between ducts 2 and 3 ; the outlet is open.

Eq. (2.4) provides the scattering matrix coefficients, as well as an estimation of the least-square error. The second index j runs from 1 to $N = 4$ and denotes the i-th independent state. This scattering matrix is easily converted into the mobility matrix required for the Matrix Boundary Condition.

3.3.2 LES matrices and modes

The 2-port matrices and acoustic eigenmodes can also be determined through LES computations performed with the AVBP solver, co-developed by CERFACS and IFP-EN [143]. This solver is widely used and has been validated in numerous situations [144, 145, 121, 24, 146, 147, 15], to cite a few. The results will serve to check the experiments in comparison C1 and to perform comparisons C2-LES (Fig. 3.3). This section presents the methodology used to obtain the numerical matrices and eigenmodes.

In order to obtain acoustic matrices and eigenmodes, acoustic forcing must be introduced in a computation of the domain of interest in which the mean flow is well-established. These preliminary non acoustically forced computations were done at CERFACS by Anthony Misdariis. In what follows, only the acoustically forced computations are presented.

These computations are performed with the numerical scheme TTGC which is third order accurate in time and space and was specifically designed to properly represent unsteady compressible flows with or without combustion [148]. The σ-model [149, 150] is used to model the subgrid scale stress tensor accurately.

The diaphragm and swirler parts are modelled as adiabatic no-slip walls, while the duct walls are represented with adiabatic slip conditions. The acoustic losses due to shear stress or thermal diffusion in the main duct are therefore neglected. This is because this effect is small compared to hydro-acoustic damping in the low frequency range.

Characteristic Navier-Stokes inlet and outlet boundary conditions [151] are used for pulsed computations. For AMT computations, the inlet and outlet are switched to completely reflecting boundaries unless stated otherwise, so as to measure the damping rate associated with the diaphragm or swirler, and not the one due to losses at boundaries.

LES matrices

To compute the 2-port matrix from LES data, two independent harmonic forcing states are used [152, 142]. In state 1, the acoustic element is excited from the inlet, with a non-reflective condition prescribed at the outlet. In state 2, the acoustic element is excited from the outlet, with a non-reflective inlet. This is the only difference with the approach used in the experiments, where the independent states were obtained by changing the outlet impedance, while always forcing at the inlet.

The geometry and overview of the mesh are shown in Fig. 3.6 for the diaphragm and Fig. 3.7 for the swirler. The duct lengths used in the LES do not have to correspond to the experimental tubes. They were chosen long enough to let acoustic waves become one dimensional away from the dissipative elements, and short enough to minimize computational times. The swirler vanes are discretized with 18 points along the smallest dimension, and the diaphragm is meshed with 40 points in the diameter. Both meshes contain a few million nodes (2.5 million points for the swirler and 1 million points for the diaphragm).

The pressure is measured at probes equi-distributed along the pipe circumference for several axial locations. For the diaphragm, 7 upstream stations and 11 downstream stations are used. For the swirler, only 4 upstream stations and 5 downstream stations are used because the hydrodynamic fluctuations created by the swirler extend further than in the diaphragm case. The wave amplitudes and the scattering matrix are then reconstructed with the same method as for the experimental data.

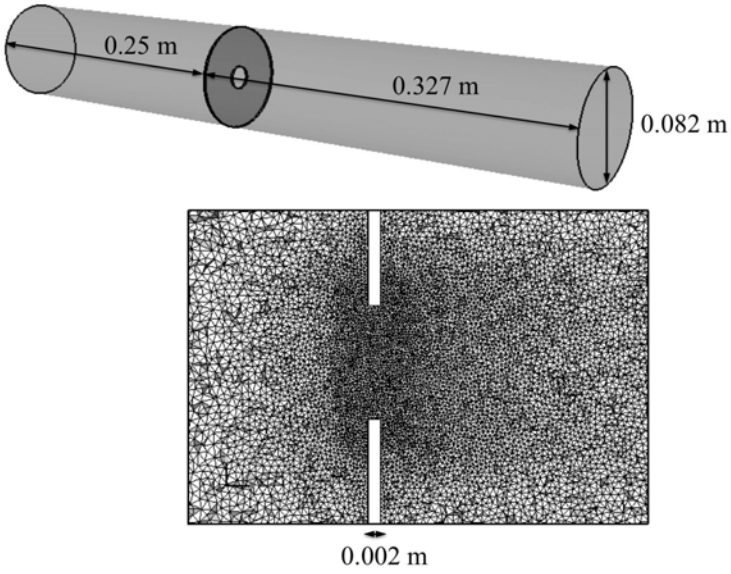


FIGURE 3.6: Geometry for the pulsed computations of the diaphragm, and zoom of the mesh near the diaphragm aperture.

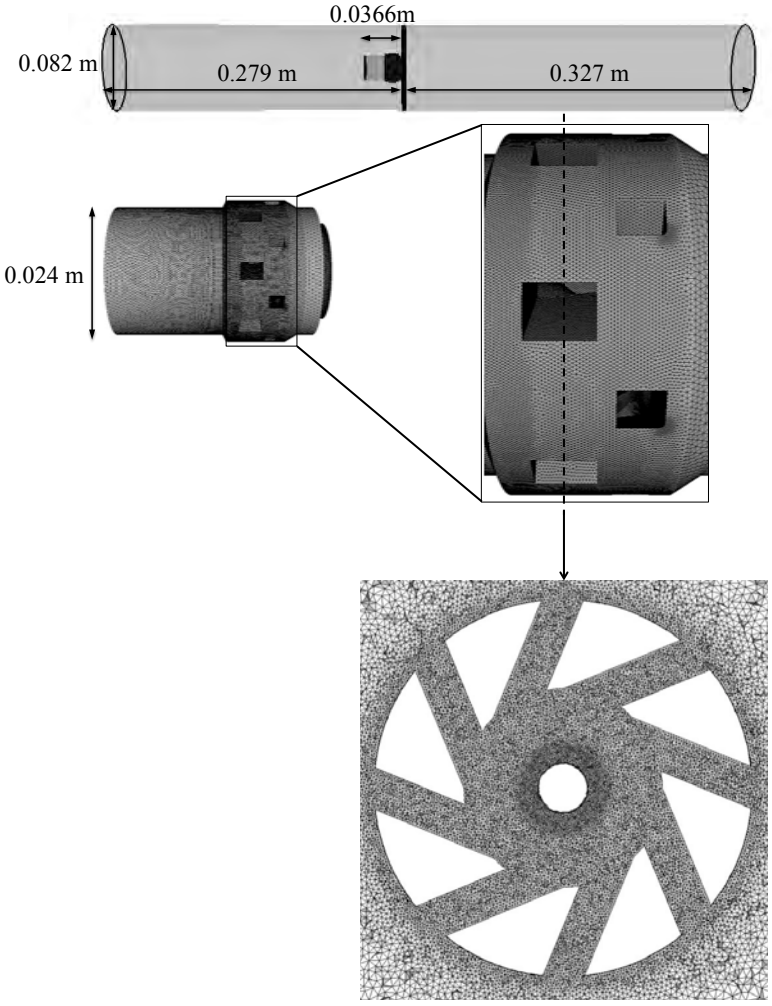


FIGURE 3.7: Geometry for the pulsed computations of the swirler, and zoom of the mesh near the swirler.

LES eigenmodes and damping rates

The experimental data provides references for the real eigenfrequencies and the associated mode structure. This was obtained by forcing the experiment at hundreds of frequencies and constructing the $\mathcal{E}(f)$ curve of Fig. 3.4, which is not practical in LES. Therefore a different method is used to obtain the dissipation rates from LES: the Acoustic Mode Triggering (AMT) approach [153].

The idea of AMT is to superimpose at a given instant an acoustic mode (computed from a Helmholtz solver, say), to the mean flow fields computed by a non-disturbed LES [153]. The resulting disturbed solution is used to initialize a new LES computation, where the initial acoustic perturbations are damped by the presence of the diaphragm or swirler. No forcing is applied after the simulation starts. The acoustic system is simply initially displaced from equilibrium. As for a damped oscillator, this results in decaying acoustic oscillations, whose decay rate and frequency are captured by the LES (Fig. 3.9).

The geometries used in the AMT computations are basically the same as those used for the pulsed computations (Fig. 3.6 and 3.7), but the duct lengths are modified to match the experimental duct lengths, plus the end corrections. The mesh refinement is the same as for the pulsed computations. A velocity-imposed, fully reflective boundary condition is enforced at the inlet. For the outlet, a pressure-imposed characteristic condition with relaxation towards a target value was tuned to obtain a reflection coefficient with radiation losses [77] $R_{rad}(\omega) = -\frac{\frac{1}{4}(ka)^2-1}{\frac{1}{4}(ka)^2+1}$ (where a is the pipe radius). The formulation of the outlet boundary condition is an extension of the one described in the work of Selle et al. [144]. With their notation, the incoming wave amplitude $\mathcal{L}_1$ is set to $\mathcal{L}_1 = K(P - P_\infty) - R_K\mathcal{L}_5$ and the associated reflection coefficient is (Fig. 3.8):

$$R_{LES}(\omega) = -R_K - \frac{1 - R_K}{1 - \frac{2i\omega}{K}} \tag{3.9}$$

with K the relaxation coefficient and R_K the value of the reflection coefficient when $K \to 0$. For the diaphragm, K is fixed to ensure no pressure drift, while R_K is adjusted to set $|R_{LES}|(\omega_0) = |R_{rad}(\omega_0)|$ at the desired angular frequency ω_0 (Tab. 3.1). For the swirler, K is fixed to the highest value allowed in the LES code to obtain a fully-reflective boundary as will be recalled later.

To measure the real frequency and damping rate, Dynamic Mode Decomposition (DMD) [133] is performed on the pressure and velocity signals measured at upstream and downstream probes. DMD is able to isolate the frequency of the excited mode and its decay

Frequency [Hz]	$\mathbf{R_{rad}}$	$\mathbf{\lvert R_{LES}\rvert}$	$\arg(\mathbf{R_{LES}})$ **[rad]**
77	- 0.9984	1.0063	3.1408
269	- 0.9803	0.9847	3.1413
387	- 0.9596	0.9597	3.1727
604	- 0.9039	0.9029	3.1551
757	- 0.8534	0.8500	3.1438
894	- 0.8012	0.8022	3.1414

TABLE 3.1: Reflection coefficient R_{LES} effectively measured in the diaphragm AMT computations, vs theoretical values with radiation losses R_{rad}

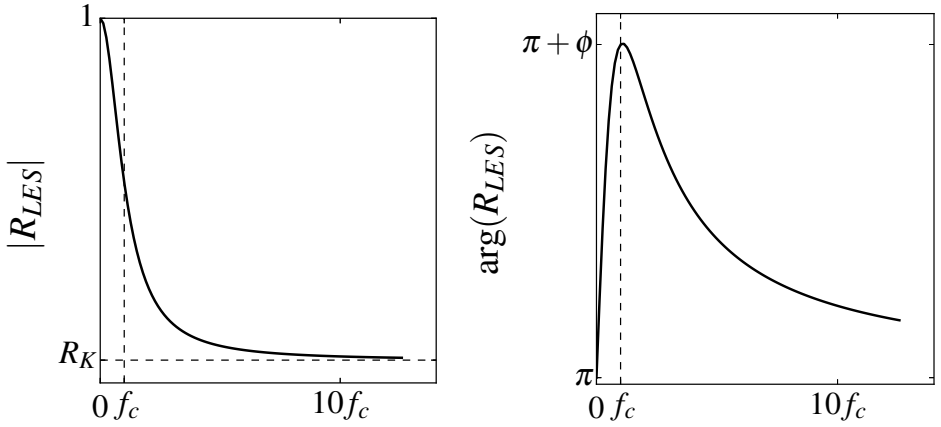


FIGURE 3.8: Modulus (left) and phase (right) of the AMT outlet reflection coefficient. A cut-off frequency can be defined as $f_c = \frac{K}{4\pi}$ at which the phase is equal to $\pi + \phi$ with $\phi = \tan^{-1}(\frac{1-R_K}{1+R_K})$.

rate (Fig. 3.9). It also provides the amplitude and phase of the acoustic fluctuations for each frequency. This information could be used directly to reconstruct the eigenmode, but an additional least-square fit was performed to determine the acoustic quantities as a sum of plane wave amplitudes, as done for the experiments in Section 3.3.1. The pressure signals at LES probes are used to construct system (3.3), that is inverted using Eq. (3.4). This procedure smoothes the acoustic fields and helps separating them from noise or hydrodynamic fluctuations (Fig. 3.10).

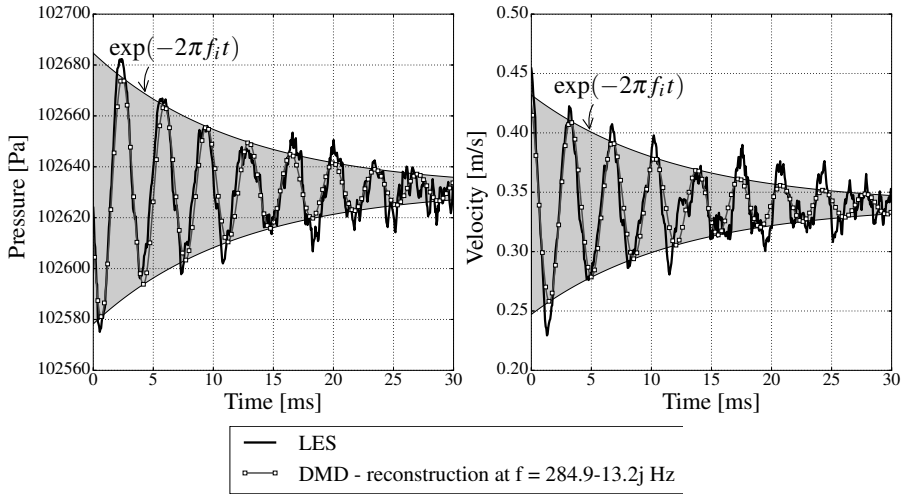


FIGURE 3.9: Typical LES temporal signals and DMD reconstruction for pressure (left) and axial velocity (right) (swirler mode at f = (284.9 - 13.2i) Hz and $U = 0.34$ m/s).

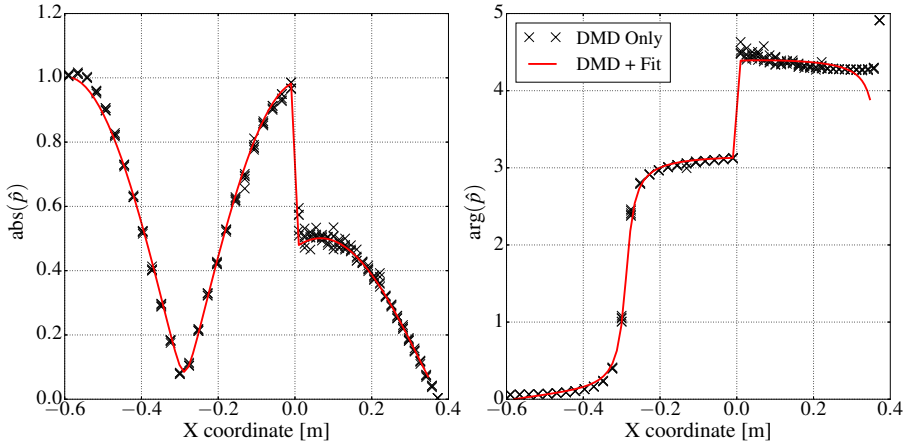


FIGURE 3.10: Acoustic mode with a swirler as acoustic element, f = (284.9 - 13.2i) Hz, at $U = 0.34$ m/s. Fit of a DMD complex pressure field as a sum of plane waves.

3.4 Setup for standard and MBC Helmoltz computations

Once the experimental (3.3.1) and LES (3.3.2) matrices are measured, they can be used in the Helmholtz solver with MBC. To use MBC, the setup geometry has to be modified. As explained in section 2.3, the acoustic element is not meshed anymore. Instead, the upstream and downstream tubes are cut so as to remove completely the acoustic element. The matrices constructed in Section 3.3.1 and 3.3.2 are used to represent adequately the transition between up- and downstream cuts (Fig. 3.11b).

At the test rig ends, the boundary conditions are similar for both swirler and diaphragm cases (Fig. 3.11b). The inlet and outlet patches are defined respectively as a "u'=0" boundary condition with an end correction of $\delta_{in} = 1$cm and a "p'=0" boundary condition with an end correction of $\delta_{out} = 2.5cm$ (see Section 3.1). With $k = \omega/c$ being the wave number, the inlet and outlet reduced impedances $\hat{p}/(\rho_o c_o \hat{u})$ are then:

$$Z_{in} = -\frac{i}{\tan(k\delta_{in})} \tag{3.10}$$

$$Z_{out} = i\tan(k\delta_{out}) - \frac{1}{4}\alpha(ka)^2 \tag{3.11}$$

When comparing the Helmholtz eigenmodes with experiments or LES runs with a partially reflective outlet (C2-EXP and C2-LES in Fig. 3.3), α is set to 1 and the term $-\frac{1}{4}ka^2$ accounts for radiation losses [77]. For the diaphragm study, α is therefore fixed to 1. In the swirler case, Helmholtz solutions are compared only to LES data with a fully reflective outlet, so that no radiation loss is added in the Helmholtz computation ($\alpha = 0$).

The mean thermodynamic properties are the same as the experimental ones, given in Section 3.1.

Additionally, Helmholtz computations on the complete geometry (i.e. with same duct lengths as the experimental setup and with a discretized diaphragm/swirler, see Fig. 3.11a for the diaphragm case) are performed for two reasons:

- To get acoustic fluctuations for LES eigenmode runs with the AMT approach,

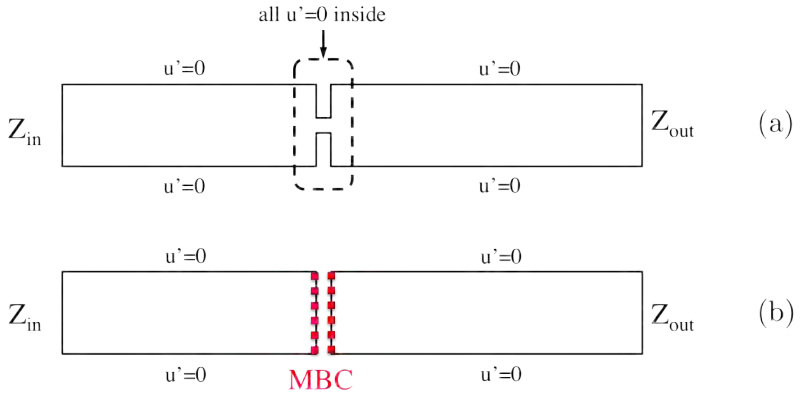


FIGURE 3.11: Boundary conditions for (a) the AVSP complete runs, where the acoustic element is meshed and wall boundary conditions are applied and (b) MBC runs, where the acoustic element is replaced by its 2-port representation.

- To compare the result of a conventional Helmholtz solution (i.e. assuming the Helmholtz equation holds within the diaphragm and the swirler) with one obtained thanks to the MBC methodology in comparisons C2-LES and C2-EXP (Fig. 3.3).

The meshes for the complete geometries and MBC geometries are optimized for the Helmholtz solver and are consequently coarser and more uniform than the LES ones. All but one meshes contain around 100 000 nodes and 500 000 cells, with a typical cell size of 3.6 mm. The exception is the complete swirler mesh which contains 300 000 nodes and 1 500 000 cells necessary to discretize the fine swirler vanes. The typical cell size for the latter mesh varies from 1 mm in the vanes to 8.2 mm in the pipes.

3.5 Application to a diaphragm

The methodology is first validated on the diaphragm configuration of IMFT (Fig. 3.2a). It was checked that the chosen boundary conditions provide values of eigenfrequencies close to the experiment when computing the complete geometry with the Helmholtz solver, see Tab. 3.2. Taking into account the radiation losses at the outlet only introduces a small damping rate. For the first mode however, a 10Hz discrepancy is observed. This is most probably due to acoustic coupling between the test rig and the loudspeaker casing at low frequencies. It was checked but not shown here that the first eigenfrequency is better predicted (around 90 Hz) when including the loudspeaker casing in the Helmholtz geometry. For higher order modes, the coupling between the rig and the loudspeaker cavity is negligible. In order to simplify the LES and Helmholtz computations, we decided to remove the loudspeaker casing from all geometries, keeping in mind that this makes comparison with the first experimental mode unappropriate.

For the diaphragm case, the quality of the results and the subsequent conclusions are the same for $U = 0.17$ m/s and $U = 0.34$ m/s. Therefore, all results shown here are valid for $U = 0.34$ m/s if nothing is mentioned. The scattering matrix coefficients acquired experimentally for the diaphragm of Fig. 3.2a, as well as the values obtained numerically are plotted on Fig. 3.12. The agreement between experimental, numerical and theoretical

Experiment	Standard Helmholtz ($\alpha = 0$)	Standard Helmholtz with end losses ($\alpha = 1$)
87.5	78.1 - 0.0i	78.1 - 0.0i
267.2	268.1 - 0.0i	268.1 - 0.8i
372.3	375.4 - 0.0i	375.4 - 1.0i
605.2	604.9 - 0.0i	604.9 - 0.6i
751.4	760.1 - 0.0i	759.8 - 9.7i
898.7	897.0 - 0.0i	896.7 - 0.9i

TABLE 3.2: Eigenfrequencies (in Hz) for the $U = 0$ m/s, in the experiments and the AVSP computation of the complete geometry with no matrix dissipation. The inlet and outlet impedances are given in Eq. (3.10) and Eq. (3.11) and include the end corrections plus radiation losses if $\alpha = 1$.

(Howe's model[1] [111]) results is good: the numerical coefficients match almost exactly the experimental ones, confirming that LES is suitable to compute acoustic matrices.

The $\mathbf{S}$ matrix already contains information relevant to dissipation. For example, an acoustic flux balance criterion [154] based on the eigenvalues $\lambda_{\min}, \lambda_{\max}$ of the real-valued matrix $\mathbb{I} - \mathbf{S}^\dagger\mathbf{S}$, with $\mathbf{S}^\dagger$ the hermitian form (complex conjugate transpose) of $\mathbf{S}$, states that:

- If $\lambda_{\min} > 0$ and $\lambda_{\max} > 0$, $\mathbf{S}$ dissipates acoustic energy,
- If $\lambda_{\min} < 0$ and $\lambda_{\max} < 0$, $\mathbf{S}$ produces acoustic energy,
- If $\lambda_{\min} < 0$ and $\lambda_{\max} > 0$, $\mathbf{S}$ can produce or dissipate acoustic energy. Nothing can be said *a priori*. The sign of the acoustic flux balance can change depending on the inlet acoustic variables, which are not known before connecting the matrix to the Helmholtz solver.

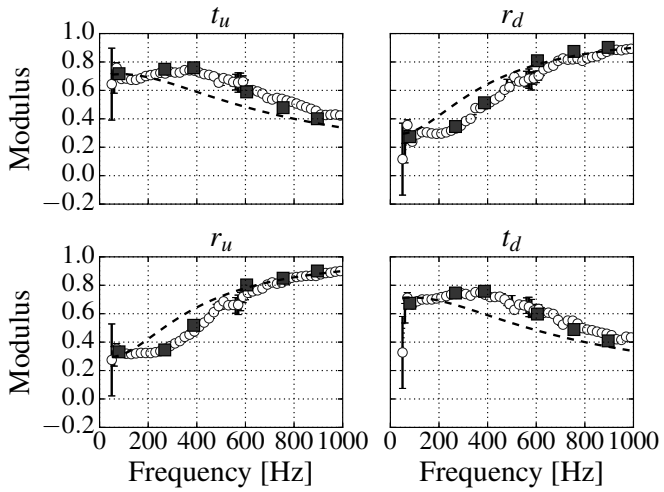
Fig. 3.13 confirms the dissipative behaviour of experimental and numerical matrices, although numerical matrices seem to dissipate slightly less than experimental matrices. For reference, the criterion is also computed for Howe's model[2] on Fig. 3.13.

This dissipative behaviour is fairly well captured in the eigenfrequencies computed with Helmholtz-MBC, compared to the ones measured in the experiment and in the LES (Fig. 3.14). The exception is the first experimental mode as expected and explained earlier. The agreement is much better when comparing MBC with LES, since the LES and Helmholtz solver geometries were the same in this case. Compared to the standard Helmholtz approach, the introduction of MBC improves the damping rate prediction for all modes computed. It also provides the correct evolution of the eigenfrequencies with a flow rate increase, as shown for the first four modes in Figs. 3.15 - 3.16.

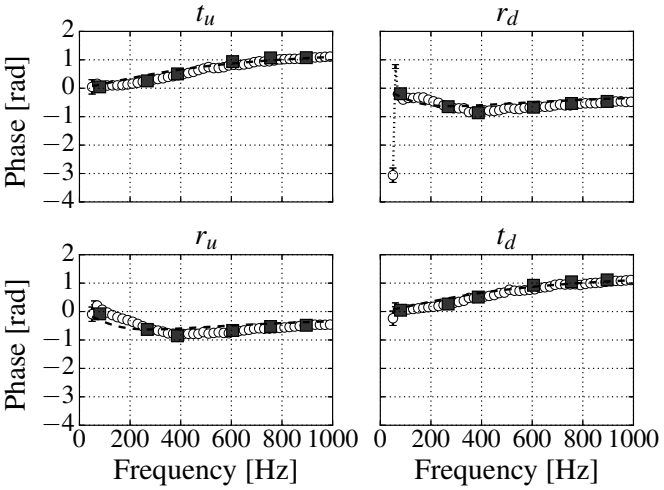
To further evaluate the impact of the dissipative diaphragm on the surrounding acoustics, the structure of the second eigenmode is now compared between experiments, LES and Helmholtz solver computations. This is done by plotting the modulus and phase of $\hat{p}$, normalized at $x = -0.58$m. Both experiments (Fig. 3.17) and LES (Fig. 3.18) show that

[1] The matrix associated to Howe's model is defined as $\mathbf{S}(\omega) = \frac{1}{1-\xi(\omega)} \begin{pmatrix} 1 & -\xi(\omega) \\ -\xi(\omega) & 1 \end{pmatrix}$ with $\xi(\omega) = \frac{i\omega d^2}{2c_0 K_R}$ for a plate of size d and Rayleigh conductivity K_R.

[2] The eigenvalues $\lambda_{\min}$, $\lambda_{\max}$ can be computed analytically for Howe's model as $\lambda_{\min}(\omega) = 0$ and $\lambda_{\max}(\omega) = -\frac{4\Re[\xi(\omega)]}{|1-\xi(\omega)|^2}$. The quantity $\Re[\xi(\omega)] = -\frac{\omega d^2 \Delta(\omega)}{4c_0 a(\Gamma(\omega)^2 + \Delta(\omega)^2)}$ depends on the real-valued functions $\Gamma(\omega)$ and $\Delta(\omega)$ defined in [111]. Since $\Delta(\omega)$ is positive for all ω, $\lambda_{\max}(\omega)$ is always positive. According to Howe's model, the perforated plate always dissipates acoustic energy.



(A) Moduli of the 2-port matrix for the diaphragm at $U = 0.34$ m/s



(B) Phases of the 2-port matrix for the diaphragm at $U = 0.34$ m/s

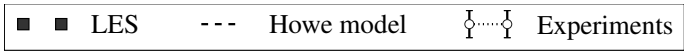


FIGURE 3.12: Diaphragm case - Comparison C1 in Fig. 3.3. Scattering matrix coefficients for $U = 0.34$ m/s. Experimental coefficients (from IMFT) are plotted as white circles with error bars and LES data is denoted by black squares. Howe's model [111] coefficients are also shown for reference (dashed lines).

the presence of a mean flow through the diaphragm modifies the pressure jump accross the orifice, which is a direct indication of acoustic losses. This effect is captured by the Helmholtz solver with MBC but not by a standard Helmholtz computation (Figs. 3.17 - 3.18). These good results support our initial assumption that at first order, the impact of mean flow is important only at locations where damping through vortex shedding is present, and can be neglected elsewhere, so that acoustics are well-represented by the zero mean flow Helmholtz equation (1.24).

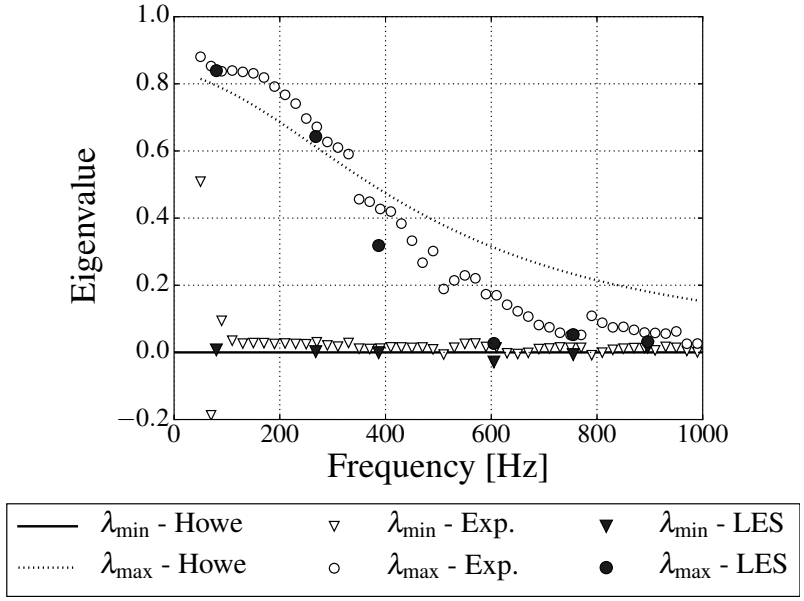
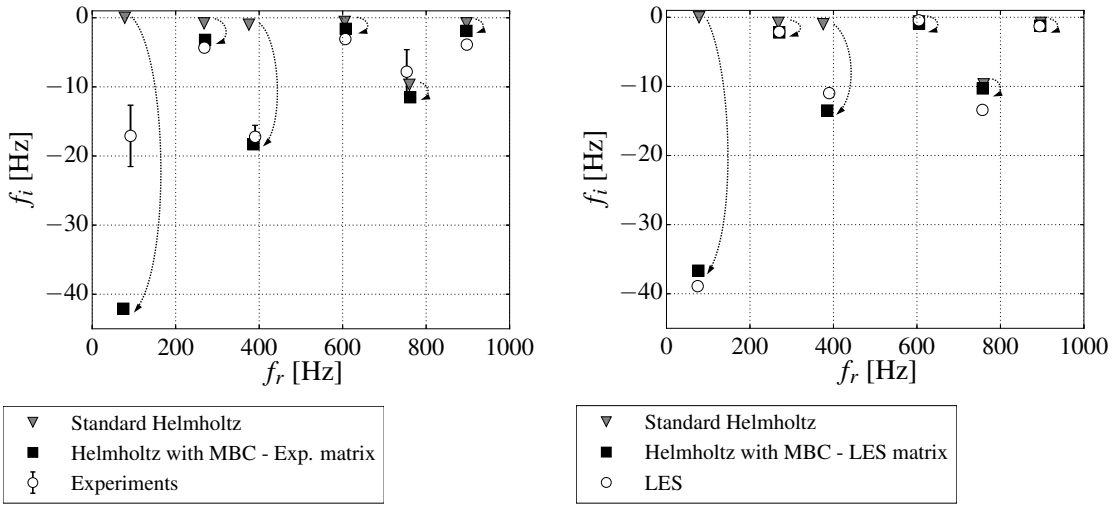


FIGURE 3.13: Diaphragm case - Comparison C1 in Fig. 3.3. Acoustic flux balance criterion based on the eigenvalues of $\mathbb{I}-\mathbf{S}^\dagger\mathbf{S}$ where $\mathbf{S}$ is the scattering matrix. When both eigenvalues are positive, $\mathbf{S}$ dissipates acoustic energy.



(A) Helmholtz solver with MBC vs experiments (C2-EXP in Fig. 3.3)

(B) Helmholtz solver with MBC vs LES (C2-LES in Fig. 3.3)

FIGURE 3.14: Diaphragm case. Comparison of standard and MBC AVSP eigenfrequencies with the experimental (C2-EXP, left) and LES (C2-LES, right) results, at $U = 0.34$ m/s. The experimental frequencies are plotted with error bars, obtained in Section 3.3.1

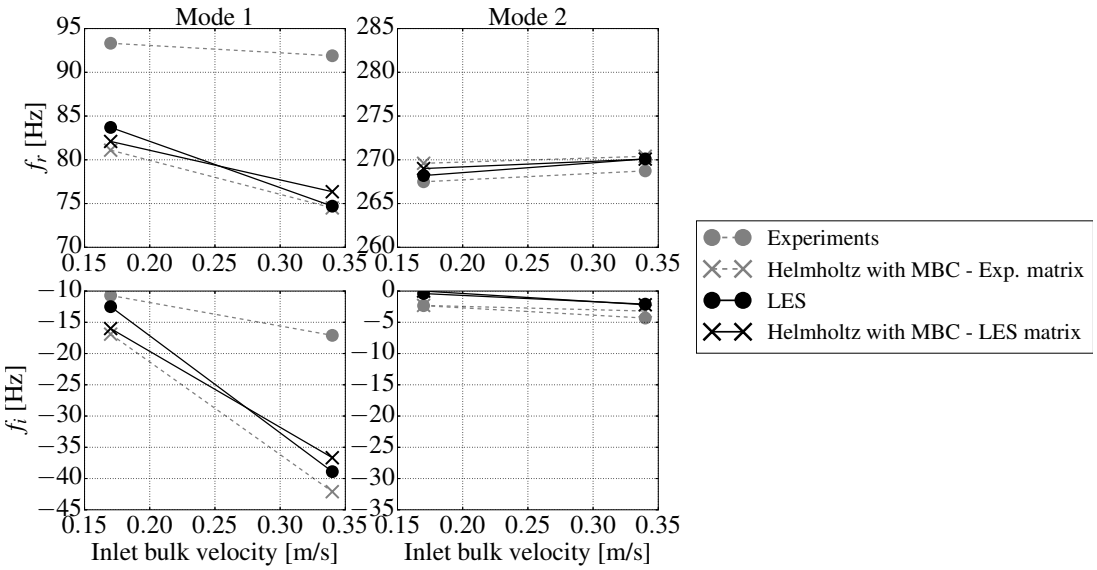


FIGURE 3.15: Diaphragm case. Comparison C2-EXP, C2-LES and C3. Evolution of the eigenfrequencies of mode 1 and mode 2 with the bulk velocity U. Each column corresponds to a mode. Real parts of the eigenfrequency are featured on the top row, imaginary parts are on the bottom row.

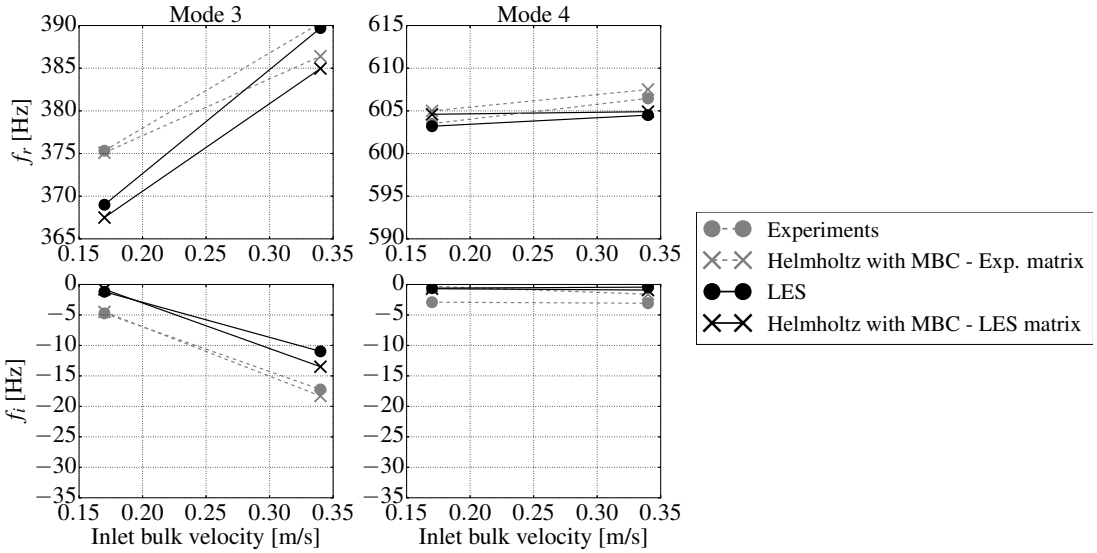


FIGURE 3.16: Diaphragm case. Comparison C2-EXP, C2-LES and C3. Evolution of the eigenfrequencies of mode 3 and mode 4 with the bulk velocity U. Each column corresponds to a mode. Real parts of the eigenfrequency are featured on the top row, imaginary parts are on the bottom row.

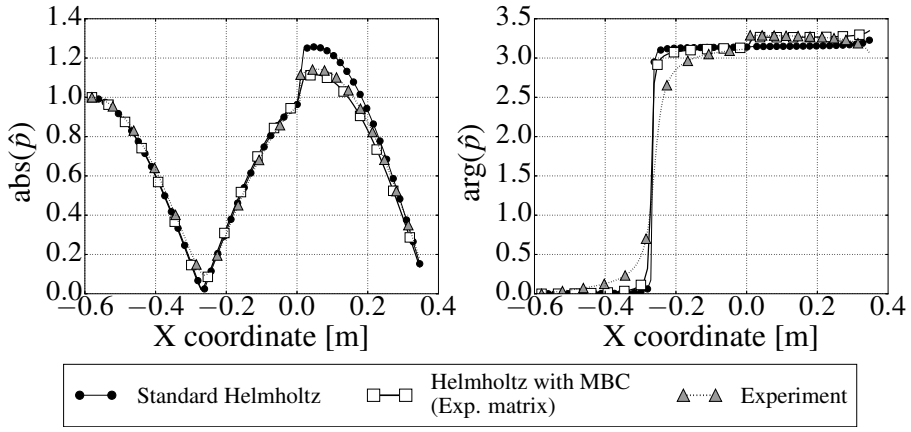


FIGURE 3.17: Diaphragm case. Comparison of the second eigenmode experimental structures at $U = 0.34$ m/s with the mode structures obtained from a standard Helmholtz computation and with the MBC approach (C2-EXP in Fig. 3.3).

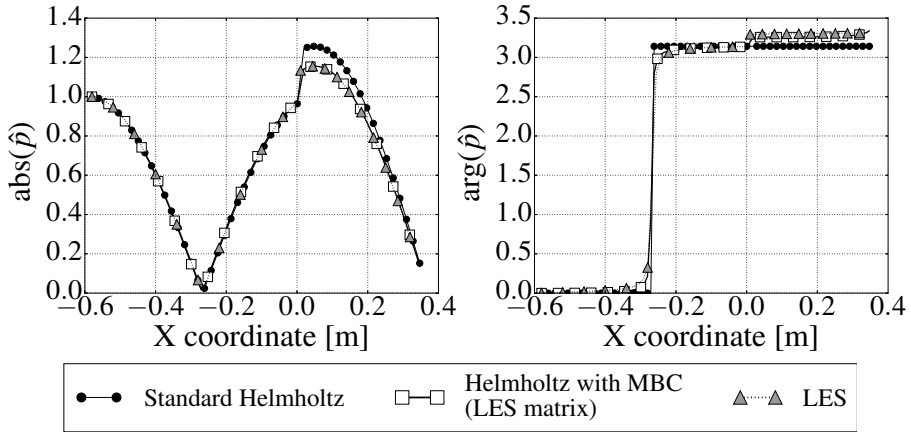


FIGURE 3.18: Diaphragm case. Comparison of the second eigenmode LES structures at $U = 0.34$m/s with the mode structures obtained from a standard Helmholtz computation and with the MBC approach (C2-LES in Fig. 3.3).

3.6 Application to a helicopter swirler

In the diaphragm configuration, the flow was laminar and fairly simple: the only complexity was the shear layer created at the downstream lips of the diaphragm. Moreover, the analytical model of Howe [111] was available for comparison. Now, the methodology is applied to the more challenging swirler element of IMFT (Fig. 3.2b) for which there is no theoretical formula. Downstream of the swirler, the flow features complex phenomena such as recirculation zones or Precessing Vortex Cores (PVC). Since the comparison with the LES (C2-LES in Fig. 3.3) gave the best results for the diaphragm, it is the only comparison performed for the swirler. The LES computations were performed for the highest bulk velocity $U = 0.34$ m/s in order to maximize the acoustic-hydrodynamic coupling. Compared to the diaphragm case, the outlet is fully reflective both in the LES and in the Helmholtz solver. Two modes are studied here: mode A and mode B with frequencies around 285 Hz and 590 Hz respectively at $U = 0.34$ m/s (as assessed by LES, Tab. 3.4). The swirler matrix coefficients were computed at 280 Hz, 290 Hz, 370 Hz and 590 Hz and are listed in Tab. 3.3, and linear interpolation is used to obtain the effective coefficients at the Helmholtz solver frequency. With the exception of 370 Hz, which is used later to assess the error made if the matrix is not measured at the correct frequency, the other frequencies were chosen close to the frequencies of mode A and mode B.

In Tab. 3.4, the results of the Helmholtz solver are compared to the LES for mode A and mode B. In terms of damping rates, the MBC methodology captures the correct order of magnitude, contrary to the standard Helmholtz solver which leads to $\omega_i = 0$, as expected. The relative error on the frequencies, computed as $|\frac{f_{\text{Helmholtz}} - f_{\text{LES}}}{f_{\text{LES}}}|$ remains around 1% for both modes. The eigenmode structures are also well retrieved by the MBC approach, as illustrated in Figs. 3.19-3.20.

In a general case with turbulent complex flow, as is the case with the swirler, it can be difficult to properly separate acoustic fluctuations from hydrodynamic ones. This results in uncertainties in the acoustic matrix coefficients. Moreover, the frequencies of the modes of interest are not always available beforehand. In this case, the matrix can be measured for a chosen set of frequencies, and linearly interpolation applied to retrieve the coefficients at the desired frequency, as was done here. This introduces an additional uncertainty. To assess the effect of these uncertainties on the result of the MBC-Helmholtz methodology, 50 additional Helmholtz computations are performed for mode A by varying the coefficients of the scattering matrix as follows. Each coefficient can have 5 different values: the nominal value, the nominal value plus Δ_S, the nominal value minus Δ_S, the nominal value plus $j\Delta_S$, and the nominal value minus $j\Delta_S$. The total number of matrix combinations amounts to 695, among which 50 combinations are sampled randomly. Δ_S is a real number chosen arbitrarily to 0.03, and accounts for the uncertainty on the matrix due

	280 Hz	**290 Hz**	**370 Hz**	**590 Hz**
$\mathbf{t_u}$	0.189 + 0.002j	0.268 - 0.054j	0.465 + 0.043j	0.043 + 0.117j
$\mathbf{r_d}$	0.833 + 0.099j	0.775 + 0.076j	0.568 + 0.203j	0.946 + 0.012j
$\mathbf{r_u}$	0.806 + 0.079j	0.712 + 0.094j	0.538 + 0.033j	0.955 + 0.001j
$\mathbf{t_d}$	0.170 - 0.014j	0.217 + 0.005j	0.392 - 0.079j	0.034 + 0.196j
$\boldsymbol{\lambda_{min}}$	-0.006	0.016	0.003	-0.038
$\boldsymbol{\lambda_{max}}$	0.582	0.741	0.965	0.176

TABLE 3.3: Swirler case. Scattering matrix coefficients from LES for $U = 0.34$ m/s and eigenvalues of $\mathbb{I} - \mathbf{S}^\dagger\mathbf{S}$

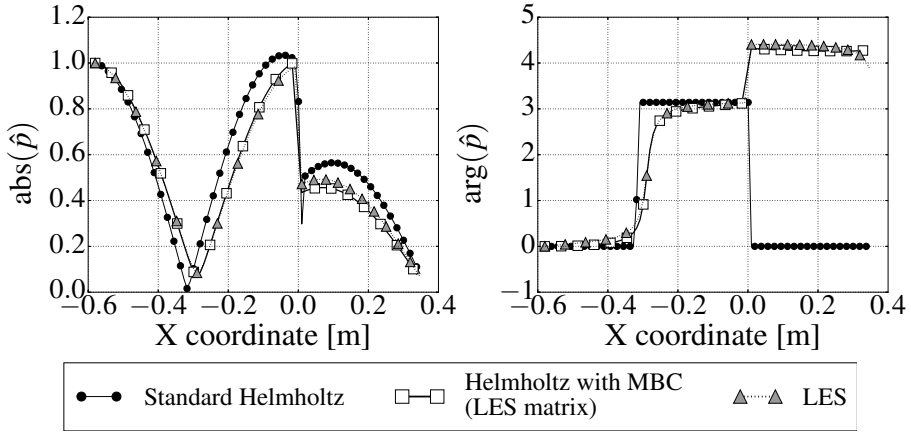


FIGURE 3.19: Swirler case. Structure of mode A at $U = 0.34$ m/s: Standard Helmholtz (black circles), Helmholtz solver with MBC (white squares) and LES results (grey triangles).

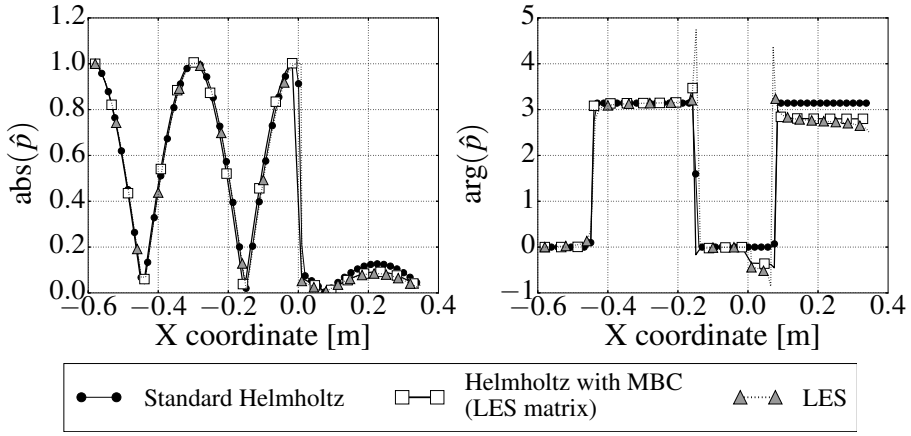


FIGURE 3.20: Swirler case. Structure of mode B at $U = 0.34$ m/s: Standard Helmholtz (black circles), Helmholtz solver with MBC (white squares) and LES results (grey triangles).

to the measurement method, but also on the frequency at which measurements are taken. Variations of the order of Δ_S on the scattering matrix were observed when interpolating the matrix between 280 Hz and 290 Hz instead of 280 Hz and 370 Hz (Tab. 3.3).

Figure 3.21 shows that the complex eigenfrequency computed with MBC-Helmholtz is indeed sensitive to the value of the matrix coefficients. In particular, the variations of the imaginary part of the frequency can reach up to 3.5 Hz, corresponding to approximately 25% of the nominal value. The eigenmode structure is also greatly impacted (Fig. 3.22). In Fig. 3.22, the normalisation is different from that used in Fig. 3.19, since fixing $\hat{p} = 1$ at x= -0.58 m would force all modes to collapse in the upstream section. To better see the changes in both upstream and downstream mode structures, $\hat{p}$ is fixed to 1 at $x = 0$, the matrix location. The great dispersion of mode shapes suggests that the matrices should be carefully measured to obtain satisfying results with the MBC methodology. In our experience, the biggest source of error is the frequency of measurement, which should ideally be chosen as close as possible to the frequency of the mode found by AVSP.

	Mode A	Mode B
Standard Helmholtz	317.4 - 0.0i	591.2 - 0.0i
LES	284.9 - 13.2i	589.1 - 3.2i
Helmholtz with LES matrix	287.5 - 13.7i	597.7 - 1.3i
Relative error	0.9%	1.5%

TABLE 3.4: Complex frequencies (in Hz) of mode A and mode B with the swirler at $U = 0.34$ m/s, from LES, Helmholtz solver with LES matrix and standard Helmholtz solver. The relative difference between Helmholtz and LES results is also displayed.

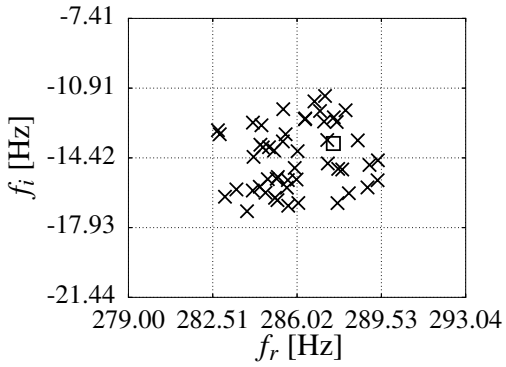


FIGURE 3.21: Swirler case, mode A. Frequencies obtained from 50 additional Helmholtz computations where the coefficients were "randomly" varied (see body text). The nominal result is recalled as a white square.

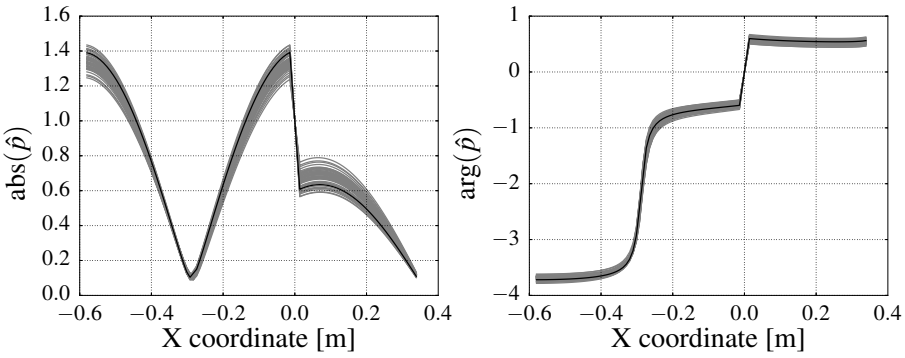


FIGURE 3.22: Swirler case. Structure of mode A when varying the scattering matrix coefficients (grey curves). The nominal result of Fig. 3.19 is recalled in black. The modified matrix coefficient is indicated for the outermost curves.

Chapter 4

Extending the Matrix Boundary Condition to industrial configurations

4.1 Introduction

In Chapter 3, the acoustic behaviour of elements characterized by a strong hydro-acoustic interaction was successfully captured in the Helmholtz computation of a simple quasi 1D rig, using a Matrix Boundary Condition (MBC) with matrix data measured from the experiments and the LES. The methodology presented in Chapter 3 is however not flexible enough to be applied to industrial configurations.

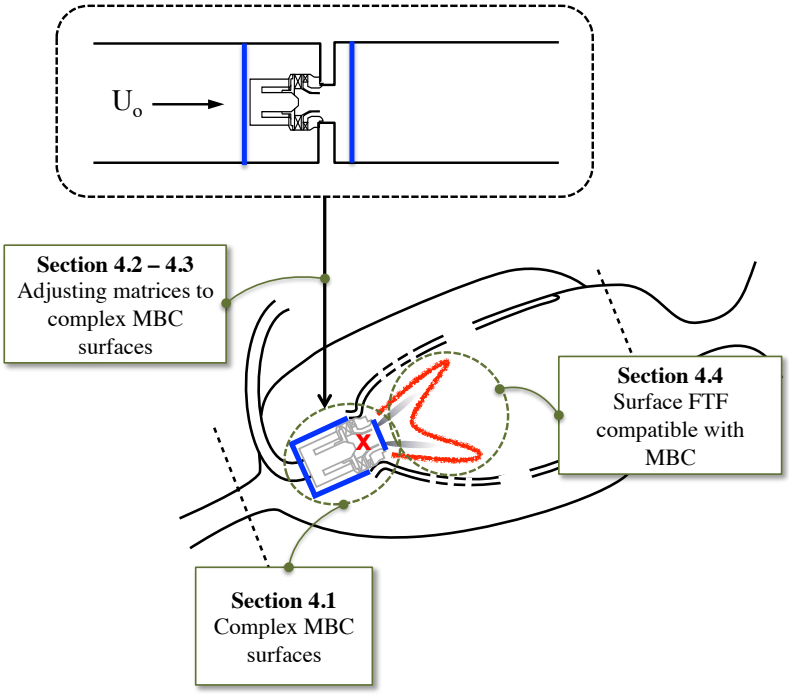


FIGURE 4.1: Extensions of the HMBC methodology required for an industrial combustor.

Indeed, compared to the simple case of Chapter 3, the use of HMBC for an industrial configuration raises a few issues (Fig. 4.1):

1. **Where should the Matrix Boundary Condition be applied ?** The simple geometry of Chapter 3 was essentially 1D. The MBC surfaces could be imposed at any cross-section far enough from the disturbing element, with the guarantee of plane acoustics. In a complex geometry such as the one of Fig. 1.18, it is very difficult and even impossible to define plane surfaces with plane normal acoustics. MBC surfaces are rather chosen so as to fit into the combustor geometry (Fig. 1.18). Since the plane wave assumption is not necessarily satisfied anymore, the validity of this type of surfaces is investigated in Section 4.2.

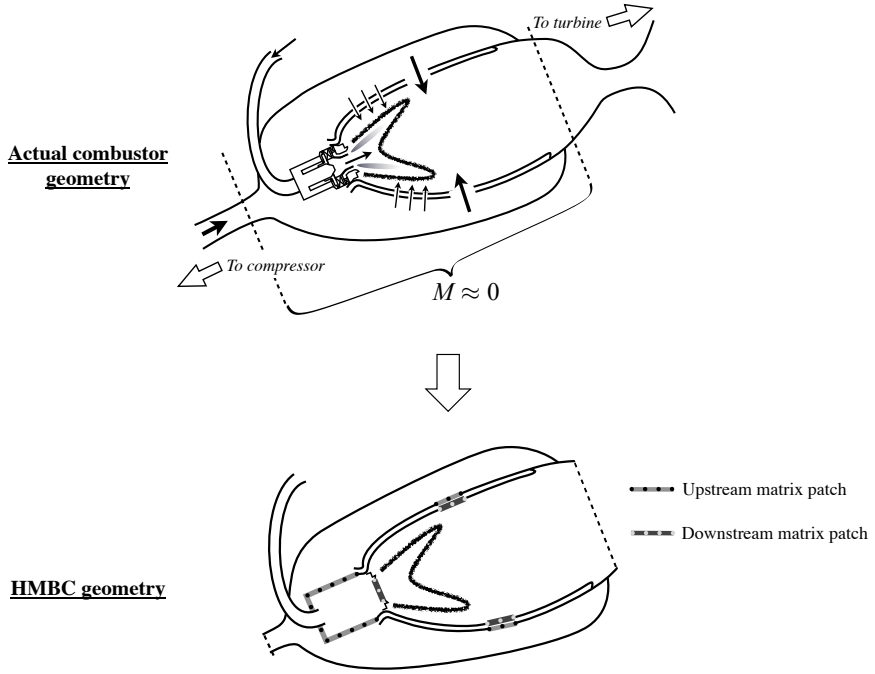


FIGURE 4.2: MBC surfaces chosen in this thesis for a complex combustor geometry

2. For the choice of Fig. 4.2, it is still desirable to obtain the matrices of damping elements from a clean, 1D plane wave configuration such as the one of Chapter 3. This reference matrix should however be adjusted to provide the correct result when applied to the set of surfaces of Fig. 4.2. **How can this adjustment be performed ? And does it still provide the correct results ?** These two questions are investigated in Section 4.3.

3. Ultimately, the HMBC methodology will be used to improve the prediction of combustion instabilities. Therefore, it should be compatible with a flame response model. In AVSP, the Flame Transfer Function is used to relate the unsteady heat release to the acoustic velocity at a reference point. Ideally, this reference point should be located in a zone of low turbulence, upstream of but not too far from the flame [72]. In industrial combustors, the flame is sometimes anchored very close to the injector, and the reference point is consequently chosen within it [17, 155, 147]. This is a problem if the injector is to be replaced by its equivalent matrix, since all acoustic information inside the element is lost ! For this reason, an alternative formation of the FTF was derived in this thesis, with the reference point replaced by a reference surface, on which MBC is imposed. An additional reason motivating the use of an FTF with a reference surface is that the acoustic velocity averaged over a surface

should be more robust to turbulent fluctuations (i.e. noise for acoustic analysis) than the velocity measured at a probe. The new surface FTF is explored in Section 4.5.

4.2 The validity of complex MBC surfaces

The first point to check is the validity of the HMBC approach when non-plane, non-coincident matrix surfaces with a non uniform pressure and velocity are used. This is a requirement for the matrix surfaces of the injector in the choice of Fig. 4.2. In this thesis, a distinction is made between:

- *Plane* surfaces. They refer to surfaces that are not only plane but also characterized by uniform acoustic quantities.
- *Complex* surfaces. These surfaces have a 3D geometry with potentially non-uniform acoustic quantities.

For complex, non coincident matrix surfaces, the pointwise Robin condition derived in system (2.14), Chapter 2 is not valid anymore. The pointwise pressure, sound speed and density are replaced by surface averaged values.

$$\begin{cases} \nabla\hat{p}_u \cdot \mathbf{n_u} = M_{11}\dfrac{i\omega}{< c_{o,u} >} < \hat{p}_u > + M_{12}\dfrac{i\omega}{< c_{o,d} >}\dfrac{< \rho_{o,u} >}{< \rho_{o,d} >} < \hat{p}_d > \\ \nabla\hat{p}_d \cdot \mathbf{n_d} = M_{22}\dfrac{i\omega}{< c_{o,d} >} < \hat{p}_d > + M_{21}\dfrac{i\omega}{< c_{o,u} >}\dfrac{< \rho_{o,d} >}{< \rho_{o,u} >} < \hat{p}_u > \end{cases} \tag{4.1}$$

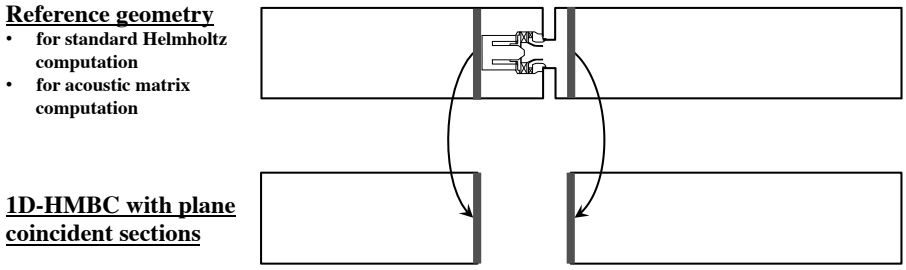
where $< \bullet >= \frac{1}{S}\int_S \bullet \, dS$ is the average over a surface S. The corresponding matrix could be measured likewise by inverting a least square system whose coefficients depend on the surface averaged pressure and velocity.[1] This new implementation is called 3D-HMBC because it is associated with complex 3D surfaces with non uniform acoustic quantities. By opposition, the previous implementation is now referred to as 1D-HMBC since it is truly applicable only in 1D geometries. It was checked that on 1D cases, 3D-HMBC and 1D-HMBC computations provide the same results as expected.

To test if the surface averaged implementation of HMBC provides adequate results, it is applied to the geometry of the swirler in a tube of Chapter 3 (Fig. 4.3, middle), with a purely acoustic matrix. The swirler matrix is measured every 10 Hz with two forced computations of the acoustic propagation code AVSP-f [156]. The technique is essentially the same as the one presented in Chapter 3. An acoustic forcing is imposed, first at the tube inlet, then at the outlet, while an anechoic boundary condition is set at the other end. The only difference is that acoustics are propagated in an inviscid zero mean flow fluid so that the corresponding matrix does not contain losses. It simply mimics the behaviour of the swirler in a standard Helmholtz computation.

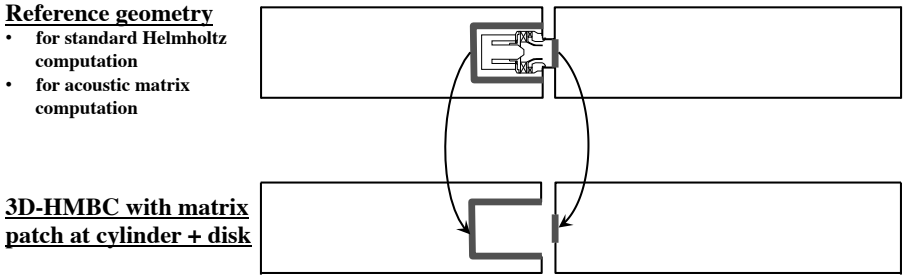
Two matrices are measured (Fig. 4.4) on the complete swirler mesh (Fig. 4.5, top):

- Matrix 1 is measured at plane, coincident surfaces (Fig. 4.3a).
- Matrix 2 is obtained with the pressure and velocity averaged over a cylinder upstream, and a disk downstream (Fig. 4.3b).

[1] An alternative, presented in the next section, consists in obtaining the matrix for a simple plane-wave matrix and adjust it to the desired set of MBC surfaces. This is explained in details in Section 4.3



(A) 1D-HMBC



(B) 3D-HMBC

FIGURE 4.3: Validation of complex MBC surfaces on the swirler in a tube configuration. Two HMBC computations are performed : one with plane coincident MBC surfaces (top) and one with complex MBC surfaces (bottom). Both are compared to a reference standard Helmholtz computation where the complete geometry is discretized.

RUN #	Matrix type	Geometry
1	None	Discretized swirler in a tube.
2	Matrix 1	Geometry truncated at plane coincident surfaces (Fig. 4.3, bottom).
3	Matrix 2	Geometry truncated at complex surfaces (Fig. 4.3, top).
4	None	Plain tube.

TABLE 4.1: Helmholtz computations for the validation of complex MBC surfaces.

Four Helmholtz computations are performed and compared (Tab. 4.1), with a velocity imposed inlet and a pressure imposed outlet. Two computations are done with MBC: one with Matrix 1 and the other with Matrix 2. Two others are performed with the standard solver on a completely discretized geometry. The corresponding meshes are provided in Fig. 4.5. Note that the mesh used for the 3D-HMBC computation should have the same resolution as the one on which the matrix is measured, at least in the vicinity of the complex MBC surfaces. This is not necessary for the 1D-HMBC run since acoustic quantities are uniform over the plane MBC surfaces.

The swirler matrix used in both HMBC runs is purely acoustic. Including it in an HMBC computation should be equivalent to running a standard Helmholtz computation with a discretized swirler. The two HMBC runs should therefore provide the same results as the standard Helmholtz computation on the complete geometry. This is indeed the case, both in terms of eigenfrequencies (Tab. 4.2) and eigenmode structures (Fig. 4.6), even if the mode structure with the two matrices is different close to the matrix surfaces (Fig. 4.7). The use of complex MBC surfaces is therefore justified.

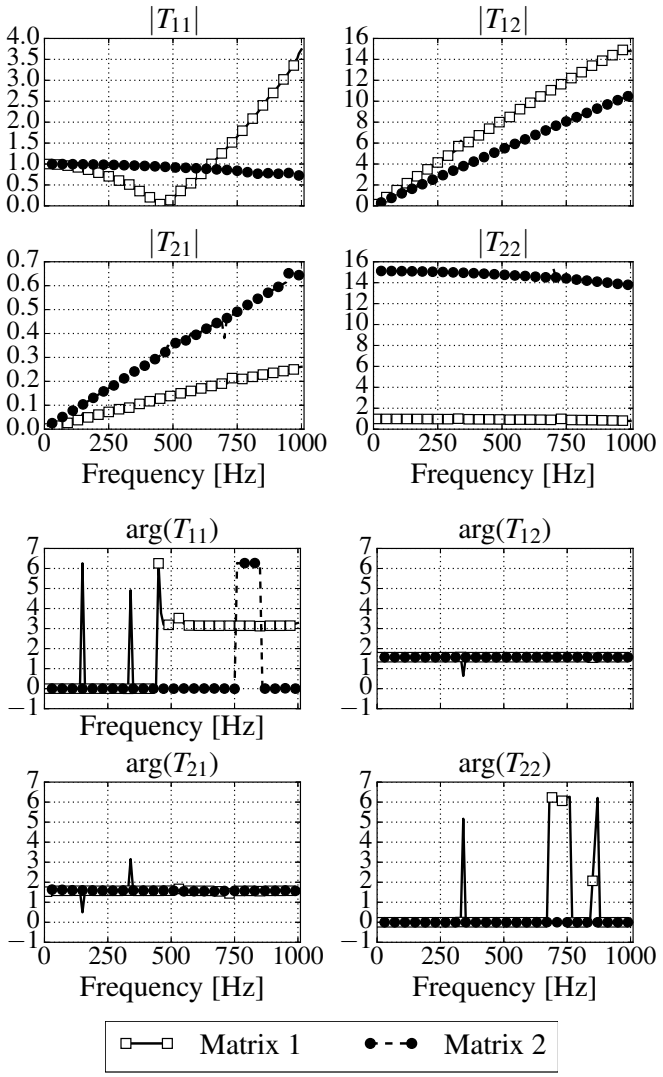


FIGURE 4.4: Matrix 1 and Matrix 2 coefficients.

RUN 1	**RUN2**	**RUN3**	**RUN4**
58.0	58.8	59.6	93.5
259.6	259.9	259.5	280.6
317.4	317.3	318.6	467.5
591.2	590.6	591.3	654.4

TABLE 4.2: Eigenfrequencies (in Hz) of the Helmholtz computations of Tab. 4.1

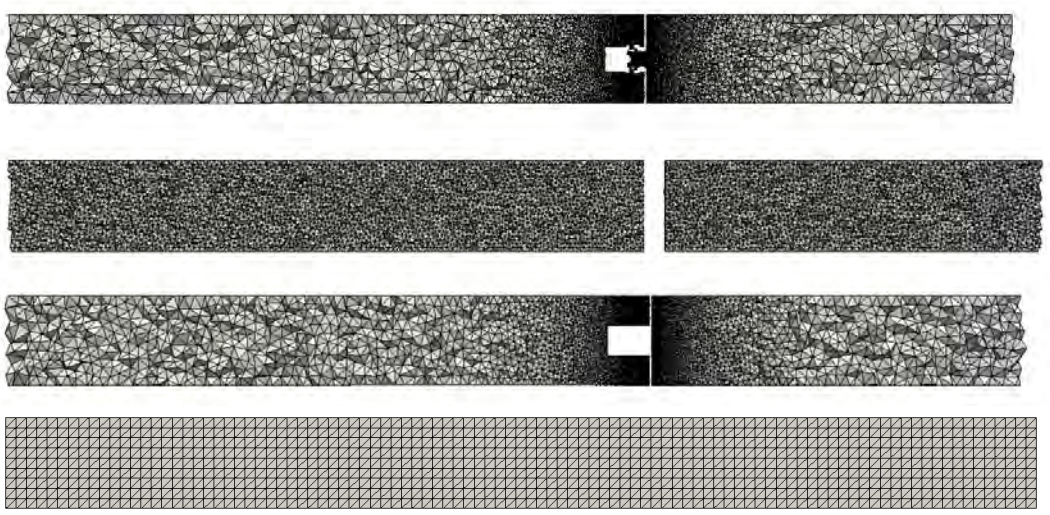
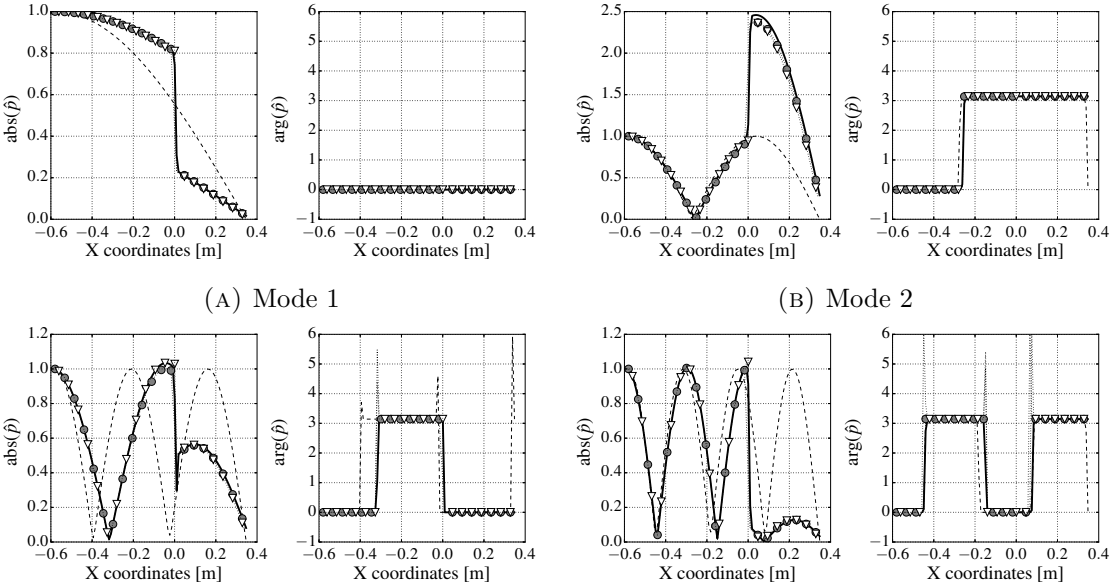


FIGURE 4.5: Overview of the meshes used in the Helmholtz computations of Tab. 4.1. From top to bottom : runs 1, 2, 3, and 4.



(A) Mode 1

(B) Mode 2

(C) Mode 3

(D) Mode 4

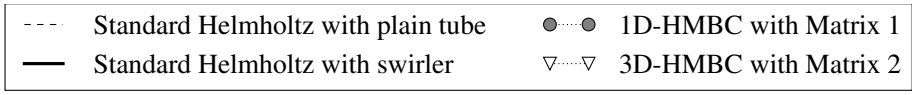


FIGURE 4.6: First four eigenmodes for the computations of Tab. 4.1. The modulus and argument of pressure is plotted as a function of the axial coordinate.

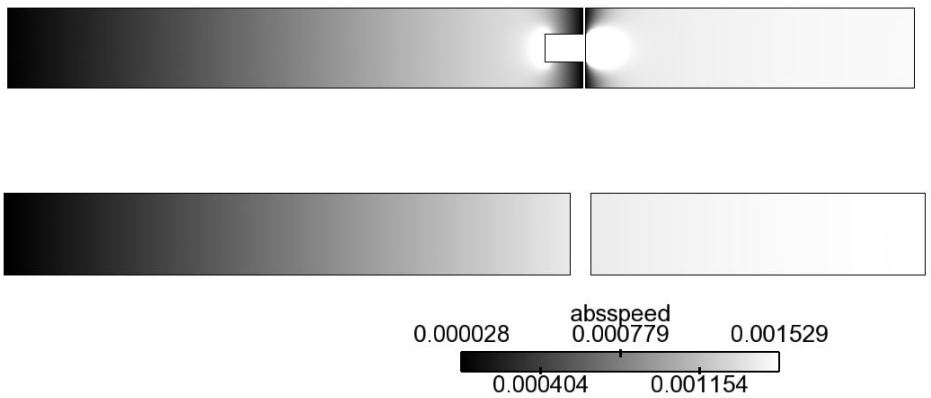


FIGURE 4.7: Modulus of axial acoustic velocity amplitude for the first mode of run 2 and run 3.

4.3 Adjusting plane-wave matrices to complex MBC surfaces

4.3.1 Principle

Measuring the matrix with dissipation effects is a critical step of the HMBC methodology because it is the most time consuming (especially if done by LES) and its accuracy determines the quality of the final result, as the sensitivity analysis of Section 3.6, Chapter 3 showed.

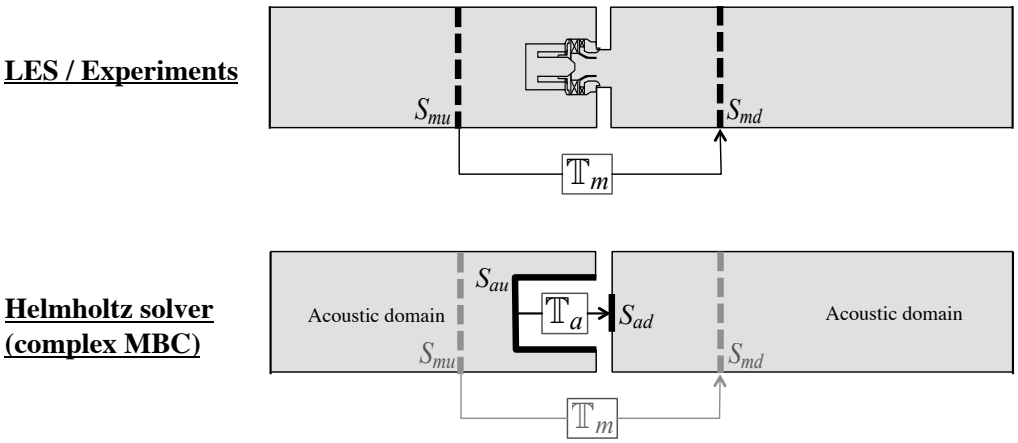


FIGURE 4.8: How can the matrix measured at plane transverse cuts in LES be used in a Helmholtz computation with complex MBC surfaces ?

If a matrix on complex MBC surfaces is required but only the data for a matrix on plane coincident surfaces is available, is there a way to use this data instead of computing a new matrix altogether (Fig. 4.8) ? Concerning the accuracy of the matrix data, it is also probably better to measure it on plane surfaces in a tube like geometry, rather than directly on the complex MBC surfaces as done in the previous section. In this section, a method is presented to adjust matrices, i.e. obtain the matrix at complex MBC surfaces from the data at plane, coincident surfaces.

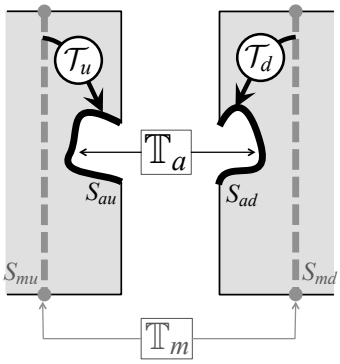


FIGURE 4.9: The matrix data measured at surfaces S_m cannot be applied directly to the surfaces S_a and provide the correct results. For this, the matrix needs to be adjusted from S_m to S_a.

The basic principle of this adjustment is to apply some compensation matrices $\mathcal{T}_u$ and $\mathcal{T}_d$ to displace the initial matrix $\mathbb{T}_m$ measured at sections S_{mu} and S_{md}, to the matrix required for the Helmholtz geometry $\mathbb{T}_a$, applied at sections S_{au} and S_{ad} (Fig. 4.9). In

what precedes, indices u and d stand for "upstream" and "downstream" respectively, while indices m and a stand for "measured" and "applied".

The matrices $\mathcal{T}_u$ and $\mathcal{T}_d$ are defined as follows, using the acoustic variables $\hat{p}$ and $\hat{u}$:

$$\begin{pmatrix} \hat{p} \\ \rho_o c_o \hat{u} \end{pmatrix}_{S_{au}} = \mathcal{T}_u \begin{pmatrix} \hat{p} \\ \rho_o c_o \hat{u} \end{pmatrix}_{S_{mu}} \tag{4.2}$$

$$\begin{pmatrix} \hat{p} \\ \rho_o c_o \hat{u} \end{pmatrix}_{S_{ad}} = \mathcal{T}_d \begin{pmatrix} \hat{p} \\ \rho_o c_o \hat{u} \end{pmatrix}_{S_{md}} \tag{4.3}$$

If $\mathcal{T}_u$ and $\mathcal{T}_d$ are known, the transfer matrix $\mathbb{T}_a$ can be derived from $\mathbb{T}_m$. If $\mathbb{T}_m$ is defined as

$$\begin{pmatrix} \hat{p} \\ \rho_o c_o \hat{u} \end{pmatrix}_{S_{md}} = \mathbb{T}_m \begin{pmatrix} \hat{p} \\ \rho_o c_o \hat{u} \end{pmatrix}_{S_{mu}} \tag{4.4}$$

Then it is straightforward to show that

$$\begin{pmatrix} \hat{p} \\ \rho_o c_o \hat{u} \end{pmatrix}_{S_{ad}} = \underbrace{\mathcal{T}_d \mathbb{T}_m \mathcal{T}_u^{-1}}_{\mathbb{T}_a} \begin{pmatrix} \hat{p} \\ \rho_o c_o \hat{u} \end{pmatrix}_{S_{au}} \tag{4.5}$$

Note that the compensations $\mathcal{T}_u$ and $\mathcal{T}_d$ are purely acoustic and should not introduce any parasite dissipation or amplification. Their only role is to displace the matrix on the adequate set of surfaces in the Helmholtz solver.

4.3.2 Measuring $\mathcal{T}_u$ and $\mathcal{T}_d$

The adjustment matrices $\mathcal{T}_u$ and $\mathcal{T}_d$ can be measured numerically with an acoustics propagation solver such as AVSP-f [156]. The principle is the same as the one presented in Section 2.2.1. Two acoustically forced computations are performed for each matrix, with a monochromatic excitation at the frequency of interest. The first computation is excited at the inlet, and an anechoic boundary condition is set at the outlet. The second computation is excited at the outlet, with an anechoic inlet. The advantage of using AVSP-f for the determination of $\mathcal{T}_u$ and $\mathcal{T}_d$ is that it uses the same discretization as in AVSP.

The acoustic quantities on S_{au} and S_{ad} must be measured with some care. For example, one might be tempted to use the acoustic pressure and acoustic velocity averaged over the nodes of S_{au} and S_{ad}. However, the acoustic velocity can be strongly underestimated with this method, in the case where the MBC patch shares a common edge with a hard wall. To illustrate this phenomenon, the three setups of Fig. 4.10 are examined. These setups are composed of two tubes, linked by a plane MBC surface upstream and a complex MBC surface downstream (a disk for the first two geometries, and a half-sphere for the last one). All geometries are meshed with two uniform mesh sizes $dx_1 = 0.0036$ m and $dx_2 = 0.0018$ m (this corresponds to approximately 5 and 10 cells per hole diameter respectively).

The identity matrix $\mathbb{I}$ is imposed between both MBC surfaces, but the same conclusions still hold for any other matrix. The idea is to test if $\mathbb{I}$ is well retrieved with the surface averages of pressure and velocity over the downstream MBC patch. On the upstream

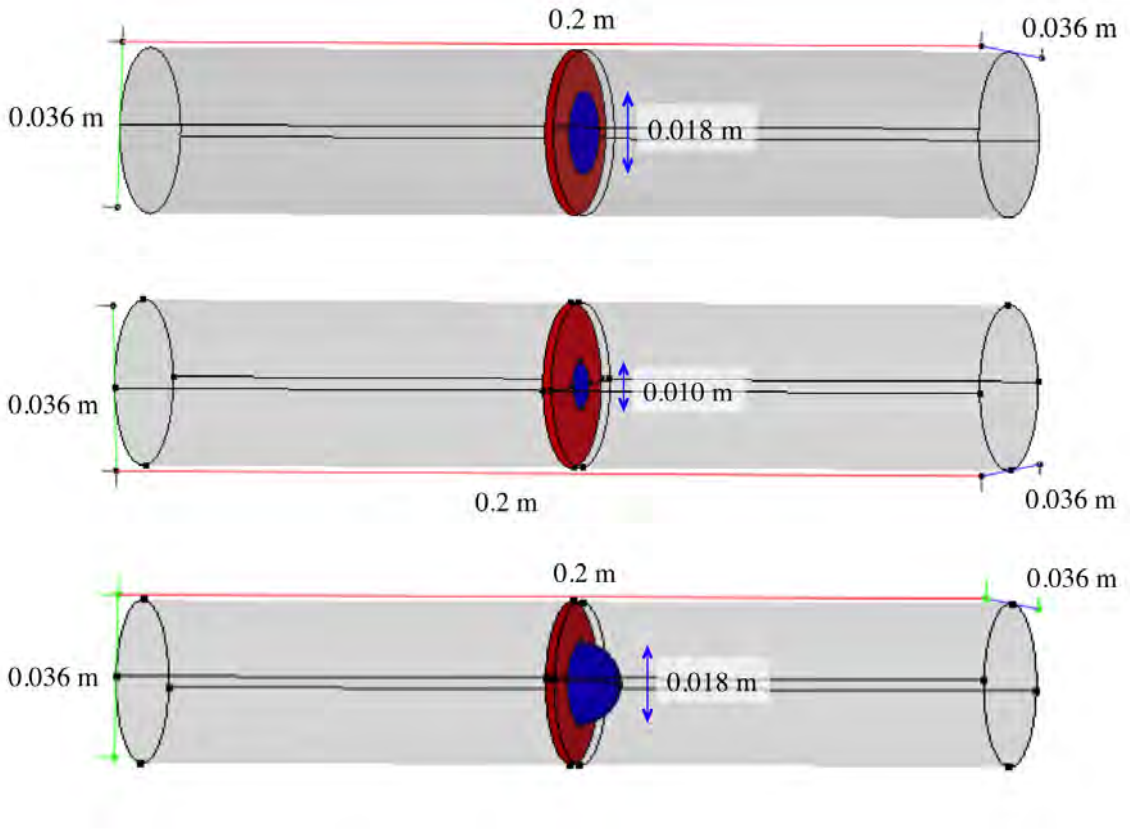


FIGURE 4.10: Geometries used for the error assessment of MBC surface averaged quantities. From top to bottom : geometry 1, 2 and 3. MBC surfaces are represented in red and blue.

patch, pressure and velocity are uniform and their surface average corresponds to the acoustic quantities effectively seen by the matrix condition. Therefore, any error in the identity matrix retrieval comes from the measure on the downstream MBC surface. The matrix effectively retrieved from the surface averages of pressure and velocity is refered to as $\mathbb{T}_{\text{surface}}$.

$$\begin{pmatrix} < \hat{p} >_d \\ < \rho_o c_o \hat{u} >_d \end{pmatrix} = \mathbb{T}_{\text{surface}} \begin{pmatrix} < \hat{p} >_u \\ < \rho_o c_o \hat{u} >_u \end{pmatrix} \tag{4.6}$$

where $< \bullet >_u = \frac{1}{S_u} \int_{S_u} \bullet \, dS$ and $< \bullet >_d = \frac{1}{S_d} \int_{S_d} \bullet \, dS$ denote the surface average on the upstream and downstream surface respectively. As Fig. 4.11 shows for geometry 1 with mesh size dx_1, there is indeed a strong error on the transfer matrix linking the surface-averaged pressure and velocity over the MBC patches. This error involves mainly the coefficient relating the acoustic velocities (T_{22}). Its value is much lower than the target of which is unity. This was observed on all geometries for both mesh sizes (Tab. 4.3).

The misprediction of T_{22} with surface averages is due to the discretization used in AVSP. As shown in Appendix C, the term $\nabla \cdot \left(\frac{1}{\rho_o(\mathbf{x})} \nabla \hat{p}(\mathbf{x}) \right)$ is computed at each node using the value of pressure at the closest neighbors. Therefore, points in the vicinity of an edge shared by two different boundary conditions will receive a contribution from the two boundary conditions. As a consequence, the theoretical velocity discontinuity at an edge

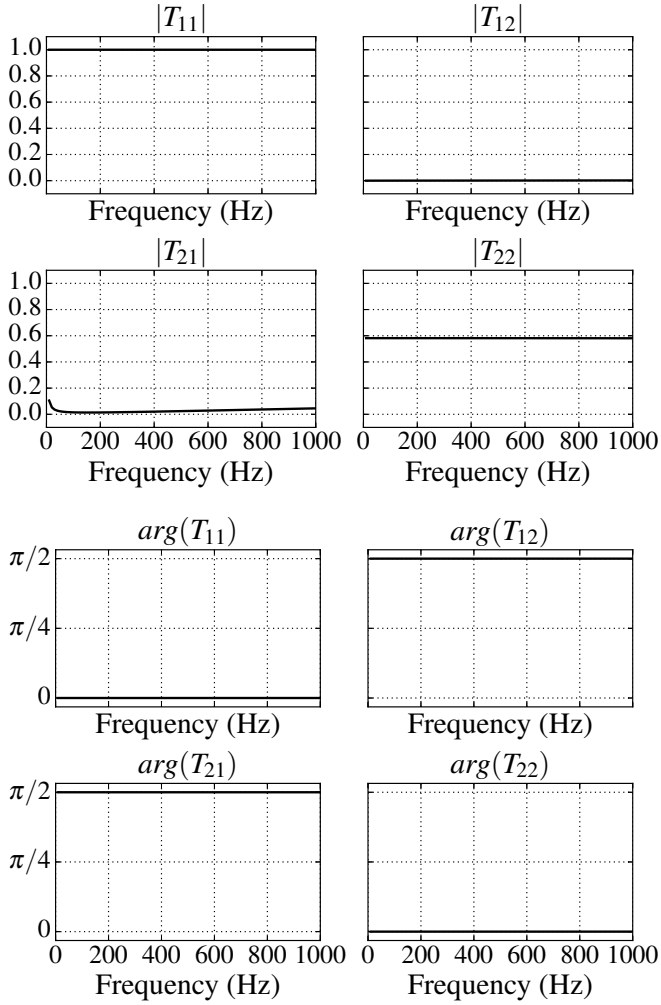


FIGURE 4.11: Matrix linking surface averaged value of $\hat{p}$ and $\rho_o c_o \hat{u}$ on MBC patches. Geometry 1 with mesh size dx_1. (Top: modulus, Bottom: phase).

shared by a hard wall and another boundary condition with non-zero acoustic velocity is smoothed out in AVSP and AVSP-f (Fig. 4.12). This is indeed what we observe in the AVSP-f solution of Fig. 4.13 and it explains why the value of T_{22} measured only with the MBC nodes is lower than the target of 1.

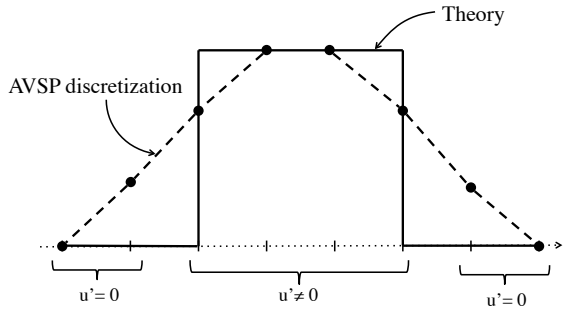


FIGURE 4.12: 1D velocity discontinuity : theory versus AVSP discretization.

If the smoothing is assumed to occur over one cell size (as Fig. 4.13 suggests), the velocity

Geometry	Mesh size	Theoretical T_{22}	Measured T_{22}	Prediction of measured T_{22}
1	dx_1	1.0	0.581	0.550
1	dx_2	1.0	0.748	0.710
2	dx_1	1.0	0.387	0.398
2	dx_2	1.0	0.582	0.579
3	dx_1	1.0	0.648	0.712
3	dx_2	1.0	0.809	0.833

TABLE 4.3: Error on T_{22} in $\mathbb{T}_{\text{surface}}$. The effectively measured value can be predicted with Eqs. E.1 and E.2

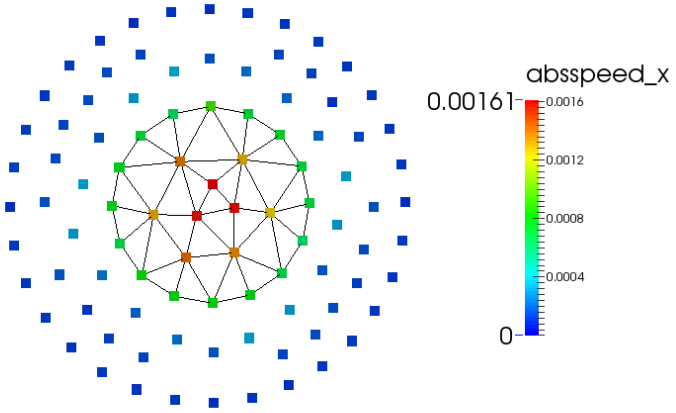


FIGURE 4.13: Absolute value of axial velocity at the downstream MBC surface (black lines) and surrounding wall. Geometry 1 with dx_1.

integrated over MBC nodes neglects a surface of the order of $\mathcal{C}dx$ with the notation of Fig. 4.14. The associated value of coefficient T_{22} is therefore reduced by a factor $\alpha = \dfrac{1}{1+\dfrac{\mathcal{C}dx}{\mathcal{S}}}$ compared to the imposed value. For the simple geometries of Fig. 4.10, α can be estimated analytically with the expressions of Appendix E. The agreement with numerical values is good (Tab. 4.3), providing support to the explanation proposed here.

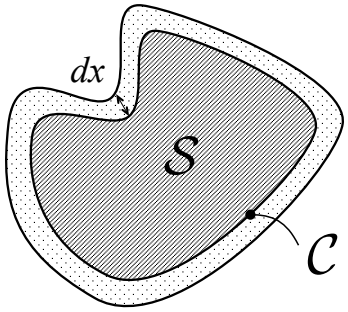


FIGURE 4.14: Real MBC surface $\mathcal{S}$ (in dark grey) versus effective MBC surface, approximately extended by $\mathcal{C}dx$ (in light grey).

It is now clear that $\mathcal{T}_u$ and $\mathcal{T}_d$ cannot be computed numerically with a direct surface average

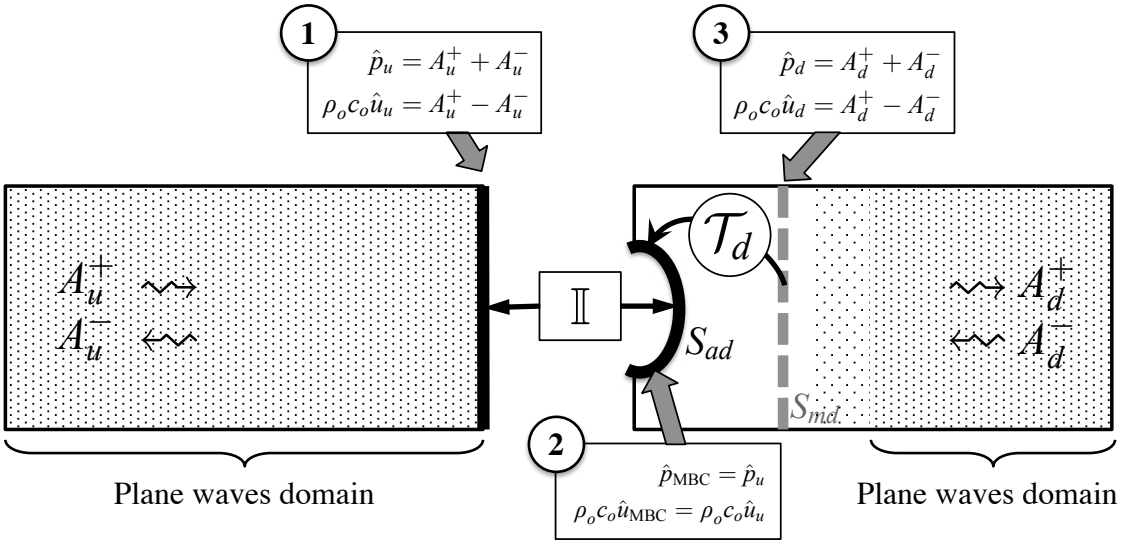


FIGURE 4.15: Measurement method for $\mathcal{T}_u$ and $\mathcal{T}_d$ without error on T_{22}.

on complex MBC patches, because of boundaries mixing. Instead, $\mathcal{T}_u$ and $\mathcal{T}_d$ should be measured on geometries similar to that of Fig. 4.15. These geometries are composed of two pipes linked by MBC surfaces. One of the surfaces is plane which results in plane acoustics in the corresponding pipe. The other is the complex MBC surface of interest. The principle, illustrated in Fig. 4.15, consists in the following steps:

1. Measure the acoustic quantities $\hat{p}_u$ and $\hat{u}_u$ on the upstream plane MBC patch, either by performing a plane-wave decomposition with several pressure and velocity probes in the upstream tube, or directly by using surface averages. The two are equivalent since this upstream tube is designed to contain purely plane acoustics.

2. Obtain the non-plane acoustic quantities $\hat{p}_{\text{MBC}}$ and $\hat{u}_{\text{MBC}}$ on the downstream complex MBC patch S_{ad}, by imposing for example an identity matrix between both MBC surfaces (identity is convenient but any matrix would do).

3. Obtain the plane acoustic quantities $\hat{p}_d$ and $\hat{u}_d$ downstream at the LES measurement plane S_{md} by measuring acoustic quantities far from the complex MBC surface.

4. Compute the matrix $\mathcal{T}_d$ relating $\hat{p}_{\text{MBC}}$ and $\hat{u}_{\text{MBC}}$ to $\hat{p}_d$ and $\hat{u}_d$.

With this technique, the matrix $\mathcal{T}_d$ can be measured without any error on the value of T_{22}, as opposed to the method where surface averages on MBC patches are used. As an example, the value of coefficient T_{22} for $\mathcal{T}_d$ is measured on the coarse mesh of geometry 1 with MBC surface averages and the present method (Fig. 4.16). The expected value of T_{22} is purely real and corresponds to the section ratio between S_{md} and S_{ad}, equal to 4.1 for geometry 1 with mesh size dx_1.

4.3.3 Application to the IMFT swirler

The adjustment procedure is now tested for the IMFT swirler of Chapter 3. Its matrix $\mathbb{T}_m$ was already measured with LES at plane locations for four frequencies (see Chapter 3, Tab. 3.3) and needs to be adapted to the 3D-HMBC setup of Fig. 4.3b. The corresponding mesh is displayed in Fig. 4.5 (third from the top). The adjustment matrices $\mathcal{T}_u$ and $\mathcal{T}_d$, provided in Fig. 4.17, are computed on the meshes of Fig. 4.18.

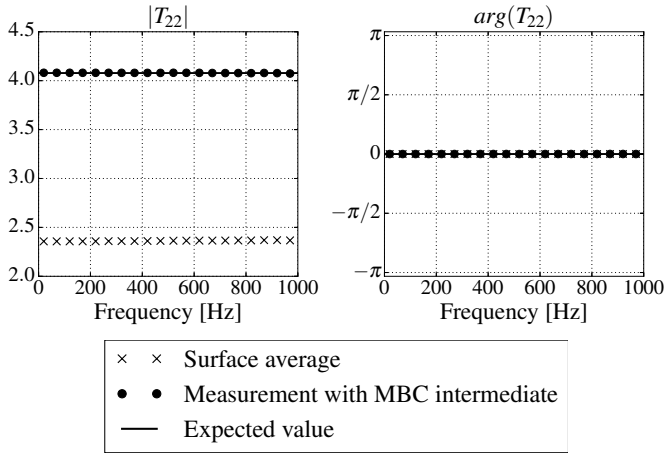


FIGURE 4.16: Coefficient T_{22} for $\mathcal{T}_d$ measured on geometry 1 with mesh size dx_1, using surface averages (crosses) or an intermediate MBC surface as presented in the main text (circles). The expected value is recalled in solid lines.

It was noticed that the results with the adjusted matrix $\mathbb{T}_a$ are better if the evolution of $\mathcal{T}_u$ and $\mathcal{T}_d$ with frequency is sufficiently sampled. If $\mathcal{T}_u$, $\mathcal{T}_d$ are simple propagation matrices for example, it is important to perform the ajdustment with a frequency resolution high enough to maintain the cosine and sine behavior of $\mathcal{T}_u$ and $\mathcal{T}_d$. For the IMFT swirler, $\mathcal{T}_u$ and $\mathcal{T}_d$ were measured every 10 Hz between 280 Hz and 600 Hz and the adjustment is performed at the same frequencies, with linearly interpolated values of $\mathbb{T}_m$. The original and adjusted matrices are plotted in Fig. 4.19. $\mathbb{T}_a$ is then introduced in a 3D-HMBC computation with complex matrix surfaces (Fig. 4.5, third image from the top) and compared to:

- a 1D-HMBC solution with plane, coincident matrix surfaces. The latter is used as a reference since it agrees well with the LES modes, as shown in Chapter 3, Section 3.6,
- a 3D-HMBC solution with $\mathbb{T}_m$ (without adjustment),
- a standard Helmholtz solution (complete geometry discretized).

Although some accuracy is lost in the adjustment process, the 3D-HMBC computation with $\mathbb{T}_a$ provides a good agreement with the 1D-HMBC results, in terms of eigenfrequencies (Tab. 4.4) and eigenmodes (Fig. 4.20), and a major improvement compared to the standard Helmholtz solution and to the 3D-HMBC computation without adjustment.

	Mode 3	**Mode 4**
Standard Helmholtz	317.4 - 0.0i Hz	591.2 - 0.0i Hz
1D-HMBC with $\mathbb{T}_m$	287.7 - 13.8i Hz	598.2 - 1.3i Hz
3D-HMBC with $\mathbb{T}_m$	267.8 - 12.1 Hz	583.8 - 1.9i Hz
3D-HMBC with $\mathbb{T}_a$	287.7 - 14.9i Hz	597.4 - 0.9i Hz

TABLE 4.4: Eigenfrequencies of the HMBC computations with $\mathbb{T}_m$ and the adjusted matrix $\mathbb{T}_a$. The solutions of a standard Helmholtz computation are also recalled

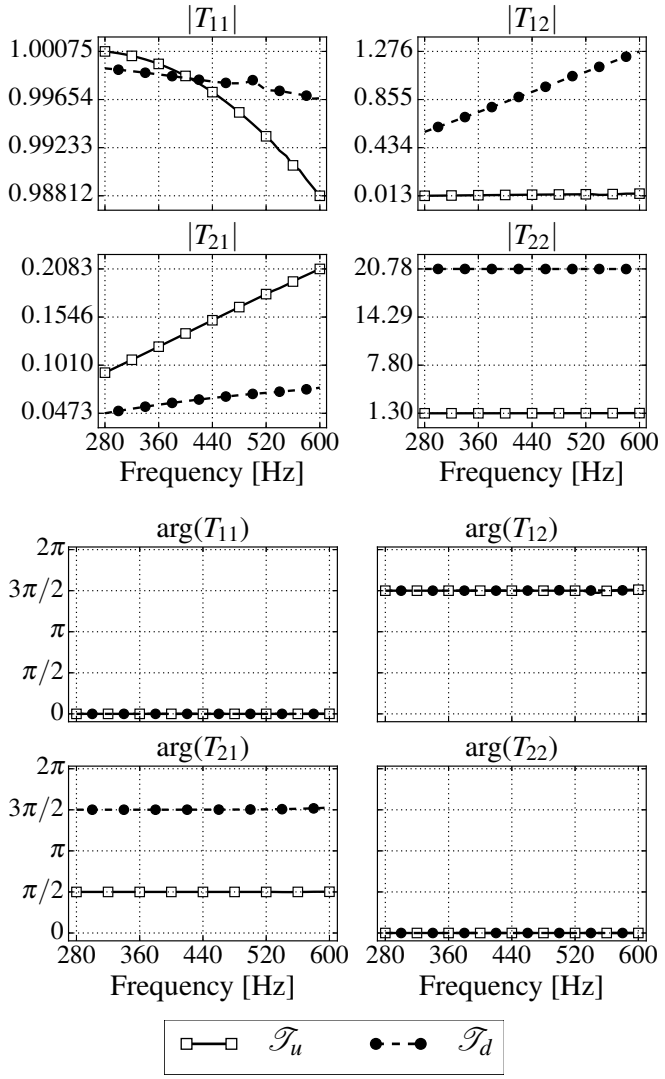
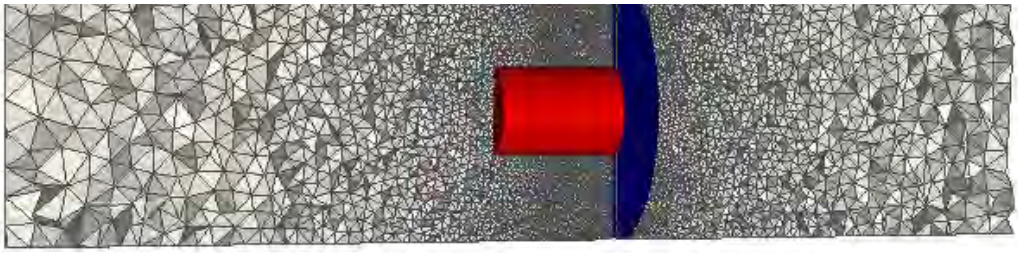
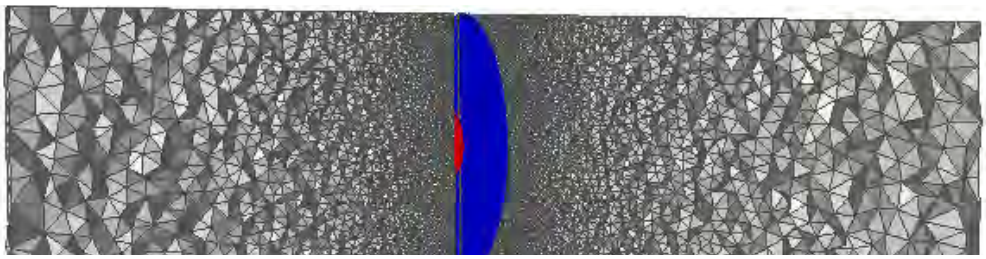


FIGURE 4.17: $\mathcal{T}_u$ and $\mathcal{T}_d$ coefficients as a function of frequency (top: absolute value, bottom: argument), linking the complex MBC surfaces of Fig. 4.3, top, to the plane coincident surfaces of Fig. 4.3, bottom.



(A) Mesh for $\mathcal{T}_u$



(B) Mesh for $\mathcal{T}_d$

FIGURE 4.18: Mesh for the measure of $\mathcal{T}_u$ (top) and $\mathcal{T}_d$ (bottom) for the IMFT swirler (complex MBC in red, plane MBC in blue).

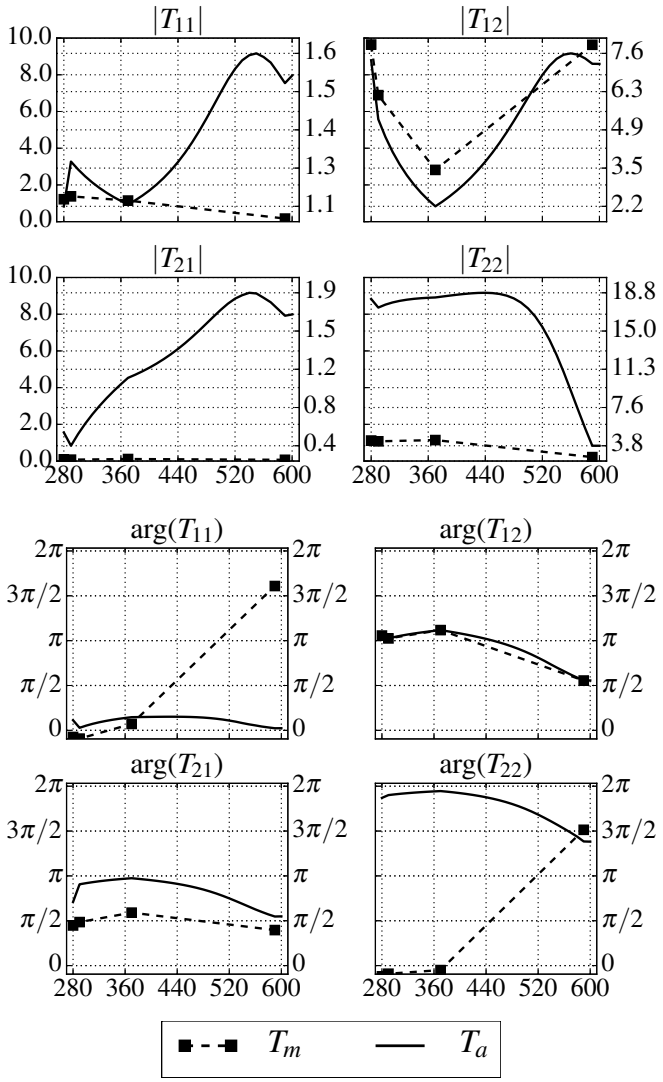
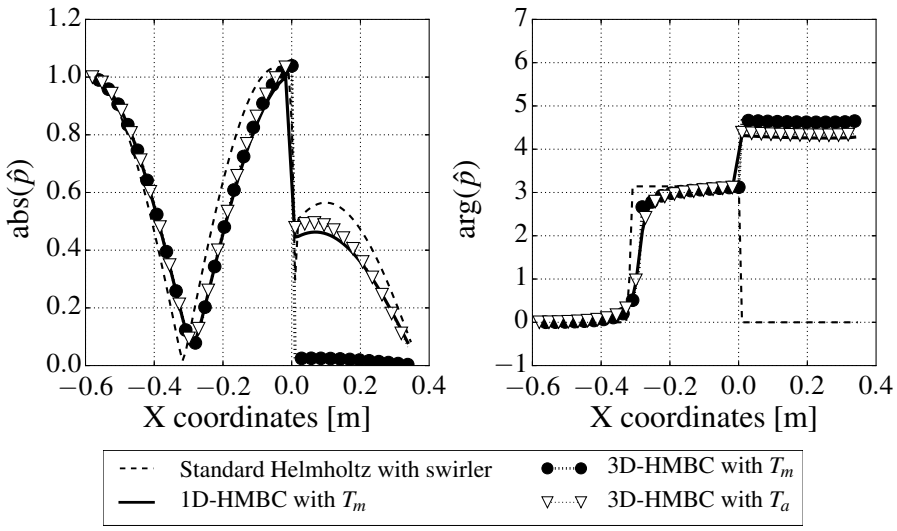
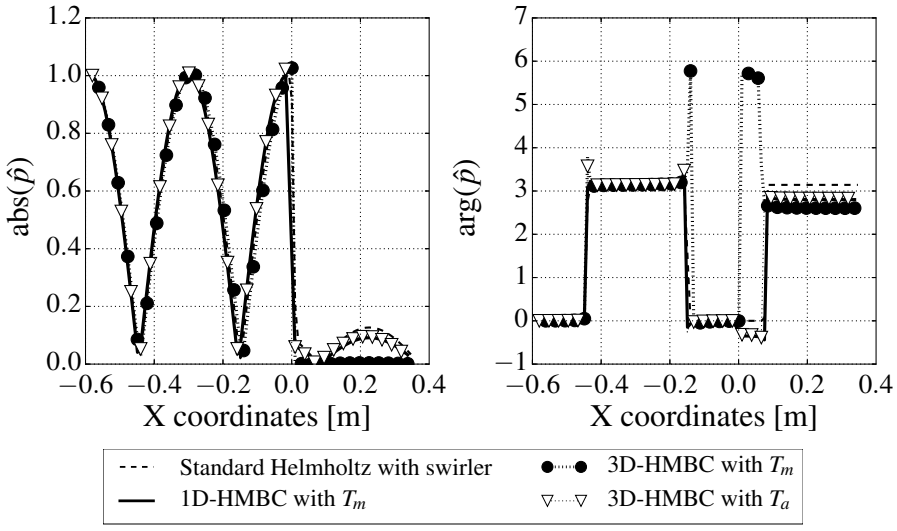


FIGURE 4.19: Coefficients of the adjusted matrix $\mathbb{T}_a$ (top: absolute value, bottom: argument), compared to the original matrix $\mathbb{T}_m$. (For absolute values, the left y-scale corresponds to $\mathbb{T}_m$ and the right one to $\mathbb{T}_a$.)



(A) Mode 3



(B) Mode 4

FIGURE 4.20: Third and fourth eigenmode structures from HMBC computations with $\mathbb{T}_m$, $\mathbb{T}_a$ and from a standard Helmholtz computation.

4.4 The case of dilution holes

4.4.1 Analytical derivation of $\mathcal{T}_u$ and $\mathcal{T}_d$

A specificity of combustion chambers is the existence of numerous dilution holes which are likely to induce dissipation and are good candidates for the MBC method. In this case, the MBC surfaces are imposed on the upstream and downstream surfaces of the hole. If the orifice matrix is measured in a cylindrical rig, then the matrix at orifice surfaces can be determined from the matrix at plane surfaces thanks to the adjustment matrices $\mathcal{T}_u$ and $\mathcal{T}_d$ (Fig. 4.21).

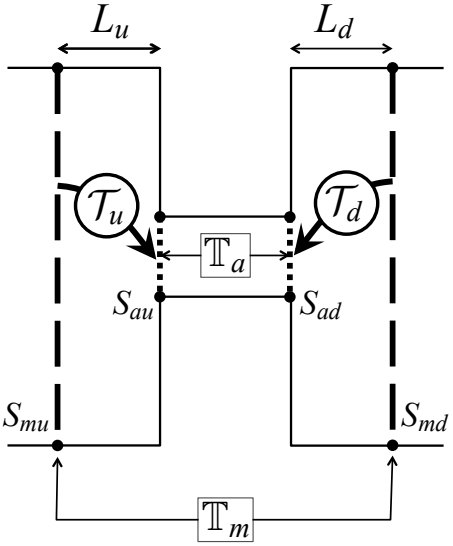


FIGURE 4.21: Orifice matrix measured at plane surfaces (dashed lines) and at orifice surfaces (dotted lines).

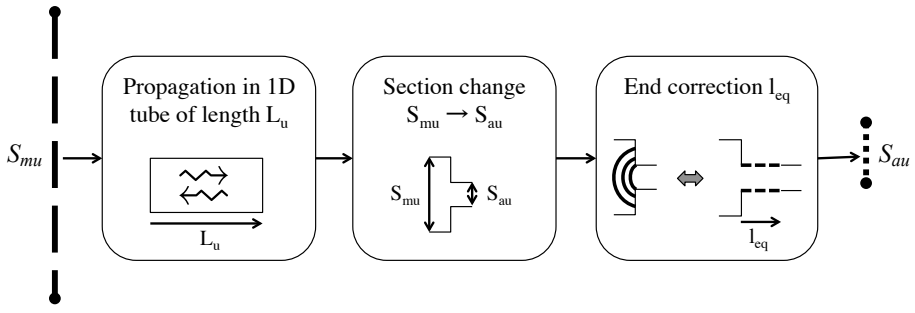
For this choice, matrices $\mathcal{T}_u$ and $\mathcal{T}_d$ can actually be determined analytically with the acoustic network analysis of Fig. 4.22. These networks model the propagation of an acoustic wave from S_m to S_a in three steps:

- First, the acoustic wave propagates in a portion of 1D tube of length L_u or L_d.
- Then it encounters a compact section change. The first effect of the section change is to multiply the acoustic velocity by the ratio of cross-sections.
- In reality, the section change introduces evanescent higher order modes that have an impact on the acoustic pressure (even for a zero-mean flow inviscid fluid). This impact can be modelled as a correction length, also called equivalent length l_{eq} in this manuscript.

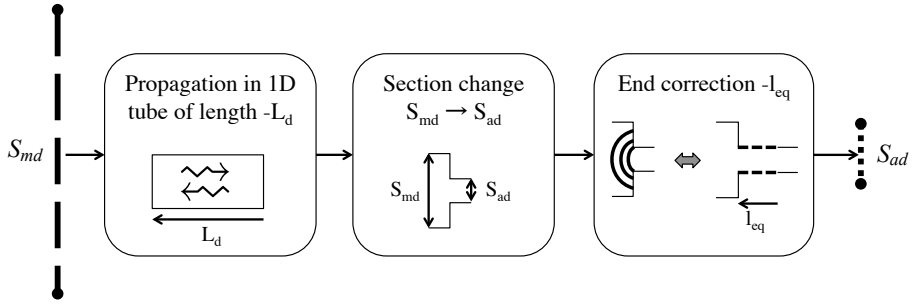
In terms of equations, $\mathcal{T}_u$ and $\mathcal{T}_d$ can be expressed as:

$$\mathcal{T}_u = \begin{pmatrix} 1 & ikl_{eq} \\ 0 & 1 \end{pmatrix} \begin{pmatrix} 1 & 0 \\ 0 & \dfrac{S_{mu}}{S_{au}} \end{pmatrix} \begin{pmatrix} \cos(kL_u) & i\sin(kL_u) \\ i\sin(kL_u) & \cos(kL_u) \end{pmatrix} \tag{4.7}$$

$$\mathcal{T}_d = \begin{pmatrix} 1 & -ikl_{eq} \\ 0 & 1 \end{pmatrix} \begin{pmatrix} 1 & 0 \\ 0 & \dfrac{S_{md}}{S_{ad}} \end{pmatrix} \begin{pmatrix} \cos(kL_d) & -i\sin(kL_d) \\ -i\sin(kL_d) & \cos(kL_d) \end{pmatrix} \tag{4.8}$$



(A) $\mathcal{T}_u$



(B) $\mathcal{T}_d$

FIGURE 4.22: 1D acoustic network decomposition of domains (a) between S_{mu} and S_{au}, (b) between S_{md} and S_{ad}

While S_{mu}/S_{au} and S_{md}/S_{ad} are geometrical parameters, l_{eq} is an acoustic quantity and in a real configuration with mean flow, it is a function of:

- The orifice radius a.
- The porosity or confinement parameter σ. In the case of a multiperforated plate, σ is the ratio of perforated surface over total surface. In the case of a single orifice in a confinement tube, σ is defined as the ratio of the orifice surface $S_a = \pi a^2$ over the confinement tube cross-section S_m. The two situations are similar in that they both curb the flow and the acoustics, in one case because of the walls, in the other case because of the interaction with the other orifices.
- The bias flow velocity in the orifice U_{ori}.
- The acoustic velocity in the orifice u_{ac}.

Because the adjustment procedure is carried out within the framework of linear acoustics, the dependency of l_{eq} with U and u_{ac} is dropped. The value of l_{eq} can be determined from analytical models [157] or correlations [158, 159], for given values of a and σ, but it can also be computed numerically.

If computed numerically, one method is to measure the plane-wave quantities up- and downstream of the element introducing non plane acoustic fields, in an acoustically forced computation (with AVSP-f for example). In theory, this element should simply be the section changes upstream and downstream of the orifice. However, the correction length l_{eq} measured this way is not exactly the one seen by the HMBC computation, because of the absence of corners in the MBC geometry (the orifice tube is removed from the geometry in Fig. 4.21). Therefore, l_{eq} is rather measured on the configuration of Fig. 4.23.

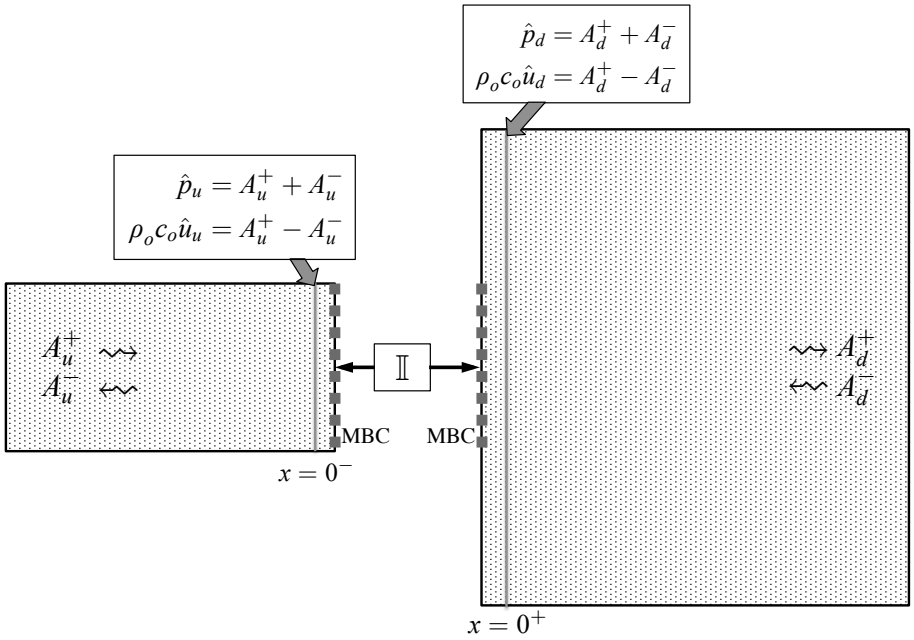


FIGURE 4.23: Measurement of l_{eq} for the adjustment procedure of orifices.

Once the plane wave amplitudes are obtained, they are combined to reconstruct the fictive plane-wave pressures and velocity $(\hat{p}_u, \hat{u}_u)$ and $(\hat{p}_d, \hat{u}_d$ at $x = 0^-$ and $x = 0^+$ in Fig. 4.23. There is a pressure discontinuity at $x = 0$ and the pressure jump is related to $\hat{u}_u$ by the correction length:

$$\frac{\hat{p}_d - \hat{p}_u}{\rho_o c_o \hat{u}_u} = ikl_{eq} \tag{4.9}$$

The value of l_{eq} can then be retrieved by measuring the quantity $\dfrac{\hat{p}_d - \hat{p}_u}{\rho_o c_o \hat{u}_u}$ for several frequencies and fitting it with a linear function. The correlation coefficient between the numerical data and a linear fit is always excellent (> 0.99) in the AVSP-f computations of this work.

Remark

The quantities l_{eq} and S_m/S_a must be treated carefully because they are mesh dependent. The dependency of S_m/S_a is easy to understand since the mesh used in the Helmholtz computation is only an approximation of the geometry of interest. For example, the surface of a disk of radius a, discretized with a uniform mesh size of dx is slightly smaller than πa^2. It can be approximated by a regular polygon of side length dx, inscribed in a circle of radius a, with a surface $\mathcal{S}$ of:

$$\mathcal{S}(a, \eta) = \pi a^2 \sqrt{1 - \left(\frac{1}{2}\eta\right)^2} \frac{\frac{1}{2}\eta}{\sin^{-1}\left(\frac{1}{2}\eta\right)} \tag{4.10}$$

	Coarse	**Fine**
Area S_m [m^2]	$5.27561{\cdot}10^{-3}$	$5.27544{\cdot}10^{-3}$
Area S_a [m^2]	$2.47979{\cdot}10^{-4}$	$2.54303{\cdot}10^{-4}$
Orifice radius $a = \sqrt{S_a/\pi}$ [mm]	8.88	9.00
Section change S_m/S_a	21.274	20.745
Mesh resolution $\eta = dx/a$	0.4	0.05

TABLE 4.5: Properties of the meshes used for the numerical computation of $\mathcal{T}_u$ and $\mathcal{T}_d$.

with $\eta = \dfrac{dx}{a}$. This expression can be used to compute S_{mu}/S_{au} and S_{md}/S_{ad} for circular orifices in cylindrical tubes. For general geometries, S_m/S_a can simply be measured directly on the mesh. This is the method used here, and Eq. (4.10) is only used to illustrate the dependency of the ratios S_{mu}/S_{au}, S_{md}/S_{ad} on the mesh resolution η.

The quantity l_{eq} is also sensitive to the mesh size, since it strongly depends on the discretization of the locally non-plane acoustic fields at the section change. This dependency has been observed by Komkin et al. [160] but is rarely accounted for in the literature. However, in the Helmholtz computations of industrial geometries, the mesh size at dilution holes is often quite important and this effect needs to be assessed. For this purpose, l_{eq} was determined numerically for different values of σ and η, with the AVSP-f solver. From this database, a correlation of $l_{eq}(\sigma, \eta)$ is then proposed in Appendix F.

4.4.2 Comparison of numerical and analytical values of $\mathcal{T}_u$ and $\mathcal{T}_d$

The matrices $\mathcal{T}_u$ and $\mathcal{T}_d$ are now computed numerically with AVSP-f for the orifice geometry of Chapter 3, for $L_u \to 0$ and $L_d \to 0$[2]. Since the cross-section of the outer tube is constant in this case, $\mathcal{T}_u$ and $\mathcal{T}_d$ are complex conjugates and can be determined on the same configuration. The section ratios S_{mu}/S_{au} and S_{md}/S_{ad} are identical and noted S_m/S_a in the following.

The methodology of Section 4.3.2 is used, on a coarse and a fine mesh (Fig. 4.24). The characteristics of the meshes are provided in Tab. 4.5. The numerical values are compared to the analytical ones with S_m/S_a from Tab. 4.5 and l_{eq} obtained with Kang's correlation [159] (see Appendix F) with again the parameters of Tab. 4.5. The comparison for $\mathcal{T}_d^{-1}$ is plotted in Fig. 4.25 and Fig. 4.26. The advantage of plotting $\mathcal{T}_d^{-1}$ over $\mathcal{T}_d$ directly is that the values of l_{eq} and S_m/S_a can be visualized directly as the slope of T_{12} and the value of T_{22} respectively.

The agreement between the analytical and numerical values of $\mathcal{T}_d^{-1}$ is good on both meshes. Very small errors can be observed on coefficients T_{11} and T_{21}, and the value of T_{22} is an excellent match of the section ratio S_a/S_m. The correlation of Kang et al. predicts the slope of coefficient T_{12} quite well, although it gives a larger value than the numerical one for the coarse mesh, and a smaller value for the fine mesh. The variation of the slope of T_{12} with the mesh size was expected since it is related to l_{eq}.

[2]These matrices are actually measured at transverse sections far from the orifice ($L_u > 0$ and $L_d > 0$), and reconstructed at $L_u = L_d = 0$ with 1D propagation matrices.

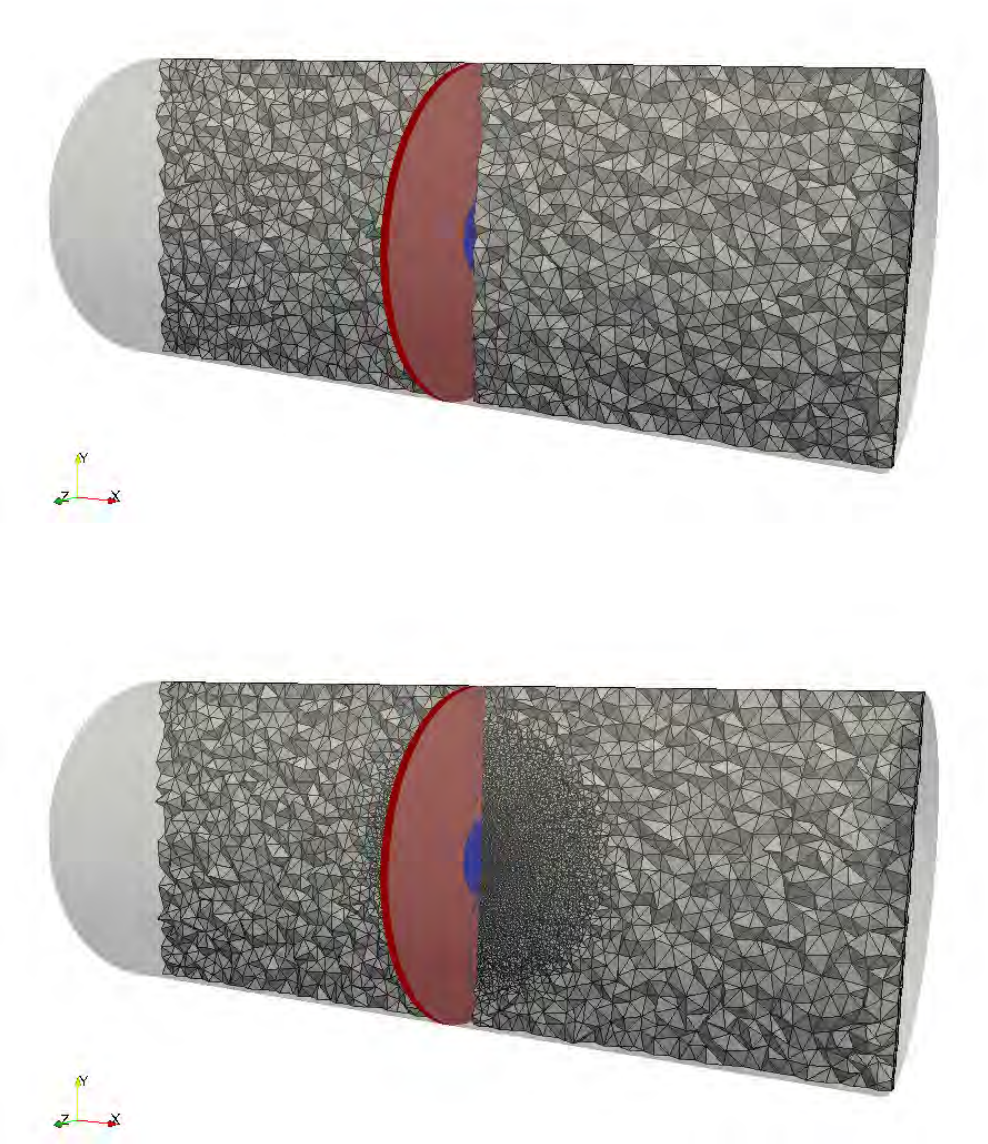


FIGURE 4.24: Overview of the meshes for the numerical computation of $\mathcal{T}_u$ and $\mathcal{T}_d$ for the IMFT orifice (top: coarse, botom: fine). MBC surfaces linked by an identity matrix are displayed in red and blue.

The numerical values of $\mathcal{T}_d$ and $\mathcal{T}_u$ (complex conjugate of $\mathcal{T}_d$) are used to adjust the LES matrix of the orifice of Chapter 3. The adjusted matrix is plugged in a 3D-HMBC computation on a coarse and a fine mesh with the same characteristics as the ones of Fig. 4.24. This computation, refered to as R1, is compared to the reference 1D-HMBC solution of Chapter 3 (R0) (Tab. 4.6). The agreement between R0 and R1 is good on both meshes, in terms of eigenfrequencies (Fig. 4.27) and eigenmode structure (the poorest agreement is obtained for mode 1, displayed in Fig. 4.28). Additionally, the result of a 3D-HMBC computation without adjustment (R2) is also provided for the coarse mesh. As Fig. 4.27 and Fig. 4.28 show, performing the adequate matrix adjustment substantially improves the results of the 3D-HMBC computation.

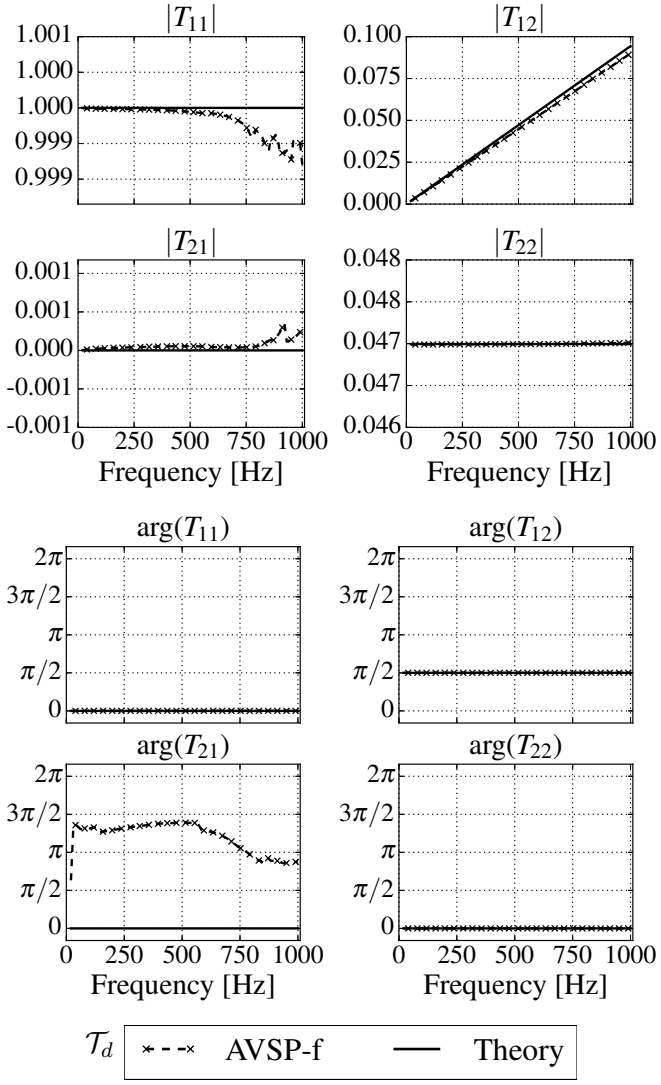


FIGURE 4.25: Numerical and analytical values of $\mathcal{T}_d^{-1}$ on coarse mesh

It was checked, but not shown here that the small errors on T_{11}, T_{21} and T_{22} have no impact on the frequencies and modes of a 3D-HMBC computation. Setting these coefficients to respectively 1, 0 and S_a/S_m (measured on the 3D-HMBC mesh) for $\mathcal{T}_d^{-1}$ instead of using the numerical values does not change the Helmholtz solution.

The impact of coefficient T_{12} on the 3D-HMBC computation is now examined more closely, because the correction length l_{eq} can be obtained in many different ways. In addition to the numerical value of l_{eq}, four models/correlations are used. The 3D-HMBC computations associated to each l_{eq} model are listed in Tab. 4.6.

1. The model of Rayleigh [157]. It is valid for an orifice in an infinite plate of zero thickness.
2. The correlation of Kang et al. [159] valid for a section change of ratio σ.
3. The correlation of Bellucci et al. [158]. It is similar to the correlation of Kang but with slightly different coefficients, and depends weakly on the frequency through the Helmholtz number ka.

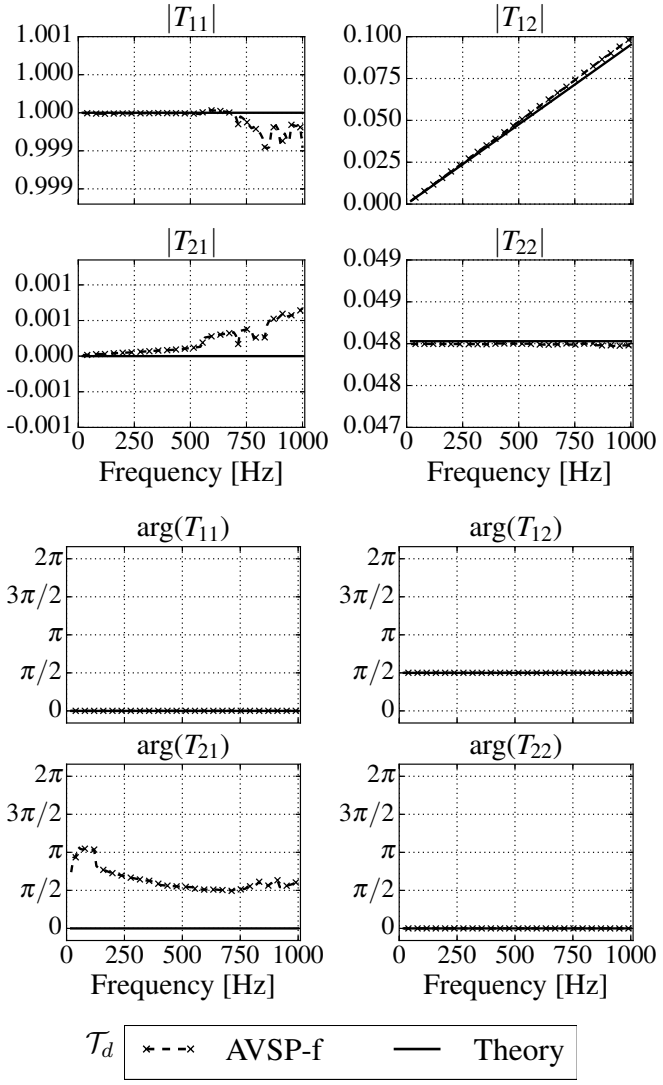


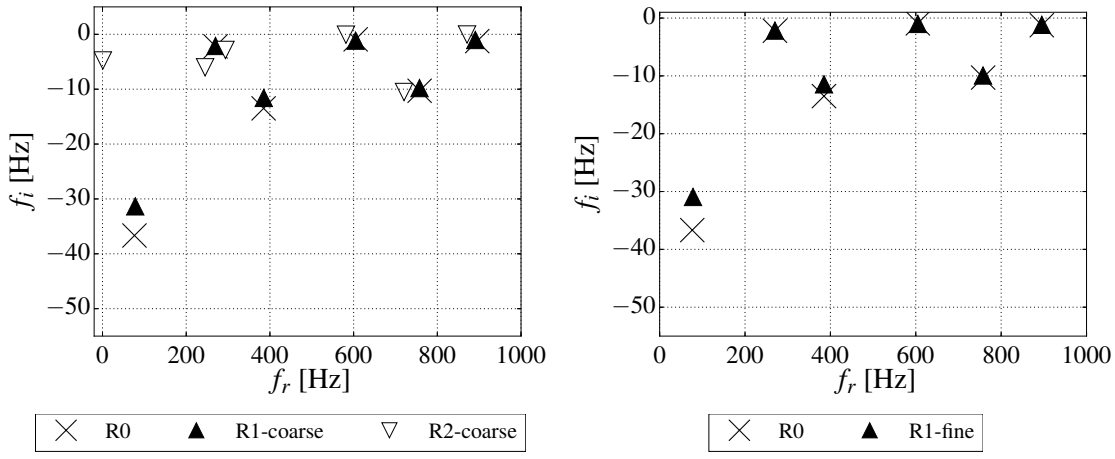
FIGURE 4.26: Numerical and analytical values of $\mathcal{T}_d^{-1}$ on fine mesh

4. The η-correlation proposed in Appendix F, Eq. (F.5). It depends on σ and on $\eta = dx/R$.

The value of l_{eq} as a function of the Helmholtz number and the confinement $\sigma = S_a/S_m$ is plotted in Fig. 4.29. The model of Rayleigh is valid only for $\sigma = 0$ and its value is recalled in dashed lines in Fig. 4.29b. The value of σ for the orifice of Chapter 3 is also recalled as a vertical grey line. It is interesting to note that the $\eta-$correlation decreases linearly with $\sqrt{\sigma}$ with a slope similar to the one of the correlation of Kang et al., but different from the one of Bellucci et al.

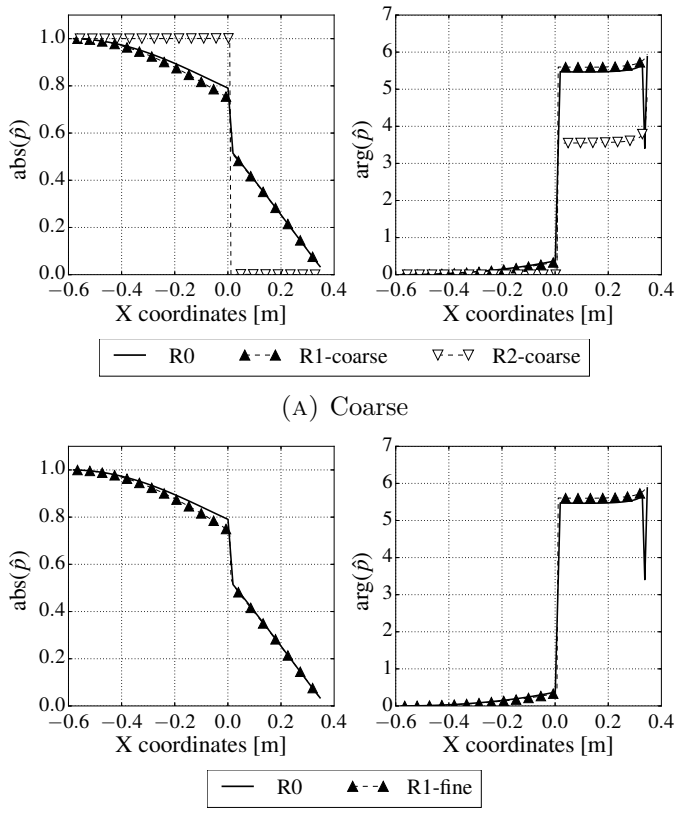
The reference result R0 is compared to R3, R4, R5 and R6, on the fine and the coarse meshes. On the fine mesh, all l_{eq} models provide acceptable estimations of the eigenfrequencies (Fig. 4.30b) and fairly similar mode structures at low frequencies (such as mode 3 in Fig. 4.32). However, there is more variability for modes at higher frequencies and only our correlation is able to capture the correct structure (Fig. 4.32).

On the coarse mesh, all models except the η-correlation overpredict the damping rate for mode 3 (Fig. 4.30a). The worst results are obtained with the model of Rayleigh



(A) Coarse (B) Fine

FIGURE 4.27: Eigenfrequencies of a 3D-HMBC computation of the orifice of Chapter 3 with numerical $\mathcal{T}_u$ and $\mathcal{T}_d$ (black triangles). The frequencies found with a 1D-HMBC computation are recalled as black crosses.



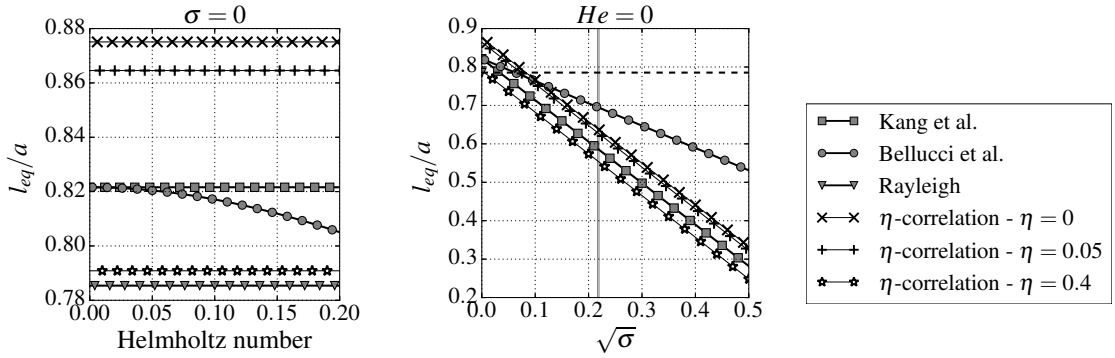
(A) Coarse

(B) Fine

FIGURE 4.28: Influence of the model for l_{eq} on the eigenfrequencies of the 3D-HMBC computation (see Tab. 4.6).

(R5) as expected, since it should work only for orifices in an infinite plate of zero thickness. Concerning the eigenmode structures, the observations on the fine mesh also apply here (Fig. 4.31).

This comparison shows how important it is to have a good estimation of l_{eq} when



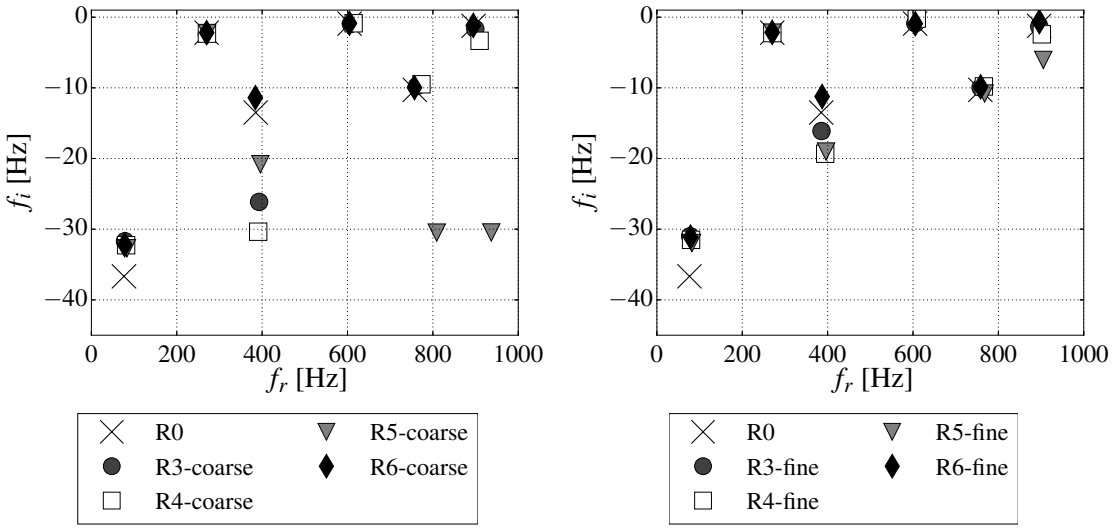
(A) As a function of $He = ka$ (B) As a function of σ.

FIGURE 4.29: Correction length l_{eq} from various models.

Run	HMBC type	Model for l_{eq}
R0	1D-HMBC	-
R1	3D-HMBC	Numerical
R2	3D-HMBC	-
R3	3D-HMBC	Kang et al. [159]
R4	3D-HMBC	Bellucci et al. [158]
R5	3D-HMBC	Rayleigh [157]
R6	3D-HMBC	η-correlation (F.5)

TABLE 4.6: List of HMBC computations with different values of l_{eq}.

$\mathcal{T}_u$ and $\mathcal{T}_d$ in our tube-like geometry, especially on coarser meshes. On an industrial configuration however, the impact of l_{eq} will probably be less important. Indeed, it modifies the acoustics in a direction normal to the dilution holes, and should not influence much the azimuthal modes we are most of the time interested in.



(A) Coarse (B) Fine

FIGURE 4.30: Influence of the model for l_{eq} on the eigenfrequencies of the 3D-HMBC computation (see Tab. 4.6).

To summarize, $\mathcal{T}_u$ and $\mathcal{T}_d$ can be determined analytically for orifices, in the case

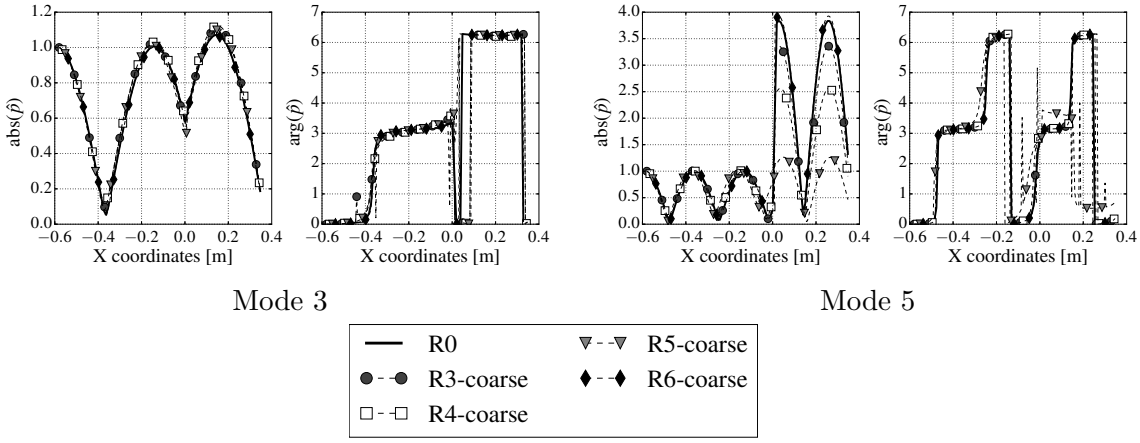


FIGURE 4.31: Third and fifth mode for the 3D-HMBC computations on the coarse mesh (see Tab. 4.6).

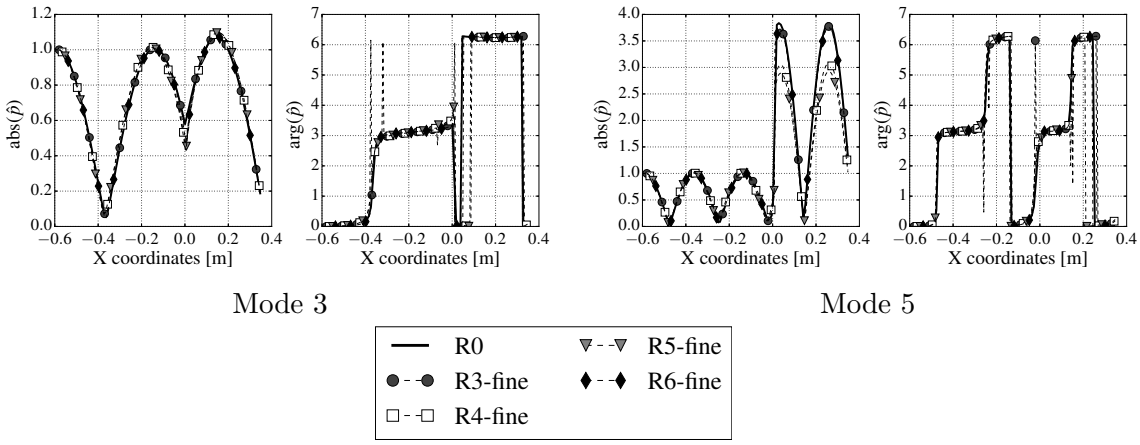


FIGURE 4.32: Third and fifth mode for the 3D-HMBC computations on the fine mesh (see Tab. 4.6).

where MBC is imposed at the orifice surfaces. This analytical expression involves two key quantities:

- the area ratio S_m/S_a between the cross-section of the measurement tube and the section of the orifice
- the correction length l_{eq}

The area ratio S_m/S_a to consider is the one of the discretized mesh and can be slightly different from the theoretical one if the mesh is coarse. Similarly, the correction length l_{eq} is also mesh dependent and taking into account this dependency greatly improves the accuracy of the 3D-HMBC computations. The correlation of Appendix F provides an easy way to estimate l_{eq} correctly as a function of the mesh size and the confinement σ.

4.4.3 Towards an intrinsic formulation of the dilution hole

Our choice of matrix surfaces for an orifice is unique and depends only on the orifice geometry. A legitimate question is therefore to check if an intrinsic matrix can be defined for an orifice. This matrix would depend only on the orifice properties : radius and bias flow velocity. The question is not only of theoretical interest. For an industrial combustor, it is quite difficult to define the confinement parameter σ of a dilution hole, as illustrated in Fig. 4.33. The existence of an intrinsic matrix would make it possible to apply the HMBC procedure without worrying about σ.

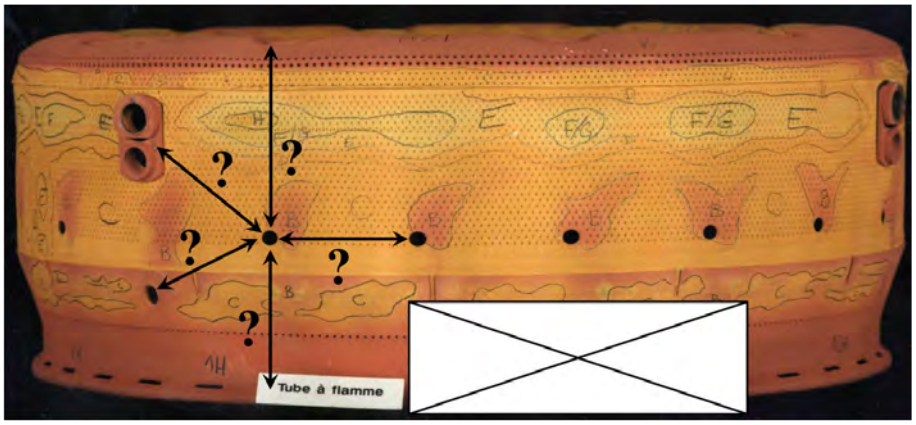


FIGURE 4.33: Outer casing of a real annular combustor (courtesy of Safran Helicopter Engines) showing the difficulty to define the confinement of a dilution hole in a real geometry.

To investigate this problem, the semi-analytical model of Bellucci for an orifice of radius a in a tube of cross-section S is used [158]. This model relies on Howe's analytical expression of the Rayleigh conductivity for the resistance of the orifice in the presence of a bias flow velocity [111], but uses empirical correlations to obtain the reactance. The transfer matrix associated to both Howe's and Bellucci's model are provided in Appendix D. For the reactance, Bellucci et al. define a new correction length noted ℓ that differs from the previously defined l_{eq} on two aspects:

- It takes into account the presence of a non-zero bias flow, i.e. $U_{ori} \neq 0$.
- Contrary to l_{eq}, ℓ is not a numerical adjustment parameter but has a true physical meaning. It should come either from an analytical model or from a *well-resolved* CFD computation. The key word here is *well-resolved*, i.e. $\eta = dx/a \ll 1$.

The expression of ℓ proposed by Bellucci et al. is recalled in Appendix D. However, it was shown in Section 4.4.2 that the value of ℓ for $St \leftarrow \infty$ is not the one observed in our Helmholtz computations. Therefore, the model of Bellucci et al. is modified to include the η-correlation. The expressions of $\phi(He)$ and $\chi(\sigma)$ in Eq. (D.10) and (D.11) are replaced by:

$$\phi(He) = 0.875087a\left(1 + \frac{(0.77He)^2}{1 + 0.77He}\right)^{-1} \tag{4.11}$$

$$\chi(\sigma, \eta) = 1 - 1.239825\sigma - 0.240636\eta = 1 - A\sigma - B\eta \tag{4.12}$$

The nonlinear behaviour of the orifice is neglected so that $\theta = 1$ in Eq. D.13. The modified model of Bellucci provides a good agreement with LES matrix measurements (see Appendix D). In particular, the impact of confinement on ξ is correctly retrieved when increasing the section of the outer tube.

The adjustment matrices $\mathcal{T}_u$ and $\mathcal{T}_d$ defined in equations (4.7) and (4.8) are applied to the analytical orifice matrix of (D.2) to obtain its value at the orifice surfaces, with the correlation of Appendix F. In order to simplify the problem, it was assumed that σ is independent of the mesh.[3] The resulting matrix $\mathbb{T}_a$ is:

$$\mathbb{T}_a = \begin{pmatrix} 1 & R_a + iX_a \\ 0 & 1 \end{pmatrix} \tag{4.13}$$

with

$$R_a = \frac{\pi a^2}{S} R = \Re\left(\frac{i\omega\pi a^2}{c_o K_R}\right), \tag{4.14}$$

and

$$X_a = k(h + 2(\ell - l_{eq})). \tag{4.15}$$

The expressions of R_a and X_a are compared with numerical and experimental matrices of the orifice of Chapter 3, characterized by $a = 0.009m$ and $U_{ori} = 7.1m/s$, in two confinement tubes of radius 0.041 m and 0.082 m. These matrices were adjusted with a correction length determined from Eq. (F.5) with $\eta = 0$ and the section ratios $\sigma = 0.048$ (for an outer radius of 0.041 m) and $\sigma = 0.012$ (for an outer radius of 0.082 m). Fig. 4.34 show that the resistance R_a does not vary much with σ as predicted by Eq. (4.14). Surprisingly, the reactance X_a is also little modified by σ, whereas Eq. 4.15 predicts a larger difference. For now, we don't have any explanation for this and will simply note that Eq. (4.14) and (4.15) provide a fair approximation of the LES and experiments for a first analysis.

For $\mathbb{T}_a$ to be intrinsic, its dependency with the outer tube cross-section S should be removed. As already said, this is indeed the case for the resistance R_a, but not for the reactance X_a according to Eq. (4.15) because of the term $\ell - l_{eq}$. This difference can be expressed as:

$$\ell - l_{eq} = \phi(He)[\chi(\sigma, \eta_{fine})\psi(St) - \chi(\sigma, \eta_{coarse})] \tag{4.16}$$

$$= \phi(He)[(1 - A\sigma)(\psi(St) - 1) - B(\eta_{fine}\psi(St) - \eta_{coarse})] \tag{4.17}$$

where η_{fine} is the orifice resolution in the setup where the matrix is measured (for example the LES mesh) and η_{coarse} is the orifice resolution in the Helmholtz computation and is *a priori* bigger than η_{fine}. Here we assume that the matrix data perfectly captures the acoustic behaviour of the orifice so that $\eta_{fine} = 0$ and η_{coarse} can simply be noted η. This simplifies Eq. 4.17 without changing much the conclusions of this section.

As Eq. (4.17) shows, $\ell - l_{eq}$ is independent of σ if $\psi(St) = 1$ i.e. $St \gg 1$ and $M \ll 1$. Unfortunately, Strouhal numbers for dilution holes in industrial combustors

[3] In practice, the error associated with this assumption is small for reasonably fine meshes. For example, if the outer tube cross-section is perfectly discretized ($\eta = 0$), but the mesh resolution at the orifice is of $\eta = 0.4$, the error on σ, estimated with Eq. (4.10), is of 3% only.

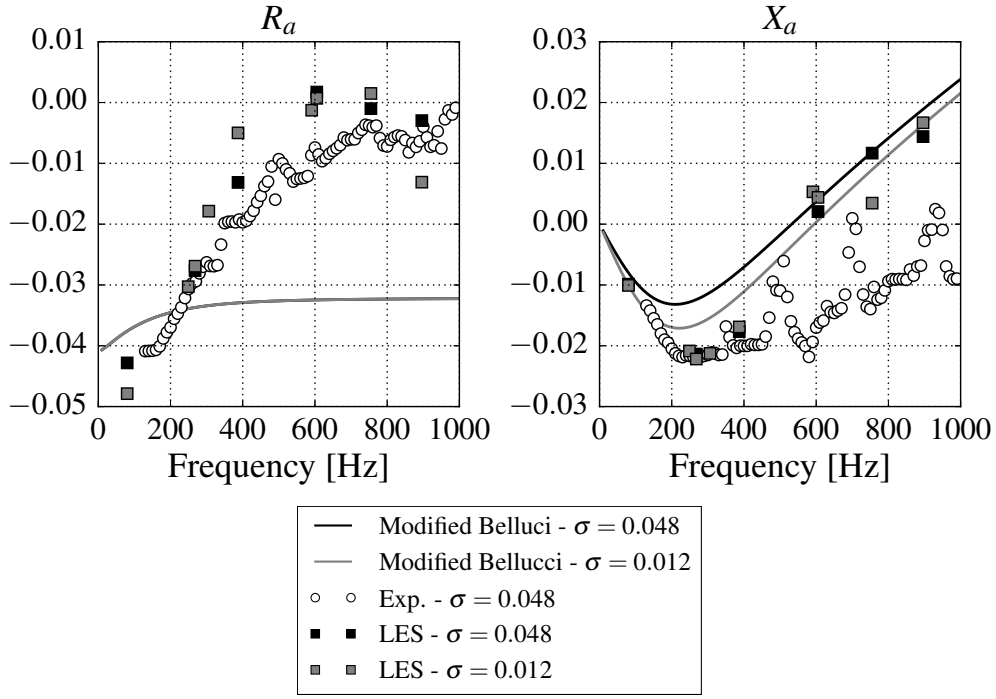


FIGURE 4.34: Comparison of R_a and X_a with LES and experiments, for $\sigma = 0.048$ and $\sigma = 0.012$.

are rather close to 1, leading to a non zero value of $\ell - l_{eq}$. This is clearly visible in Fig. 4.35, where the difference $\ell - l_{eq}$ is plotted against the Strouhal number for a typical dilution hole of radius $a = 0.005$ m, bias flow velocity $U_{ori} = 50$ m/s, and speed of sound $c = 385$ m/s for different values of σ and η. Fig. 4.36 shows the associated variation of R_a and X_a.

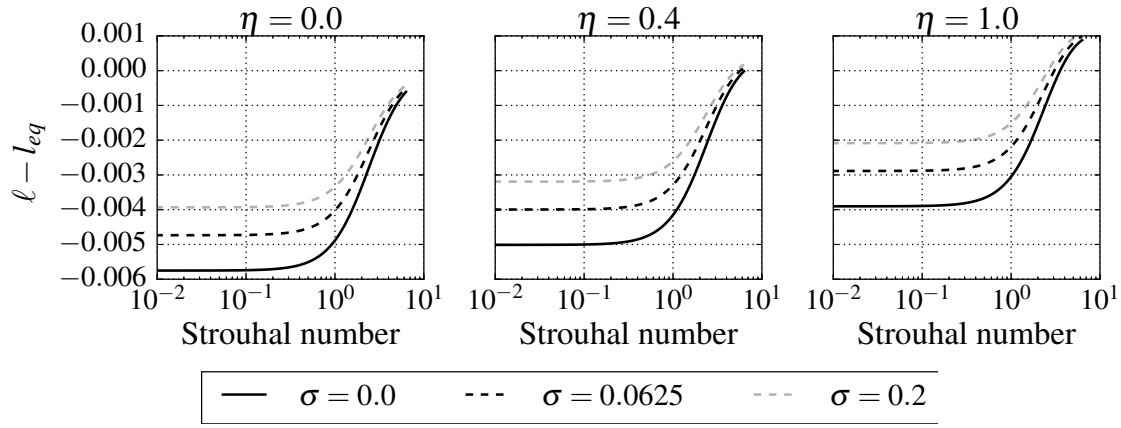


FIGURE 4.35: $\ell - l_{eq}$ against Strouhal number, for $\eta = 0.0, 0.4, 1.0$ and $\sigma = 0.0, 0.0625, 0.2$.

In order to test the effect of σ on the 3D-HMBC solution of an orifice, the geometry of Fig. 4.37 is examined. This geometry is characterized by a value of $\sigma_o = 0.0625$, and $\eta = 0.4$. The value of σ is an estimation of the maximum confinement of a dilution hole in a combustion chamber, obtained by considering the minimum distance between two dilution holes in an industrial geometry. On this configuration, four HMBC runs are performed:

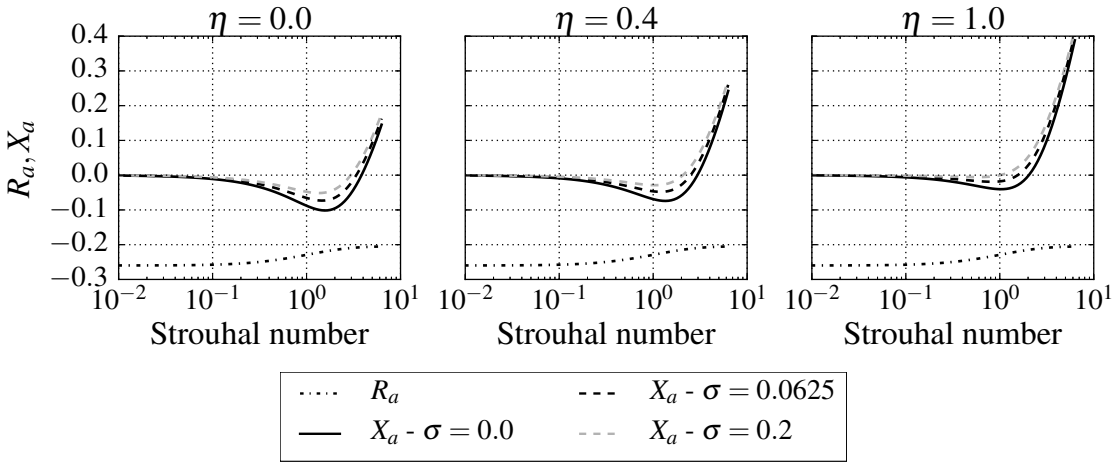
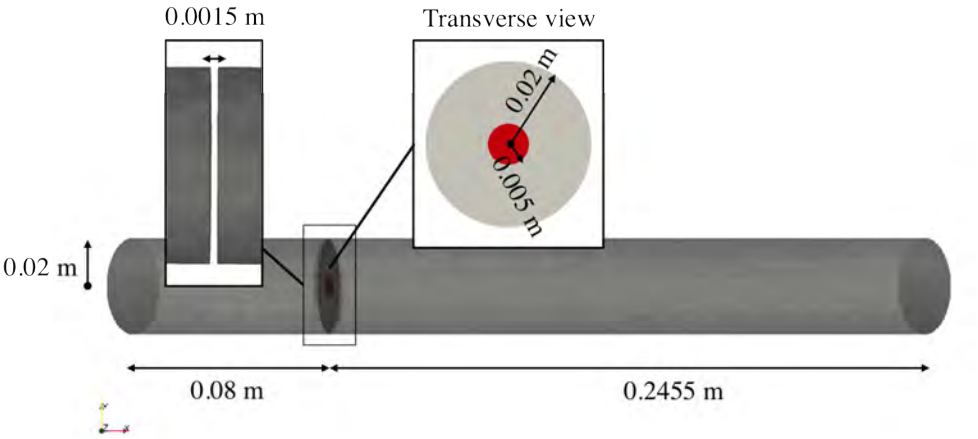


FIGURE 4.36: R_a and X_a against Strouhal number, for $\eta = 0.0, 0.4, 1.0$ and $\sigma = 0.0, 0.0625, 0.2$.

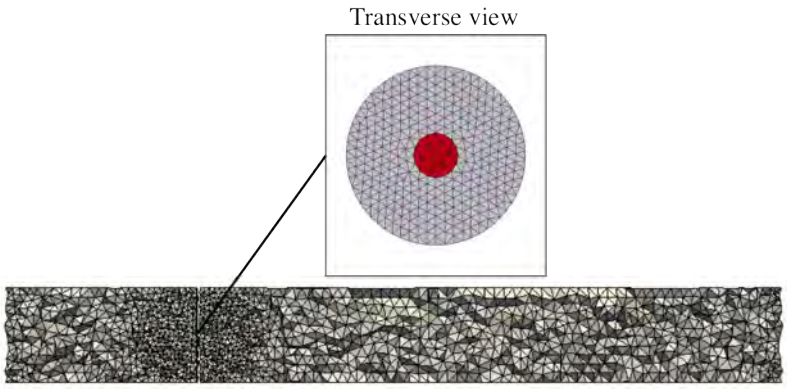
- A reference 1D-HMBC computation with $\sigma = 0.0625$.
- A 3D-HMBC computation with $\sigma = 0.0625$ and $\eta = 0.4$. This computation should reproduce perfectly the 1D-HMBC solutions.
- A 3D-HMBC computation with $\sigma = 0.0$ and $\eta = 0.4$.
- A 3D-HMBC computation with $\sigma = 0.2$ and $\eta = 0.4$.

The first four modes are computed for each setup. The eigenfrequencies (Fig. 4.38) display large negative imaginary parts (partly due to the high orifice velocity). As expected, the 3D-HMBC result with $\sigma = 0.0625$ is closer to the reference 1D-HMBC solution than the 3D-HMBC result with $\sigma = 0.0$. However, even for the fourth mode, the relative error on the frequency when using $\sigma = 0.0$ is only of 1%. This observation, added to the fact the the eigenmode structures of the 3D-HMBC computations are similar for $\sigma = 0.0, 0.2$ and 0.0625 suggests that a rough estimation of σ is suitable for a first order estimation of the eigenmodes and eigenfrequencies. For industrial applications, σ can therefore be set to 0 for all dilution holes, in a first step, then varied to check the sensitivity of the Helmholtz solution to this parameter.

Of course, the result would be more accurate if the real interaction between the dilution hole and its surrounding elements (other holes or walls) was accounted for, but this interaction is not trivial. Moreover, little has been done in the literature to the author's knowledge. A first track would be the paper of [161] but it is only valid for an inviscid fluid in the absence of mean flow. The topic should be further investigated in future works if more precise 3D-HMBC computations are required.



(A) Geometry



(B) Mesh preview

FIGURE 4.37: Orifice geometry on which the effect of σ on the HMBC solution is assessed. The 3D-HMBC surface is displayed in red.

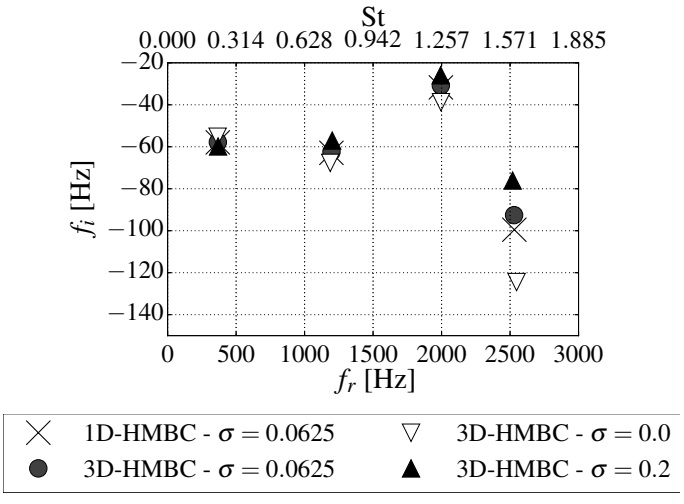
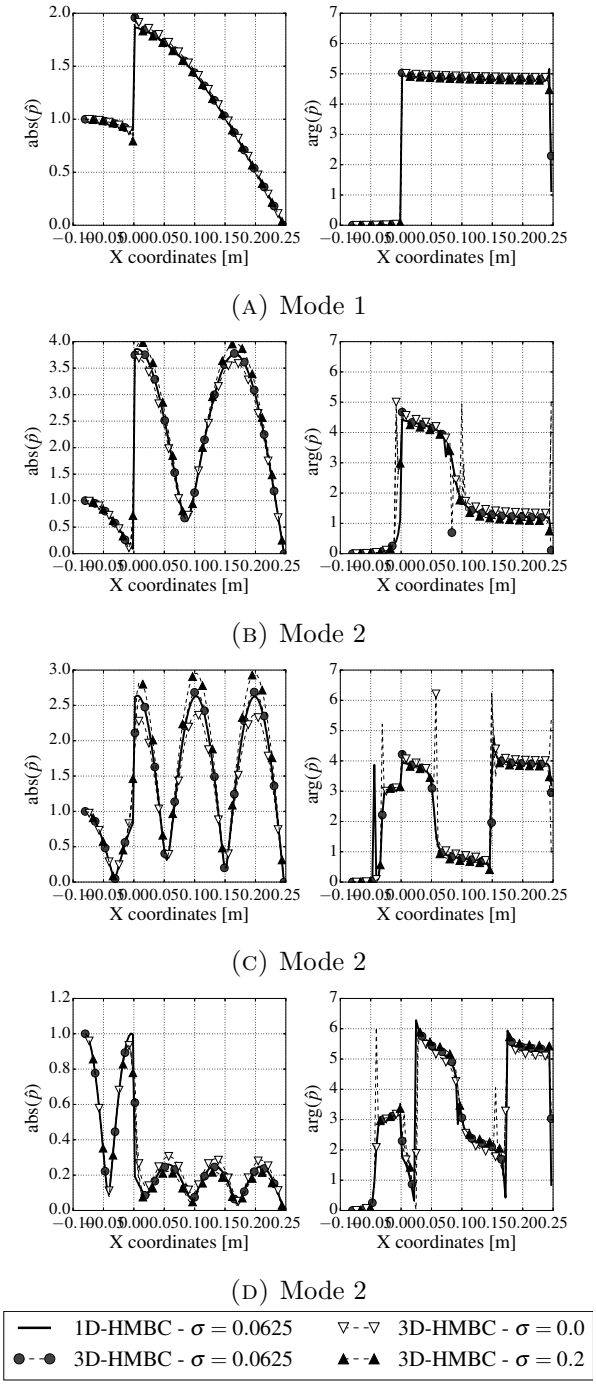


FIGURE 4.38: Eigenfrequencies of the HMBC computations with Bellucci model. The Strouhal numbers are indicated in the top horizontal axis.



(A) Mode 1

(B) Mode 2

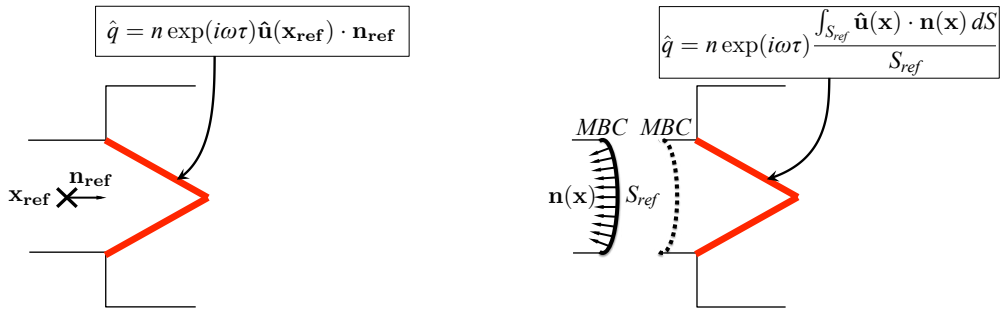
(C) Mode 2

(D) Mode 2

FIGURE 4.39: Eigenmodes of the HMBC computation with the Bellucci model.

4.5 An FTF formulation based on a reference surface

4.5.1 Principle and implementation in the Helmholtz solver



(A) Point-based FTF (B) Surface-based FTF

FIGURE 4.40: Reference point vs reference surface in the FTF definition.

As explained in Section 4.1, replacing the swirler by its equivalent matrix in the Helmholtz computation can be a problem for the Flame Transfer Function if the reference point is located inside the swirler. For this purpose, a surface based FTF is developed in this thesis. The principle is very simple: a reference surface replaces the reference point (Fig. 4.40). In order to obtain the heat release fluctuations, Eq. (C.1) is replaced by:

$$\hat{q}(\mathbf{x}) = n_{local}(\mathbf{x},\omega)e^{i\omega\tau_{local}(\mathbf{x},\omega)}\frac{\int_{\mathcal{S}_{ref}}\hat{\mathbf{u}}(\mathbf{x})\cdot\mathbf{n}(\mathbf{x})dS}{\mathcal{S}_{ref}} \tag{4.18}$$

with the notation of Fig. 4.40. In the Helmholtz solver AVSP, this surface based FTF was implemented, only for boundary surfaces for now (this is enough to use it with Matrix Boundary Conditions). The reference velocity is simply obtained by looping over all nodes of the reference surface, performing the dot product of the acoustic velocity with the surface normal, then summing this quantity and dividing it by the total surface.

Remarks

- The surface dS in the implementation of Eq. (4.18) is the *nodal* surface.
- The surface FTF was implemented within the parallel computing framework of AVSP.

4.5.2 Validation of the implementation on single flame configuration

The implementation of the surface FTF in the AVSP solver is tested for a Rijke tube configuration: a 1D tube of constant temperature $T_o = 300$ K, starting at $x_o = -0.198$ m and ending at $x_f = 0.409$ m with an active flame located between $x_1 = 0.115$ m and $x_2 = 0.225$m. The reference geometry and a mesh overview are depicted in Fig. 4.41. For the flame, a local interaction index of $n_{local} = 2\times10^7$ J/m^4 and a time delay of $\tau = 0.2$ ms were chosen arbitrarily. The reference point is chosen

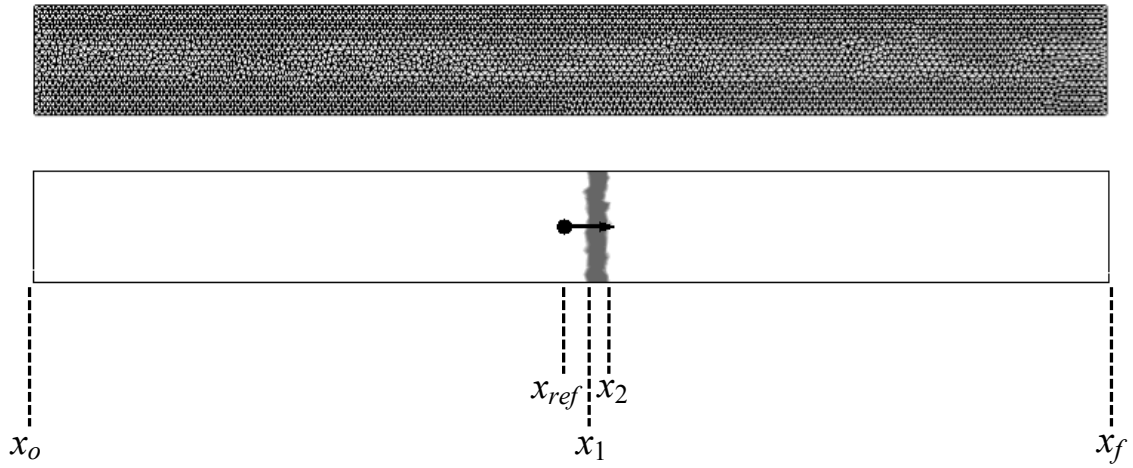


FIGURE 4.41: Reference setup of the Rijke tube (top: mesh, bottom: flame zone in grey with reference point and reference vector).

at $x_{ref} = 0.102$ m, at a small distance upstream of the flame. The pressure is imposed at the outlet and the velocity at the inlet. The eigenfrequencies and eigenmodes of this configuration can be obtained very easily with the standard AVSP solver with a point based FTF (Tab. 4.7).

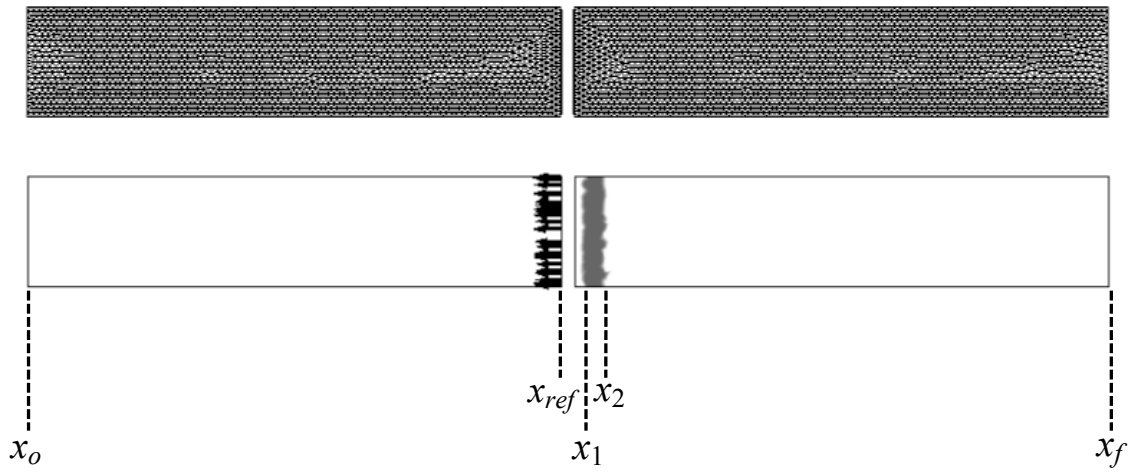
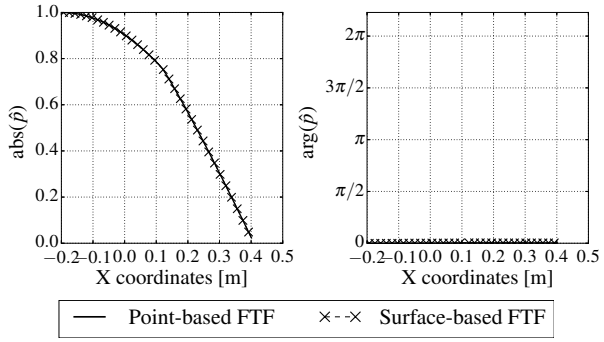


FIGURE 4.42: MBC setup of the Rijke tube (top: mesh, bottom: flame zone in grey with reference surface visualized with surface normals).

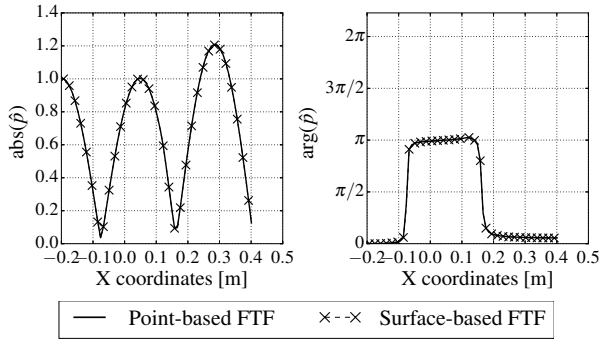
A second setup of the same Rijke tube, with Matrix Boundary Conditions, is presented in Fig. 4.42. The 1D tube was cut in half and a portion of length $l = 0.0076$ m was removed from the geometry, defining two plane MBC surfaces linked by a propagation matrix of length l. The upstream plane is located at $x_{ref} = 0.102$ m, just like the reference point in the reference geometry. This surface is used to define a surface based FTF for the HMBC computation. The time delay is kept identical. Because only plane acoustics are present in the reference geometry and in the MBC geometry, the HMBC solution should be identical to the standard Helmholtz one. This is indeed the case, both in terms of eigenfrequencies (Tab. 4.7), and eigenmodes (Fig. 4.43). Both point-based and surface-based FTF computations are performed with 24 processors.

	Mode 1	Mode 3
Point based FTF	137.1 - 3.0i	779.7 - 13.4i
Surface based FTF	137.2 - 3.0i	779.9 - 13.2i

TABLE 4.7: Eigenfrequencies of the Rijke tube with a point-based FTF (reference geometry) and surface-based FTF (MBC geometry).



(A) Mode 1



(B) Mode 2

FIGURE 4.43: Eigenmodes of the Rijke tube with point-based FTF and surface-based FTF

4.5.3 Validation of the implementation on a multi-flame configuration

The code is now verified on a simple annular geometry, composed of two cylindrical tori connected by four small cylinders (Fig. 4.44). This configuration, studied in [58] is a simple representation of an annular combustor composed of a plenum and a chamber connected by burners, refered to as PBC (Plenum Burners Chamber). Simplified mean flow fields are considered, with hot gases in the chamber and colder ones in the plenum and burners. A thin and plane flame zone with constant n and τ parameters is located between $x = -0.03$ and $x = 0$ (Fig. 4.45). The mean flow field, thermodynamic and flame parameters are listed in Tab. 4.8, as well as the dimensions of the geometry.

As for the Rijke tube, two configurations are compared: 1) the full configuration with a traditional reference point, and 2) a truncated geometry with a pair of MBC surfaces whose upstream patch also serves as a reference for the FTF (Fig. 4.45). The average acoustic quantities on the two MBC surfaces are linked by a simple propagation matrix over a distance $\delta x = 0.01$, corresponding to the portion of burner removed from the full geometry. The length of the removed portion is arbitrary and

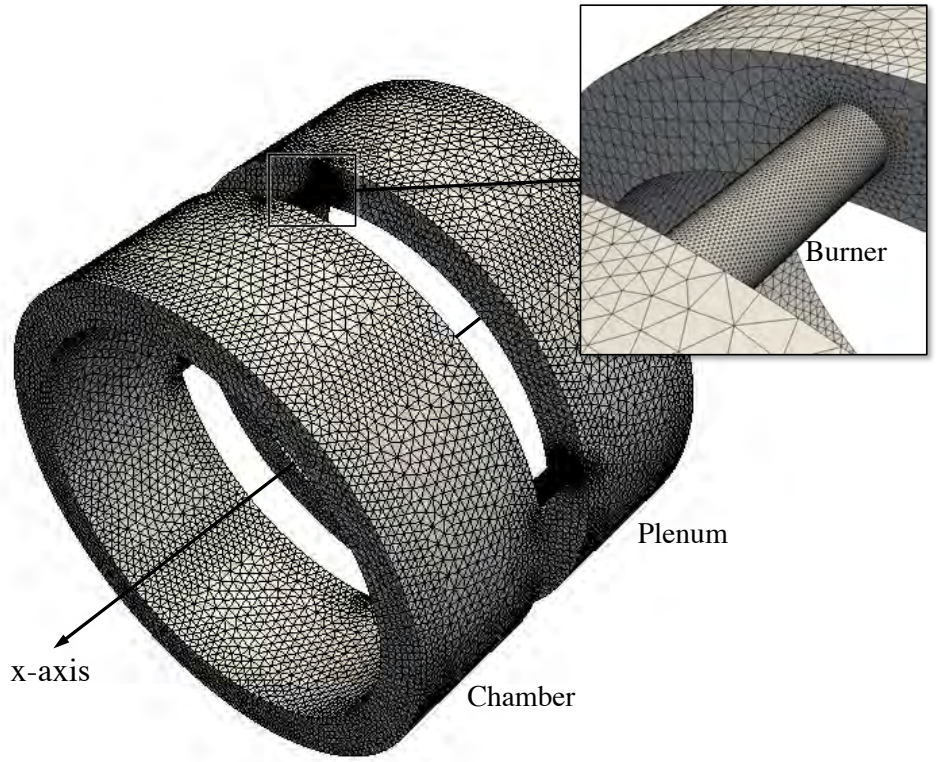


FIGURE 4.44: Annular PBC geometry with four burners.

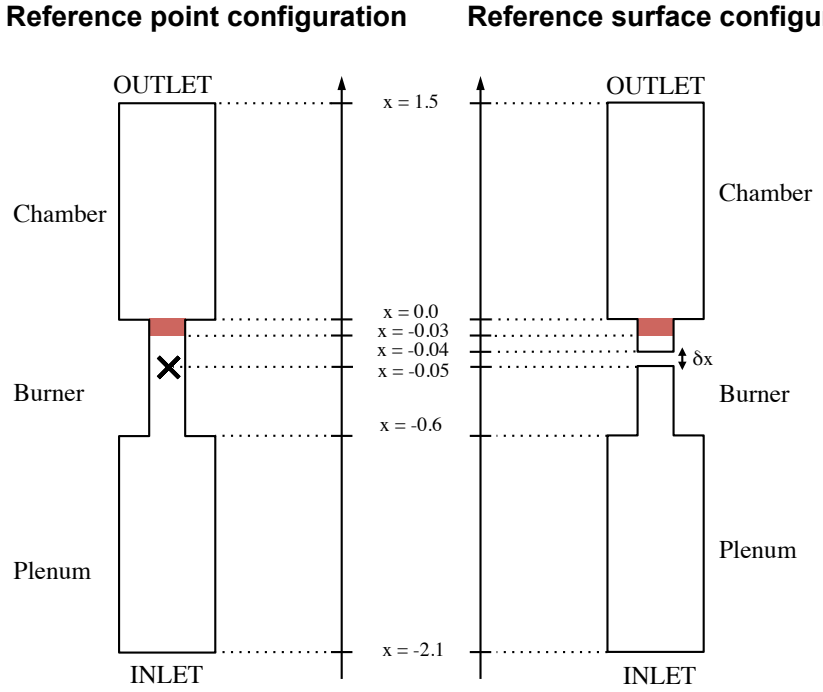


FIGURE 4.45: Transverse representation of the PBC configuration with reference point (left) and reference surface (right).

Dimensions	
Chamber/Plenum inner radius	1.9 m
Chamber/Plenum outer radius	2.3 m
Chamber/Plenum length	1.5 m
Burner radius	0.0975 m
Burner length	0.6 m
Mean flow fields	
Average temperature for $x \leq 0.0$ m	700 K
Average temperature for $x \geq 0.0$ m	1800 K
Average pressure	20 bars
Heat capacity ratio	2.7
Flame parameters	
Flame location	-0.03 m $\leq$ x $\leq$ 0.0m
Global interaction index	762 353
Time delay	11.07 ms
Reference point/surface	x= -0.05m

TABLE 4.8: Dimensions, mean flow fields and flame parameters for the 4 burners PBC configuration.

it was chosen to make it as small as possible in order to minimize the differences between reference point / surface geometries. Zero acoustic velocity boundary conditions are imposed on all walls and at the inlet of the plenum. The pressure is set to zero at the outlet[4].

Four reference points and four reference surfaces are defined, one for each burner. As an example, one quarter of configuration 1 and of configuration 2 are shown in Fig. 4.46. The reference point in configuration 1 is located in the middle of the burner, at the same axial coordinate x as the reference surface in configuration 2. One mode is examined in this section : the first azimuthal mode of the plenum, refered to as mode P1. The conclusions can however be generalized to the rest of the modes.

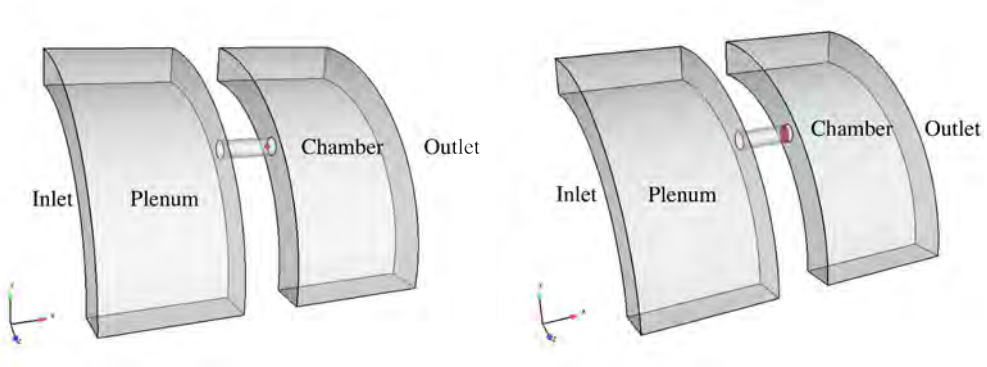


FIGURE 4.46: One sector of configuration 1 (left) and configuration 2 (right). The reference point / surface is highlighted in red.

In the absence of a flame, mode P1 has a frequency of 58.8 Hz that is correctly retrieved with configuration 1 and 2. The mode structure is almost identical (Fig. 4.47),

[4]Note that this differs from the work of [58] where a zero-velocity outlet is imposed.

but the amplitude of pressure fluctuations are lower in the plenum for configuration 2.

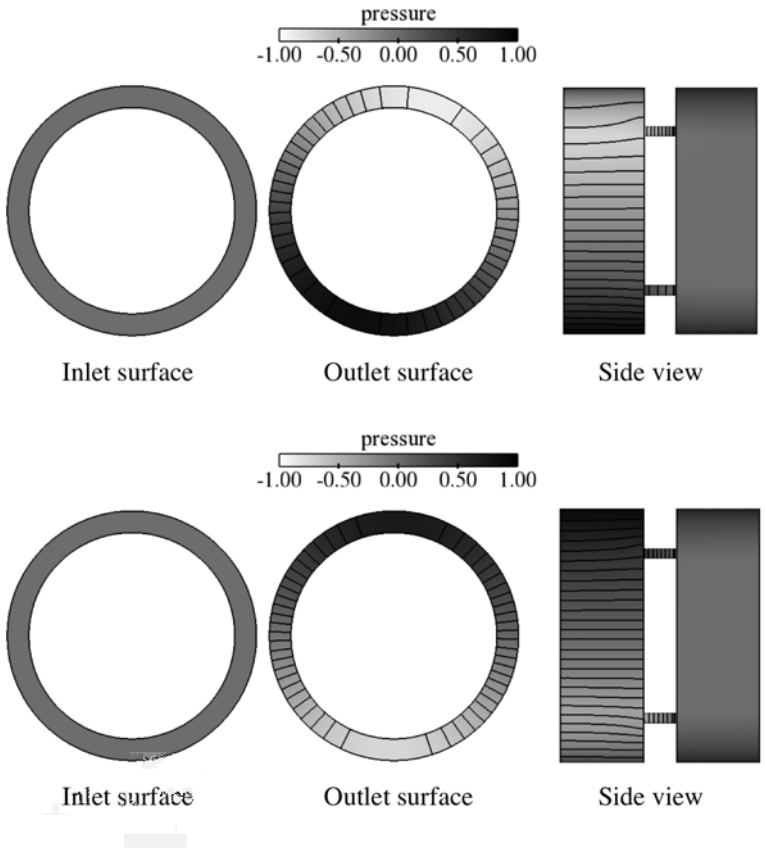


FIGURE 4.47: Structure of mode P1 with no FTF (top: configuration 1, bottom: configuration 2). The color field and lines correspond to $|\hat{p}|\cos[arg(\hat{p})]$.

When adding the flame, the frequency of P1 for configuration 1 and 2 is provided in Tab. 4.9. As Tab. 4.9 shows, the evolution of the real and imaginary parts with configuration 2 matches quite well the result of configuration 1. However, as in the case without flame, the mode structure differs (Fig. 4.49), and exhibits a lower acoustic pressure in the plenum in configuration 2 than in configuration 1.

This is due to the fact that the acoustics of the burners are different in configuration 1 and 2, thus modifying the reference velocity, the unsteady heat release and ultimately the eigenfrequencies. Indeed, the acoustic velocity is not perfectly plane in configuration 1, but is forced to adopt a plane behavior in configuration 2 because of the MBC boundaries.

To illustrate this effect, the modulus of axial and transverse acoustic velocity are plotted along the axis of one burner for the case with flame in Fig. 4.48. The transverse velocities are completely removed upstream of the reference surface (at x= -0.05m) in configuration 2, while they progressively go to zero in configuration 1. The axial acoustic velocity at $x = -0.05$ m that directly rules the unsteady heat release is also impacted and this explains the difference in the imaginary part of the frequency. Overall these modifications of the burner acoustics lead to different mode structures, as seen in Fig. 4.47 and Fig. 4.49.

Despite the small differences in mode structure and frequency, the main objective of this test case, which was to prove the operability of the surface FTF code for multi-burners combustors, is satisfied.

	Real part	**Imaginary part**
Configuration 1	58.3 Hz	1.6 Hz
Configuration 2	58.9 Hz	1.7 Hz
Relative difference	1%	6 %

TABLE 4.9: Complex eigenfrequencies for the first azimuthal mode of the chamber with FTF. The relative difference is normalized using the values of configuration 1.

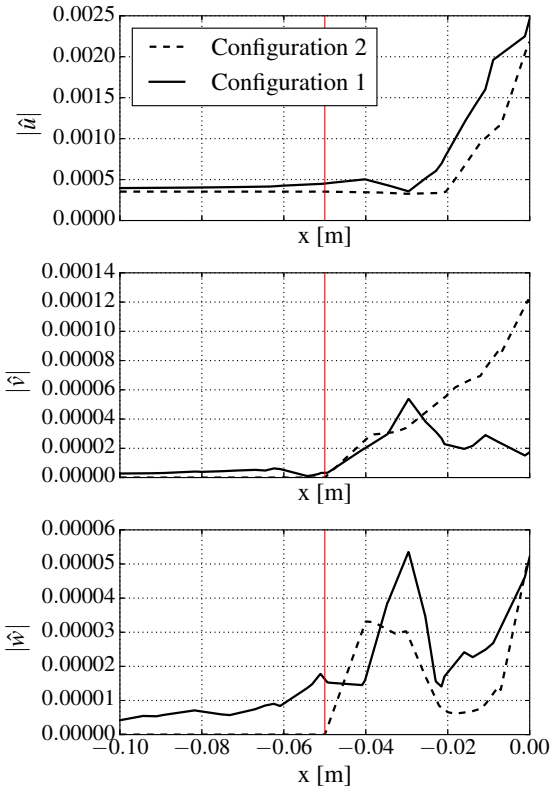


FIGURE 4.48: Modulus of axial and transverse velocity along a burner centerline, close to the reference location (red vertical line) for configuration 1 (solid lines) and configuration 2 (dotted lines).

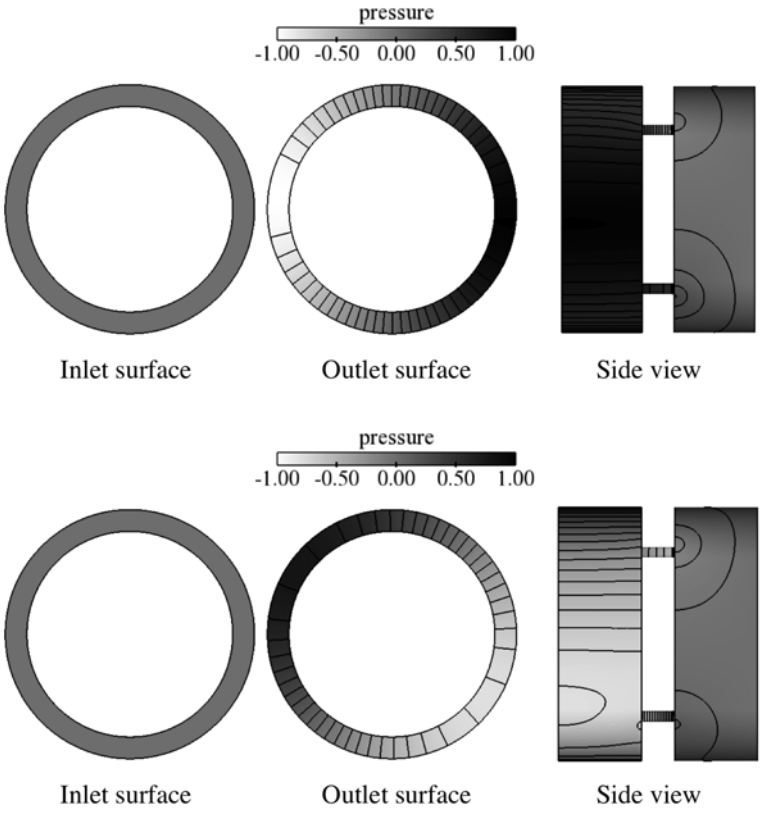


FIGURE 4.49: Structure of mode P1 with point-wise FTF (top) and surface FTF (bottom). The color field and lines correspond to $|\hat{p}|\cos[arg(\hat{p})]$.

Chapter 5

Application of the MBC methodology to an industrial combustor

There are strong presumptions that neglecting the complex flow-acoustic interactions when using a Helmholtz solver at zero Mach number might lead to inaccuracies in terms of acoustic mode structure and frequencies. As explained in Chapter 1, this mechanism should be important for industrial combustors where the mean flow can interact with the acoustics at many places : perforated plates, dilution holes or swirled injector. Up to now, the effects of this interaction have never been assessed in a realistic turbine combustor.

The objective of the present chapter is therefore to evaluate the impact of complex flow-acoustic features in an industrial combustor with the extended Helmholtz MBC methodology presented in Chapter 4. Unfortunately, the amount of experimental or numerical data on the combustor of interest is very limited so the results of the 3D-HMBC methodology on this configuration will need validation in the future.

This chapter is organized as follows. It starts in Section 5.1 with a quick description of the combustor which was chosen, and explains what parts of it will be modeled with the matrix approach and how. From then on, 3D-HMBC computations are performed by adding progressively the perforated plates (Section 5.3), dilution holes (Section 5.4), swirled injectors (Section 5.5) and finally surface-based Flame Transfer Functions (Section 5.6). Finally, an energy balance analysis is performed in order to better understand the contribution of complex flow elements (Section 5.7).

5.1 Description of the configuration of interest

5.1.1 Geometry

The case considered in this study is an annular combustor developed by the SAFRAN group for aero-engine applications (Fig. 5.1). The combustor is composed of X identical sectors[1], with X a confidential number. The design is quite typical of SAFRAN combustors (Fig. 5.2). The air flows from the compressor and is slowed down at the inlet of the combustor by a diffuser. Inside the combustor, the air separates into two streams. The primary air flow is mixed to kerosene and injected

[1]This is not exact. In fact, igniters are placed on some sectors, but not all, thus breaking the sector periodicity. These igniters are neglected here.

thanks to a swirler into the flame tube, where combustion takes place. The exhaust gas then go through a high pressure distributor and proceed to the high pressure turbine stages. In the LES simulations performed by SAFRAN, the high pressure distributor at the chamber outlet is modelled as a simple converging nozzle (Fig. 5.2). The combustion zone is encased by liners, where secondary air at the temperature of the combustor inlet is injected through perforated plates and dilution holes to cool the walls and control the size of the flame.

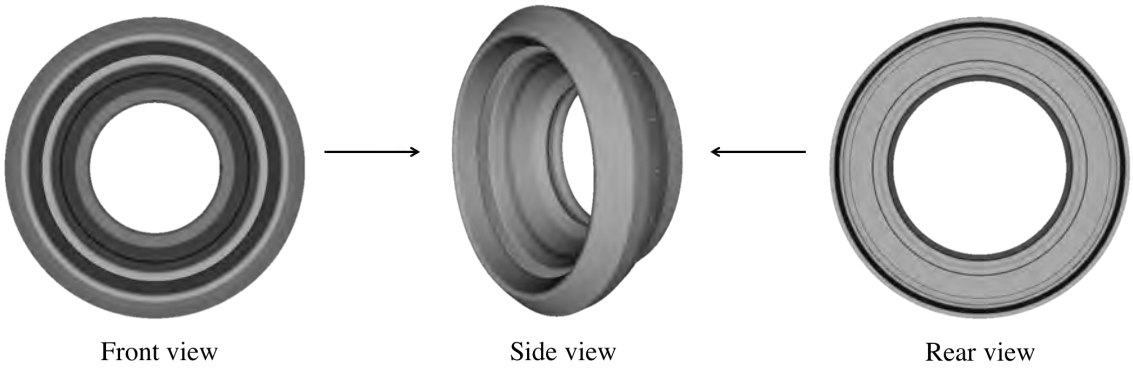


FIGURE 5.1: Annular combustor of interest. Front (left), side (middle) and rear (right) views.

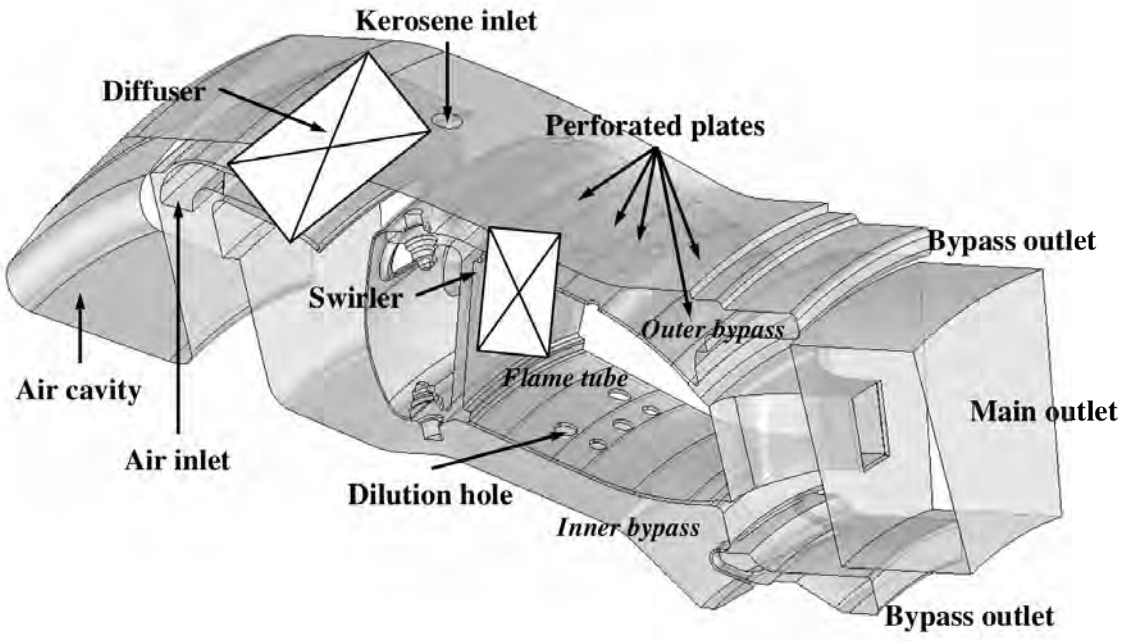


FIGURE 5.2: Design of the combustor of interest. The high-pressure distributor is replaced by a converging nozzle. For confidentiality reasons, this image is rescaled and some geometrical details are hidden.

5.1.2 Mode of interest

Two main instabilities were observed experimentally on the SAFRAN combustor, both with frequencies around 300 Hz. By measuring the phase of the pressure fluctuations for different azimuthal angles, it was determined that one mode is longitudinal while the other one is azimuthal.

On this combustor, Large Eddy Simulations of the complete annular geometry are also available and exhibit the same two instabilities, with again frequencies close to 300 Hz. While the nature of the longitudinal mode is not very clear and could be related to the conversion of entropy into acoustics in the high-pressure turbine stage, the azimuthal mode is a very classic acoustic mode and the mode of interest in this study.

In azimuthal instabilities, it has been shown in previous studies [24] that the main mechanism for heat release fluctuations is often associated to longitudinal velocity fluctuations through the fluctuations of mass flow rate. The transverse fluctuations of the flame, although impressive-looking have an overall small contribution to the unsteady heat release.

In order to minimize the CPU cost, the flame dynamics are therefore examined in an LES of a single sector of the combustor, excited by the longitudinal instability. This instability triggers itself after the flow is established in the domain, and is visible in the Fourier spectra of the heat release and velocity signals (Fig. 5.3).

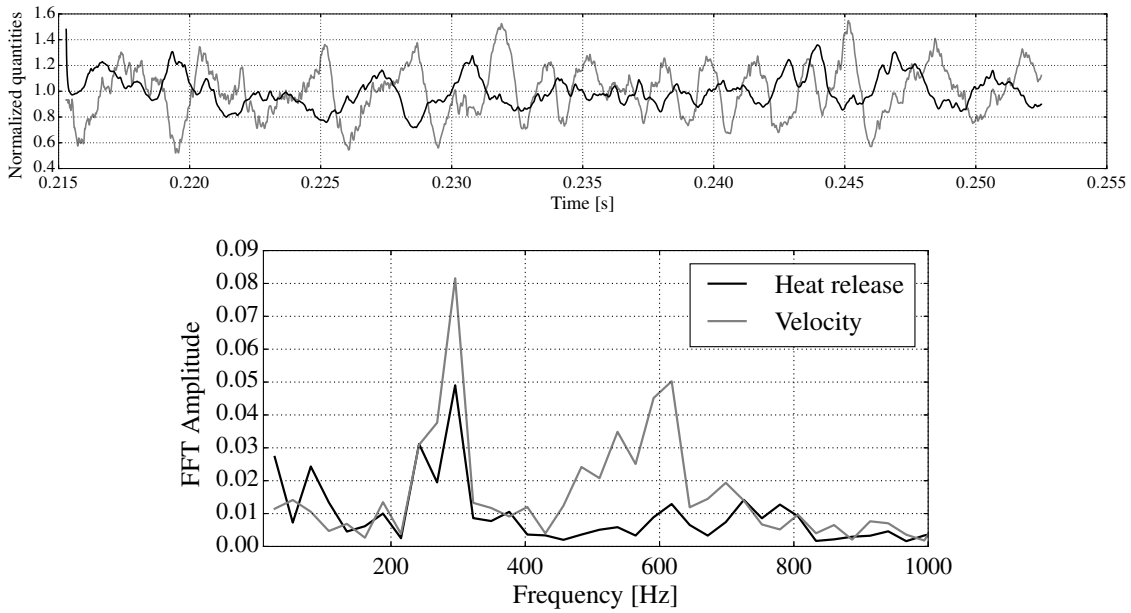
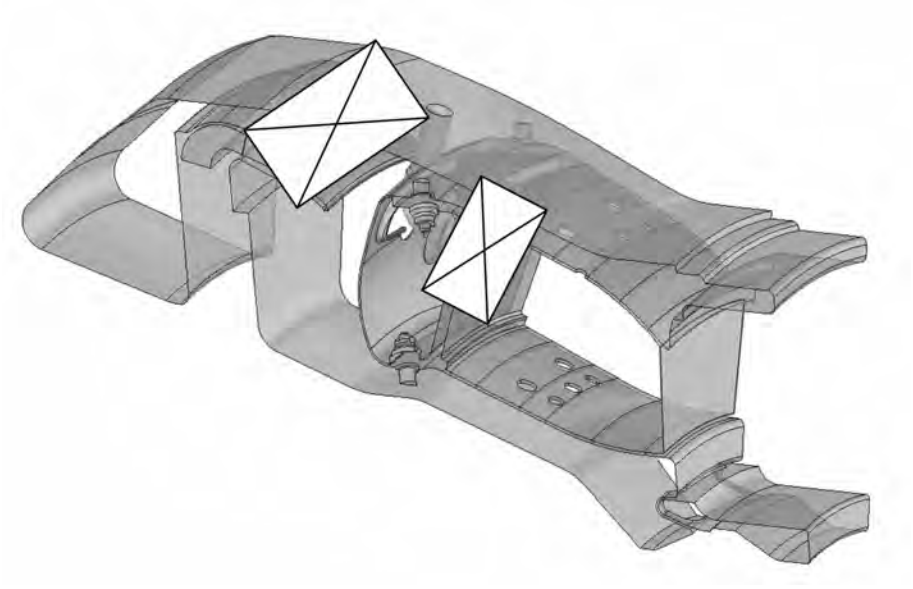


FIGURE 5.3: Top: Time samples of the global heat release (black) and velocity in the injector (grey) from a mono-sector reactive LES. Both signals are normalized by their time average. Bottom: FFT amplitudes of the normalized heat release (black) and velocity (grey). The amplitude corresponding to 0 Hz was removed to improve clarity.

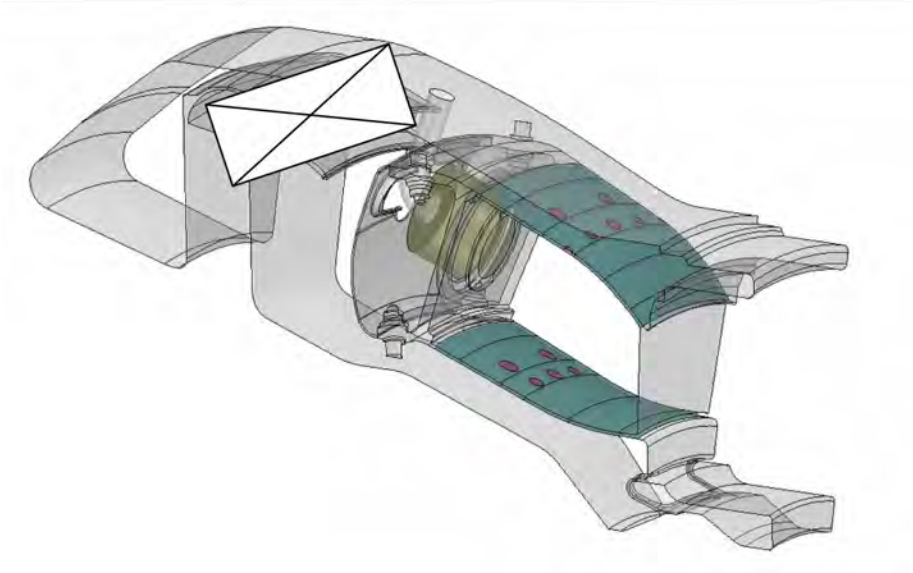
5.2 Helmholtz computations

The first azimuthal mode can be retrieved with a standard Helmholtz representation where the interaction of dilution holes and swirler with the mean flow is neglected and unsteady heat release is modelled with a point-based Flame Transfer Function (Fig. 5.4a). The configuration is truncated downstream at $M \approx 0.3$. In a first configuration, the complete geometry is represented and fixed-velocity boundary conditions are set on all patches. This very simplified representation is often used in industry, in order to get a first idea of the combustor acoustics.

This simplified representation will be compared with one where the dilution holes and swirler are replaced by their equivalent matrix and perforated plates are modeled with a homogeneous dissipative boundary (Fig. 5.4b). The matrix data for the dilution holes is obtained from models, while it is extracted from LES computations for the swirler. In the latter case, the element of interest is isolated in a tube configuration, with approximately the same confinement as in the combustion chamber, with non reactive air flowing at the same mass flow rate. The non reactive assumption is strong but it greatly simplifies the problem.



(A) Standard



(B) 3D-HMBC. The swirler and dilution holes are modeled with a matrix approach, applied on the yellow and red surfaces respectively. The perforated plates, in blue, are represented by a homogeneous boundary condition based on Howe's model.

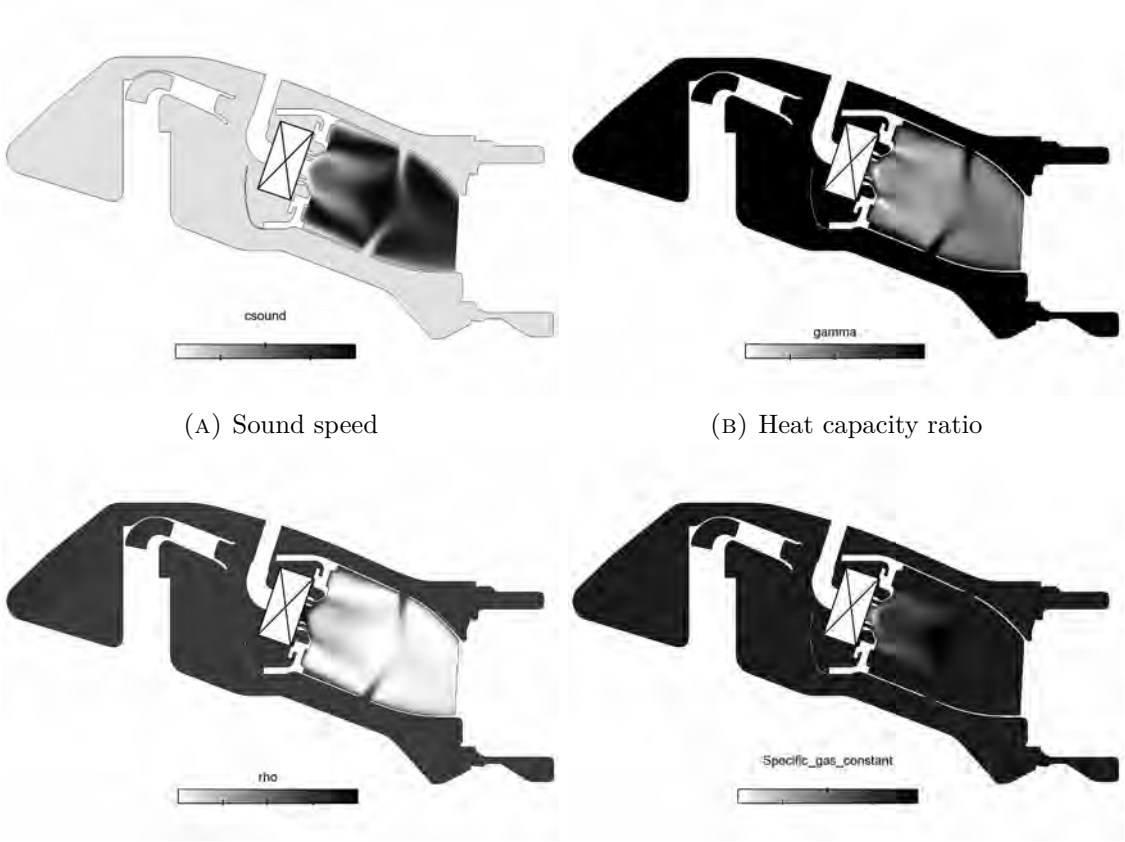
FIGURE 5.4: Standard and HMBC geometries for the Helmholtz computations.

In the following sections, the perforated plates, dilution holes, swirler and surface-based Flame Transfer Function will be progressively included in the Helmholtz computation (Tab. 5.1). These Helmholtz computations all rely on the average mean flow fields presented in Fig. 5.5 that were extracted from the reactive LES of a single sector with periodic boundaries, performed by Safran. For confidentiality reasons, the minimum (white) and maximum (black) of the scales are not displayed.

Run name	**Perforated plate model**	**Dilution holes model**	**Swirled injector model**	**Flame representation**
R0	Zero normal velocity	Resolved	Resolved	No unsteady flame
R1	Uniform model of Howe, Eq. (D.6)	Resolved	Resolved	No unsteady flame
R2	Uniform model of Howe, Eq. (D.6)	Modified Bellucci model at orifice cross-sections, Eqs. (4.14)-(4.15)	Resolved	No unsteady flame
R3	Uniform model of Howe, Eq. (D.6)	Modified Bellucci model at orifice cross-sections, Eqs. (4.14)-(4.15)	Active matrix (from LES) on complex MBC surfaces	No unsteady flame
R4	Zero normal velocity	Resolved	Passive matrix (from AVSP-f) on complex MBC surfaces	Point-based and surface-based FTF
R5	Uniform model of Howe, Eq. (D.6)	Modified Bellucci model at orifice cross-sections, Eqs. (4.14)-(4.15)	Active matrix (from LES) on complex MBC surfaces	Surface-based FTF
R6	Uniform model of Howe, Eq. (D.6)	Modified Bellucci model at orifice cross-sections, Eqs. (4.14)-(4.15)	Resolved	Point-based FTF

TABLE 5.1: Helmholtz computations performed on the industrial setup and their characteristics. Elements can be either "resolved" elements, i.e. discretized in the geometry and computed by the Helmholtz solver, or modeled with a matrix model. For the swirler, two matrices are measured: a "passive" one, representing the acoustic behaviour in the absence of mean flow and viscosity, and an "active" one, containing the flow-acoustic interaction.

A baseline Helmholtz computation is performed, with the mean flow fields of Fig. 5.5, wall boundary conditions everywhere and no unsteady heat release (R0). Two degenerated azimuthal modes at $f \approx 293$ Hz are found by the Helmholtz solver. The two modes are normal and feature a similar azimuthal structure displayed in Fig. 5.6. One can be obtained from the other with a rotation of $\pi/2$ around the combustor axis.



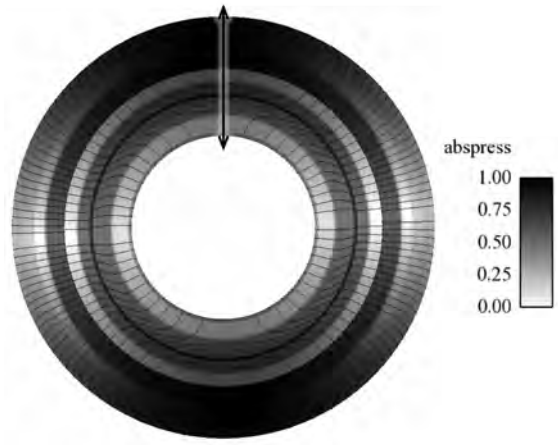
(A) Sound speed

(B) Heat capacity ratio

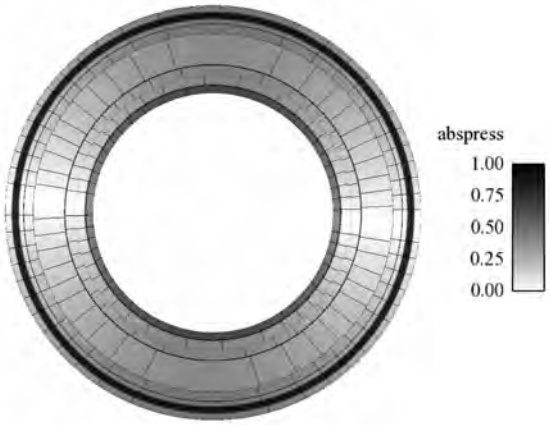
(C) Density

(D) Ideal gas constant

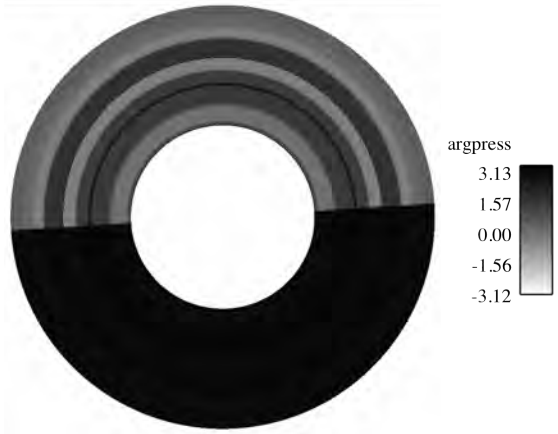
FIGURE 5.5: Mean flow fields for the Helmholtz computations of the industrial combustor.



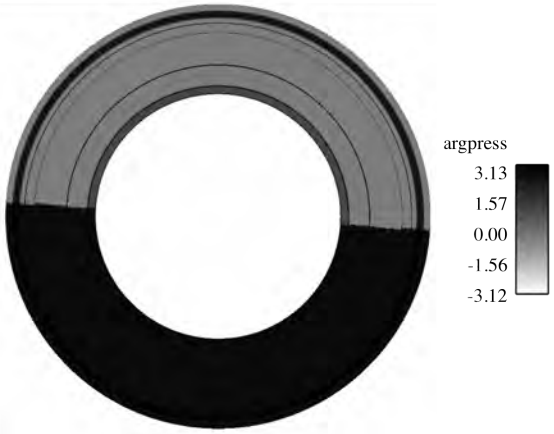
(A) Modulus of pressure - Front.



(B) Modulus of pressure - Back.



(C) Phase of pressure - Front.



(D) Phase of pressure - Back.



(E) Modulus of pressure in a transverse cut (indicated on Fig. 5.6a).

FIGURE 5.6: First azimuthal mode at $f = 292.7 - 0.0i$ Hz for R0.

5.3 Multiperforated plates

The combustor liners are composed of multiperforated plates. An example is visible on the helicopter chamber of Fig. 4.33. Originally, the perforated plates have a cooling purpose: cold air is blown through the tiny holes and form a protective film on the liner. However, as already mentioned, these plates also have an impact on the acoustics of the combustor, that can be accounted for with a homogeneous boundary condition based on Howe's model, with a correction for the plate thickness [111, 112, 43].

This model, described in Appendix D.1, assumes that all orifices have a circular cross-section, an axis normal to the plate, and are evenly distributed. It requires the knowledge of four quantities (see Fig. D.1):

- The radius of the perforates a.
- The average distance between perforations d.
- The bias flow velocity through the perforations U_{ori}.
- The thickness of the plate h.

If the average distance between perforations d and the bias flow velocity U_{ori} are not directly available, they can be retrieved from

- the mass flow rate across the plate $\dot{m}$,
- the porosity σ, defined as the ratio between the perforated surface and the total surface of the plate,
- the sum of the cross-sections of all perforates $S_b = N\pi a^2$ with N the number of perforates.

In addition, perforations in industrial combustors are not normal to the plate. They are characterized by two angles : a streamwise angle α_1 and a compound angle α_2 (Fig. 5.7). The streamwise angle introduces a tilt compared to the plate normal but no azimuthal component with respect to the axis of the motor $\mathbf{t_1}$ (i.e. gyration). The azimuthal component is controlled by the compound angle. The projection of the perforate axis $\mathbf{m}$ and the plate normal $\mathbf{n}$ is:

$$\mathbf{m} \cdot \mathbf{n} = \cos(\alpha_1)\cos(\alpha_2) \tag{5.1}$$

And the angle α between $\mathbf{n}$ and $\mathbf{m}$ can be defined as :

$$\alpha = \cos^{-1}(\cos(\alpha_1)\cos(\alpha_2)) \tag{5.2}$$

If N is the number of perforations, the total perforated surface S_{perf} is therefore not equal to the sum of the cross-sections $S_b = N\pi a^2$ anymore (Fig. 5.8). The two are related by:

$$S_{perf} = \frac{S_b}{\cos(\alpha)} \tag{5.3}$$

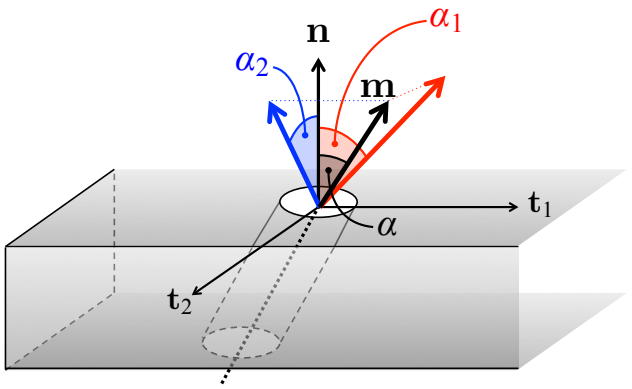


FIGURE 5.7: A tilted perforation, with a streamwise angle α_1 and a compound angle α_2.

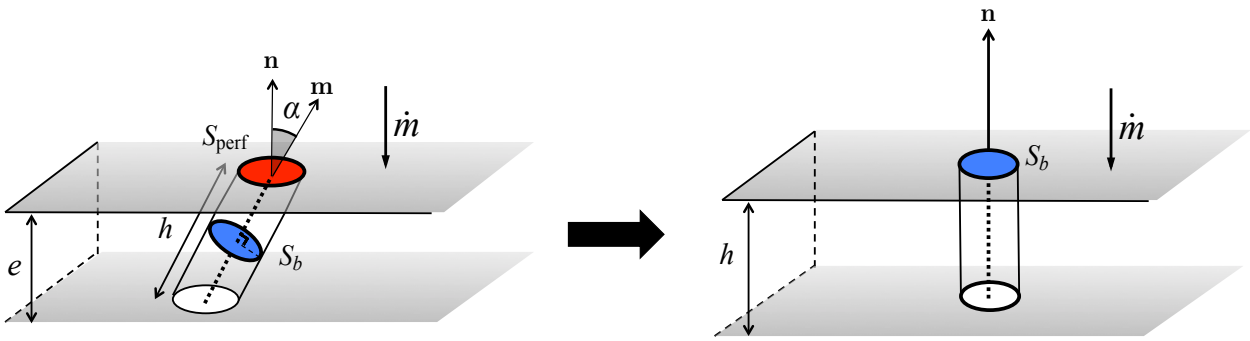


FIGURE 5.8: Straightened perforate used for the analysis of perforated plates

If the density of the flow is assumed constant in the orifice and equal to its upstream value ρ_{up}, the bias flow velocity U_{ori} is given by :

$$U_{ori} = \frac{\dot{m}\cos(\alpha)}{\rho_{up} S_{perf}} = \frac{\dot{m}}{\rho_{up} S_b} \tag{5.4}$$

The upstream density is measured from an average solution of a reactive LES of the combustor.

The average distance between apertures can be derived from the porosity, aperture angle and aperture radius as:

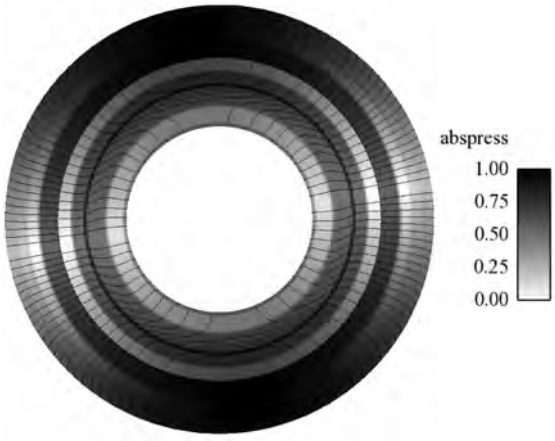
$$d = \sqrt{\frac{S_{tot}\pi a^2}{S_b}} = \sqrt{\frac{\pi a^2 \cos(\alpha)}{\sigma}} \tag{5.5}$$

Finally, the plate thickness is recovered by considering the straightened orifices of Fig. 5.8. The flow is assumed to travel a distance h equal to the length of the longest cylinder fitting in the perforation. If e is the thickness of the plate, then

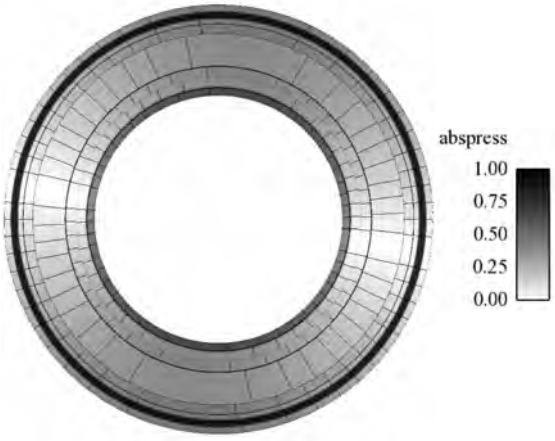
$$h = \frac{e}{\cos(\alpha)} - \frac{4a}{\tan(\alpha)} \tag{5.6}$$

The inner and outer liners of the combustor are divided into 10 zones characterized by constant plate properties (Fig. 5.4b). For confidentiality reasons, these parameters are not provided here. For all the plates however, the Strouhal number for the first azimuthal mode is close to 0.01, so the damping effect is expected to be small.

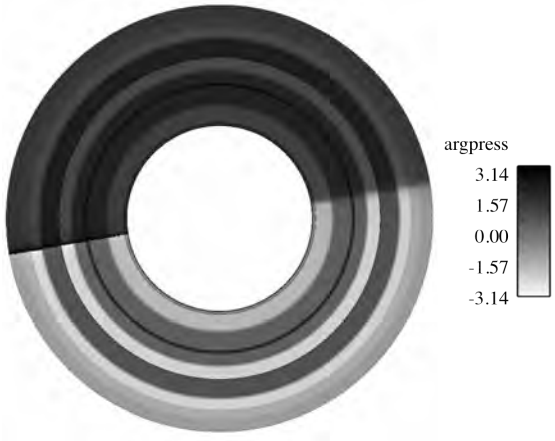
This is indeed what is observed on the solution of the Helmholtz computation with perforated plate boundaries (R1). The mode structure (Fig. 5.9) is nearly identical to R0 and the frequency, found at $293.0 - 0.90i$ Hz is also very close to the one of mode 0. The main effect of the perforated plates is to introduce a small damping rate.



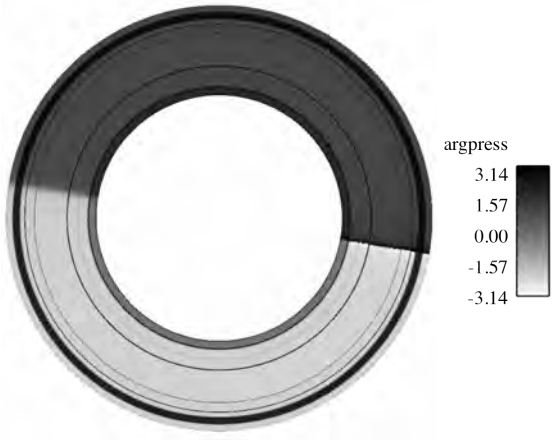
(A) Modulus of pressure - Front.



(B) Modulus of pressure - Back.



(C) Phase of pressure - Front.



(D) Phase of pressure - Back.



(E) Modulus of pressure in a transverse cut (indicated on Fig. 5.9a).

FIGURE 5.9: First azimuthal mode at $f = 293.0 - 0.90i$ Hz for R1.

5.4 Dilution holes

Eleven dilution holes per sector are drilled in the liners of the combustor of interest (Fig. 5.4b). In order to account for hydro-acoustic interaction at their location, a new mesh is considered.The geometry of Fig. 5.4a is modified: the side walls of the dilution holes are removed and the upstream and downstream sections of the holes are filled in order to apply the Matrix Boundary Condition. This new geometry is meshed with an identical mesh size to R0 and R1, but with a fixed resolution of $\eta = 0.2$ at dilution holes, thanks to spherical sources slightly bigger than the holes.

RUN	Dilution hole model
R2a	Modified Bellucci model ($\sigma = 0.0$)
R2b	Modified Bellucci model ($\sigma = 0.1$)
R2c	Modified Bellucci model ($\sigma = 0.5$)
R2d	Propagation over length e

TABLE 5.2: List of R2x computations.

The quantity η was defined in Chapter 4 as the ratio between the mesh size and the orifice radius.

The matrix data is obtained from the modified Bellucci model of Section 4.4.3. As for Howe's model, the radius of the dilution holes, the bias flow velocity through them and the length (thickness) of the hole are required and are retrieved in the same way as for perforated plates. This time, the dilution hole is perforated normal to the plate (to check) so that $\alpha_1 = \alpha_2 = 0$. Two additional quantities must be provided : the mesh resolution at the orifice η, and the confinement / porosity ratio σ.

As explained in Sec. 4.4.3, the exact value of σ is not well-defined. Three computations are performed with $\sigma = 0$, $\sigma = 0.1$ and $\sigma = 0.5$ for all dilution holes. In reality, different values of σ should be used for each dilution hole. But these three computations are a first step to check the impact of σ on the acoustics of an annular chamber.

Additionally, a fourth computation is run with a 1D propagation matrix over e the thickness of the plate (represented on the left side of Fig. 5.8), in order to control that the change of mesh and geometry has only a minor effect on the combustor acoustics. In this run, the matrix associated to the modified Bellucci model is replaced by:

$$\begin{pmatrix} \cos(ke) & i\sin(ke) \\ i\sin(ke) & \cos(ke) \end{pmatrix} \tag{5.7}$$

with k the wavenumber. Matrix (5.7) describes the propagation of acoustics in the resolved holes, and the associated run is expected to provide results similar to R1. The characteristics of these four runs, named R2a, R2b, R2c and R2d are summarized in Tab. 5.2.

The density and speed of sound are different upstream and downstream of the dilution holes (Fig. 5.10). In all the R2 runs, this is treated by assuming that the density and speed of sound are constant, equal to their upstream value over the whole length of the hole. The cold hole is then followed by a compact temperature jump. If $\mathbb{T}_{\text{cold}}$ is the matrix of the cold hole, then the final matrix applied in the Helmholtz computation $\mathbb{T}$ is:

$$\mathbb{T} = \begin{pmatrix} 1 & 0 \\ 0 & \frac{\rho_{o,d} c_{o,d}}{\rho_{o,u} c_{o,u}} \end{pmatrix} \mathbb{T}_{\text{cold}} \tag{5.8}$$

with $\rho_{o,u}, \rho_{o,d}$ the densities up- and downstream, $c_{o,u}, c_{o,d}$ the speeds of sound up- and downstream of the hole. The values of $\mathbb{T}$ for R2a to R2d are plotted in Fig. 5.11 for one dilution hole. As for the perforated plates, the parameters of the dilution

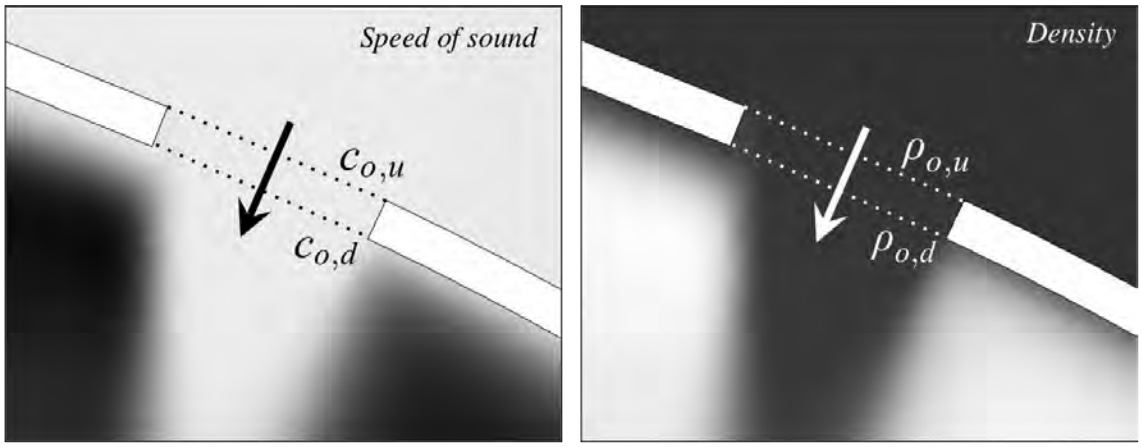


FIGURE 5.10: Density and speed of sound in the transverse cut of a dilution hole (from an average LES solution). The color scale is the same as in Fig. 5.5.

holes cannot be provided for confidentiality reasons. For the geometry and operating point of interest, they correspond to a Strouhal number of $St \approx 0.1$.

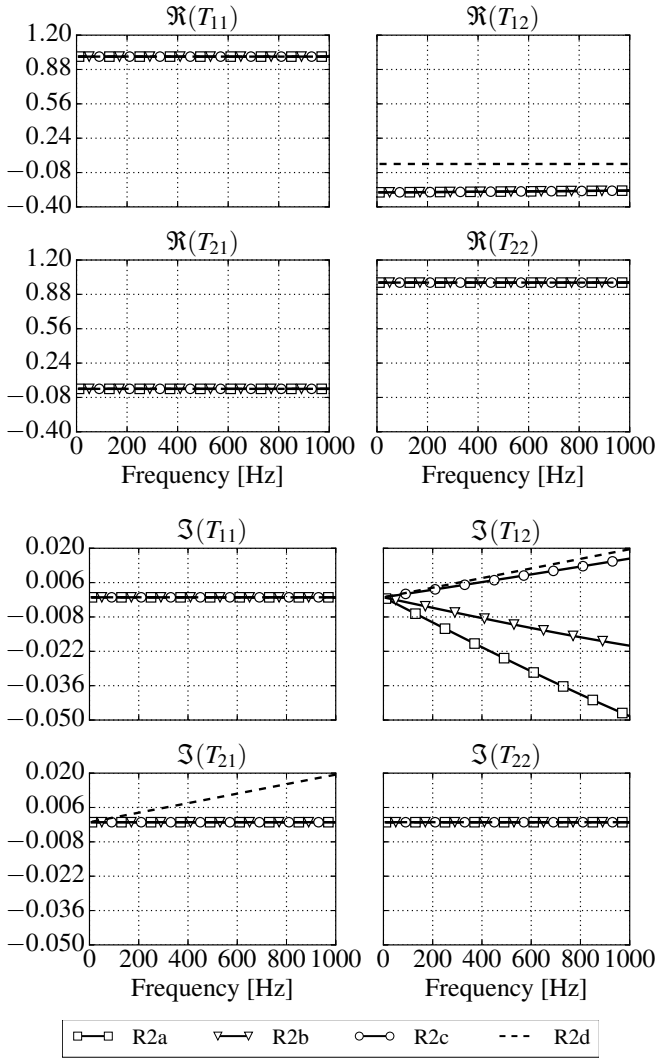
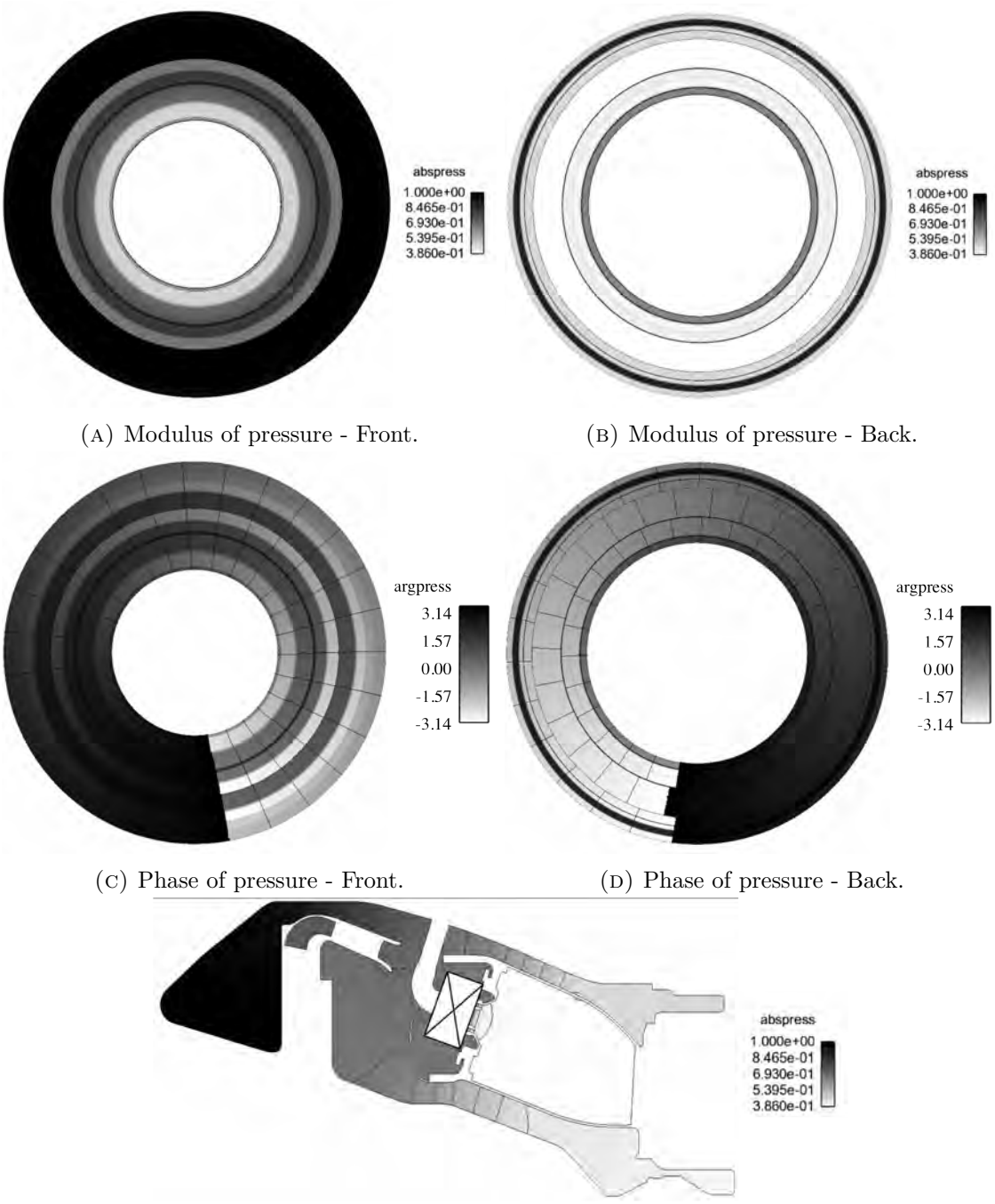


FIGURE 5.11: Matrix of one dilution hole in R2a, R2b, R2c and R2d.

The azimuthal mode of R2d is examined first (Fig. 5.12). With the new dilution hole geometry, the Helmholtz solver finds a pair of rotating modes, instead of standing modes as in R0 and R1. Indeed, the module of the pressure is constant Fig. 5.12 while the phase varies azimuthally. This is not a problem as standing modes and rotating modes can be obtained from one another with simple linear combinations. The structure in one transverse section seems similar to the one found in R0 and R1, with higher pressure amplitudes in the cavity, intermediate values in the bypass, and a minimum in the flame tube. The frequency, $f = 292.5 - 1.01i$ Hz is very close to the value found in R1.



(A) Modulus of pressure - Front.

(B) Modulus of pressure - Back.

(C) Phase of pressure - Front.

(D) Phase of pressure - Back.

(E) Modulus of pressure in a transverse cut (indicated on Fig. 5.9a).

FIGURE 5.12: First azimuthal mode at $f = 292.5 - 1.01i$ Hz for R1.

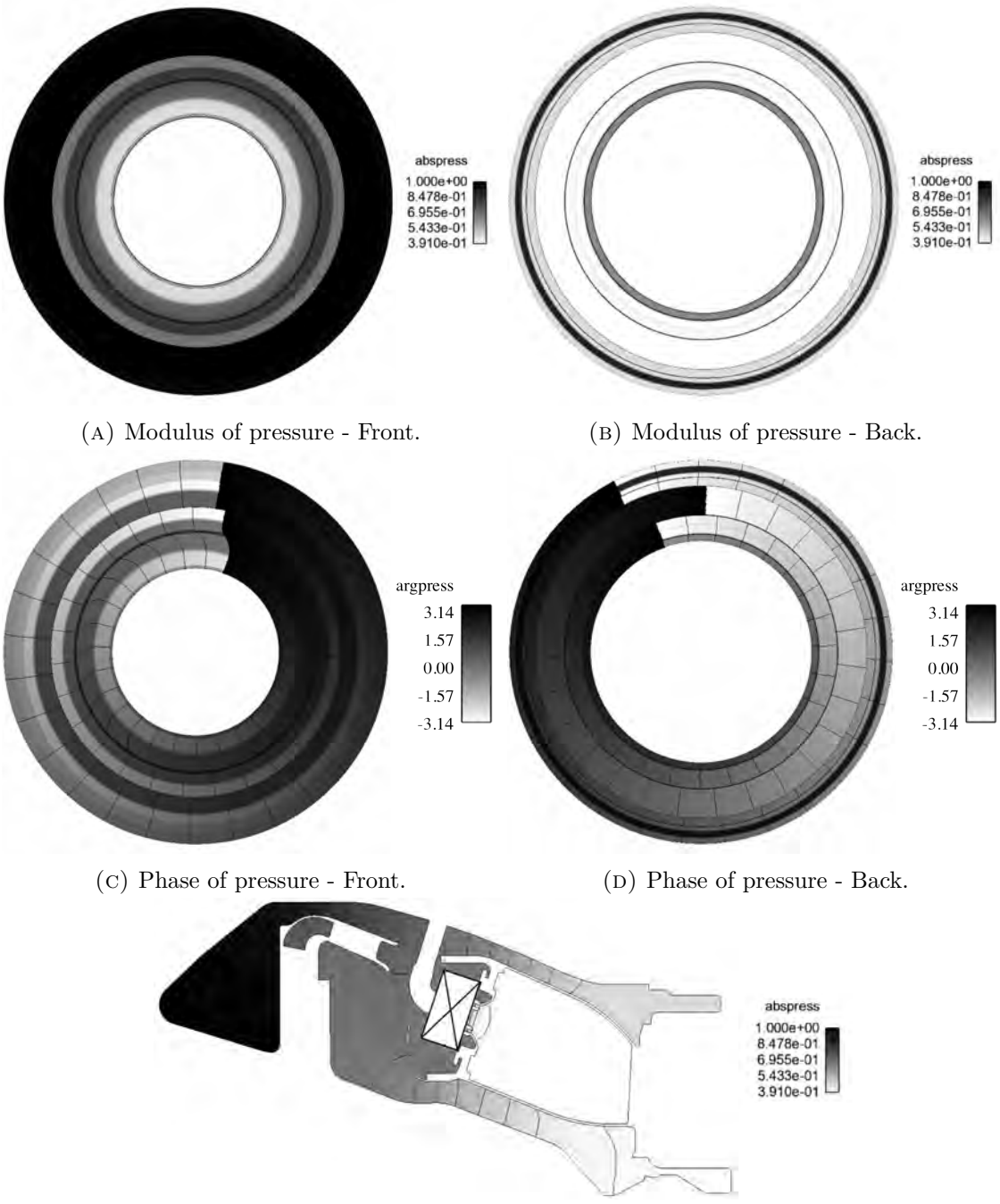
RUN	First azimuthal mode frequency [Hz]
R2a	291.7 - 9.83i
R2b	291.6 - 9.78i
R2c	291.6 - 9.72i
R2d	292.5 - 1.01i
R1	293.0 - 0.90i

TABLE 5.3: Frequencies of the first azimuthal mode for R2x computations. The result of R1 is also recalled.

When introducing the modified Bellucci model, an immediate change is visible in the frequencies of R2a, R2b and R2c (Tab. 5.3). With this model, the dilution holes have a strong damping effect on the first azimuthal mode and the damping rate goes from 1 s^{-1} in R2d to $\approx$ 10 s^{-1} in R2a, R2b and R2c. Interestingly, the value of σ does not change much the frequency result, and this is also the case for the mode structure. Hence, only the solution of R2a is plotted in Fig. 5.13. Compared to R2d, an azimuthal phase delay appears between the bypass sections and the flame tube when introducing the modified Bellucci model. In a transverse cut however, the pressure amplitudes are almost identical to R2d.

The R2x computations show that including the interaction between acoustics and mean flow at dilution holes is important for the prediction of combustion instabilities. Indeed it can greatly modify the damping rate and to some extent, the structure of the combustor modes. The effect could be even more important for other geometries and operating points where the Strouhal number is closer to 1 (since maximum dissipation is observed for orifices at this value). In the configuration studied here, the Strouhal number is only of 0.1 but the impact on the Helmholtz solution is already sensible.

At first order, the confinement parameter of each orifice can be set very loosely as no major difference was observed for $\sigma = 0, 0.1$ and 0.5 for this case. In the following Helmholtz computations, σ will be set to 0. As explained in Section 4.4.3, this conclusion might not hold when the Strouhal number gets closer to 1 and new tests should be performed in this case.



(A) Modulus of pressure - Front.

(B) Modulus of pressure - Back.

(C) Phase of pressure - Front.

(D) Phase of pressure - Back.

(E) Modulus of pressure in a transverse cut (indicated on Fig. 5.9a).

FIGURE 5.13: First azimuthal mode at $f = 291.7 - 9.83i$ Hz for R2a.

5.5 Swirler

5.5.1 LES computation of the swirler matrix

Unlike dilution holes, swirled injectors feature complex interactions between flow and acoustics. These interactions can be accounted for by measuring the equivalent matrix of the swirler, with the same methodology as in Chapter 3. One major difference with Chapter 3 however is that the flow is reactive in the final Helmholtz

computation. Ideally, the swirler matrix should therefore be computed in a similar reactive flow, but this would defeat the purpose of the modular 3D-HMBC approach.

To keep the modularity, it is assumed that the swirler matrix is identical for the reactive and the non reactive flow. This is a strong assumption but it greatly simplifies the problem. One possible justification is the following: as for orifices, hydro-acoustic coupling should be located in a very small area close to the outlet of the swirler vanes. At this location, the flow is not fully heated by the flame and the temperature remains close to its value at the inlet.

It is also assumed that the effect of confinement on the swirler matrix is marginal and the matrix is measured in a parallelepipedic box of approximately the same size as one sector of the chamber (Fig. 5.14). The associated mesh is shown in Fig. 5.15.

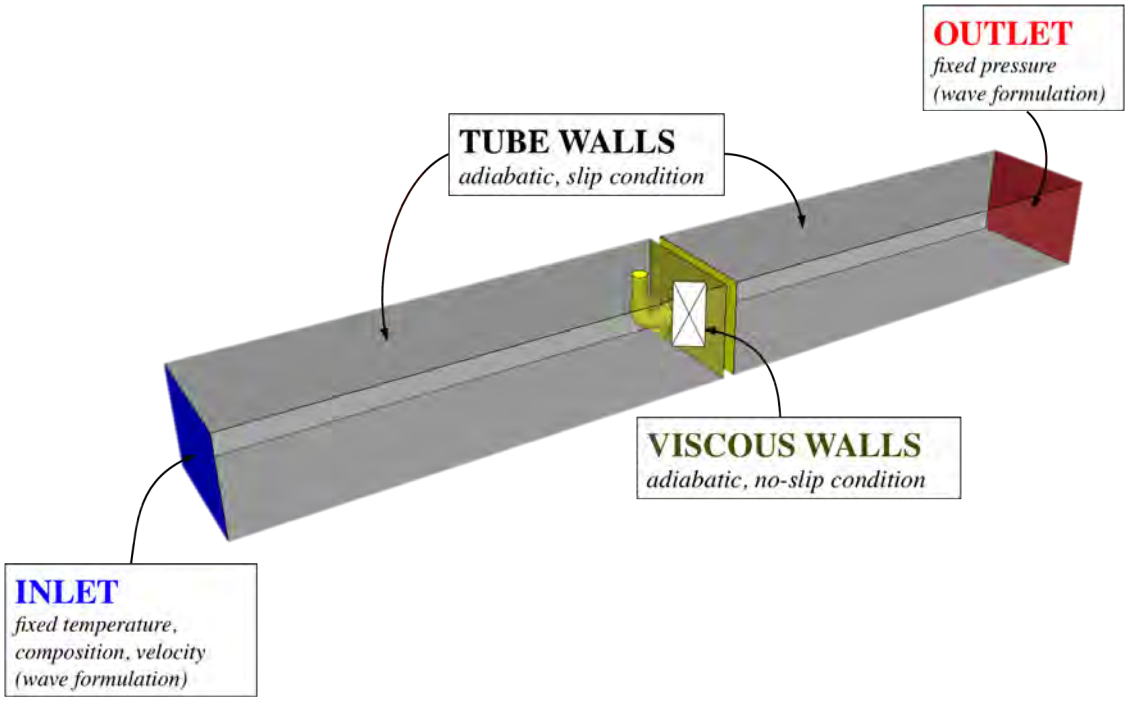


FIGURE 5.14: Geometry and boundary conditions for the LES computation of the industrial swirler matrix.

The length of the tube is arbitrary and chosen long enough to have plane acoustics at the frequency of interest. The cross-section dimensions are set as the average of the lengths displayed in Fig. 5.16, but not given here for confidentiality reasons. The difference in confinement is not expected to have a strong impact on the final matrix, especially after adjusting it to fit the MBC surfaces of Fig. 5.21.

The boundary conditions are indicated on Fig. 5.14. Adherence is imposed on all swirler walls, while slip conditions are set on the tube walls to prevent acoustic losses in the boundary layer there. No wall law is used and the mesh refinement leads to maximum y^+ values of 60 at the swirler outlet. At the inlet, air is injected at the temperature of the combustor inlet. The mass flow rate going through the swirler is determined from a Safran 1D tool that computes the distribution of the flow in the different elements of the combustor, based on the Bernoulli equation with discharge coefficients obtained from correlations. At the outlet, the pressure is set equal to the average pressure in a plane downstream of the swirler in the reactive combustor

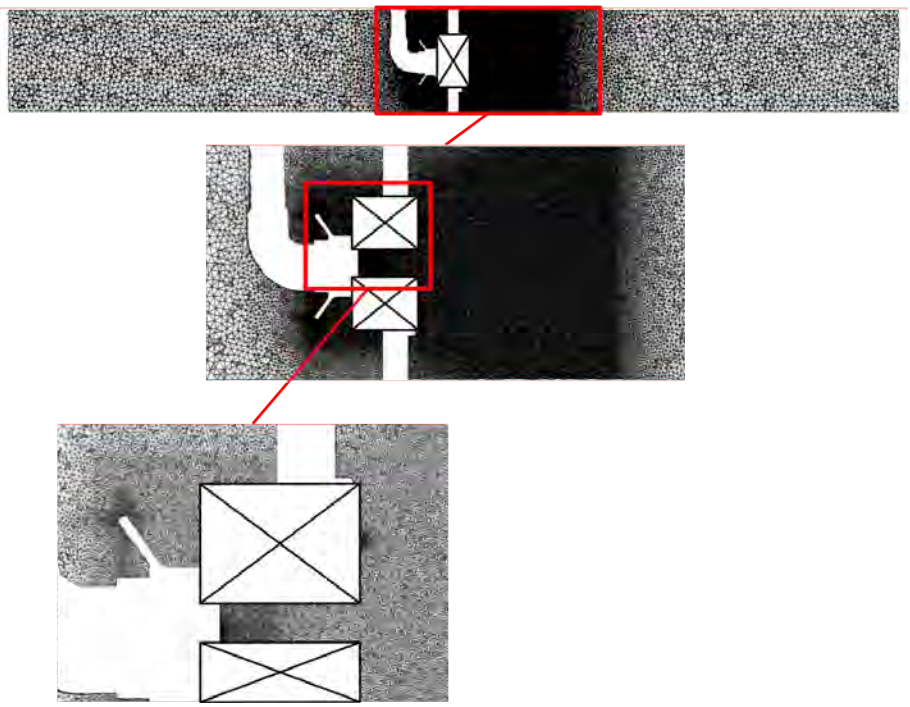
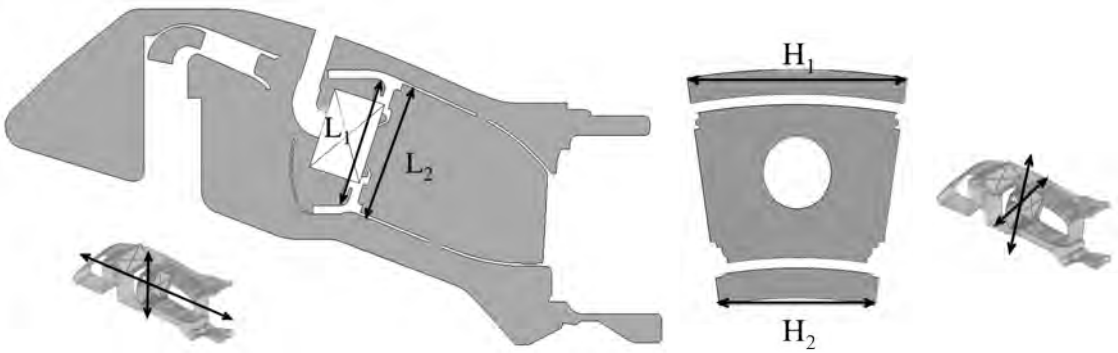


FIGURE 5.15: Overview of the mesh for the LES of the swirler in a tube (12 millions of nodes).



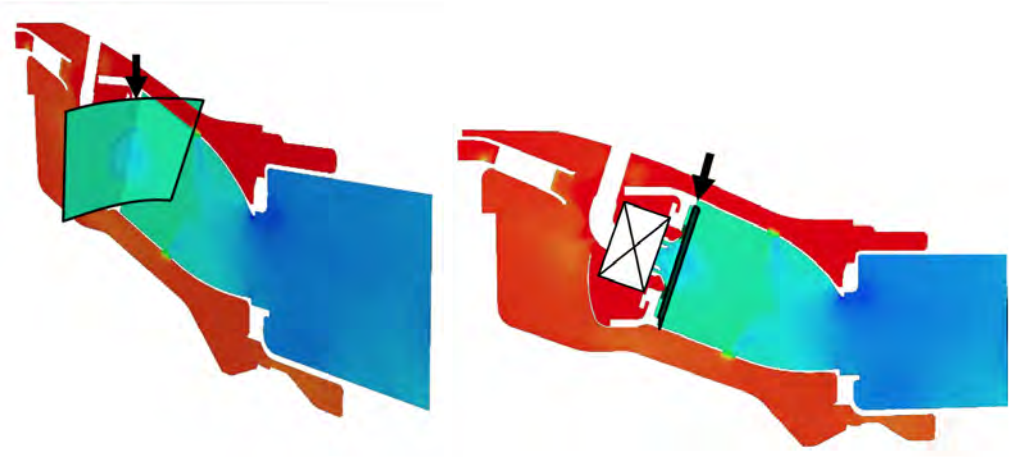
(A) Width L (B) Height H

FIGURE 5.16: Lengths used to define the size of the tube cross-section in Fig. 5.14.The combustor miniatures indicate the location of the cut. In each cut, the average of the two lengths displayed is used to define the matrix configuration.

LES (Fig. 5.17). Since slip conditions are enforced on the tube walls, the pressure downstream of the swirler should be close to the pressure at the outlet.

The LES is performed with the Two-step Taylor Galerkin C (TTGC) scheme developed by [162], which is third order accurate in time and space. The sigma model developed by [149] is used for the subgrid stress tensor. A first computation is run without acoustic forcing in order to establish the flow displayed in Fig. 5.18.

When the stationary flow is well established, acoustic forcing is introduced in two ways : by the inlet or by the outlet. In both cases, the acoustic forcing is monochromatic at the frequency of 290 Hz. When pulsating by the inlet, a velocity fluctuation u' of 20% the value of the average inlet velocity is introduced. When pulsating by the



(A) View 1 (B) View 2

FIGURE 5.17: Reference plane from which the target pressure at the outlet of Fig. 5.14 is extracted. The color scale corresponds to the pressure field (blue : low, red : high).

	Value	**Uncertainty**
t_u	0.145-0.014i	0.008
r_d	0.732-0.066i	0.004
r_u	0.929-0.220i	0.008
t_d	0.113+0.027i	0.005
λ_{min}	-0.028	0.012
λ_{max}	0.542	0.004

TABLE 5.4: Scattering matrix coefficients and eigenvalues of $\mathbb{I} - \mathbf{S}\dagger\mathbf{S}$ of the swirler of the industrial configuration at 290 Hz. The notation is the same as for Tab. 3.3.

outlet, a pressure fluctuation is imposed instead, with an amplitude of $p' = \rho_o c_o u'$. As in Chapter 3, Dynamic Mode Decomposition is used to filter the signals at the forcing frequency.

Fig. 5.19 show some examples of pressure and velocity signals up- and downstream of the swirler, for the two computations. For the computation excited at the outlet, all signals are amplified because the outlet is too reflecting. Decreasing the value of the relaxation parameter destroys this amplification but this was performed too late to obtain enough signal for the DMD analysis. The amplified signals are used instead even though this is not optimal.

The two-source method of Section 3.3.2 is applied to recover the matrix data, using pressure and velocity probes regularly arranged along the tube walls. The plane-wave fit along the axis of the configuration is displayed in Fig. 5.20. The industrial swirler matrix coefficients at 290 Hz are provided in Tab. 5.4, as well as the eigenvalues of $\mathbb{I} - S\dagger S$. These eigenvalues show that the swirler has an almost completely damping effect at 290 Hz.

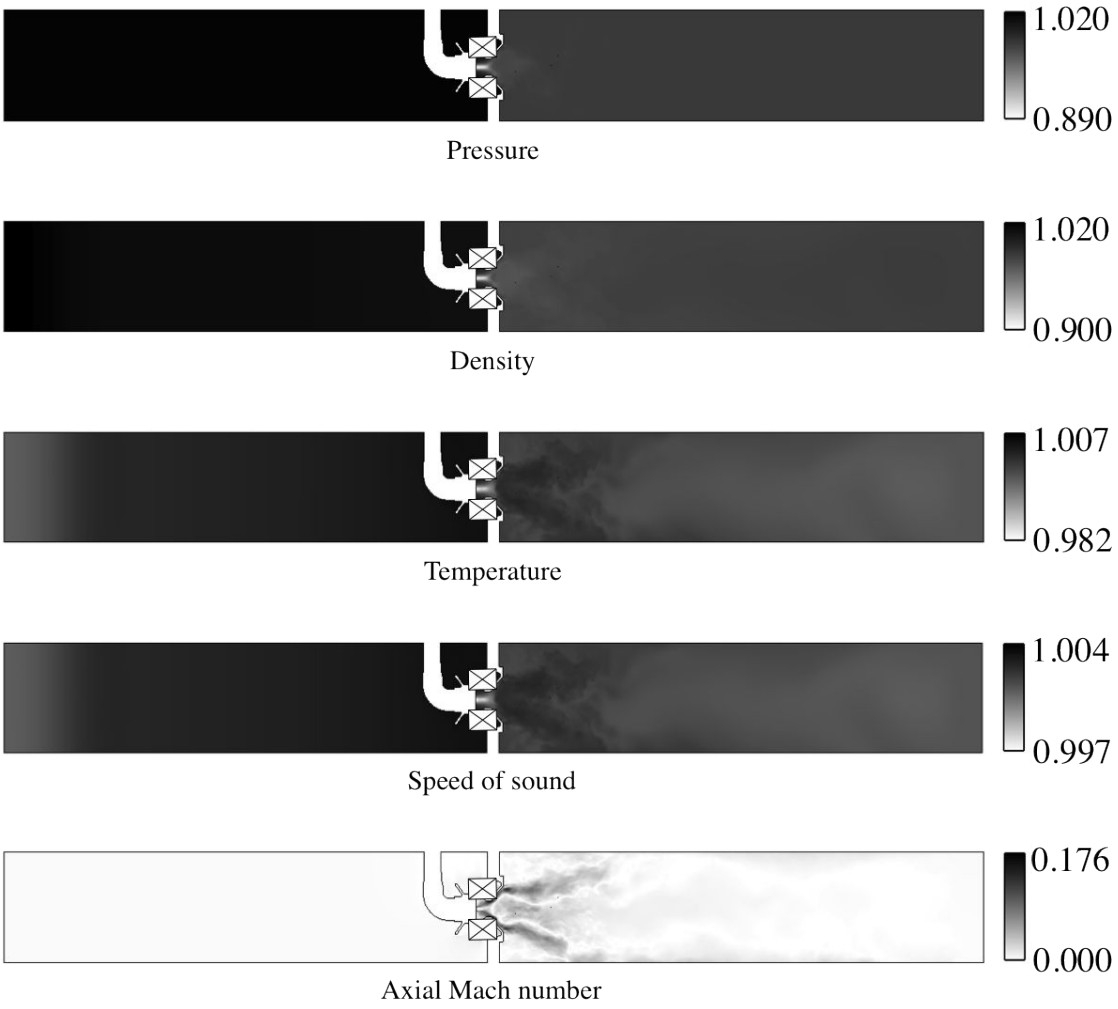


FIGURE 5.18: Flow fields of the non-reactive swirler computation without acoustic forcing. All variables except for the axial Mach number are normalized by their spatial average.

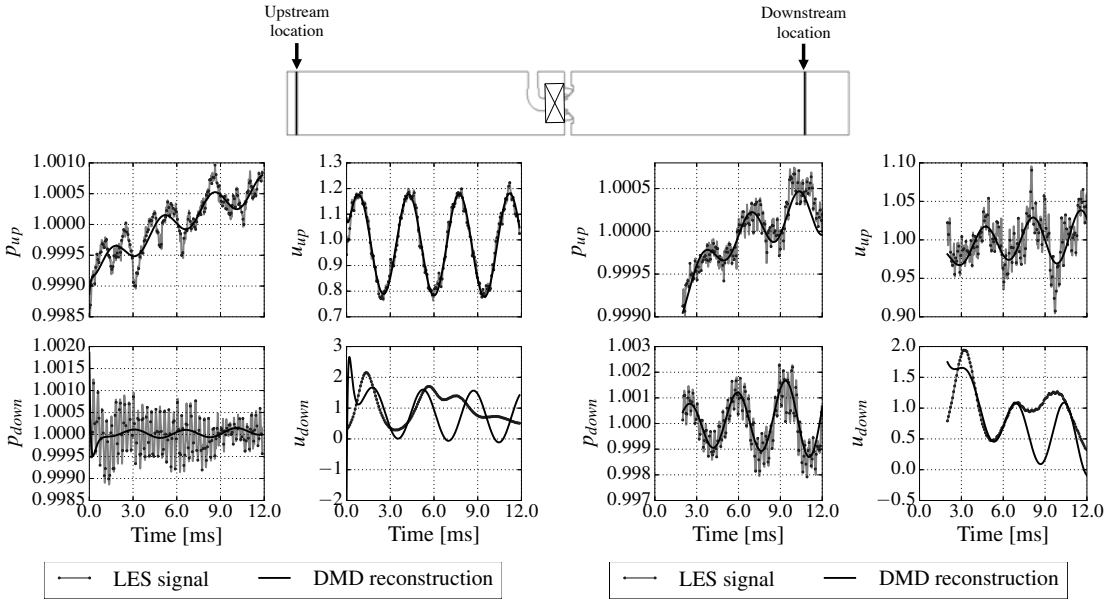
RUN	Swirler model
R3a	Non-dissipative matrix (from AVSP-f) on S1
R3b	Dissipative matrix (from LES) on S1
R3c	Dissipative matrix (from LES) on S2
R3d	Dissipative matrix (from LES) on S3

TABLE 5.5: List of R3x computations

5.5.2 Helmholtz computation with swirler matrices

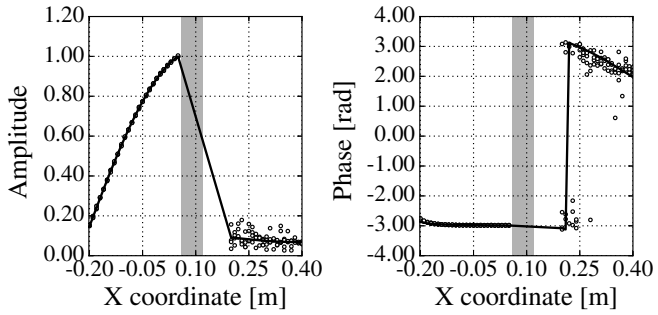
Helmholtz computations with matrix data for the swirler are performed on the configuration of Fig. 5.4b. The swirler matrix is applied on three sets of MBC surfaces of similar shape but different size (Fig. 5.21): an intermediate surface S1, a small surface S2 and a big surface S3. On this configuration, four Helmholtz computations are performed (Tab. 5.5).

In the first one (R3a), the impact of the change of geometry is assessed by substituting the discretized swirler with its non-dissipative, purely acoustic matrix, measured

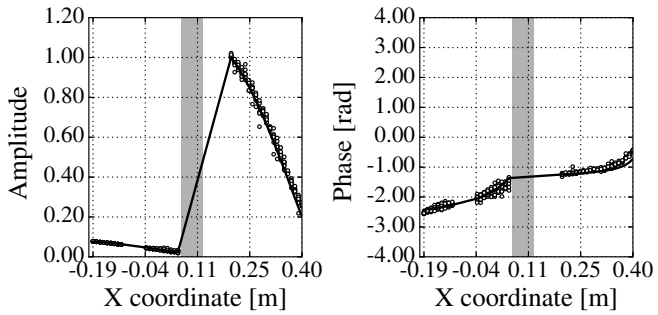


(A) Inlet forcing (B) Outlet forcing

FIGURE 5.19: Pressure and velocity signals up- and downstream of the swirler. Each signal is normalized by the time average and plotted with the fit from the DMD (sum of the carrier at 0 Hz and fluctuation at 290 Hz).



(A) Inlet forcing



(B) Outlet forcing

FIGURE 5.20: Pressure amplitude and phase from DMD (points) and plane-wave fit (lines). The grey zone represents the swirler location.

with AVSP-f on the tube geometry of Fig. 5.14 with non-reactive flow and adjusted on surface S1. In R3b, R3c and R3d, the LES dissipative matrix is used instead and is adjusted on surfaces S1, S2 and S3 respectively.

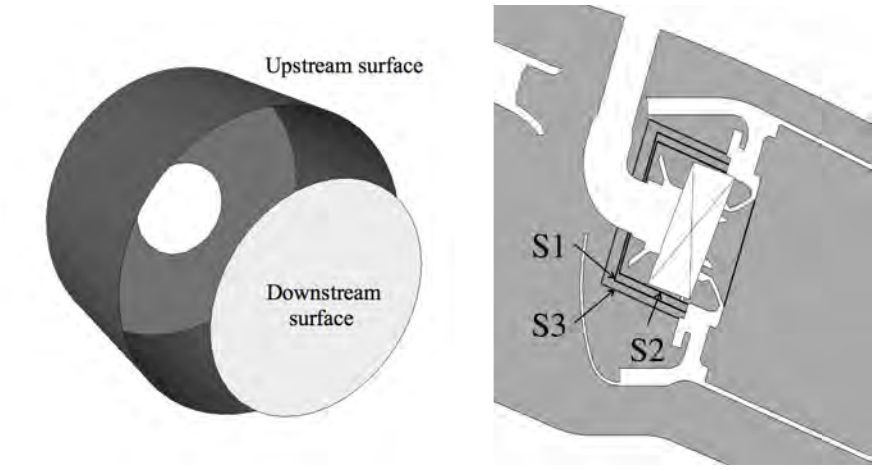


FIGURE 5.21: Left: example of matrix surfaces for the swirler. The upstream surface is a portion of cylinder enclosing the swirler. The downstream surface is a disk. Right: Three sets of matrix surfaces S1, S2 and S3, shown in the transverse cut of one sector. The downstream surface is common to S1, S2 and S3.

All matrices (dissipative and non-dissipative) describe the acoustic behaviour of a cold non-reactive discretized swirler, with nearly constant mean flow properties (Fig. 5.18). In the combustor however, the flow inside the swirler is progressively heated by the flame as it progresses towards the swirler exhaust. This effect is partially accounted for by applying the adequate temperature jumps to the swirler matrix, as illustrated in Fig. 5.23. This procedure assumes however that the temperature inside the swirler is the same in the reactive combustor and in the non-reactive tube configuration, which is not verified in practice.

Before examining the results of the Helmholtz computations with dissipative matrix, the impact of the change of geometry is assessed by comparing R3a and R2a. In R2a, the swirlers are discretized and computed by the Helmholtz solver directly. In R3a, the swirlers are replaced by their equivalent purely acoustic (non-dissipative) matrices and the results are expected to be the same as in R2a. As Table 5.6 shows, this is not exactly the case as the real part in R3a is lowered by about 1% and the imaginary part by 15%. This could be due to the fact that a quasi-uniform cold mean flow was used to obtain the swirler matrix, while the mean flow in the discretized swirler is progressively heated by the flame and therefore not constant. Another reason behind this difference is that the acoustic matrix and adjustment matrices (not shown here) are measured numerically with small errors leading to a non-zero acoustic flux balance. This is shown in Appendix G by computing the criterion of Auregan and Starobinski [154]. On the mode structure, no major difference is observed and it is hence not provided here.

In a second Helmholtz computation called R3b, the LES coefficients are introduced and the associated change of frequency and mode structure is assessed. As Fig. 5.22 shows, these coefficients greatly differ from the purely acoustic (non-dissipative) matrix which justifies the approach adopted here. The behaviour of the swirler is far from being purely acoustic. The dissipative effect of the meanflow-acoustics interaction is clearly visible as the damping rate (i.e. opposite of imaginary part) increases (Tab. 5.6).

A good point of the adjustment procedure for the swirler is that it seems quite

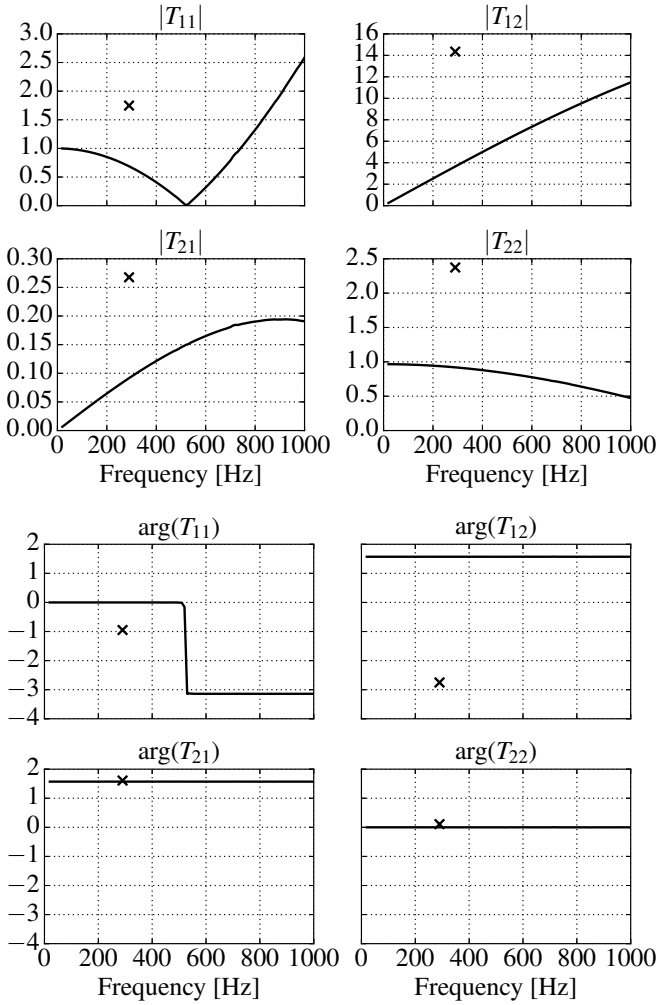


FIGURE 5.22: Swirler of the industrial combustor: non-dissipative plane matrix measured with AVSP-f (lines) and dissipative plane matrix from the LES (crosses). Top: modules. Bottom: phases.

robust to the change of matrix surface. Runs R3b, R3c and R3d provide the same frequency and the same mode structure (with slight differences close to the injector). This mode structure is similar to the solution of R3a and R2 (Fig. 5.24). The biggest modification lies in the phase difference between the inner bypass and flame tube. It is greater on R3a than on R2a and on R3b than on R3a.

To conclude this section, the overall effect of the hydro-acoustic interaction in a swirler was succesfully accounted for in the Helmholtz simulation of an annular industrial combustor, with a matrix extracted from two forced LES. The solution is shown to be robust to the choice of matrix surfaces. On this configuration, this operating point, and for the first azimuthal mode, the effect of the swirler is threefold. First, it increases the damping rate, linked to the conversion of acoustics into vorticity at the swirler. Second, it modifies the real frequency, probably because the propagation of acoustics is modified in the presence of a mean flow. Third, it introduces a phase delay between the flame tube and the inner bypass.

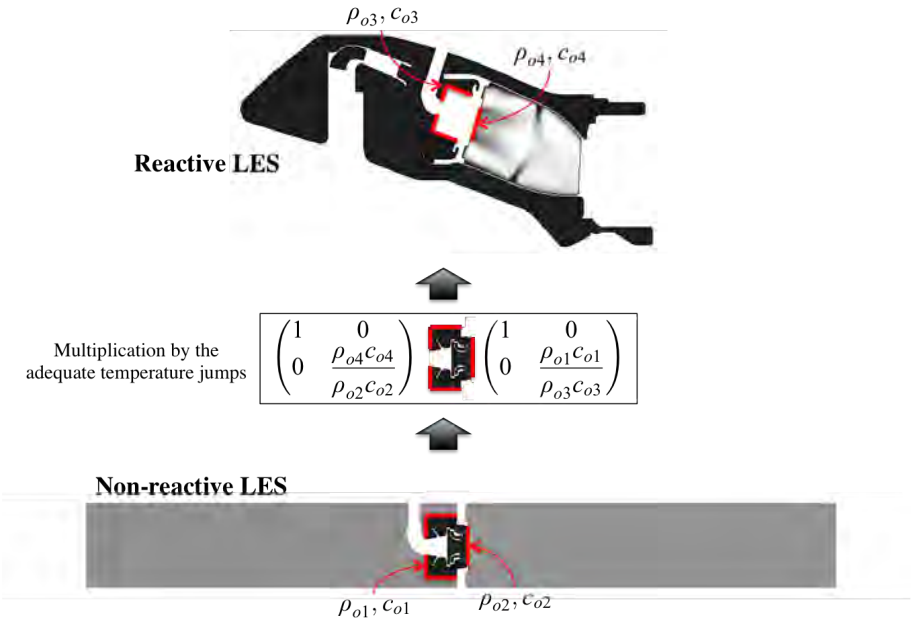
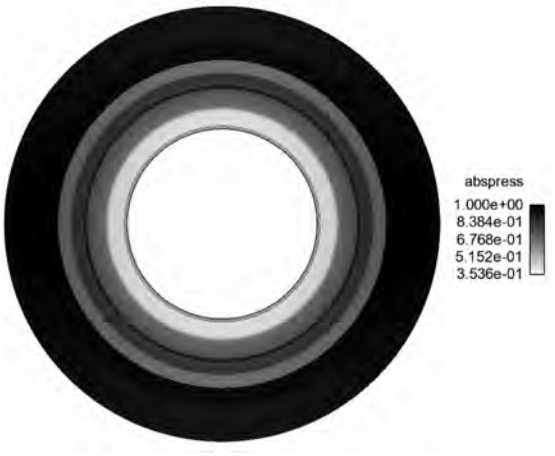


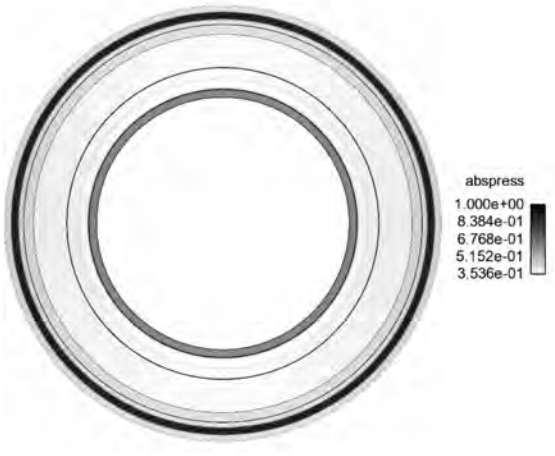
FIGURE 5.23: Procedure to readjust the speed of sound and density when using the matrix of a non-reactive LES with a mean flow field from a reactive LES.

RUN	First azimuthal mode frequency [Hz]
R3a	287.4 - 11.3i
R3b	281.7 -14.4i
R3c	281.9 -14.4i
R3d	281.2 -14.5i
R2a	291.7 - 9.83 i

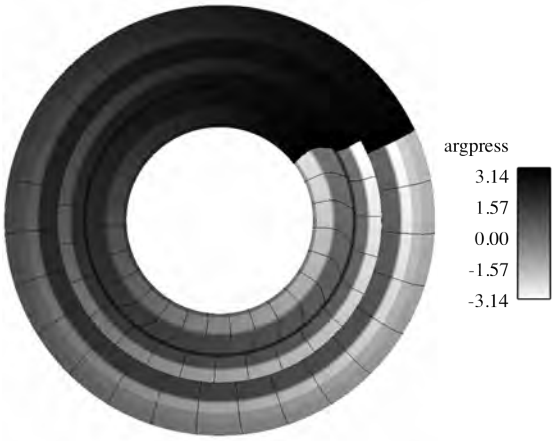
TABLE 5.6: First azimuthal mode frequency for R3x computations. The result of R2a is also recalled.



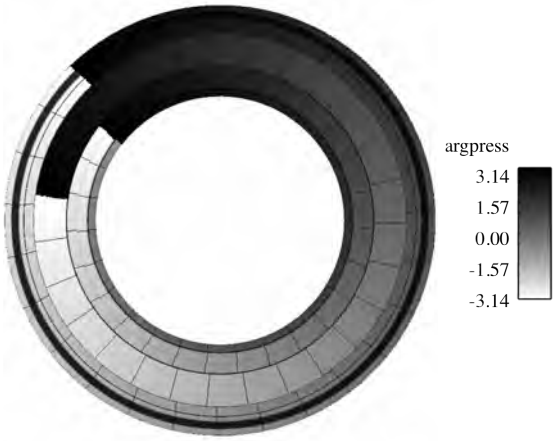
(A) Modulus of pressure - Front.



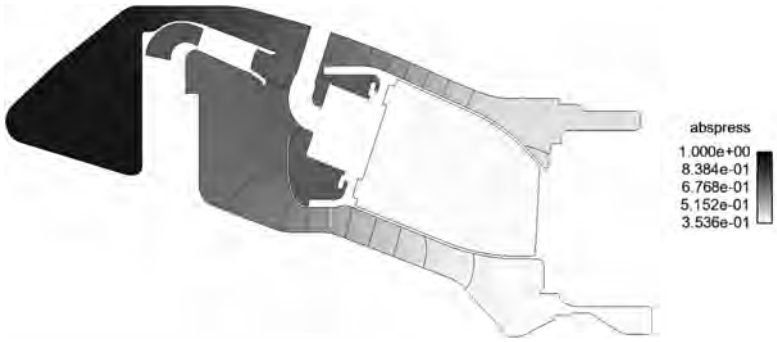
(B) Modulus of pressure - Back.



(C) Phase of pressure - Front.



(D) Phase of pressure - Back.



(E) Modulus of pressure in a transverse cut (indicated on Fig. 5.9a).

FIGURE 5.24: First azimuthal mode at $f = 281.7 - 14.4i$ Hz for R3b computation. The mode structure for R3a is similar.

5.6 Flame representation

Until now, only dissipative elements have been introduced in the Helmholtz computation, leading to modes which are all damped (i.e. with negative growth rates). Now the source term associated to the unsteady heat release will be included with the Flame Transfer Function (FTF) formalism. This FTF links the total heat release fluctuation per sector (integrated over the flame region associated to each swirler) to a reference acoustic velocity. As explained in Section 4.5, the reference velocity can be point-based (i.e. measured at discrete probes) or surface-based (i.e. integrated over a reference surface). The two formalisms will be tested here. These FTF are measured on the reactive LES of a single sector provided by Safran, which naturally features an instability at 290 Hz.

When using the global heat release, and assuming that all flames share the same response, only one value of the gain N and time delay τ is required for the complete combustor. They are defined as follows.

$$\hat{Q} = \begin{cases} N \exp(i\omega\tau) \sum_{i=1}^{N_{probes}} \hat{\mathbf{u}}(\mathbf{x_{i,ref}}) \cdot \mathbf{n_{i,ref}} & \text{for point-based FTFs} \\ N \exp(i\omega\tau) \int_{S_{ref}} \hat{\mathbf{u}}(\mathbf{x}) \cdot \mathbf{n}(\mathbf{x}) dS & \text{for surface-based FTFs} \end{cases} \tag{5.9}$$

with $\hat{Q}$ the total heat release, $\hat{\mathbf{u}}$ the acoustic velocity, $\mathbf{x_{i,ref}}$ the reference points, $\mathbf{n_{i,ref}}$ the reference vectors, S_{ref} the reference surface, and $\mathbf{n}$ the surface normal. The field of heat release fluctuations is accordingly modeled in a simple way. The flame zone is delimited by a heat release contour (extracted from an average LES solution). Inside the contour, constant values of the volumic gain n and the time delay τ are applied. The value of the volumic gain n is chosen so as to recover the total gain N when integrating over the flame volume.

$$N = \int_{V_f} n dV \tag{5.10}$$

with V_f the volume of the flame (i.e. the volume inside the threshold heat release contour) and N defined in Eq. (1.37). Outside of the flame zone, n and τ are set to zero. The flame zone used in the present Helmholtz computations is shown in Fig. 5.25.

5.6.1 Description of the LES computation

The FTF for the first azimuthal mode of the industrial combustor are measured on the reactive mono-sector configuration of Fig. 5.2 with axi-symmetric periodic boundary conditions. An overview of the mesh is presented in Fig. 5.26.

Air is injected at the main inlet with a relaxed characteristic boundary condition where the mass flow rate, temperature and composition are set. Some additional air is also injected with non-characteristic boundaries at films and at the swirler. Perforated plates are modeled with a pair of suction/injection patches with the model of [163]. Other walls are assumed adiabatic, and the velocity at the wall is imposed through a classical wall law. At periodic boundaries, an axi-symmetric

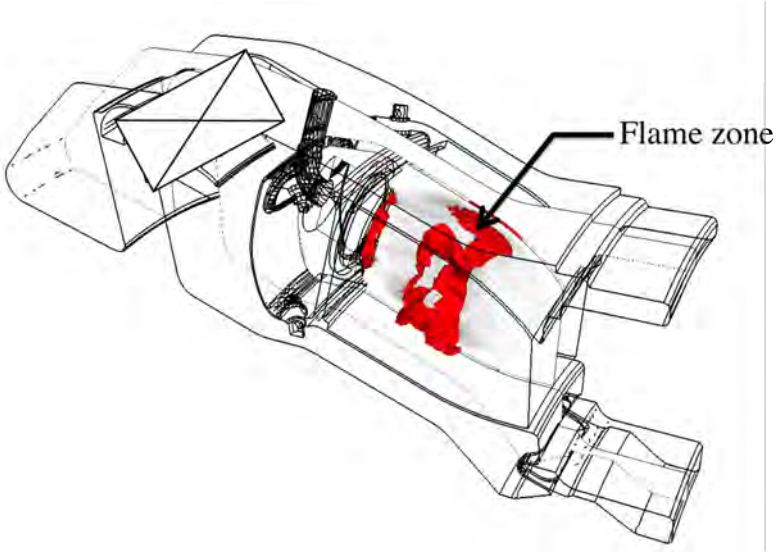


FIGURE 5.25: Flame zone in red (with non zero FTF parameters) for R4x and R5x computations.

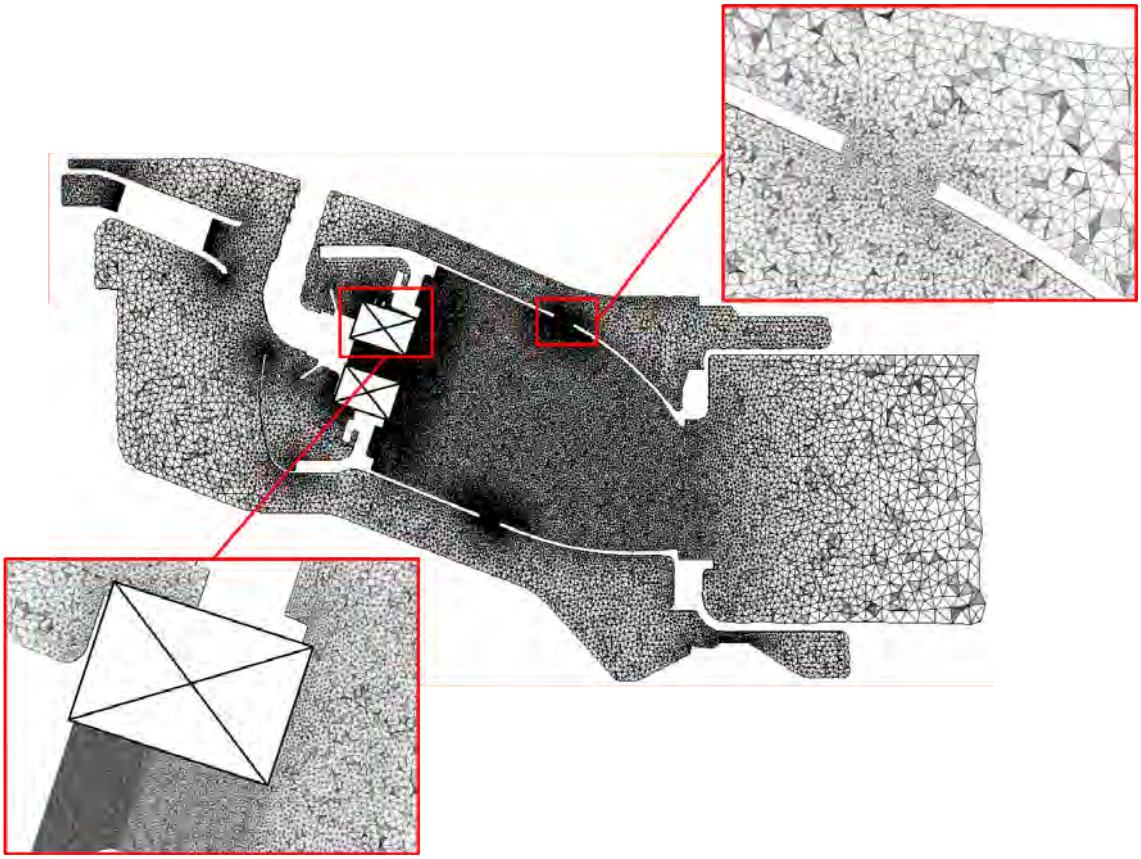


FIGURE 5.26: Transverse cut of the mesh used in the reactive LES of the industrial combustor.

boundary condition is applied: all scalar quantities at one side are replicated on the other and vector quantities at one side are reinjected on the other side after rotating them by the sector angle.

The combustion process is represented by a reduced two-step mechanism for premixed kerosene-air flames called 2S_KERO_BFER [164]. The scheme is composed of two reactions corresponding to the fuel oxidation into CO and H_2O and the $CO - CO_2$ equilibrium, for a surrogate of kerosene. The correct 1D flame properties are recovered by tuning the Arrhenius pre-exponential constants. The flame front is thickened, following the approach of [162].

The fuel is injected as a dispersed continuous phase that obeys to the same filtered Navier-Stokes equations as the gas (Euler-Euler approach). The dispersed and gas phase are coupled through two terms : a two-way drag force and an evaporation source term. The injection profile is a hollow cone whose shape is determined from global and geometrical parameters [165]. A new set of boundary conditions is defined for the dispersed phase, composed of characteristic inlets and slip walls.

Both dispersed and gas phase are solved with the Two-step Taylor Galerkin 4A scheme (TTG4A) [148]. This scheme is third-order accurate in space and fourth order accurate in time but diffuses more medium wave numbers than the TTGC scheme. Finally, the subgrid stress tensor is computed with the Smagorinsky model [166]. This reactive LES naturally features an instability at a frequency close to 290 Hz, the frequency of the first azimuthal mode found in R0, R1, R2 and R3 (Fig. 5.3). It was chosen not to force the LES and rather use the fluctuations already present in the combustor to determine the Flame Transfer Functions, assuming that the flame/acoustics coupling remains linear.

5.6.2 Reference signals for the FTF

In the next sections, point-based and surface-based FTF will be included in the Helmholtz computations. As explained in Section 5.1.2, these FTFs are measured on an LES of a single sector, based on the assumption that the flames are sensitive to the fluctuations of mass flow rate, and therefore to the *longitudinal* velocity fluctuations at first order. The acoustic excitation is provided by a longitudinal instability that is naturally triggered at the same frequency as the azimuthal mode of interest. In order to remain in the linear regime of the flame/acoustics interaction, low levels of heat release and acoustic fluctuations are maintained by using a downstream nozzle geometry associated to a low level of acoustic reflection.

For both formalisms, a legitimate question is where to choose the reference point/surface. Ideally, the Helmholtz solution should be robust to this choice so that any reference location with a relevant velocity signal can be used. In order to check this, different probe sets (Fig. 5.27) and surfaces (Fig. 5.21) are used. In the case of probes, this robustness check is almost certain to fail with only one probe, especially if it is located close to the swirler outlet, because the acoustic velocity can be mixed with turbulent fluctuations. For this reason, an average over a dozen of probes revolving around the swirler axis is used to compute the FTF instead and Fig. 5.27 only shows one element of the set. The reference vectors for sets A, B and C are radially directed towards the swirler axis. The reference vector for sets D and E is chosen constant and parallel to the swirler axis. When a surface of reference is used instead of a point of reference, the local normal is used as a vector of erference.

The reference velocities obtained from the reference points and surfaces are plotted in Fig. 5.28. In this plot, all velocities are normalized by their time average. Fig. 5.28 shows that there is a great variability in the shape and amplitude of fluctuations in

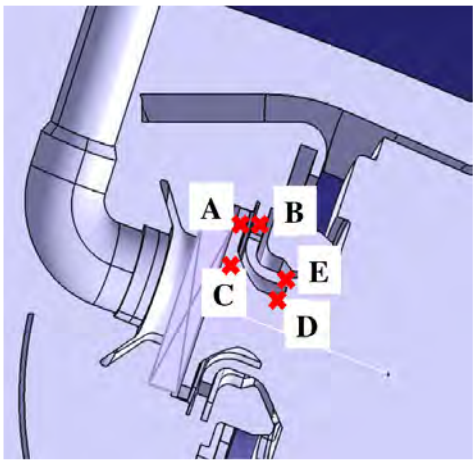
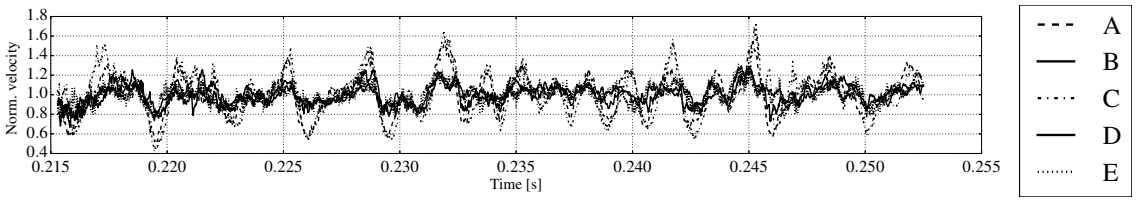
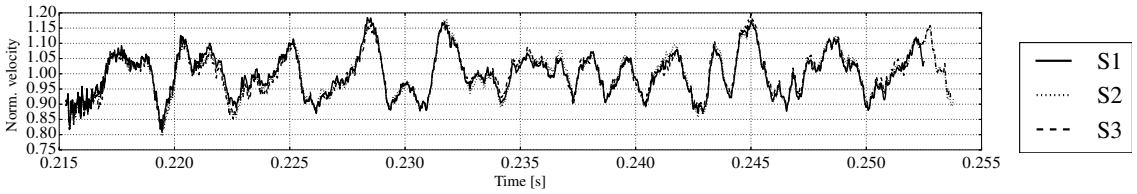


FIGURE 5.27: Points (each set of probe is represented with only one probe)

the point-based velocities. On the contrary, surface-based velocities have very similar shapes and normalized amplitudes and this tends to prove that surface averaging is more robust to the choice of reference location than probe averaging. Additionally, the surface average velocities seem smoother than the velocities from probes.



(A) From probe averaging



(B) From surface averaging

FIGURE 5.28: Reference velocities from probes (top) and surface averaging (bottom). All signals are normalized by their time average.

In order to compute the Flame Transfer Functions, the velocity and heat release signals must be filtered at the frequency of the instability and this can be done either with a Fast Fourier Transform (FFT) or with a Dynamic Mode Decomposition (DMD). Fourier Transform is used for both point-based and surface-based signals. The comparison between Fourier Transform and DMD is performed only for surface-based signals. The gains and delays obtained with each method are provided in Tab. 5.7.

The agreement between DMD and FFT is fairly good, although results are not identical. Contrary to the FFT, DMD does not filter the signal at a given frequency, but rather extracts the relevant frequencies of the signal. In this case, DMD finds a main fluctuation at 298 Hz with amplitudes different from the FFT. This is illustrated in Fig. 5.29 where the heat release and surface-averaged velocity signals are compared with the DMD and FFT reconstructions.

Concerning the comparison between point-based and surface-based FTF, Tab. 5.7 shows that the two formalisms provide similar values of the FTF delay τ (around 2 ms) but drastically different values of the FTF gain N. The difference in gains is due to the difference between the reference velocities. Probes A, B, C, D and E are all located either in the swirler vanes or at their exit, where the velocity is extremely high since the vanes cross-section is narrow. The reference velocities at these probes is consequently much more important than the ones measured at surfaces S1, S2 and S3, located upstream of the swirler. In fact, the reference velocity ratio between point-based and surface-based measurements corresponds the ratio of FTF gains. For example, the reference velocity measured on surface S1 is approximately 20 times smaller than the reference velocity measured on probes A. Accordingly, the FTF gain for surface S1 is 20 times higher than the FTF gain for probes A.

Reference location	**N [J/m]**		**τ [ms]**		**CC**	
	FFT	**DMD**	**FFT**	**DMD**	**FFT**	**DMD**
Probes A	2856	-	2.283	-	0.49	-
Probes B	3466	-	2.135	-	0.48	-
Probes C	5454	-	2.196	-	0.54	-
Probes D	3147	-	2.078	-	0.41	-
Probes E	3339	-	2.188	-	0.48	-
Surface S1	66467	57672	2.163	2.340	0.54	0.52
Surface S2	49024	43606	2.130	2.325	0.54	0.53
Surface S3	81013	75546	2.140	2.342	0.54	0.52

TABLE 5.7: FTF gain and delay, from an FFT filtering at 290 Hz and from the DMD mode at 298 Hz. The FTF parameters N and τ are defined in Eq. (5.9). The correlation coefficient CC is defined in Eq. (5.11).

In order to estimate the quality of the FTF, a correlation coefficient is computed between the delayed reference velocity and the heat release signal.

$$CC = \frac{\overline{(\dot{Q}(t) - \overline{\dot{Q}(t)})(u(t-\tau) - \overline{u(t-\tau)})}}{\sigma_{\dot{Q}}\sigma_u} \tag{5.11}$$

where $\overline{\bullet}$ denotes time average and $\sigma_X = \sqrt{\overline{(X - \overline{X})^2}}$ is the standard deviation of X. The correlation coefficient ranges between -1 and 1. A correlation coefficient close to 1 is an indication that the FTF representation is adequate and in particular, that the time delay is correctly computed. These correlation coefficients are provided in Tab. 5.7. However, the correlation coefficient does not indicate if the value of the gain is correct or not. For this, visual checks are performed by plotting the transformed velocity $Nu'(t-\tau)$ against the heat release (Fig. 5.30). Both the correlation coefficient and the visual examination suggest that the surface-based FTFs are correctly measured with DMD and FFT. Moreover, the correlation coefficient is greater for surface-based signals than for point-based and this is a further argument in favor of reference surfaces.

Examining the correlation between FTF signals is one thing, but ultimately, the quality and robustness of the FTF should be assessed by checking the result of the Helmholtz computation. For surface-based FTFs, two points are of particular interest.

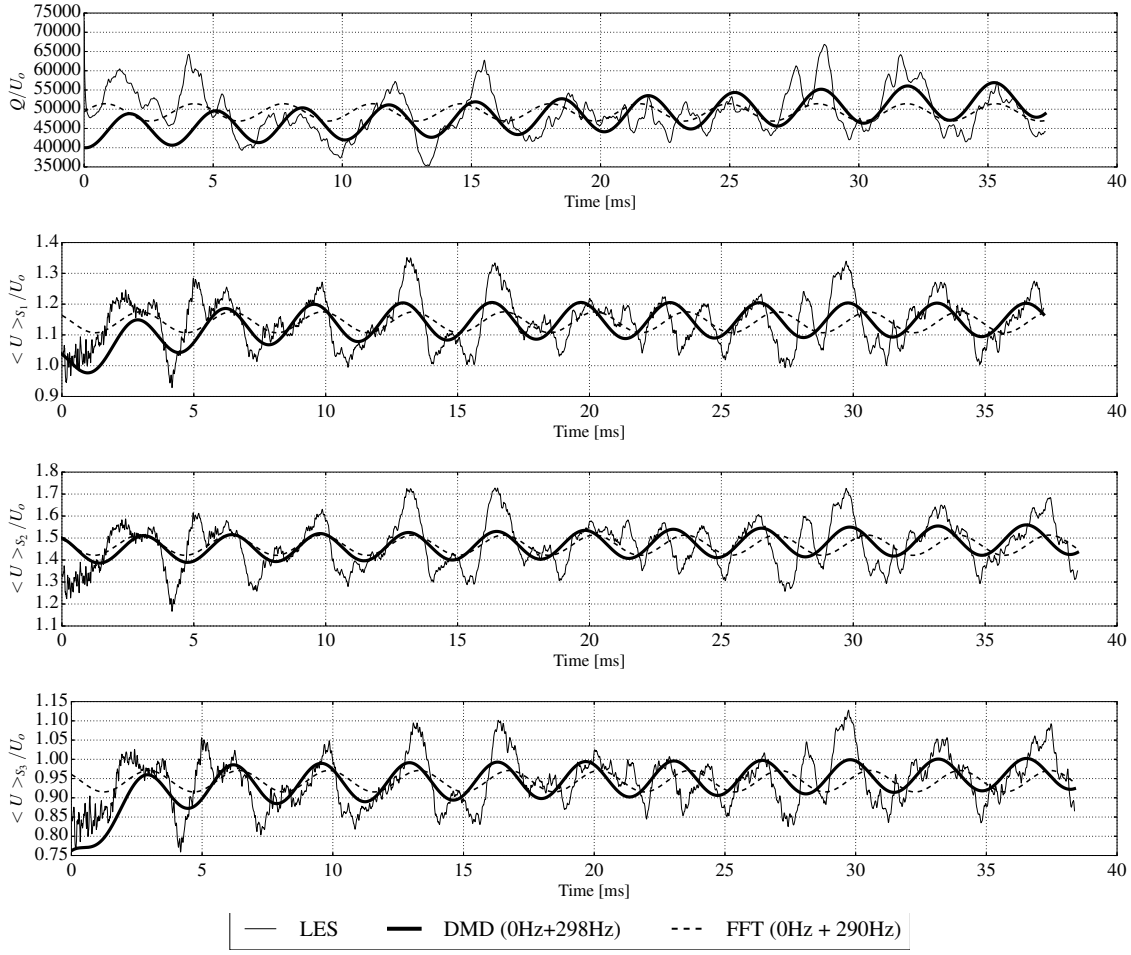


FIGURE 5.29: Heat release and surface averaged velocity signals with the DMD and FFT reconstructions. All quantities are normalized by an arbitrary constant U_o.

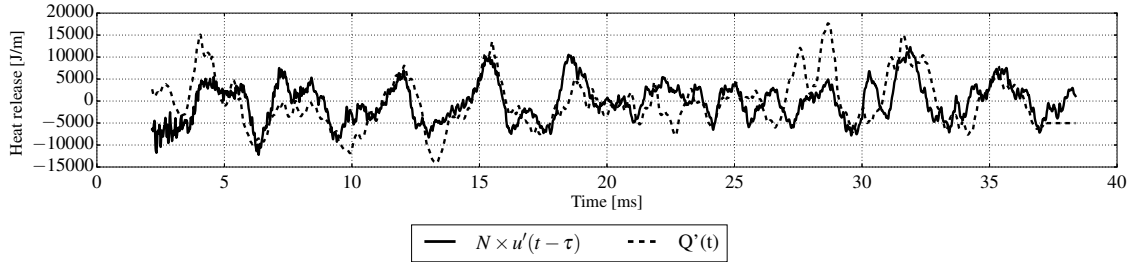


FIGURE 5.30: Heat release fluctuations $\dot{Q}'(t)$ against transformed velocity fluctuations $Nu'(t-\tau)$ for surface S1, with the FTF parameters obtained from Fourier analysis (R=0.54).

- Do surface-based FTFs and point-based FTFs provide the same stability results when included in the Helmholtz computation ?
- Surface-based velocity signals seem more robust to the choice of reference surface. The associated Helmholtz computations are therefore expected to produce similar results. Is this indeed the case ?

These two questions are investigated in Appendix H by performing R4 type computations (Tab. 5.1) where the flame is the only source of growth/damping rate, with

RUN	Upstream swirler matrix surface
R5a	S1
R5b	S2
R5c	S3

TABLE 5.8: R5x computations with flame, dilution holes and swirlers models.

no dissipative model for the perforated plates, swirlers and dilution holes. In these computations, it is found that both surface-based and point-based FTFs predict the existence of an unstable azimuthal mode of first order around 290 Hz. However, the growth rate is much more important with surface-based FTFs than with point-based ones, probably because the gains of surface-based FTFs are much higher. Also, the robustness of surface-based velocity signals to the choice of reference surface does not translate into stability robustness. The growth rate almost doubles in value when switching from surface S2 to S3. For now, we do not have any definite explanation for this somewhat disappointing result.

5.6.3 Helmholtz computations with active flame

Now that the effect of surface-based FTFs is better understood, three computations associated with surfaces S1, S2 and S3 are performed, this time with a model for the unsteady flame, dilution holes and injectors (Tab. 5.8). The introduction of an unsteady flame in the computation creates a distinction between the two azimuthal modes, mainly on the imaginary part. Both modes are amplified compared to the no-flame case, but one more than the other (Tab. 5.9). However, even the most amplified modes are still predicted stable for surfaces S1 and S2. Only surfaces S3 lead to a linearly unstable mode.

These observations are compared to R6 computation. In R6, a point-based FTF associated to set B (defined in Fig. 5.28a) is used in conjunction with a dissipative model for the perforated plates and dilution holes, but a resolved swirler. The first azimuthal mode frequencies are displayed in Tab. 5.9. Even though there are less dissipative elements in R6, the imaginary part with the point-based FTF is still much lower than with surface-based FTFs. In this regard, reference surfaces are in better agreement with the reactive LES, where an instability was observed at ≈ 290 Hz. However, the real frequency obtained with point-based results is closer to 290 Hz.

Concerning the mode structure, fairly similar results are obtained for both R5x and R6 computations, but the Helmholtz solver finds spinning modes (i.e. constant modulus and azimuthally varying phase) in R5a, R5b, R6 and standing modes (i.e. constant phase and azimuthally varying modulus) in R5c. It could be that the portion of geometry removed when using MBC for the swirlers is too important so that the acoustics of the overall geometry is modified. Only the structure of the most amplified mode of R5a (at 271.44 - 0.60i Hz) is shown in Fig. 5.31. Again, it shares the same characteristics as R1, R2 and R3 solutions.

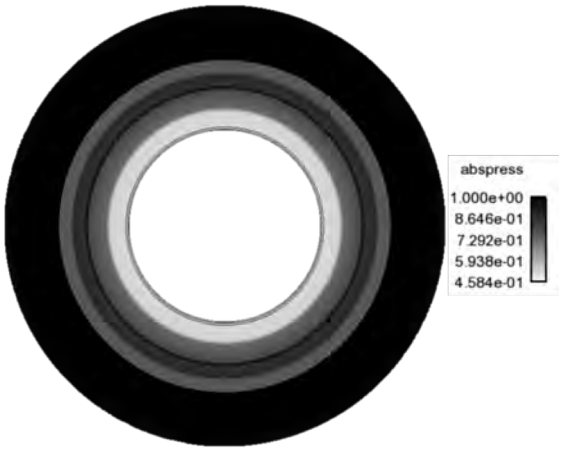
To conclude this part, a new formalism of the FTF, based on a reference surface, was tested on an industrial annular combustor. The FTF was measured on a reactive LES of a single sector that featured a thermoacoustic instability at the frequency of the first azimuthal mode. The reference velocities measured on surfaces was compared

RUN	Least amplified mode	Most amplified mode
R5a	270.52 -1.36i	271.44 - 0.60i
R5b	275.00 - 5.14i	275.50 - 4.01i
R5c	271.49 - 1.50i	272.57 + 1.99i
R6	293.43 - 7.90i	293.00 - 7.46i

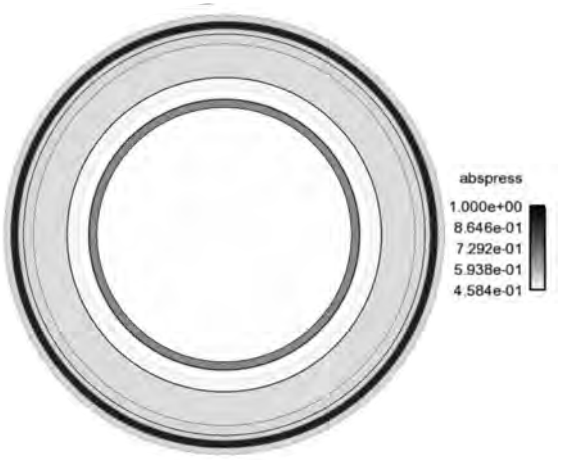
TABLE 5.9: Frequencies of the first order azimuthal modes of R5x and R6 computations.

to the one measured at points, and were shown to be less noisy and more robust to the choice of the reference location. However, this apparent robustness does not translate into the Helmholtz computation. Although all FTF parameters predict an unstable azimuthal mode at around 290 Hz in the absence of dissipative elements, the frequency change is considerable when using a different surface. This variation is not well understood but two mechanisms are suspected. First, the FTF gains found with the surface-averaged velocities are very high and a small relative change of the flame parameters (location, gain or delay) could lead to large modifications of the acoustics of the burner. Second, the use of a truncated geometry with matrix boundaries could remove some of the velocity fluctuation produced at the flame. This observation was also made on the toy combustor of Section 4.5.3. The result with reference surfaces also presents much higher growth rates and levels of pressure than the one obtained with reference points. These issues should be investigated in the future.

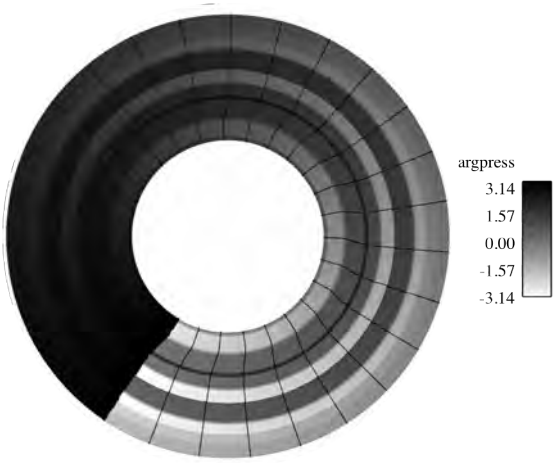
When including dissipative elements, only the largest set of surfaces (S3) provides an unstable azimuthal mode. Other reference surfaces and points lead to linearly stable modes, but reference surfaces provide a better agreement with the LES observations, as the associated damping rate is lower than the one obtained with reference points. Therefore, surface-based FTFs remain an interesting option for the prediction of combustion instabilities on realistic annular combustors, with the HMBC methodology. Moreover, using reference surfaces makes it possible to use simpler geometries, lighter meshes, potentially leading to a reduction of CPU cost (but CPU cost was not analyzed in detail here).



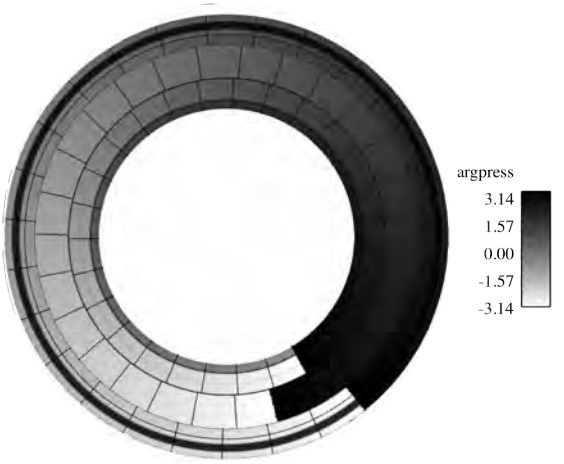
(A) Modulus of pressure - Front.



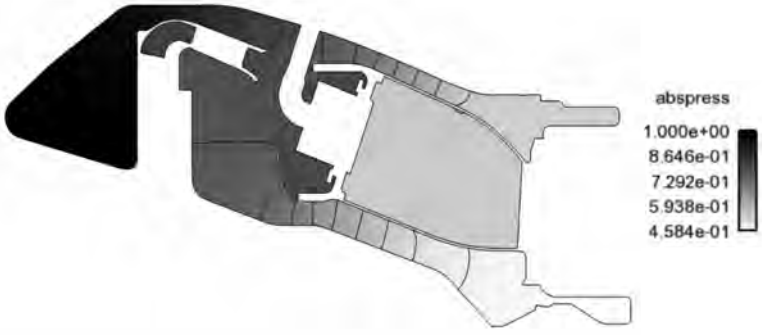
(B) Modulus of pressure - Back.



(C) Phase of pressure - Front.



(D) Phase of pressure - Back.



(E) Modulus of pressure in a transverse cut (indicated on Fig. 5.31a).

FIGURE 5.31: First azimuthal mode at $f = 272.6 + 2.01i$ Hz for R5 computation.

5.7 Summary of acoustic contributions - Energy balance

Figure 5.32 summarizes the frequencies found in the previous Helmholtz solutions, with the progressive addition of models for the perforated plates, dilution holes, swirler and flame. In order to investigate the causes of the growth rate changes, an acoustic energy balance is performed for runs R0, R1, R2a, R3a, R3b R5a, R5b and R5c. For the runs with an active flame (R5a, R5b and R5c), only the most amplified

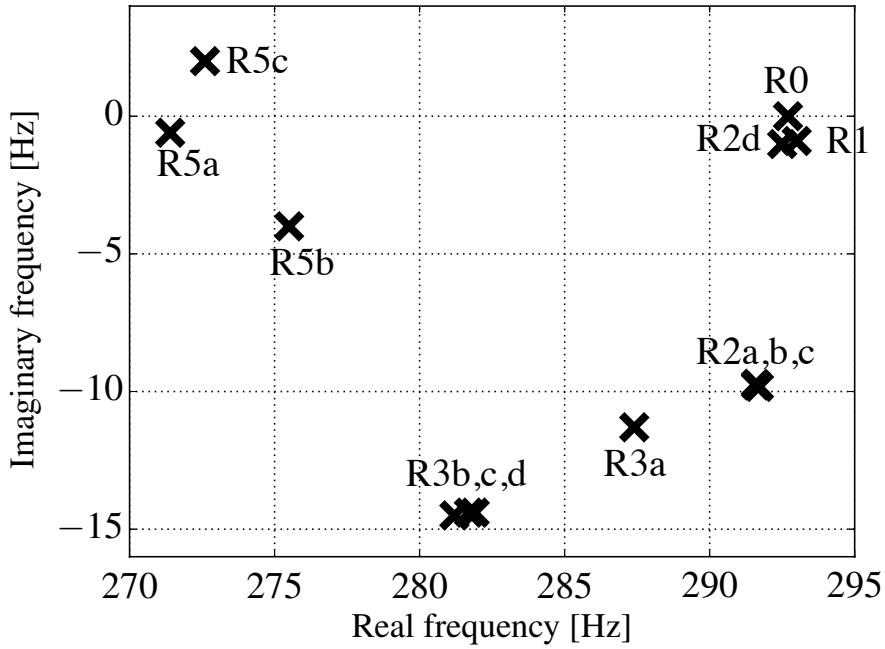


FIGURE 5.32: Complex frequencies of the first azimuthal mode for the Helmholtz computations of Tab. 5.1

mode is examined. The principle of the acoustic balance is detailed in [138] and explained here briefly. This analysis starts from the Euler equations for mass and momentum conservation, here recalled in time domain.

$$\frac{1}{\rho_o c_o^2}\frac{\partial p'}{\partial t} + \frac{\partial u_i'}{\partial x_i} = \frac{\gamma - 1}{\gamma p_o}\dot{q}' \tag{5.12}$$

$$\frac{\partial u_i'}{\partial t} = -\frac{1}{\rho}\frac{\partial p'}{\partial x_i} \tag{5.13}$$

Multiplying Eq. (5.12) by p' and Eq. (5.13) by $\rho_o u_i'^2$ and adding them gives

$$\frac{\partial}{\partial t}\left(\frac{1}{2}\frac{p'^2}{\rho_o c_o^2} + \frac{1}{2}\rho_o u_i' u_i'\right) + \frac{\partial}{\partial x_i}(p' u_i') = \frac{\gamma - 1}{\rho_o c_o^2} p' \dot{q}' \tag{5.14}$$

The acoustic energy $\mathcal{E}$, flux $\mathcal{F}$ and source term $\mathcal{S}$ are hence defined by:

$$\mathcal{E} = \frac{1}{2}\frac{p'^2}{\rho_o c_o^2} + \frac{1}{2}\rho_o u_i' u_i' \tag{5.15}$$

$$\mathcal{F}_i = p' u_i' \tag{5.16}$$

$$\mathcal{S} = \frac{\gamma - 1}{\rho_o c_o^2} p' \dot{q}' \tag{5.17}$$

Equation (5.14) can be integrated over the volume of the combustor. After application of the Green-Ostrogradsky theorem, the integrated energy balance equation can be expressed as:

$$\frac{d}{dt}\underbrace{\int_V \mathcal{E}dV}_{E} + \underbrace{\int_{\partial V} \mathcal{F}_i n_i dS}_{F} = \underbrace{\int_V \mathcal{S}dV}_{S} \tag{5.18}$$

with n_i the outward surface normal. Over one period $T = 2\pi/\omega_r$, the total acoustic energy in the domain E is modified by the acoustic flux leaving/entering at boundaries F and by the heat release source term S. This change is assessed by integrating Eq. (5.18) over T.

$$E(T) - E(0) + \int_T F dt = \int_T S dt \tag{5.19}$$

The expressions of the terms in Eq. (5.19) can all be computed from the Helmholtz frequency and solution fields $\hat{p}$ and $\hat{u}_i$ $(i = 1, .., 3)$.

$$E(0) = \int_V \left(\frac{1}{2}\frac{\Re(\hat{p})^2}{\rho_o c_o^2} + \frac{1}{2}\rho_o \Re(\hat{u}_i)\Re(\hat{u}_i) \right) dV \tag{5.20}$$

$$E(T) = \exp(2\omega_i T)E(0) \tag{5.21}$$

$$\int_T F dt = \int_{\partial V} \Big(\mathbf{I_A}\, \Re(\hat{p})\Re(\hat{u}_i n_i) + \mathbf{I_B}\, \Im(\hat{p})\Im(\hat{u}_i n_i) + \mathbf{I_C}\, [\Re(\hat{p})\Im(\hat{u}_i n_i) + \Im(\hat{p})\Re(\hat{u}_i n_i)] \Big) dS \tag{5.22}$$

$$\int_T S dt = \int_V \frac{\gamma - 1}{\rho_o c_o^2} \Big(\mathbf{I_A}\, \Re(\hat{p})\Re(\hat{q}) + \mathbf{I_B}\, \Im(\hat{p})\Im(\hat{q}) + \mathbf{I_C}\, [\Re(\hat{p})\Im(\hat{q}) + \Im(\hat{p})\Re(\hat{q})] \Big) dV \tag{5.23}$$

The quantities $\mathbf{I_A}$, $\mathbf{I_B}$ and $\mathbf{I_C}$ appear when performing time integration over one acoustic period. With $\omega = \omega_r + i\omega_i$ the complex pulsation, the values are:

$$\mathbf{I_C} = \int_T \exp(2\omega_i t)\cos(\omega_r t)\sin(\omega_r t) dt = \begin{cases} \dfrac{\omega_r(1 - \exp(2\omega_i T))}{4(\omega_r^2 + \omega_i^2)} & \text{for } \omega_i \neq 0 \\ 0 & \text{for } \omega_i = 0 \end{cases}, \tag{5.24}$$

$$\mathbf{I_A} = \int_T \exp(2\omega_i t)\cos^2(\omega_r t) dt = \begin{cases} \dfrac{\exp(2\omega_i T) - 1}{2\omega_i} + \dfrac{\omega_r}{\omega_i}\mathbf{I_C} & \text{for } \omega_i \neq 0 \\ \dfrac{T}{2} & \text{for } \omega_i = 0 \end{cases}, \tag{5.25}$$

$$\mathbf{I_B} = \int_T \exp(2\omega_i t)\sin^2(\omega_r t)dt = \begin{cases} -\dfrac{\omega_r}{\omega_i}\mathbf{I_C} & \text{for } \omega_i \neq 0 \\ \dfrac{T}{2} & \text{for } \omega_i = 0 \end{cases}. \tag{5.26}$$

It is important to note that the volume integration in Eq. (5.20) is performed over a volume of inviscid fluid only, thus excluding any dissipative elements modeled thanks to a two-port matrix (perforated liners, dilution holes and swirlers). The contribution of these elements on the acoustic energy budget is thus contained in the flux term. Namely, the dissipation of each compact element corresponds to the sum of fluxes on the two surfaces surrounding the element and connected by the two port matrix. In Figure 5.33, all contributions to the change of acoustic energy are plotted, in a normalized form. The four columns (indicated as 1, 2, 3 and 4 in Fig. 5.33) are normalized forms of respectively:

$$-\frac{\int_T F dt}{E(0)}, \quad \text{the ingoing acoustic boundary flux,} \tag{5.27}$$

$$\frac{\int_T S dt}{E(0)}, \quad \text{the energy gained in the heat release coupling,} \tag{5.28}$$

$$\epsilon = \frac{E(T)}{E(0)} - 1 + \frac{\int_T F dt}{E(0)} - \frac{\int_T S dt}{E(0)}, \quad \text{the relative error on the energy balance,} \tag{5.29}$$

$$\frac{E(T)}{E(0)} - 1, \quad \text{the change of acoustic energy,} \tag{5.30}$$

so that Eq. (5.19) can be expressed as:

$$\underbrace{\frac{E(T)}{E(0)} - 1}_{\text{Column 4}} = \underbrace{-\frac{\int_T F dt}{E(0)}}_{\text{Column 1}} + \underbrace{\frac{\int_T S dt}{E(0)}}_{\text{Column 2}} + \underbrace{\epsilon}_{\text{Column 3}} \tag{5.31}$$

The volume integration for the acoustic energy and heat release source terms is performed at mesh nodes, while the surface integration for the flux computation is obtained at boundary cells. The error term of Eq. (5.29) should be zero in theory. This is however not the case in AVSP. One of the reasons is that most of the boundary conditions (all except the Dirichlet condition) are imposed under a weak form, thus inducing errors in the evaluation of the acoustic flux actually present in the computation. In most cases, the error remains smaller than 6%.

In Fig. 5.33, the contributions from the walls, the dilution holes, perforated plates and swirlers are distinguished by considering separately the cells of each type of boundary condition. This distinction should be examined with caution. Indeed, as already explained in Section 4.3.2, nodes and cells shared by two boundary conditions receive a contribution from the two. In a first attempt to separate the contributions of each type of boundary condition, the procedure of Appendix I is applied. Without this procedure, the acoustic flux distribution cannot be trusted. For example, in a Helmholtz computation of the industrial geometry where the only dissipative

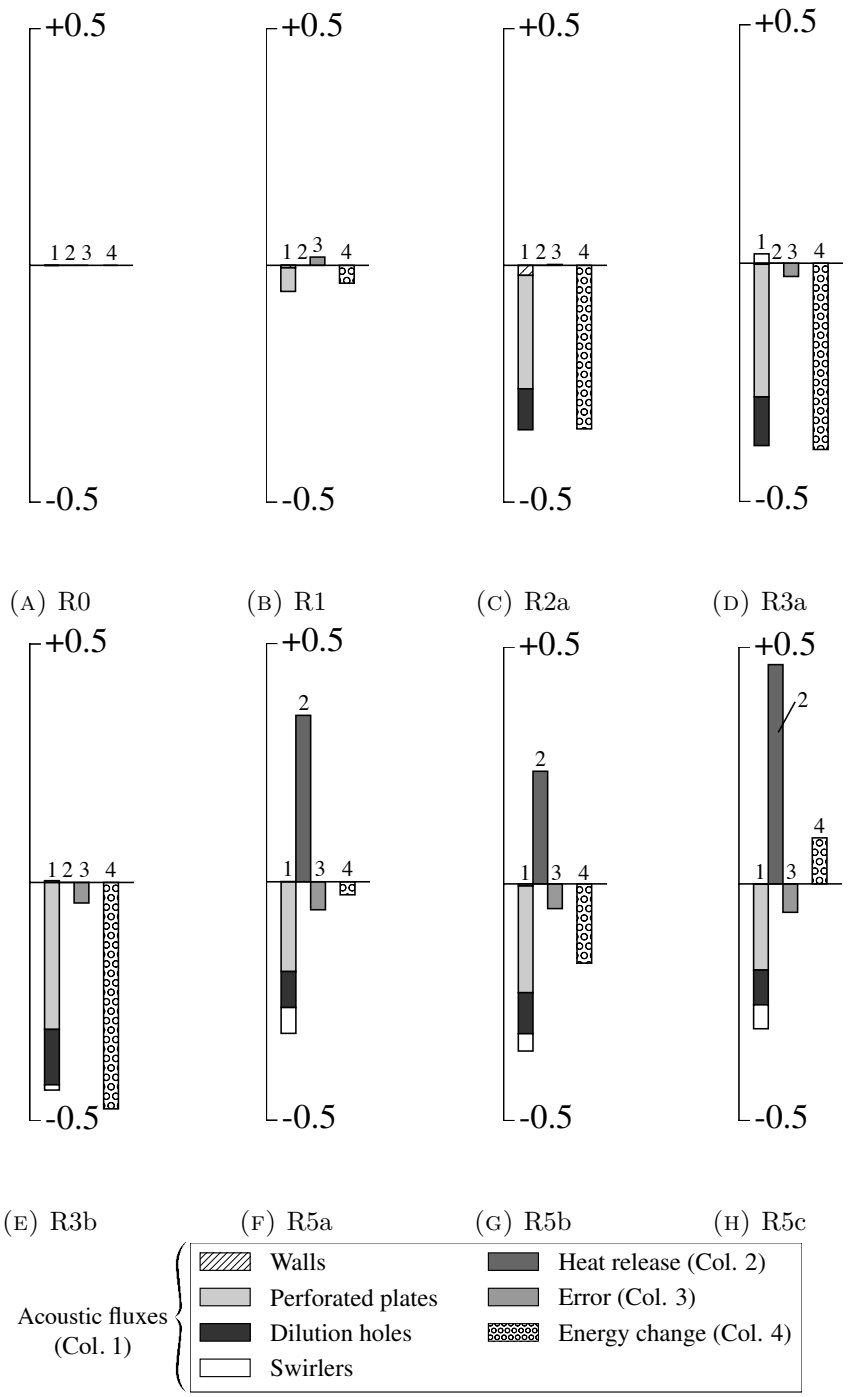


FIGURE 5.33: Contributions to the acoustic energy balance as defined in Eq. (5.31). The sum of the three first columns (acoustic flux $-\frac{\int_T Fdt}{E(0)}$, heat release $\frac{\int_T Sdt}{E(0)}$, and error ϵ defined in Eq. (5.29)) is equal to the last one (total energy change $\frac{E(T)}{E(0)} - 1$).

boundaries are at dilution holes, the acoustic flux distribution without correction indicates that only 70% of the flux actually comes from the dilution holes, while the remaining 30% are attributed to walls. With the proposed procedure, a coherent acoustic flux distribution is obtained, with 100% of the flux coming from the dilution holes.

The acoustic energy distributions of Fig. 5.33 are now analyzed. As expected, all contributions are equal to zero for R0, since no damping or amplifying element is present in the computation. In R1, approximately 6% of the acoustic energy leaves the domain through the perforated plates. In R3b, where all damping elements are included, the energy balance analysis shows that the top contributors to dissipation are perforated plates and dilution holes. The damping effect of the swirlers, although visible on the damping rate, is negligible from an acoustic energy point of view.

When including the flame with a surface-based FTF, the portion of energy dissipated in the swirlers increases (probably because the level of acoustic fluctuation close to the swirlers is more important when a flame is present), but remains smaller than the one dissipated by dilution holes and perforated plates. Concerning R5a, R5b and R5c the acoustic energy balance confirms the observations made previously on the eigenfrequencies. The differences observed on the frequencies are mainly due to the differences in the FTF gain. While the acoustic flux distribution remains similar for all R5x computations, the heat release source terms varies importantly, from nearly 50% of the initial acoustic energy for R5c (highest gain) to less than 25% for R5b (smallest gain).

Chapter 6

Conclusion

Complex flow-acoustic interactions can be the source of important acoustic damping in industrial combustors, at elements such as dilution holes or swirled injectors, because of the conversion of acoustics into vorticity at sharp edges which leads to the dissipation of acoustic energy. In this thesis, a methodology was developed in order to assess the effect of these interactions in a zero mean-flow Helmholtz solver. The methodology is based on an acoustic matrix formalism. Taking advantage of the fact the hydro-acoustic damping is a very local, compact mechanism, the damping elements are modeled by their equivalent 2×2 matrix, which accounts for dissipation effects. For simple elements such as circular orifices, this matrix can be determined analytically or from correlations. The strong point of the matrix approach is that more complex systems such as swirlers can also be included in the Helmholtz computation, since the matrix can be measured experimentally or numerically, with LES for example.

The matrix is included in the Helmholtz computation by means of a Matrix Boundary Condition. The methodology consisting in introducing matrices in the Helmholtz solver was therefore called the HMBC approach (Helmholtz with Matrix Boundary Condition). HMBC was successfully applied to an academic configuration : two tubes connected by either an orifice or a swirler, in the presence of a small axial inlet flow. With the HMBC methodology, the changes in frequency and damping rate introduced by the flow/acoustics interaction in the orifice or swirler are correctly captured, while a standard Helmholtz computation completely misses them.

However, the HMBC methodology with plane 1D matrices is difficult to apply on complex industrial geometries as it requires the use of plane surfaces for the matrix boundaries. Thus, an extended methodology is proposed. This extension makes it possible to apply the matrix methodology on any type of surface. It relies on two elements: 1) Average acoustic quantities are used instead of local ones. This is more consistent with the plane-wave approach where acoustics are characterized by two quantities, but is probably a source of error if the matrix patch is too large compared to the wavelength of the mode of interest. 2) Matrix data is obtained from a clean, 1D configuration, on well-defined plane surfaces. The matrix can be adjusted to suit a pair of complex surfaces by multiplying it with adjustment matrices. These matrices establish the link between the plane measurement surfaces and the complex surfaces of the final Helmholtz computation. They can be computed easily for any type of surface using an acoustics propagation solver.

The extension provides satisfactory results on the academic configuration, with both the orifice and the swirler. The correct frequencies and modes are obtained with adjusted matrix data, while non-adjusted matrices give completely wrong solutions.

In the case of the orifice, the adjustment matrices and the matrix data can be derived analytically. Thanks to this analytical model of the adjusted matrix, the existence of an intrinsic model for dilution holes was examined. Unfortunately, it was demonstrated that if the resistance of the orifice is indeed an intrinsic quantity, this is not the case of the reactance. The reactance depends on the confinement of the orifice (i.e. bounding effects due to walls or other orifices) that can be measured through a porosity or a section ratio in general. The dependency is stronger for Strouhal numbers close to 1, which happens quite often for the dilution holes of industrial combustors. However, first tests on a simple configuration show that the result of the Helmholtz computation might not be too sensitive to this effect at first order.

Another line of work was dedicated to modeling unsteady heat release for the prediction of combustion instabilities with the HMBC methodology. The main motivation behind this work is the incompatibility between the application of HMBC for a swirler and the use of a point-based Flame Transfer Function. Indeed, on industrial combustors, the flame is often anchored very close to the swirler and the reference point is chosen inside of it. This poses a problem when the swirler is removed from the geometry in HMBC. In this thesis, a variation of the Flame Transfer Function is proposed, where the reference velocity is obtained as the average over a reference surface. It was shown on the reactive LES of an industrial combustor that this approach seems to provide smoother signals that are more robust to the change of reference location.

The extended HMBC methodology with the surface-based FTF is finally applied to a full annular industrial combustor from Safran. The perforated plates are modeled with a homogeneous boundary condition that accounts for acoustic/bias flow interaction at the perforations. The effect of dilution holes and swirlers is included using analytical or LES matrix data. It is shown in particular that, while perforated plates have a minor damping effect, swirlers (to some extent) and dilution holes (more particularly), strongly dissipate acoustics in the combustor.

The application of surface-based FTF on the industrial geometry is less successful. Indeed, the apparent robustness of the reference velocities to the choice of the reference surface does not guarantee a similar robustness of the Helmholtz results. This issue is still under investigation and three suspects have been identified. First, the FTF might not be correctly measured, as the input signals of heat release and velocity were very noisy. Second, the FTF gain associated to reference surfaces is very high. Hence, a small error on the flame location / acoustic velocity at the reference surface or delay could lead to large modifications of the stability of the combustor. Third, the matrix boundary conditions could remove some of the acoustic velocity created at the flame, a mechanism that was also observed on a simple toy combustor. Indeed, the Matrix Boundary Condition only treats acoustics normal to matrix surfaces and discards any transverse component.

Despite these problems, it was demonstrated that the instabilities of a full annular combustor can be predicted with the HMBC approach combined to a surface-based FTF. The methodology therefore seems promising but a few warnings and bottlenecks have been identified.

Cost Clearly, the most expensive step of the HMBC methodology comes from the measurement of the matrix. It requires either long LES computations, or an experimental facility that it is not always available. While many analytical

models are available for dilution holes, the same cannot be said of swirlers. The computational cost could be reduced by using less accurate but cheaper solvers such as Lattice-Boltzmann methods or Linearized Navier-Stokes solvers. However, a better work plan would be to develop models and correlations for swirlers. The first step for this is to identify the key parameters controlling the behaviour of a swirler. Nothing was done on this topic during this thesis, but some good candidates would probably be : the mass flow rate, the number, angle and cross-section of the inlet vanes, the section of the outlet.

Matrix dependency with confinement tube The matrix is measured on a 1D tube of different cross-section than the final Helmholtz application. How to choose adequately this cross-section and what the impact on the final Helmholtz computation is remains unclear for now. The present computations indicate that the effect should be minor but this observation might not be generic.

Matrix dependency with mixture properties In this study, the matrix is always measured with pure air at non-reactive conditions, even when combustion is present in the final application. However, the matrix of a swirler might be very different under reactive and non-reactive conditions. Indeed, the presence of a flame downstream can greatly modify the flow. For example, a Precessing Vortex Core present under non-reactive conditions can disappear when combustion is introduced.

Surface-based FTF The concept of surface-based FTF was initiated in this work but many uncertainties remain about: 1) How to assess the quality of these FTFs ? 2) Do they really provide satisfactory results when combined to an HMBC geometry ?

To conclude, this work proposes a simple methodology to include complex flow-acoustic interactions into a zero mean flow Helmholtz solver. Combined with the adequate matrix data, this methodology provides a simple and relatively fast way of predicting combustion instabilities in the presence of hydro-acoustic damping. Because the damping elements are removed from the geometry, the associated meshes are lighter and simpler. For now, this does not directly translate into a reduction of the computational cost though. FTF with reference surfaces were introduced and could be an interesting alternative to traditional FTFs with reference points, provided the uncertain points of the previous paragraph find an answer.

Appendix A

Navier-Stokes Equations

The equations are written with the index notation. Summation rule is implied over repeated indices (Einstein's rule of summation). Indices i and j are reserved for space coordinates while index k is reserved for species. The Navier-Stokes equations are presented below for an ideal gas mixture composed of $k = 1, \ldots, N$ species, characterized by

- a mass fraction Y_k (or a mole fraction X_k),
- a molecular weight W_k,
- a diffusivity D_k,
- a specific sensible enthalpy $h_{s,k}$
- a specific formation enthalpy $\Delta h^o_{f,k}$.

The sum of all mass fractions is equal to 1 and it is easy to show that the molecular weight of the mix is $\frac{1}{W} = \sum_{k=1}^{N} \frac{1}{W_k}$. The medium is further assumed to act like a calorically perfect gas.

Conservation of mass

The global mass balance is expressed as:

$$\frac{\partial}{\partial t}\rho + \frac{\partial}{\partial x_i}\rho u_i = 0 \tag{A.1}$$

It is the sum of the conservation equations for each species k:

$$\frac{\partial}{\partial t}(\rho Y_k) + \frac{\partial}{\partial x_j}(\rho Y_k u_j) = -\frac{\partial}{\partial x_j}[J_{j,k}] + \dot{\omega}_k \tag{A.2}$$

In Eq. (A.2), $J_{i,k}$ is the i-th component of the diffusion flux of species k. It can be modeled with the Hirschfelder Curtis approximation, as done in AVBP.

$$J_{i,k} = -\rho \left(D_k \frac{W_k}{W} \frac{\partial X_k}{\partial x_i} - Y_k V_i^c \right) \tag{A.3}$$

with V_i^c the correction velocity

$$V_i^c = \sum_{k=1}^{N} D_k \frac{W_k}{W} \frac{\partial X_k}{\partial x_i} \tag{A.4}$$

Another term of Eq. (A.2) needs to be modeled: the reaction rate $\dot{\omega}_k$. In CFD codes, this information is usually provided by chemical schemes, composed of a series of elementary reactions and the associated rate constants, expressed as a function of pressure and temperature with the empirical Arrhenius law. Details are not provided here but can be found in most combustion textbooks, for example [3], chapter 1. As mentioned in Chapter 1, complete chemical schemes are too heavy to be transported in CFD codes but greatly condition the quality of the results. Many techniques are being developed to reduce these schemes while retaining a maximum of their properties. A good review can be found in [167].

Conservation of momentum

$$\frac{\partial}{\partial t}\rho u_j + \frac{\partial}{\partial x_i}\rho u_i u_j = -\frac{\partial p}{\partial x_j} + \frac{\partial \tau_{ij}}{\partial x_i} + \rho f_j \tag{A.5}$$

with p the pressure, f_j the volume force in the j-direction and τ_{ij} the viscous stress tensor. For a Newtonian isotropic fluid, τ_{ij} is given by:

$$\tau_{ij} = -\frac{2}{3}\mu \frac{\partial u_k}{\partial x_k}\delta_{ij} + \mu\left(\frac{\partial u_i}{\partial x_j} + \frac{\partial u_j}{\partial x_i}\right) \tag{A.6}$$

Conservation of energy

Many equivalent formulations of the conservation of energy are available. First, the conservation of total energy per unit mass E (sum of the internal energy and kinetic energy) can be expressed.

$$\frac{\partial}{\partial t}(\rho E) + \frac{\partial}{\partial x_j}(\rho E u_j) = -\frac{\partial}{\partial x_j}[u_i(p\delta_{ij} - \tau_{ij}) + q_j] + \dot{\omega}_T + Q_R \tag{A.7}$$

with q_j the heat flux of species j due to heat conduction (modeled with a Fourier Law) and species diffusion

$$q_j = -\lambda \frac{\partial T}{\partial x_i} + \sum_{k=1}^{N} J_{i,k} h_{s,k}, \tag{A.8}$$

$\dot{\omega}_T$ is the heat released by the chemical reactions (combustion), assumed to be the only source term in the energy equation.

$$\dot{\omega}_T = -\sum_{k=1}^{N} \dot{\omega}_k \Delta h^o_{f,k} \tag{A.9}$$

Alternatively, the energy equation can be expressed in terms of temperature:

$$\rho c_p \left(\frac{\partial T}{\partial t} + u_i \frac{\partial T}{\partial x_i} \right) = \left(\frac{\partial p}{\partial t} + u_i \frac{\partial p}{\partial x_i} \right) + \frac{\partial}{\partial x_i} \left(\lambda \frac{\partial T}{\partial x_i} \right) + \tau_{ij} \frac{\partial u_i}{\partial x_j} + \dot{\omega}_T \tag{A.10}$$

Or in terms of pressure, using the equation of state of an ideal gas $\gamma p = \rho c^2$, with $c = \sqrt{\gamma r T}$.

$$\frac{\partial p}{\partial t} + u_i \frac{\partial p}{\partial x_i} + \rho c^2 \frac{\partial u_i}{\partial x_i} = (\gamma - 1) \left[\frac{\partial}{\partial x_i} \left(\lambda \frac{\partial T}{\partial x_i} \right) + \tau_{ij} \frac{\partial u_i}{\partial x_j} + q \right] \tag{A.11}$$

Additionally, the conservation equation for energy can be replaced by the conservation equation for entropy.

$$\frac{\partial s}{\partial t} + u_i \frac{\partial s}{\partial x_i} = \frac{r}{p} \left[\frac{\partial}{\partial x_i} \left(\lambda \frac{\partial T}{\partial x_i} \right) + \tau_{ij} \frac{\partial u_i}{\partial x_j} + \dot{Q} \right] \tag{A.12}$$

Appendix B

Transition expressions between acoustic matrix formulations

In this chapter, some transition expressions between the different acoustic matrix formulations of Tab. 2.1 are provided. All transitions are not given here but can be retrieved by combining the expressions below. In order to simplify the notation, five constant matrices $\mathbf{J^{np}}$ $(n, p \in \{1, 2\})$ and Ω are defined as:

$$\begin{aligned} \mathbf{J^{11}} &= \begin{pmatrix} 1 & 0 \\ 0 & 0 \end{pmatrix} \\ \mathbf{J^{12}} &= \begin{pmatrix} 0 & 1 \\ 0 & 0 \end{pmatrix} \\ \mathbf{J^{21}} &= \begin{pmatrix} 0 & 0 \\ 1 & 0 \end{pmatrix} \\ \mathbf{J^{22}} &= \begin{pmatrix} 0 & 0 \\ 0 & 1 \end{pmatrix} \end{aligned} \tag{B.1}$$

$$\mathbf{\Omega} = \frac{1}{2}\begin{pmatrix} 1 & 1 \\ 1 & -1 \end{pmatrix} = \frac{1}{2}\mathbf{\Omega}^{-1} \tag{B.2}$$

Note also that the acoustic velocities are projected on a constant reference vector (same direction upstream and downstream) as done in most acoustic network studies. In the Helmholtz-MBC computation, an inward normal convention is chosen at the MBC surfaces (Fig. B.1) and the expressions below should be modified to account for the change of sign of $\hat{u}_u$.

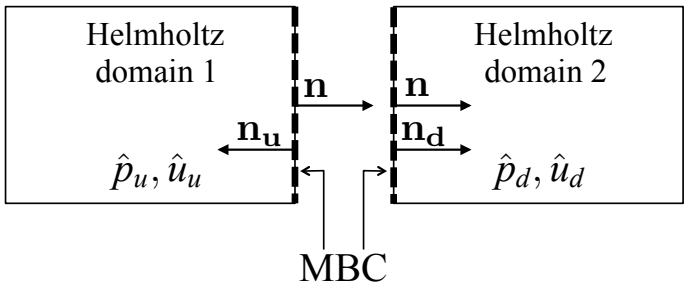


FIGURE B.1: Inward normal convention in the Helmholtz solver, compared with usual choice made in acoustic network analysis.

B.1 Scattering matrix S and wave transfer matrix $\mathbf{T_w}$

From scattering matrix $\mathbf{S}$ to wave transfer matrix $\mathbf{T_w}$:

$$\mathbf{T_w} = \left[\mathbf{J}^{11} - \mathbf{S}\mathbf{J}^{22}\right]^{-1}\left[\mathbf{S}\mathbf{J}^{11} - \mathbf{J}^{22}\right] \tag{B.3}$$

$$\mathbf{T_w} = \frac{1}{S_{22}}\begin{bmatrix} S_{11}S_{22} - S_{12}S_{21} & S_{12} \\ -S_{21} & 1 \end{bmatrix} \tag{B.4}$$

From wave transfer matrix $\mathbf{T_w}$ to scattering matrix $\mathbf{S}$:

$$\mathbf{S} = \left[\mathbf{J}^{11}\mathbf{T_w} + \mathbf{J}^{22}\right]\left[\mathbf{J}^{22}\mathbf{T_w} + \mathbf{J}^{11}\right]^{-1} \tag{B.5}$$

$$\mathbf{S} = \frac{1}{T_{w_{22}}}\begin{pmatrix} T_{w_{11}}T_{w_{22}} - T_{w_{12}}T_{w_{21}} & T_{w_{12}} \\ -T_{w_{21}} & 1 \end{pmatrix} \tag{B.6}$$

B.2 Wave transfer matrix $\mathbf{T_w}$ and acoustic transfer matrix $\mathbf{T_a}$

From wave transfer matrix $\mathbf{T_w}$ to acoustic transfer matrix $\mathbf{T_a}$:

$$\mathbf{T_a} = \mathbf{\Omega}^{-1}\mathbf{T_w}\mathbf{\Omega} \tag{B.7}$$

$$\mathbf{T_a} = \frac{1}{2}\begin{pmatrix} T_{w_{11}} + T_{w_{12}} + T_{w_{21}} + T_{w_{22}} & T_{w_{11}} - T_{w_{12}} + T_{w_{21}} - T_{w_{22}} \\ T_{w_{11}} + T_{w_{12}} - T_{w_{21}} - T_{w_{22}} & T_{w_{11}} - T_{w_{12}} - T_{w_{21}} + T_{w_{22}} \end{pmatrix} \tag{B.8}$$

Since Eq. B.7 is symmetric, superscripts a and w can be switched in the above equations to obtain the transition expressions from $\mathbf{T_a}$ to $\mathbf{T_w}$.

B.3 Acoustic transfer matrix $\mathbf{T_a}$ and mobility matrix M

From acoustic transfer matrix $\mathbf{T_a}$ to mobility matrix $\mathbf{M}$:

$$\mathbf{M} = \left[\mathbf{J}^{22} - \mathbf{T_a}\mathbf{J}^{21}\right]^{-1}\left[\mathbf{T_a}\mathbf{J}^{11} - \mathbf{J}^{12}\right] \tag{B.9}$$

$$\mathbf{M} = \frac{1}{T_{a_{12}}}\begin{pmatrix} -T_{a_{11}} & 1 \\ T_{a_{12}}T_{a_{21}} - T_{a_{11}}T_{a_{22}} & T_{a_{22}} \end{pmatrix} \tag{B.10}$$

From mobility matrix $\mathbf{M}$ to acoustic transfer matrix $\mathbf{T_a}$;

$$\mathbf{T_a} = \left[\mathbf{J^{22}}\mathbf{M} + \mathbf{J^{12}}\right]\left[\mathbf{J^{21}}\mathbf{M} + \mathbf{J^{11}}\right]^{-1} \tag{B.11}$$

$$\mathbf{T_a} = \frac{1}{M_{12}} \begin{pmatrix} -M_{11} & 1 \\ M_{12}M_{21} - M_{11}M_{22} & M_{22} \end{pmatrix} \tag{B.12}$$

Appendix C

Resolution of the Helmholtz equation with the AVSP solver

C.1 The Helmholtz problem

The Helmholtz problem is defined as follows: Find $\hat{p}(\mathbf{x})$ and ω solution of (1.24) in the bulk and satisfying the boundary conditions. In Eq. (1.24), a model is required for the heat release fluctuation $\hat{q}$. In AVSP, a distributed Flame Transfer Function is used, where the interaction index n_{local} and the time delay τ_{local} are space-dependent.

$$\hat{q}(\mathbf{x}) = n_{local}(\mathbf{x},\omega)e^{i\omega\tau_{local}(\mathbf{x},\omega)}\hat{\mathbf{u}}(\mathbf{x_{ref}})\cdot\mathbf{n_{ref}} \tag{C.1}$$

Eq. 1.17 can be combined to Eq. C.1 ($\hat{u}$ is replaced by $\frac{1}{\rho_o i\omega}\nabla\hat{p}$) to obtain a reactive Helmholtz equation with only $\hat{p}$ as acoustic variable.

$$\rho_o(\mathbf{x})c_o(\mathbf{x})^2\,\nabla\cdot\left(\frac{1}{\rho_o(\mathbf{x})}\nabla\hat{p}(\mathbf{x})\right)+\omega^2\hat{p}(\mathbf{x}) = \left[\gamma(\mathbf{x})-1\right]n_{local}(\mathbf{x},\omega)e^{i\omega\tau_{local}(\mathbf{x},\omega)}\frac{\nabla\hat{p}(\mathbf{x_{ref}})\cdot\mathbf{n_{ref}}}{\rho_o(\mathbf{x_{ref}})} \tag{C.2}$$

In order to solve Eq. C.2, the gradient and divergence operators must be discretized on the mesh for the computation $\hat{p}(x_{ref})$ and $\nabla\cdot\left(\frac{1}{\rho_o(\mathbf{x})}\nabla\hat{p}(\mathbf{x})\right)$. In AVSP, this is performed for unstructured meshes with a finite volume approach. The pressure $\hat{p}$ is stored at nodes and the gradients are computed at the cells. The principle of this discretization is recalled quickly here in 2D (3D extension is available and can be derived in a similar way). More details are available in the thesis of P. Salas [168].

C.2 Discretization of $\nabla\cdot\left(\frac{1}{\rho_o(\mathbf{x})}\nabla\hat{p}(\mathbf{x})\right)$ for interior nodes

Fig. C.1 depicts a triangle element Ω_{e1} in 2D, defined by three nodes j, 1, 2 and three edges $L_1\mathbf{n_1}$, $L_{a1}\mathbf{n_{a1}}$ and $L_{a2}\mathbf{n_{a2}}$. The gradient of pressure $\hat{p}$ is computed as the mean value over the cell:

$$\nabla\hat{p}\Big|_{\Omega_{e1}} = \frac{1}{S_{\Omega_{e1}}}\int_{\Omega_{e1}}\nabla\hat{p}dS \tag{C.3}$$

Using Green-Ostrogradsky theorem, the surface integral is expressed as:

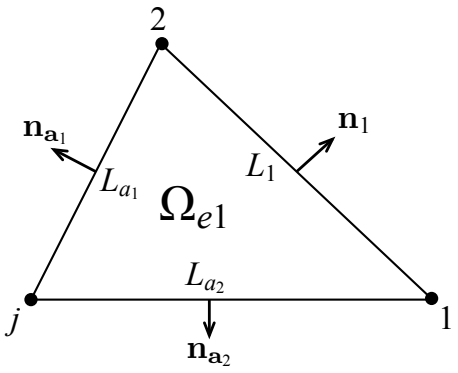


FIGURE C.1: Triangle cell element in 2D

$$\nabla\hat{p}\Big|_{\Omega_{e1}} = \frac{1}{S_{\Omega_{e1}}} \oint_{\partial\Omega_{e1}} \hat{p}\mathbf{n}dL \tag{C.4}$$

The line integral is computed assuming a linear evolution of the pressure on each edge and the gradient is finally recast as:

$$\nabla\hat{p}\Big|_{\Omega_{e1}} = \frac{1}{2S_{\Omega_{e1}}} \left[\hat{p}_j L_1 \mathbf{n_1} + \hat{p}_1 L_{a1} \mathbf{n_{a1}} + \hat{p}_2 L_{a2} \mathbf{n_{a2}}\right] \tag{C.5}$$

In order to compute $\nabla \cdot \left(\frac{1}{\rho_o(\mathbf{x})} \nabla\hat{p}(\mathbf{x})\right)$, the density ρ_o, stored at nodes, must be estimated at the element. This is simply done by averaging over the node values:

$$\frac{1}{\rho_o}\Big|_{\Omega_{e1}} = \frac{1}{3}\left(\frac{1}{\rho_{o,j}} + \frac{1}{\rho_{o,1}} + \frac{1}{\rho_{o,2}}\right) \tag{C.6}$$

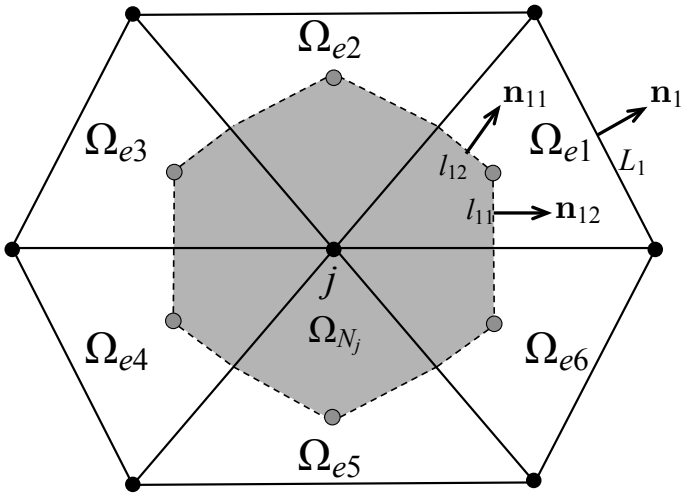


FIGURE C.2: 2D interior node j with its dual cell in grey.

Now, the divergence of $\frac{1}{\rho_o(\mathbf{x})} \nabla\hat{p}(\mathbf{x})$ must be computed at nodes. A dual cell Ω_{N_j} is defined for this purpose and represented in Fig. C.2 for an interior node. The dual cell is obtained by linking the centroid (intersection of medians) of each neighboring cell Ω_{ei} $(i = 1 \ldots 6)$ to the middle of the edges passing through j. The edges of the

dual cell are noted $l_{ij}\mathbf{n_{ij}}$ ($i = 1 \dots 6$, $j = 1, 2$ in 2D). As an example, l_{11} and l_{12} are represented in Fig. C.2.

As before, the divergence is evaluated as the mean value over the dual cell:

$$\nabla \cdot \left(\frac{1}{\rho_o(\mathbf{x})}\nabla\hat{p}(\mathbf{x})\right)\Big|_j = \frac{1}{S_{\Omega_{N_j}}} \int_{\Omega_{N_j}} \nabla \cdot \left(\frac{1}{\rho_o(\mathbf{x})}\nabla\hat{p}(\mathbf{x})\right) dS \tag{C.7}$$

And the surface integral is transformed into a line integral by applying Green-Ostrogradsky theorem:

$$\nabla \cdot \left(\frac{1}{\rho_o(\mathbf{x})}\nabla\hat{p}(\mathbf{x})\right)\Big|_j = \frac{1}{S_{\Omega_{N_j}}} \oint_{\partial\Omega_{N_j}} \frac{1}{\rho_o(\mathbf{x})}\nabla\hat{p}(\mathbf{x}) \cdot \mathbf{n}\, dS \tag{C.8}$$

The gradient of pressure is assumed uniform over each element Ω_{ei} ($i = 1 \dots 6$) and the line integrals over l_{ij} ($i = 1 \dots 6$, $j = 1, 2$) are straightforward.

$$\nabla \cdot \left(\frac{1}{\rho_o(\mathbf{x})}\nabla\hat{p}(\mathbf{x})\right)\Big|_j = \frac{1}{S_{\Omega_{N_j}}} \sum_{i=1}^{6} \left(\frac{1}{\rho_o}\nabla\hat{p}\right)\Big|_{\Omega_{ei}} \cdot (l_{i1}\mathbf{n_{i1}} + l_{i2}\mathbf{n_{i2}}) \tag{C.9}$$

The previous relationship can be simplified with an application of Thales theorem: $l_{i1}\mathbf{n_{i1}} + l_{i2}\mathbf{n_{i2}} = \frac{1}{2}L_i\mathbf{n_i}$.

$$\nabla \cdot \left(\frac{1}{\rho_o(\mathbf{x})}\nabla\hat{p}(\mathbf{x})\right)\Big|_j = \frac{1}{2S_{\Omega_{N_j}}} \sum_{i=1}^{6} \left(\frac{1}{\rho_o}\nabla\hat{p}\right)\Big|_{\Omega_{ei}} \cdot L_i\mathbf{n_i} \tag{C.10}$$

Using Eq. C.5 and Eq. C.6, replacing indices 1 and 2 by i and $i+1$ respectively, the gradient of pressure at each cell Ω_{ei} can be expressed as a function of the pressure at nodes and can be inserted into Eq. C.10 to obtain the expression of $\nabla \cdot \left(\frac{1}{\rho_o(\mathbf{x})}\nabla\hat{p}(\mathbf{x})\right)\Big|_j$ as a function of the pressure at node j and its immediate neighbors.

C.3 Discretization of $\nabla \cdot \left(\frac{1}{\rho_o(\mathbf{x})}\nabla\hat{p}(\mathbf{x})\right)$ for boundary nodes

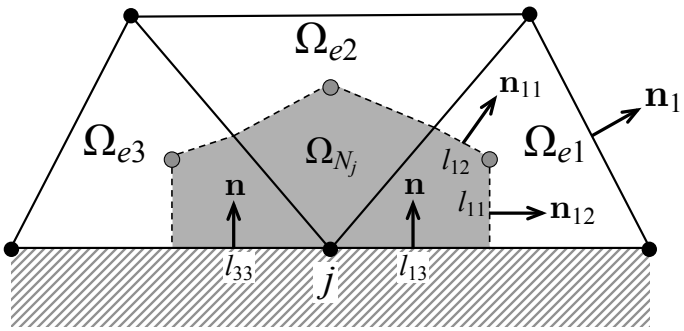


FIGURE C.3: 2D boundary node with its dual cell in grey. The boundary edge is represented by hatched lines.

For a boundary node such as the one of Fig. C.3, the dual cell is truncated. The quantity $\nabla \cdot \left(\frac{1}{\rho_o(\mathbf{x})} \nabla \hat{p}(\mathbf{x})\right)$ now depends on the gradient of the pressure along the boundary edges $l_{13}\mathbf{n}$ and $l_{33}\mathbf{n}$.

$$\begin{aligned} \nabla \cdot \left(\frac{1}{\rho_o(\mathbf{x})} \nabla \hat{p}(\mathbf{x})\right)\Big|_j = \frac{1}{S_{\Omega_{N_j}}} \Big[\sum_{i=1}^{3} \left(\frac{1}{\rho_o} \nabla \hat{p}\right)\Big|_{\Omega_{ei}} \cdot \frac{L_i}{2} \mathbf{n_i} \\ + \left(\frac{1}{\rho_o} \nabla \hat{p}\right)\Big|_{\Omega_{e1}} \cdot l_{13}\mathbf{n} \\ + \left(\frac{1}{\rho_o} \nabla \hat{p}\right)\Big|_{\Omega_{e3}} \cdot l_{33}\mathbf{n} \Big] \end{aligned} \tag{C.11}$$

Additional information is required and is provided by the boundary conditions. Unless a Dirichlet condition is imposed, in which case $\hat{p}_j$ is simply set to 0, the boundary condition can be expressed as a Robin condition.

$$(\nabla \hat{p} \cdot \mathbf{n} - \alpha\, \hat{p} + \beta)\Big|_j = 0 \tag{C.12}$$

This is used to express the gradient of pressure along $\mathbf{n}$.

$$\left(\frac{1}{\rho_o} \nabla \hat{p}\right)\Big|_{\Omega_{e1}} \cdot l_{13}\mathbf{n} + \left(\frac{1}{\rho_o} \nabla \hat{p}\right)\Big|_{\Omega_{e3}} \cdot l_{33}\mathbf{n} = \frac{1}{\rho_{o,j}}\, \alpha\, \hat{p}_j\, (l_{13} + l_{33}) \tag{C.13}$$

For a Neumann boundary,

$$\alpha = 0, \beta = 0 \tag{C.14}$$

For a boundary of impedance $Z(\omega)$,

$$\alpha = \frac{i\omega}{c_o Z(\omega)}, \beta = 0 \tag{C.15}$$

For the Matrix Boundary Condition, with the notation of Section 2.3:

Upstream patch:

$$\alpha = M_{11}(\omega) \frac{i\omega}{c_{o,u}}, \beta \quad = M_{12}(\omega) \frac{i\omega}{c_{o,d}} \frac{\rho_{o,u}}{\rho_{o,d}} \hat{p}_d \tag{C.16}$$

Downstream patch:

$$\alpha = M_{22}(\omega) \frac{i\omega}{c_{o,d}}, \beta \quad = M_{21}(\omega) \frac{i\omega}{c_{o,u}} \frac{\rho_{o,d}}{\rho_{o,u}} \hat{p}_u \tag{C.17}$$

C.4 Discretized Helmholtz equation and fixed point iteration

Once discretized, the Helmholtz equation can be written as an eigenvalue problem:

$$\mathbf{A}\hat{p} + \mathbf{B}(\omega) + \omega^2\hat{p} = \mathbf{C}(\omega)\hat{p} \tag{C.18}$$

with:

- $\mathbf{A}$ is a symmetric operator corresponding to the discretization of $\nabla\cdot\left(\frac{1}{\rho_o(\mathbf{x})}\nabla\hat{p}(\mathbf{x})\right)$
- $\mathbf{B}(\omega)$ is a frequency-dependent operator aggregating all boundary condition terms. It is non-zero only for boundary nodes.
- $\mathbf{C}(\omega)$ is another frequency-dependent operator corresponding to the flame source term.

As Eq. (C.18) shows, this eigenvalue problem is linear when no flame or complex impedance boundaries are present. In this case, the problem can be solved efficiently with classical algorithms for large and sparse eigenproblems, as presented in [168]. Otherwise, the eigenproblem is nonlinear with respect to the eigenvalue and this is solved in AVSP with the use of a fixed point iteration [17]. The principle of the fixed point iteration is the following (Fig. C.4).

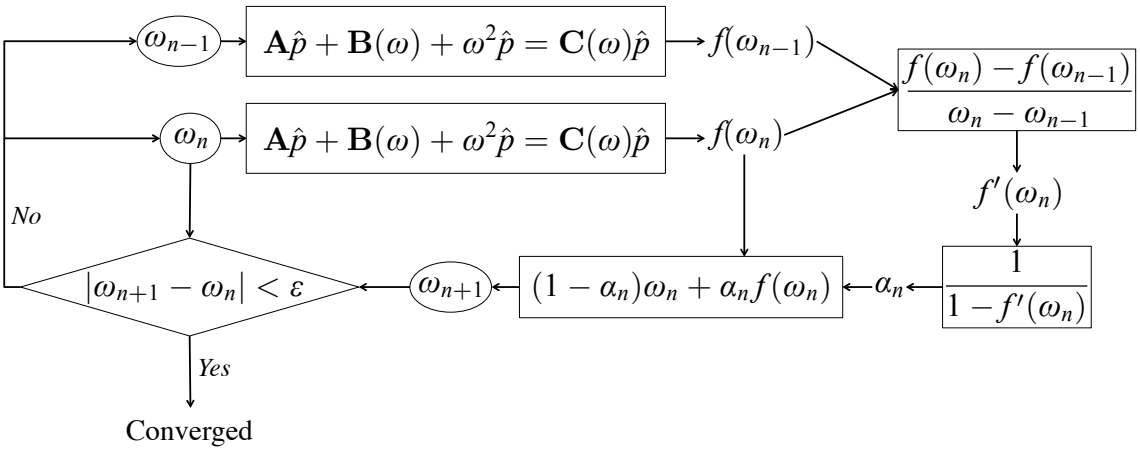


FIGURE C.4: Fixed point iteration in AVSP. For clarity, the limiter Δ is not represented.

Initialization

1. Choose an initial guess ω_o to initialize all frequency dependent operators.
2. Solve the linearized eigenproblem with $B(\omega_o)$ and $C(\omega_o)$. Only the closest frequency to ω_o is retained and is called $f(\omega_o)$. The function $f(\omega)$ corresponds to the process that associates to any complex ω the closest eigenfrequency of the Helmholtz problem (C.18).
3. Set a new target $\omega_1 = f(\omega_o)$

Recurrence At the n-th iteration (n>1):

1. Solve the linearized eigenproblem with $B(\omega_n)$ and $C(\omega_n)$. This yields a solution of frequency $f(\omega_n)$.
2. Set a new target ω_{n+1} using relaxation.

$$\omega_{n+1} = (1-\alpha_n)\omega_n + \alpha_n f(\omega_n) = g_{\alpha_n}(\omega_n) \tag{C.19}$$

The value of the relaxation coefficient α_n is optimized in order to ensure/accelerate the convergence process. Indeed, the fixed point iteration with relaxation converges only if

$$|g'_{\alpha_n}| < 1 \tag{C.20}$$

The value of α_n is therefore chosen at each iteration so that $g'_{\alpha_n} = 0$.

$$\alpha_n = \frac{1}{1 - f'(\omega_n)} \tag{C.21}$$

The derivative f' is unknown and is estimated with a simple finite difference.

$$f'(\omega_n) \approx \frac{f(\omega_n) - f(\omega_{n-1})}{\omega_n - \omega_{n-1}} \tag{C.22}$$

In order to avoid the new guess ω_{n+1} to stray too far from the previous value ω_n (this could happen because of a bad estimation of f' for example), a limiter Δ is set. If $|\omega_{n+1} - \omega_n| > \Delta$, ω_{n+1} is replaced by

$$\omega_{n+1} = \omega_n + \Delta \exp(i\phi) \quad \text{with} \quad \phi = \arg(\omega_{n+1} - \omega_n) \tag{C.23}$$

The procedure to derive the next guess (automatic computation of the relax coefficient and use of a limiter) was developed by M. Miguel-Brebion and E. Courtine from Institut de Mecanique des Fluides de Toulouse.

3. Repeat step (2) and step (3) until convergence is reached, i.e. $|\omega_{n+1} - \omega_n| < \epsilon$ with ϵ the value of the tolerance.

This fixed-point approach mimics Newton's method for the function $F(\omega) = f(\omega) - \omega$ if (C.22) is exact.

Appendix D

Analytical models for the acoustic behaviour of an orifice with bias flow

The acoustic behaviour of an orifice with bias flow has been studied for a long time, experimentally [169, 111, 170, 112, 113, 158, 171] or numerically [121, 98, 99]. Many analytical models are also available and the works of [170, 111, 112, 103, 171, 121] is only a non exhaustive list. In this thesis, only two models were considered: the famous model of Howe [111] and an adaption proposed by Bellucci [158]. The strong point of Bellucci's model is to include a simple dependency of the reactance with the bias flow U_{ori} and the porosity σ.

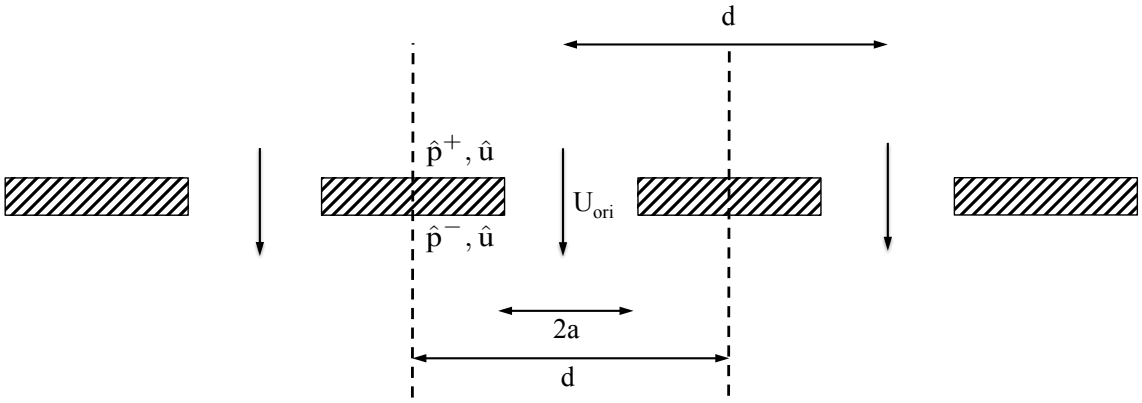


FIGURE D.1: Quantities of interest for the acoustic behavior of an orifice in bias flow.

Both of these models start from the observation that an acoustic plane wave is modified when traveling across a perforated plate. Unlike the plane-wave velocity $\hat{u}$, the plane-wave pressure $\hat{p}$ is discontinuous. This discontinuity is present even in the absence of mean flow and was studied first by Lord Rayleigh [157]. He characterized the pressure discontinuity with a quantity known as the Rayleigh conductivity K_R.

$$K_R = \frac{i\rho_o\omega\hat{G}}{[\hat{p}^+ - \hat{p}^-]} \tag{D.1}$$

where $\hat{G} = d^2\hat{\mathbf{u}} \cdot \mathbf{n}$ is the acoustic volume flow rate through the plate (Fig. D.1). With this quantity, the jump conditions across an orifice can be expressed in matrix form as:

$$\mathbf{T} = \begin{pmatrix} 1 & 2\xi \\ 0 & 1 \end{pmatrix} \text{ (Acoustic transfer matrix)} \tag{D.2}$$

$$\mathbf{S} = \frac{1}{1-\xi}\begin{pmatrix} 1 & -\xi \\ -\xi & 1 \end{pmatrix} \text{ (Scattering matrix)} \tag{D.3}$$

with $\xi = \frac{i\omega d^2}{2c_o K_R}$. The real part of ξ is linked to the resistance of the orifice and its sign determines its damping or amplifying (in the case of whistling) behaviour[1]. The imaginary part of ξ is linked to the the reactance of the orifice and does not introduce any damping or growth rate. Similarly, the imaginary part of K_R determines the damped / amplified behaviour of the orifice, while the real part of K_R has no effect on its stability. For an inviscid fluid with zero mean flow, the theoretical value of K_R for an orifice of radius a in an infinite plate of zero thickness is real and equal to $2a$ [157].

D.1 The model of Howe

In the presence of a viscous mean flow, an unstable shear layer is created at the edges of the orifice and can couple with the acoustics through viscous effects. In the model of Howe [111], this coupling always leads to an acoustic damping and the corresponding Rayleigh conductivity is:

$$K_R = 2a(\Gamma_{St} - i\Delta_{St}) \tag{D.4}$$

Γ_{St} and Δ_{St} are two real valued functions of the Strouhal number defined with the orifice bias-speed as $St = \dfrac{\omega a}{U_{ori}}$ (Fig. D.2).

$$\Gamma_{St} - i\Delta_{St} = 1 + \frac{\frac{\pi}{2} I_1(St)\mathrm{e}^{-St} - iK_1(St)\sinh(St)}{St(\frac{\pi}{2} I_1(St)\mathrm{e}^{-St} + iK_1(St)\cosh(St))} \tag{D.5}$$

Remarks:

- In the limit $St \to \infty$, the model of Howe degenerates into the theoretical value of Rayleigh.
- A simpler fit of Howe's model, derived from physical considerations, has been provided by Luong [103].
- For a plate of finite thickness h, an acceptable approximation of K_R is:

$$K_R = 2a\left(\frac{1}{\Gamma_{St} - i\Delta_{St}} + \frac{2h}{\pi a}\right)^{-1} \tag{D.6}$$

- Howe's model can also be used to compute the Rayleigh conductivity of one perforation in a circular plate of finite size, if the interaction with the outer casing is neglected (i.e. the plate if big enough compared to the orifice). In this

[1] This can be proved by computing the different between the upstream and downstream acoustic flux $\frac{1}{2}\Re[(\hat{p}^+ - \hat{p}^-)\hat{G}^*)]$

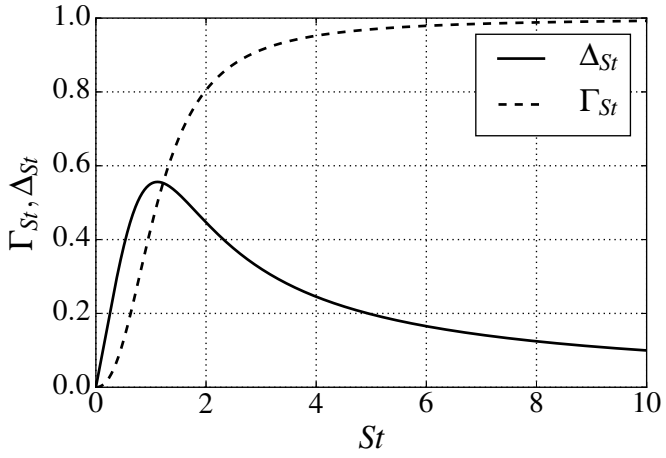


FIGURE D.2: Evolution of Γ_{St} and Δ_{St} with the Strouhal number.

case, the average distance between perforations d is replaced by $\sqrt{\pi}R$ with R the radius of the plate.

D.2 The model of Bellucci

In the model of Bellucci, the interaction between orifices, or with an outer casing is considered, but only for the reactance. This is supported by their own experiments but also by observations from Lee et al. [171]. Lee et al. noted relatively little change in the resistance compared to the reactance, when the porosity parameter was varied. For this reason, Bellucci et al. use the resistance of the model of Howe [111] for the resistance $\mathcal{R} = \Re(2\xi)$, but propose a new expression for the reactance $\mathcal{X} = \Im(2\xi)$.

$$\mathcal{R} = \Re\left(\frac{i\omega d^2}{c_o K_R}\right) \tag{D.7}$$

$$\mathcal{X} = k\frac{2\ell + h}{\sigma} \tag{D.8}$$

The quantity ℓ accounts for the end correction at the two ends of the orifice. It is defined by Bellucci et al. as:

$$\ell = \phi(He)\chi(\sigma)\psi(St)\theta(St_{ac}) \tag{D.9}$$

with $He = ka$ the Helmholtz number, σ the porosity, St the Strouhal number and $St_{ac} = \frac{\omega a}{u_{ac}}$ the acoustic Strouhal number. The functions ϕ, χ, ψ, and θ mainly come from experimental fits or correlations and have the following expressions:

$$\phi(He) = 0.8216a\left(1 + \frac{(0.77He)^2}{1 + 0.77He}\right)^{-1} \tag{D.10}$$

$$\chi(\sigma) = 1 - \sqrt{\frac{\sigma}{2}} \tag{D.11}$$

$$\psi(St) = \frac{0.3(6.0/\ St^2) + 1}{6.0/\ St^2 + 1} \tag{D.12}$$

$$\theta(St_{ac}) = 1 - \frac{0.3}{St_{ac}^{0.6}} \tag{D.13}$$

In this thesis, nonlinear hydro-acoustic damping was neglected so that $St_{ac} \to \infty$ and $\theta = 1$. Fig. D.3 shows the normalized reactance $\sigma\mathcal{X}$ as a function of frequency, for Howe's model and Bellucci's model, for an orifice of radius $a = 0.009$ m, thickness $h = 0.002$ m, bias flow velocity $U_{ori} = 10.0$ m/s and values of σ ranging from 0.0003 to 0.8.

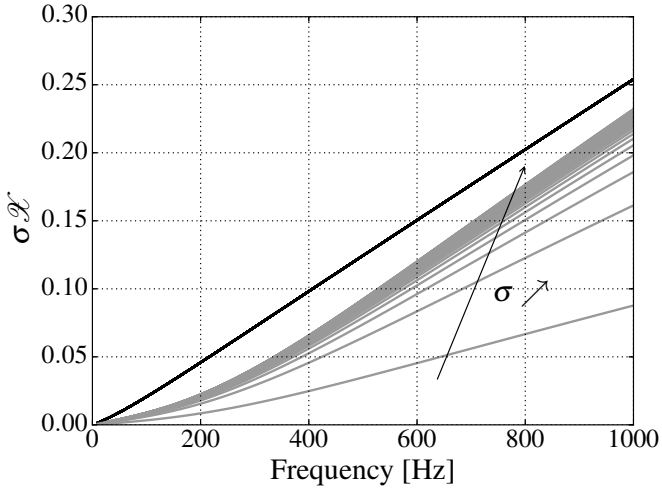


FIGURE D.3: Reactance of an orifice with Howe's model and Bellucci's model.

The validity of Bellucci's model was tested by comparing it to LES matrices of two configurations.

- The orifice in a tube of Chapter 3.
- The same orifice in a confinement tube of cross-section four times larger. The bias flow velocity in the orifice is kept constant by dividing the inlet bulk velocity by four.

As Fig. D.4 and Fig. D.5 show, Bellucci's model provide a better estimation of the imaginary part of T_{12} for both configurations and performs exactly as Howe's model for the other coefficients.

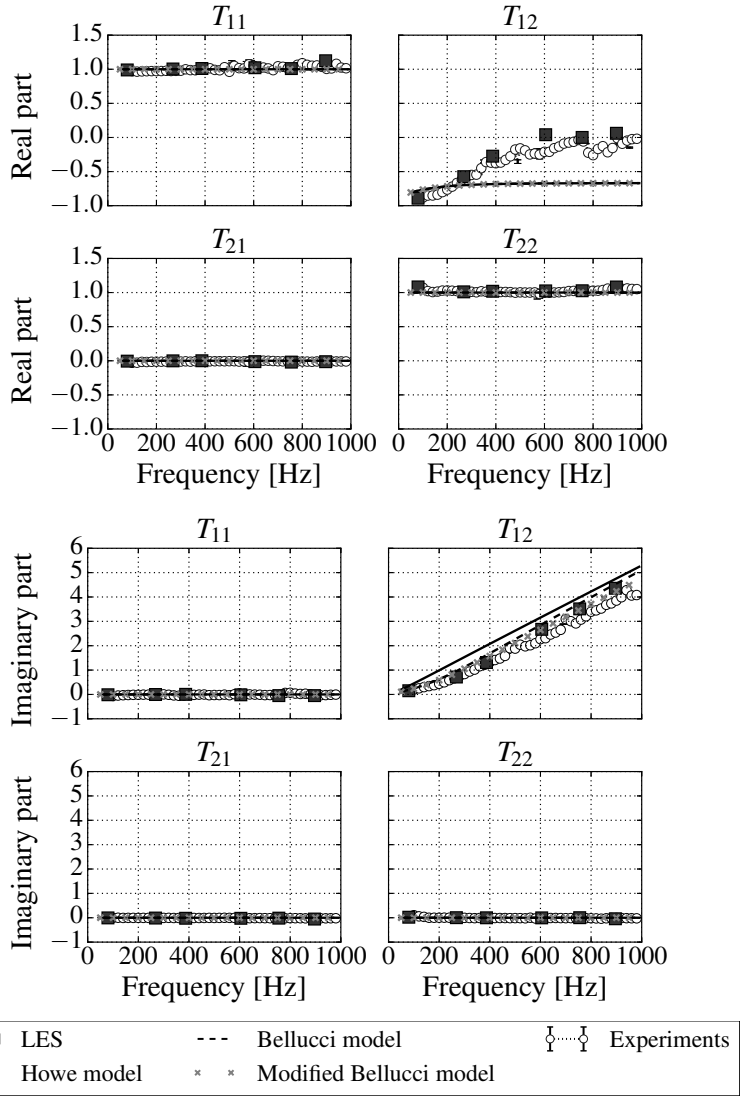


FIGURE D.4: LES transfer matrix vs Howe's model and Bellucci's model for the orifice of Chapter 3 ($U = 0.34$ m/s). Top: real part. Bottom: imaginary parts. In grey crosses, the result for the modified Bellucci model of Chapter 4 is also indicated.

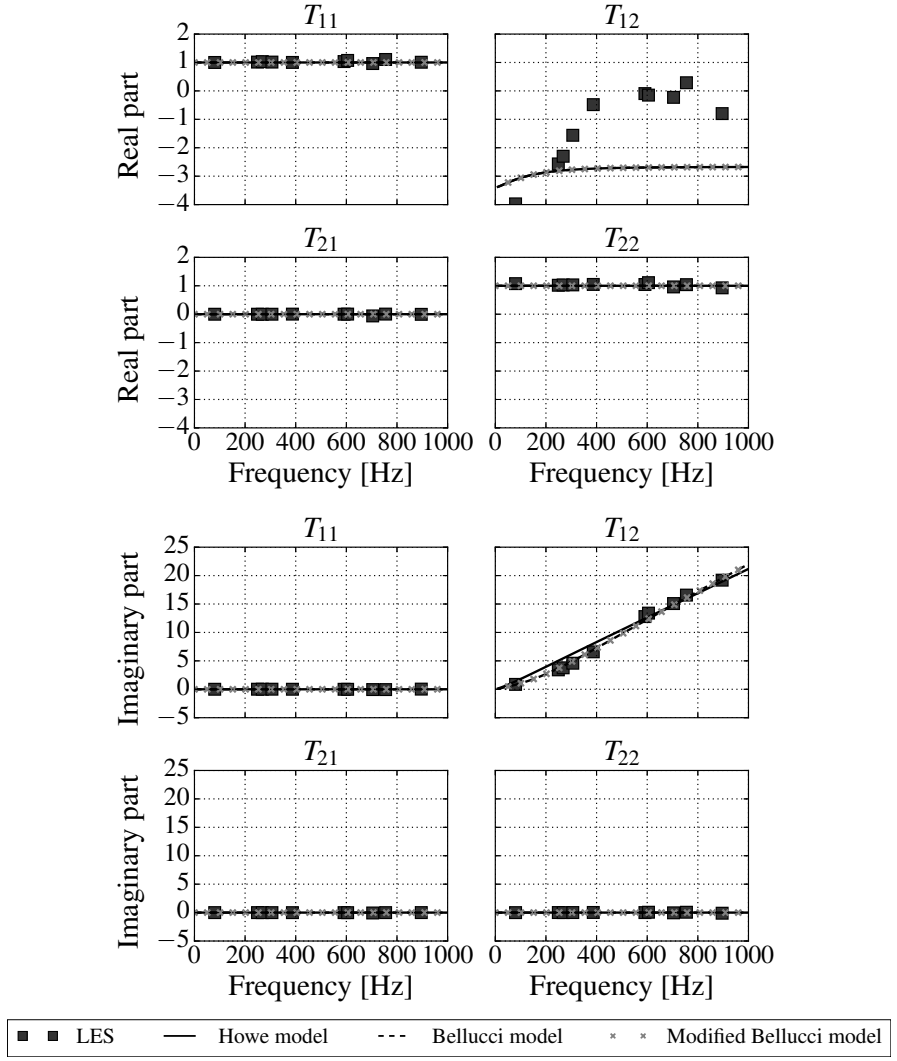


FIGURE D.5: LES transfer matrix vs Howe's model and Bellucci's model for the orifice of Chapter 3 in a larger confinement tube ($U = 0.34$ m/s). Top: real part. Bottom: imaginary parts. In grey crosses, the result for the modified Bellucci model of Chapter 4 is also indicated.

Appendix E

Analytical expressions of α for disks and half-spheres

For disks discretized by a regular inscribed polygon, α can be estimated as a function of the disk radius a and the mesh size dx.

$$\alpha(a, dx) = \frac{1}{1 + \frac{2\frac{dx}{a}}{\sqrt{1 - (\frac{1}{2}\frac{dx}{a})^2)}}} \tag{E.1}$$

A simple expression can also be determined for a half-sphere if we assume that the surface of the sphere is approximately equal to twice that of a disk of same radius.

$$\alpha(a, dx) = \frac{1}{1 + \frac{\frac{dx}{a}}{\sqrt{1 - (\frac{1}{2}\frac{dx}{a})^2)}}} \tag{E.2}$$

Appendix F

Analytical models and correlations for the correction length l_{eq}

In this appendix, the models used in the manuscript for the acoustic correction length of an orifice in the absence of mean flow and viscosity are recalled briefly in Section F.1. These models assume that the orifice geometry is perfectly discretized. As this is not the case in our Helmholtz computations, a new correlation is derived in Section F.2. For all models, the geometry is described with the notation of Fig. F.1.

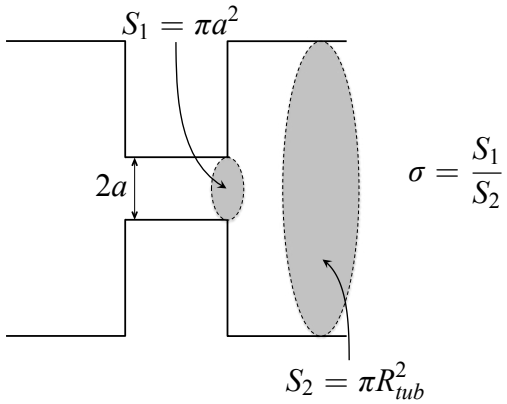


FIGURE F.1: Typical orifice geometry.

F.1 Existing models and correlations

F.1.1 Model of Rayleigh

Rayleigh [157] derived the equivalent length of an orifice in an infinite plate of zero thickness and found a value of $\frac{\pi}{2}a$. The correction length, on each side of the orifice, is then equal to half of this value.

$$\textbf{Rayleigh model} \quad \frac{l_{eq}}{a} = \frac{\pi}{4} \tag{F.1}$$

F.1.2 Model of Bellucci et al. at $M \ll 1$

The model of Bellucci [158], presented in Appendix D, can be used to obtain the correction length of an orifice with zero mean flow and small acoustic amplitudes, as is the case in our Helmholtz solver. It is actually the combination of a correlation for the correction length of a section change with an infinite flange [172], and a model for the interaction with walls or other orifices [161].

$$\textbf{Bellucci model} \quad \frac{l_{eq}}{a} = 0.8216 \left[1 + \frac{(0.77He)^2}{1 + 0.77He}\right]^{-1} \left[1 - \sqrt{\frac{\sigma}{2}}\right] \tag{F.2}$$

with $He = ka$, the Helmholtz number.

F.1.3 Correlation of Kang et al.

In the work of Kang et al. [159], the correction length of many section changes with different section ratios is computed with 2D-axisymmetric FEM solver. The correlation below is deduced from this database. Although the mesh resolution seems fine in the spatial visualizations, no information about it is provided in the article.

$$\textbf{Kang model} \quad \frac{l_{eq}}{a} = 0.8216 - 1.0795\sqrt{\sigma} \tag{F.3}$$

F.2 Determination of a new correlation for l_{eq}

Since none of the three models/correlations above take into account the orifice mesh resolution $\eta = dx/a$, a new correlation for l_{eq} was derived in this thesis. For this, the acoustic matrix of geometries similar to the ones of Fig. 4.24 was measured with AVSP-f for the acoustic quantities of Fig. 4.23, for different sizes of the confinement tube and different mesh sizes dx (Tab. F.1). The radius of the orifice is set to 0.009 m but the effective radius is mesh dependent and estimated as $\sqrt{S/\pi}$, with S the discretized orifice surface (Tab. F.2). The matrix should be equal to:

$$\mathbb{T} = \begin{pmatrix} 1 & ikl_{eq} \\ 0 & \sigma \end{pmatrix} \tag{F.4}$$

$\sqrt{\sigma}$ \ η	**1.0**	**0.4**	**0.2**	**0.1**
0.50	A0	A1	A2	A3
0.22	B0	B1	B2	B3
0.10	C0	C1	C2	C3
0.05	D0	D1	D2	D3

TABLE F.1: Configurations used for the determination of a new correlation for l_{eq}

The values of l_{eq} and σ are estimated by performing respectively a linear fit and a constant fit of coefficients T_{12} and T_{21}. As an example, the matrix obtained for case A0 is plotted in Fig. F.2, with the fits in question.

Mesh number	0	1	2	3
$\boldsymbol{\eta}$	1.0	0.4	0.2	0.1
a	0.00854	0.00888	0.00897	0.00899

TABLE F.2: Discretized orifice radius a for each mesh size.

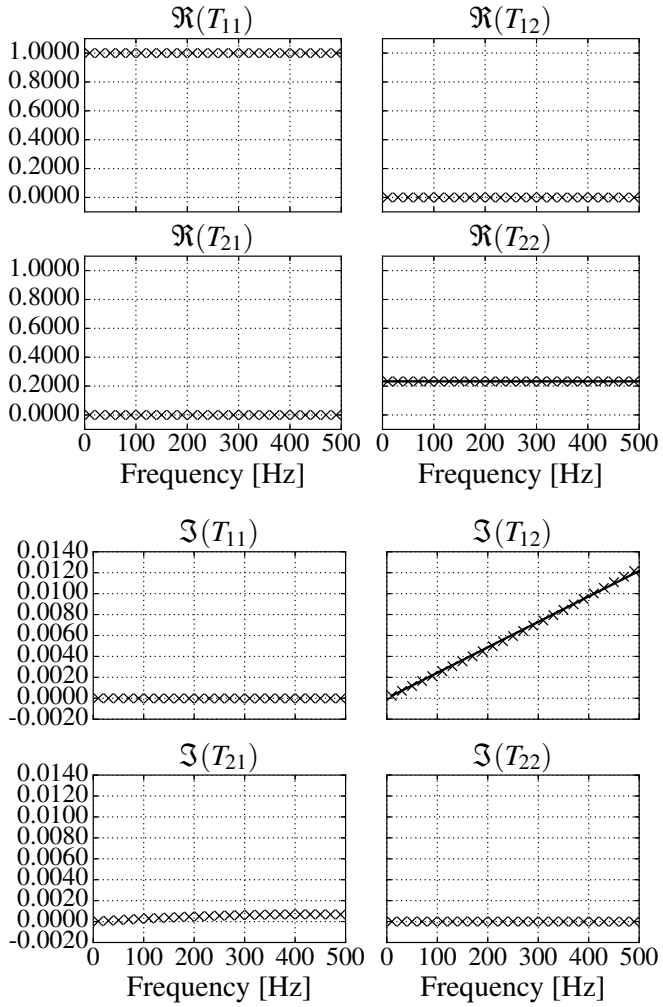


FIGURE F.2: Matrix of configuration A0 (crosses) and fits for l_{eq} and σ (solid lines).

Following the correlations of Bellucci et al. [158] and Kang et al. [159], the evolution of l_{eq}/a with $\sqrt{\sigma}$ is fitted with a linear function for each mesh resolution (Fig. F.3). Note that the value of the radius a in l_{eq}/a is the one of Tab. F.2

The coefficients A and B of the fit $l_{eq} = A\sqrt{\sigma} + B$ are then plotted against the mesh resolution η (Fig. F.4). For the constant coefficient a, no specific function seems to fit the data. Therefore, A was set to its average value $A = -1.085$. Coefficient B can be approximated by a linear function $B = 0.875 - 0.211\eta$, with a correlation coefficient of 0.99.

These expressions of A and B are finally combined into a new correlation, called η-correlation in the rest of the manuscript.

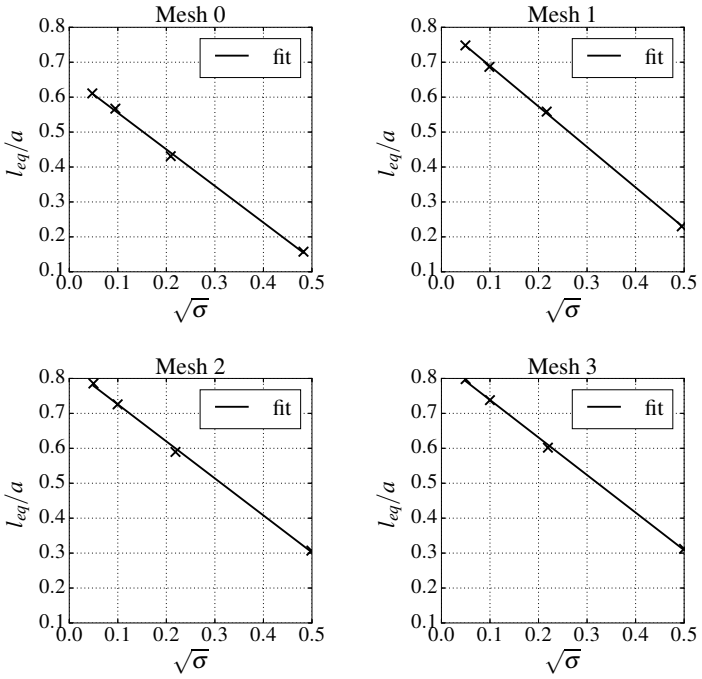


FIGURE F.3: Evolution of l_{eq} with $\sqrt{\sigma}$ for different mesh resolutions (crosses) and associated linear fit (solid lines).

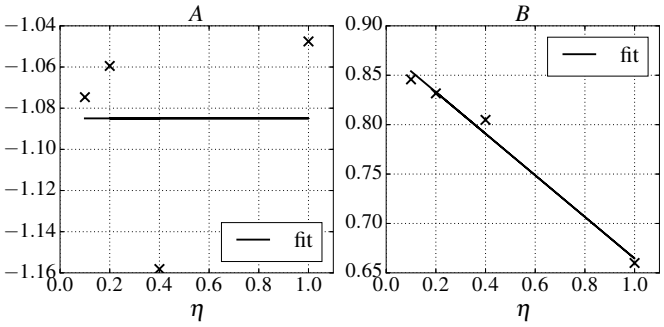


FIGURE F.4: Evolution of A and B with η.

$$\textbf{η-correlation} \quad \frac{l_{eq}}{a}(\eta,\sigma) = 0.875(1 - 1.240\sigma - 0.240\eta) \tag{F.5}$$

Appendix G

Acoustic flux balance criterion for the SAFRAN swirler

G.1 Acoustic flux balance for matrix jump conditions

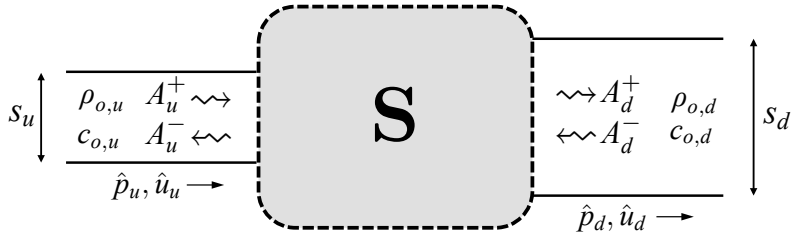


FIGURE G.1: Acoustic two-port with different up- and downstrea thermodynamic properties and sections.

Consider a set of matrix jump conditions such as the one depicted in Fig. G.1, linking an upstream and downstream states characterized by different cross-sections, densities and sound speeds. Assuming there is no source term in the system of Fig. G.1, acoustic energy is lost/gained due to acoustic fluxes. The power dissipated in the system can be derived as a function of the up- and downstream pressure and velocity.

$$P_{dis} = \frac{s_u}{2} \Re[\hat{p}_u \hat{u}_u^*] - \frac{s_d}{2} \Re[\hat{p}_d \hat{u}_d^*] \tag{G.1}$$

where * denotes the complex conjugate. The acoustic pressure and velocity can be decomposed as a sum of two plane wave amplitudes:

$$\hat{p}_{ud} = A_{ud}^+ + A_{ud}^- \tag{G.2}$$

$$\hat{u}_{ud} = \frac{1}{\rho_{o,ud}\, c_{o,ud}} (A_{ud}^+ - A_{ud}^-) \tag{G.3}$$

With these plane wave amplitudes, the dissipated power is expressed as:

$$P_{dis} = \frac{s_u}{2\rho_{o,u}c_{o,u}} (|A_u^+|^2 - |A_u^-|^2) - \frac{s_d}{2\rho_{o,d}c_{o,d}} (|A_d^+|^2 - |A_d^-|^2) \tag{G.4}$$

Two vectors Y_{in} and Y_{out} are now introduced to characterize the in- and outgoing acoustic states.

$$Y_{\text{in}} = \begin{pmatrix} \sqrt{\dfrac{s_u}{\rho_{o,u}c_{o,u}}}A_u^+ \\ \sqrt{\dfrac{s_d}{\rho_{o,d}c_{o,d}}}A_d^- \end{pmatrix} \tag{G.5}$$

$$Y_{\text{out}} = \begin{pmatrix} \sqrt{\dfrac{s_d}{\rho_{o,d}c_{o,d}}}A_d^+ \\ \sqrt{\dfrac{s_u}{\rho_{o,u}c_{o,u}}}A_u^- \end{pmatrix} \tag{G.6}$$

These two vectors are related to each other with a variant of the scattering matrix $\tilde{\mathbf{S}}$.

$$Y_{\text{out}} = \tilde{\mathbf{S}} Y_{\text{in}}, \tag{G.7}$$

with $\tilde{\mathbf{S}}$ defined as a function of the regular scattering matrix $\mathbf{S}$ (Tab. 2.1) as:

$$\tilde{\mathbf{S}} = \begin{pmatrix} \sqrt{\dfrac{s_d}{\rho_{o,d}c_{o,d}}} & 0 \\ 0 & \sqrt{\dfrac{s_u}{\rho_{o,u}c_{o,u}}} \end{pmatrix} \mathbf{S} \begin{pmatrix} \sqrt{\dfrac{\rho_{o,u}c_{o,u}}{s_u}} & 0 \\ 0 & \sqrt{\dfrac{\rho_{o,d}c_{o,d}}{s_d}} \end{pmatrix} \tag{G.8}$$

When the up- and downstream sections, sound speeds and densities are equal as it was the case in Sections 3.5 and 3.6, $\tilde{\mathbf{S}}$ reduces to $\mathbf{S}$. The dissipated power has a very simple expression when introducing the vectors Y_{in} and Y_{out}.

$$\Delta F = Y_{\text{in}}^\dagger Y_{\text{in}} - Y_{\text{out}}^\dagger Y_{\text{out}} \tag{G.9}$$

$$\Delta F = Y_{\text{in}}^\dagger \left(\mathbb{I} - \tilde{\mathbf{S}}^\dagger \tilde{\mathbf{S}} \right) Y_{\text{in}} \tag{G.10}$$

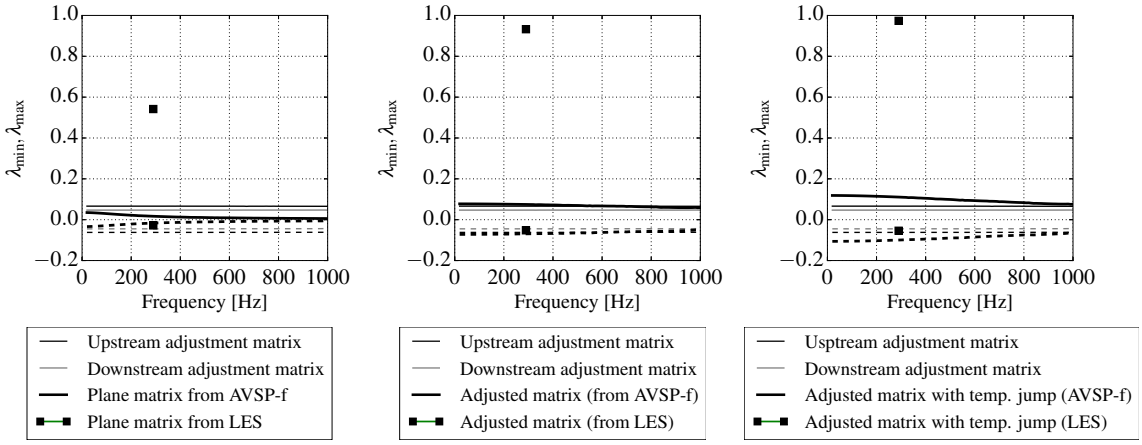
Equation (G.10) shows that the quantities of interest for the evaluation of the dissipated power are indeed the eigenvalues of $\mathbb{I} - \tilde{\mathbf{S}}^\dagger \tilde{\mathbf{S}}$. The present analysis in in fact a simplified form of the derivation proposed by Auregan and Starobinski [154], with a different notation and assuming that the mean flow is zero.

G.2 Eigenvalues of $\mathbb{I} - \tilde{\mathbf{S}}^\dagger \tilde{\mathbf{S}}$ for the SAFRAN swirler

In Section 5.5.2, a Helmholtz computation of the SAFRAN combustor is performed by replacing all swirlers by their equivalent purely acoustic (non-dissipative) matrices. In contrast to what is expected, the damping rate is increased when doing so. A plausible explanation is that the purely acoustic matrix after adjustment does not

lead to a perfectly zero acoustic flux balance. This could be due to small errors in the numerical measurement of the acoustic and adjustment matrices.

To check this, the criterion from [154] is applied, by plotting the eigenvalues of $\tilde{\mathbf{S}}^\dagger\tilde{\mathbf{S}} - \mathbb{I}$, with $\tilde{\mathbf{S}}$ defined in Eq. (G.8), for the plane cold non-dissipative matrix, the adjusted cold non-dissipative matrix, the adjusted non-dissipative matrix with temperature jumps (Fig. G.2). In addition, Fig. G.2 also provides the result of the criterion for the LES plane and adjusted matrices, and the adjustment matrices. For the plane non-dissipative matrix, the eigenvalues are very close to zero as expected in a situation where the acoustic flux is conserved. Adjustment matrices also feature eigenvalues reasonably close to zero. However, the eigenvalues for the non-dissipative adjusted matrix with temperature correction move away from this ideal situation. Since these eigenvalues are of opposite sign, the associated matrix can either amplify or damp acoustics and this could explain the additional damping rate observed in R3a. On way to reduce this error in future works would be to add the constraint that $\mathbb{I} - \tilde{\mathbf{S}}^\dagger\tilde{\mathbf{S}} = 0$ in the least-square system of Eq. (2.3), but this was not done here due to a lack of time.



(A) Plane matrices. (B) Adjusted matrices. (C) Adjusted matrices with temperature jump.

FIGURE G.2: Eigenvalues of $\mathbb{I} - \tilde{\mathbf{S}}^\dagger\tilde{\mathbf{S}}$ for the plane matrices (left), adjusted matrices (middle) and adjusted matrices with temperature jump (right). On each plot, the eigenvalues of the adjustment matrices are also recalled.

Appendix H

Helmholtz computations of the SAFRAN combustor with active flames only

In Section 5.6, surface-based Flame Transfer Functions (FTF) are computed in the reactive LES of one sector of the SAFRAN combustor. In order to assess their quality, the surface-based FTFs obtained at three different surfaces S1, S2 and S3 (Fig. 5.21) are included in a simplified Helmholtz solver setup, where the flame is the only element impacting the growth/damping rate (setup R4 in Tab. 5.1). No dissipative model is used for the perforated plates, dilution holes and swirlers. Perforated plates are represented by homogeneous walls, while dilution holes and swirlers are fully discretized. The variability of the Helmholtz solution with the choice of reference surface and with the signal processing technique (DMD or FFT) is assessed and the results obtained with surface-based FTFs are also compared with those produced with regular point-based FTFs (with sets A and B in Fig. 5.27). The associated list of runs is presented in Tab. H.1.

RUN	Reference location	Source of FTF parameters
R4a	Probe A	Fourier
R4b	Probe B	Fourier
R4c	Surface S1	Fourier
R4d	Surface S2	Fourier
R4e	Surface S3	Fourier
R4f	Surface S1	DMD
R4g	Surface S2	DMD
R4h	Surface S3	DMD

Table H.1: List of R4x computations (active flame in a simplified geometry without dissipative elements).

With all FTF parameters, a first azimuthal mode is found unstable, with the frequencies listed in Tab. H.2. While the change of geometry (i.e. removing the swirler) did not modify the acoustics of the burner in the absence of flame, the situation is radically different when introducing one. The combination of a surface-based FTF and a matrix swirler decreases the real part of the frequency by about 10% and considerably increases the imaginary component (by about a factor 30 in the worst case). The difference increases when the volume removed from the geometry is greater. The worst results are obtained with the biggest surface S3 and the best with the smallest surface S2. This drastic modification is not well understood yet. One possible

cause might be related to the observation made in Section 4.5.3: the acoustics and stability of the combustor can be modified because the transverse components of the velocity fluctuation created by the flame are removed when passing through the matrix surfaces. The difference could also be due to the high ratio between the gain for the point-based FTF and the surface-based ones. For now, there is no strong argument in favor of one formalism or the other. These issues should be investigated in the future.

RUN	**Frequency [Hz]**
R4a	293.0 + 1.51 i
R4b	294.0 + 1.74 i
R4c	268.5 + 43.2 i
R4d	279.1 + 36.5 i
R4e	262.7 + 51.4 i
R4f	270.3 + 30.0 i
R4g	276.9 + 26.3 i
R4h	262.4 + 34.0 i

TABLE H.2: Frequency of the first azimuthal mode in R4x computations.

Another surprising observation of Tab. H.2 is that the variability between the frequencies obtained with the surface-based FTFs is quite important, even though the signals used to compute the FTF were very similar. The disparity between R4c, R4d and R4e is actually much greater than the one between R4a and R4b, obtained with the point-based FTFs. Again, we have no definite explanation for now. It is possible that removing the swirler from the geometry as done here modifies the acoustics in the combustor, leading to different velocities on the reference surface in the LES and in the Helmholtz solver. To check this, R4x computations should be run again with a geometry including the swirler, and a reference surface interpolated on the complete mesh. This was not done during this thesis because it requires rather important code developments.

Concerning the mode structures (Fig. H.1), the same kind of observations can be made. The mode structure remains quite similar to the one observed in the previous runs. The level of pressure fluctuations is much more important with surface-based FTFs than with point-based ones and it increases when switching from S2 to S1 and finally S3. The phase delay between the bypass and the flame tube follows the same evolution. In Fig. H.1, only runs R4a, R4c, R4d, R4e are shown. Indeed, R4a and R4b are almost identical. The pressure level in R4f, R4g and R4h is slightly lower than in R4c, R4d and R4e but the same evolution with the size of the reference surface is observed.

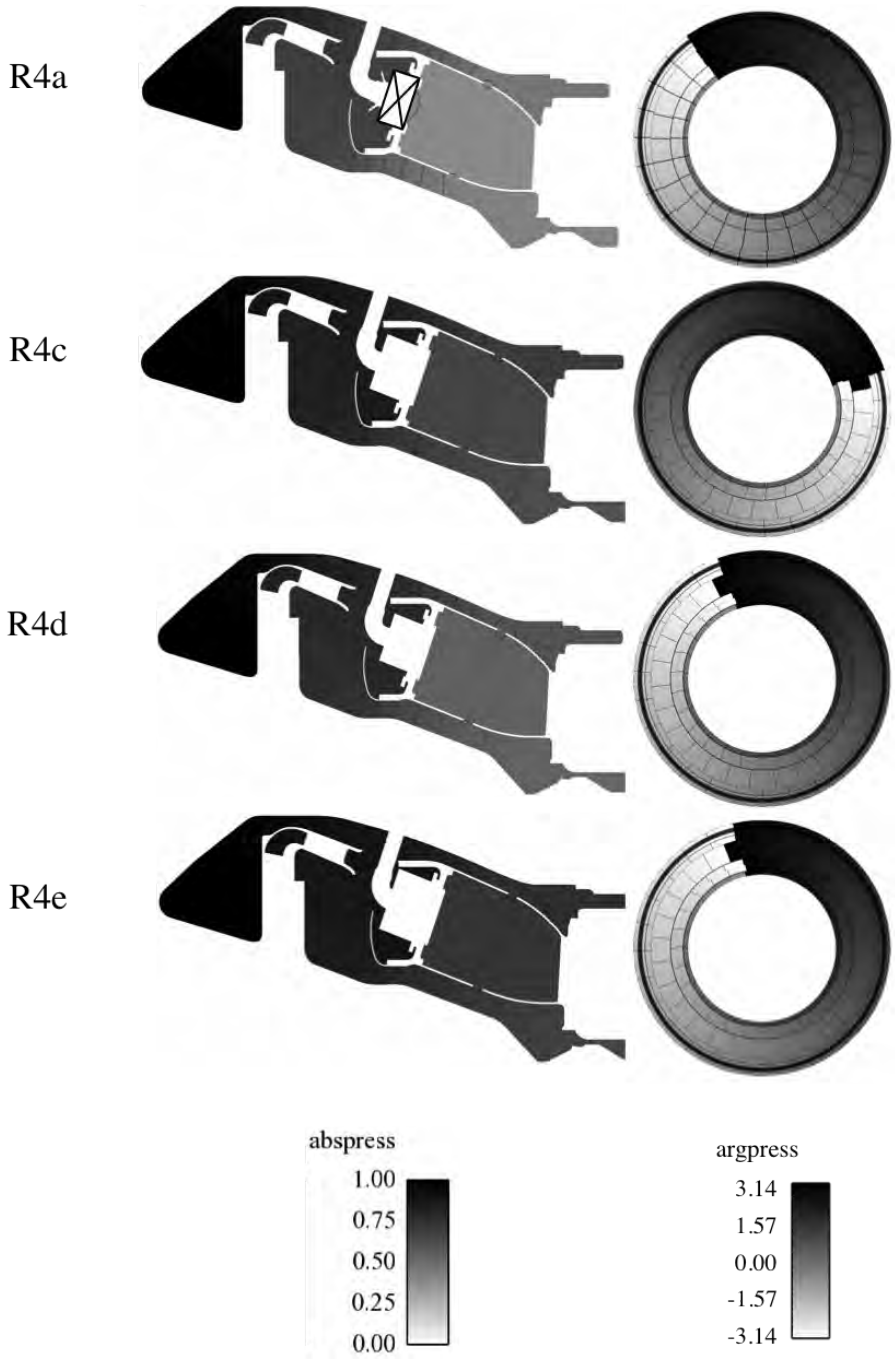


FIGURE H.1: Modulus of pressure in a transverse cut and phase of pressure seen from the back of the combustor for R4a, R4c, R4d and R4e.

Appendix I

Separation of the acoustic flux contributions in the Helmholtz computation of the SAFRAN combustor

For the acoustic energy balance analysis of Section 5.7, the total acoustic flux is decomposed into the contributions of each type of boundary condition. A naive decomposition consists in computing the acoustic flux separately on the cells of each type of boundary condition. Unfortunately, this decomposition fails when many boundaries share common edges. Indeed, as already explained in Section 4.3.2, nodes and cells shared by two boundary conditions receive a contribution from the two. In this section, a simple approximative procedure is presented to reallocate acoustic flux to the correct boundaries. In this procedure, two categories of shared edges are distinguished:

Edges shared by a dissipative boundary and a wall. In this case, some of the acoustic flux on the wall is reattributed to the dissipative boundary, following the procedure described next. Matrix patches for the swirlers and perforated plates feature this type of edges.

Edges shared by two dissipative boundaries. In the present configuration, only dilution holes and perforated plates share this type of edges. The previous Helmholtz computations indicate that the dissipative effect of dilution holes dominates the one of perforated plates. Part of the acoustic flux on perforated plates is therefore wrongly attributed and should be reassigned to dilution holes, with the procedure described below.

The redistribution of acoustic flux is performed based on the assumption that the effect of dissipative boundaries is felt not only by the cells of the boundary but also by the immediate neighbors. This effect is taken into account with a corrective factor, computed with an approach similar to the one of Section 4.3.2. The procedure is the following. For each pair of adjacent patches (k, i) (with k the ID of the dissipative patch, and i the IDs of the adjacent walls / perforated plates if i corresponds to a dilution hole):

1. Compute the total length of shared edges $\mathcal{C}$.

2. Compute a corrective factor β:

$$\beta = \frac{\mathcal{C}dx}{\mathcal{S}_k} \tag{I.1}$$

In this expression, the mesh size dx at shared edges should remain constant, and this is well-verified for all the meshes studied here. The corrective factor β mimics the fact that the effect of patch k actually extends one cell over its prescribed outline (Fig. 4.14). This is an approximation, but it works well, as demonstrated in Section 4.3.2.

3. Correct the initial acoustic flux F_k (integrated over the cells) by multiplying it by $1 + \beta$.

$$F_k \leftarrow F_k(1 + \beta) \tag{I.2}$$

In order to retain the same sum of fluxes, the fluxes from patch i must also be modified :

$$F_i \leftarrow F_i - F_k\beta \tag{I.3}$$

Without this procedure, the acoustic flux distribution cannot be trusted. For example, in a Helmholtz computation of the industrial geometry where the only dissipative boundaries are at dilution holes, the acoustic flux distribution without correction indicates that only 70% of the flux actually comes from the dilution holes, while the remaining 30% are attributed to walls. With the proposed procedure, a coherent acoustic flux distribution is obtained, with 100% of the flux coming from the dilution holes. Figure I.1 shows another illustration of the benefits of the corrective procedure on computation R5a (Tab. 5.8). The corrective procedure successively reallocates the acoustic flux from the walls to the perforated plates and swirlers, and from the perforated plates to the dilution holes.

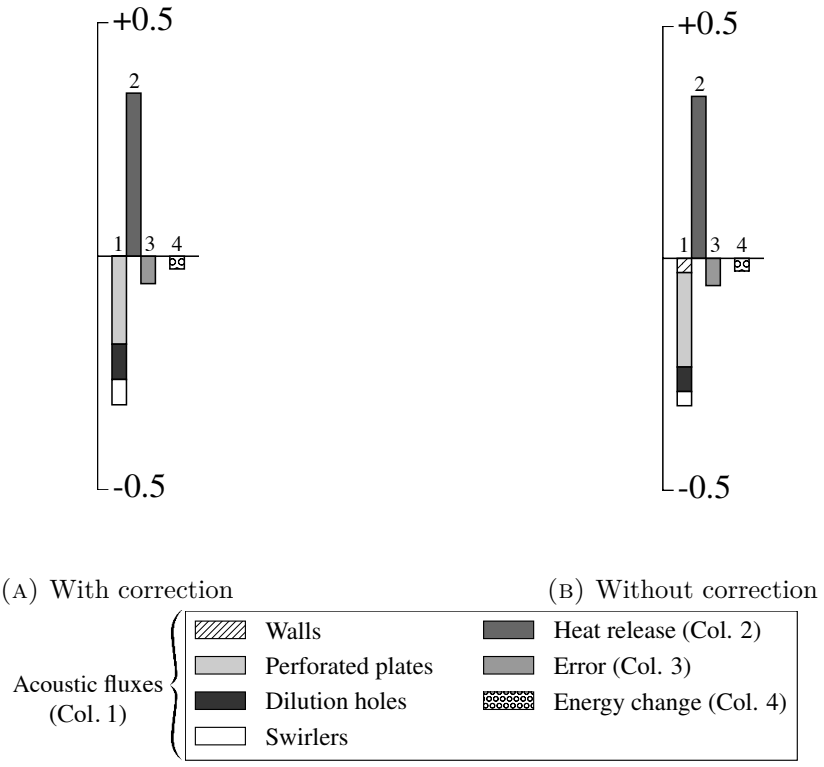


FIGURE I.1: Energy balance for the most amplified mode of R5a, with (left) and without (right) correction.

Bibliography

[1] Heywood, J. B. et al., *Internal combustion engine fundamentals*, Vol. 930, Mcgraw-Hill New York, 1988.

[2] Huang, Y. and Yang, V., "Dynamics and stability of lean-premixed swirl-stabilized combustion," *Prog. Energy Comb. Sci.* , Vol. 35, No. 4, 2009, pp. 293–364.

[3] Poinsot, T. and Veynante, D., *Theoretical and Numerical Combustion*, Third Edition (www.cerfacs.fr/elearning), 2011.

[4] Lieuwen, T. C., *Unsteady combustor physics*, Cambridge University Press, 2012, 10.1017/cbo9781139059961.

[5] Culick, F. E. C. and Kuentzmann, P., *Unsteady Motions in Combustion Chambers for Propulsion Systems*, NATO Research and Technology Organization, 2006.

[6] Rayleigh, J. W. S., "The explanation of certain acoustical phenomena," *Nature*, Vol. 18, No. 455, 1878, pp. 319–321.

[7] Rijke, P. L., "LXXI. Notice of a new method of causing a vibration of the air contained in a tube open at both ends," *Philosophical Magazine Series 4*, Vol. 17, No. 116, 1859, pp. 419–422, 10.1080/14786445908642701.

[8] Lieuwen, T. and Yang, V., *Combustion Instabilities in Gas Turbine Engines. Operational Experience, Fundamental Mechanisms and Modeling*, Progress in Astronautics and Aeronautics AIAA Vol 210, 2005.

[9] Zhao, D., A'Barrow, C., Morgans, A. S., and Carrotte, J., "Acoustic damping of a Helmholtz resonator with an oscillating volume," *AIAA journal*, Vol. 47, No. 7, 2009, pp. 1672–1679.

[10] Kaufmann, A., Nicoud, F., and Poinsot, T., "Flow forcing techniques for numerical simulation of combustion instabilities," *Combustion and Flame* , Vol. 131, 2002, pp. 371–385.

[11] Polifke, W., Poncet, A., Paschereit, C. O., and Doebbeling, K., "Reconstruction of acoustic transfer matrices by instationnary computational fluid dynamics," *Journal of Sound and Vibration*, Vol. 245, No. 3, Aug. 2001, pp. 483–510, 10.1006/jsvi.2001.3594.

[12] Bauerheim, M., Staffelbach, G., Worth, N., Dawson, J., Gicquel, L., and Poinsot, T., "Sensitivity of LES-based harmonic flame response model for turbulent swirled flames and impact on the stability of azimuthal modes," *Proceedings of the Combustion Institute*, Vol. 35, No. 3, 2015, pp. 3355–3363, 10.1016/j.proci.2014.07.021.

[13] Wieczorek, K., *Numerical study of mach number effects on combustion instability*, Ph.D. thesis, Université Montpellier II - Ecole Doctorale ISS - Mathématiques et Modélisation, 2010.

[14] Gikadi, J., Ullrich, W. C., Sattelmayer, T., and Turrini, F., "Prediction of the acoustic losses of a swirl atomizer nozzle under non-reactive conditions," *ASME Turbo Expo 2013: Turbine Technical Conference and Exposition*, American Society of Mechanical Engineers, June 2013, pp. V01BT04A035–V01BT04A035, 10.1115/gt2013-95449.

[15] Ghani, A., Poinsot, T., Gicquel, L., and Staffelbach, G., "LES of longitudinal and transverse self-excited combustion instabilities in a bluff-body stabilized turbulent premixed flame," *Combustion and Flame*, Vol. 162, No. 11, Nov. 2016, pp. 4075–4083, 10.1016/j.combustflame.2015.08.024.

[16] Pankiewitz, C. and Sattelmayer, T., "Time domain simulation of combustion instabilities in annular combustors," *Journal of Engineering for Gas Turbines and Power* , Vol. 125, No. 3, 2003, pp. 677–685.

[17] Nicoud, F., Benoit, L., Sensiau, C., and Poinsot, T., "Acoustic modes in combustors with complex impedances and multidimensional active flames," *AIAA Journal* , Vol. 45, No. 2, Feb. 2007, pp. 426–441, 10.2514/1.24933.

[18] Silva, C. F., Nicoud, F., Schuller, T., Durox, D., and Candel, S., "Combining a Helmholtz solver with the flame describing function to assess combustion instability in a premixed swirled combustor," *Combustion and Flame* , Vol. 160, No. 9, Sept. 2013, pp. 1743–1754, 10.1016/j.combustflame.2013.03.020.

[19] Ghosal, S. and Moin, P., "The basic equations for the large eddy simulation of turbulent flows in complex geometry," *Journal of Computational Physics* , Vol. 118, 1995, pp. 24 – 37.

[20] Huang, Y., Sung, H. G., Hsieh, S. Y., and Yang, V., "Large Eddy Simulation of combustion dynamics of lean-premixed swirl-stabilized combustor," *Journal of Propulsion and Power* , Vol. 19, No. 5, Nov. 2003, pp. 782–794, 10.2514/2.6194.

[21] Schmitt, P., Poinsot, T., Schuermans, B., and Geigle, K. P., "Large-eddy simulation and experimental study of heat transfer, nitric oxide emissions and combustion instability in a swirled turbulent high-pressure burner," *Journal of Fluid Mechanics* , Vol. 570, Jan. 2007, pp. 17–46, 10.1017/s0022112006003156.

[22] Srinivasan, S., Ranjan, R., and Menon, S., "Flame Dynamics During Combustion Instability in a High-Pressure, Shear-Coaxial Injector Combustor," *Flow Turbulence Combust*, Vol. 94, No. 1, sep 2014, pp. 237–262, 10.1007/s10494-014-9569-x.

[23] Morgan, C. J., Shipley, K. J., and Anderson, W. E., "Comparative Evaluation Between Experiment and Simulation for a Transverse Instability," *Journal of Propulsion and Power*, Vol. 31, No. 6, nov 2015, pp. 1696–1706, 10.2514/1.b35759.

[24] Wolf, P., Staffelbach, G., Gicquel, L., Muller, J.-D., and Poinsot, T., "Acoustic and Large Eddy Simulation studies of azimuthal modes in annular combustion chambers," *Combustion and Flame* , Vol. 159, No. 11, Nov. 2012, pp. 3398–3413, 10.1016/j.combustflame.2012.06.016.

[25] Hermeth, S., Staffelbach, G., Gicquel, L., and Poinsot, T., "LES evaluation of the effects of equivalence ratio fluctuations on the dynamic flame response in a real gas turbine combustion chamber," *Proceedings of the Combustion Institute* , Vol. 34, No. 2, 2013, pp. 3165 – 3173, http://dx.doi.org/10.1016/j.proci.2012.07.013.

[26] Miguel-Brebion, M., Mejia, D., Xavier, P., Duchaine, F., Bedat, B., Selle, L., and Poinsot, T., "Joint experimental and numerical study of the influence of flame holder temperature on the stabilization of a laminar methane flame on a cylinder," *Combustion and Flame*, Vol. 172, oct 2016, pp. 153–161, 10.1016/j.combustflame.2016.06.025.

[27] Boij, S. and Nilsson, B., "Reflection of sound at area expansions in a flow duct," *Journal of Sound and Vibration*, Vol. 260, No. 3, 2003, pp. 477 – 498, http://dx.doi.org/10.1016/S0022-460X(02)00950-1.

[28] Cummings, A. and Haddad, H., "Sudden area changes in flow ducts: Further thoughts," *Journal of Sound and Vibration*, Vol. 54, No. 4, oct 1977, pp. 611–612, 10.1016/0022-460x(77)90620-4.

[29] Marble, F. E. and Candel, S., "Acoustic disturbances from gas nonuniformities convected through a nozzle," *Journal of Sound and Vibration* , Vol. 55, 1977, pp. 225–243.

[30] Powell, A., "Theory of vortex sound," *Journal of the Acoustical Society of America* , Vol. 36, No. 1, 1964, pp. 177–195.

[31] Gikadi, J., Föller, S., and Sattelmayer, T., "Impact of turbulence on the prediction of linear aeroacoustic interactions: Acoustic response of a turbulent shear layer," *Journal of Sound and Vibration*, Vol. 333, No. 24, dec 2014, pp. 6548–6559, 10.1016/j.jsv.2014.06.033.

[32] Holmberg, A., Kierkegaard, A., and Weng, C., "A frequency domain linearized Navier–Stokes method including acoustic damping by eddy viscosity using RANS," *Journal of Sound and Vibration*, 2015.

[33] Gikadi, J., Sattelmayer, T., and Peschiulli, A., "Effects of the Mean Flow Field on the Thermo-Acoustic Stability of Aero-Engine Combustion Chambers," *Volume 2: Combustion, Fuels and Emissions, Parts A and B*, ASME International, jun 2012, 10.1115/gt2012-69612.

[34] Na, W., Efraimsson, G., and Boij, S., "Prediction of thermoacoustic instabilities in combustors using linearized Navier-Stokes equations in frequency domain." *Proceedings of the 22nd International Congress on Sound and Vibration*, 2015.

[35] Gikadi, J., *Prediction of Acoustic Modes in Combustors using Linearized Navier-Stokes Equations in Frequency Space*, Ph.D. thesis, Universitätsbibliothek der TU München, 2014.

[36] Nicoud and Wieczorek, "About the zero Mach number assumption in the calculation of thermoacoustic instabilities," *International Journal of Spray and Combustion Dynamics*, Vol. 1, No. 1, mar 2009, pp. 67–111, 10.1260/175682709788083335.

[37] Wieczorek, K., Sensiau, C., Polifke, W., and Nicoud, F., "Assessing non-normal effects in thermoacoustic systems with mean flow," *Physics of Fluids*, Vol. 23, No. 10, 2011, pp. 107103, 10.1063/1.3650418.

[38] Lehoucq, R. B. and Sorensen, D. C., "Deflation Techniques for an Implicitly Restarted Arnoldi Iteration," *SIAM. J. Matrix Anal. & Appl.*, Vol. 17, No. 4, oct 1996, pp. 789–821, 10.1137/s0895479895281484.

[39] Stewart, G. W., "A Krylov–Schur Algorithm for Large Eigenproblems," *SIAM. J. Matrix Anal. & Appl.*, Vol. 23, No. 3, jan 2002, pp. 601–614, 10.1137/s0895479800371529.

[40] Sleijpen, G. L. G. and der Vorst, H. A. V., "A Jacobi–Davidson Iteration Method for Linear Eigenvalue Problems," *SIAM Review*, Vol. 42, No. 2, jan 2000, pp. 267–293, 10.1137/s0036144599363084.

[41] Roux, S., Lartigue, G., Poinsot, T., Meier, U., and Bérat, C., "Studies of mean and unsteady flow in a swirled combustor using experiments, acoustic analysis, and large eddy simulations," *Combustion and Flame*, Vol. 141, No. 1-2, apr 2005, pp. 40–54, 10.1016/j.combustflame.2004.12.007.

[42] Laera, D., Campa, G., Camporeale, S. M., Bertolotto, E., Rizzo, S., Bonzani, F., Ferrante, A., and Saponaro, A., "Modelling of thermoacoustic combustion instabilities phenomena: Application to an experimental test rig," *Energy Procedia*, Vol. 45, 2014, pp. 1392–1401.

[43] Gullaud, E. and Nicoud, F., "Effect of Perforated Plates on the Acoustics of Annular Combustors," *AIAA Journal*, Vol. 50, No. 12, Dec. 2012, pp. 2629–2642, 10.2514/1.j050716.

[44] Motheau, E., Selle, L., and Nicoud, F., "Accounting for convective effects in zero-Mach-number thermoacoustic models," *Journal of Sound and Vibration* , Vol. 333, No. 1, Nov. 2013, pp. 246–262, In press.

[45] Culick, F., "Combustion instabilities in liquid-fuelled propulsion systems," Tech. Rep. AGARD-CP-450, AGARD, Neuilly sur Seine, France, 1988.

[46] ZINN, B. T. and LORES, M. E., "Application of the Galerkin Method in the Solution of Non-linear Axial Combustion Instability Problems in Liquid Rockets," *Combustion Science and Technology*, Vol. 4, No. 1, 1971, pp. 269–278, 10.1080/00102207108952493.

[47] Culick, F. E. C., "Some recent results for nonlinear acoustic in combustion chambers," *AIAA Journal* , Vol. 32, No. 1, 1994, pp. 146–169.

[48] AWAD, E. and CULICK, F. E. C., "On the Existence and Stability of Limit Cycles.for Longitudinal Acoustic Modes in a Combustion Chamber," *Combustion Science and Technology*, Vol. 46, No. 3-6, apr 1986, pp. 195–222, 10.1080/00102208608959800.

[49] YANG, V. and CULICK, F. E. C., "On the Existence and Stability of Limit Cycles for Transverse Acoustic Oscillations in a Cylindrical Combustion Chamber. 1: Standing Modes," *Combustion Science and Technology*, Vol. 72, No. 1-3, 1990, pp. 37–65, 10.1080/00102209008951639.

[50] Subramanian, P., Sujith, R. I., and Wahi, P., "Subcritical bifurcation and bistability in thermoacoustic systems," *Journal of Fluid Mechanics*, Vol. 715, jan 2013, pp. 210–238, 10.1017/jfm.2012.514.

[51] Nagaraja, S., Kedia, K., and Sujith, R., "Characterizing energy growth during combustion instabilities: Singularvalues or eigenvalues?" *Proceedings of the Combustion Institute*, Vol. 32, No. 2, 2009, pp. 2933–2940.

[52] Juniper, M. P., "Triggering in the horizontal Rijke tube: non-normality, transient growth and bypass transition," *Journal of Fluid Mechanics* , Vol. 667, 1 2011, pp. 272–308, 10.1017/S0022112010004453.

[53] Dowling, A. P., "The calculation of thermoacoustic oscillations," *Journal of Sound and Vibration* , Vol. 180, No. 4, 1995, pp. 557–581.

[54] Annaswamy, A. M., Fleifil, M., Hathout, J. P., and Ghoniem, A. F., "Impact of Linear Coupling on the Design of Active Controllers for the Thermoacoustic Instability," *Combustion Science and Technology* , Vol. 128, No. 1-6, 1997, pp. 131–180, 10.1080/00102209708935707.

[55] Kashinath, K., Hemchandra, S., and Juniper, M. P., "Nonlinear Phenomena in Thermoacoustic Systems With Premixed Flames," *Journal of Engineering for Gas Turbines and Power*, Vol. 135, No. 6, may 2013, pp. 061502, 10.1115/1.4023305.

[56] Krüger, U., Hüren, J., Hoffmann, S., Krebs, W., and Bohn, D., "Prediction of Thermoacoustic Instabilities With Focus on the Dynamic Flame Behavior for the 3A-Series Gas Turbine of Siemens KWU," *Volume 2: Coal, Biomass and Alternative Fuels Combustion and Fuels Oil and Gas Applications Cycle Innovations*, ASME International, jun 1999, 10.1115/99-gt-111.

[57] Dowling, A. P. and Stow, S. R., "Acoustic Analysis of Gas Turbine Combustors," *Journal of Propulsion and Power* , Vol. 19, No. 5, 2003, pp. 751–764, 10.2514/2.6192.

[58] Bauerheim, M., Parmentier, J., Salas, P., Nicoud, F., and Poinsot, T., "An analytical model for azimuthal thermoacoustic modes in an annular chamber fed by an annular plenum," *Combustion and Flame* , Vol. 161, No. 0, may 2013, pp. 1374–1389, http://dx.doi.org/10.1016/j.combustflame.2013.11.014.

[59] Stow, S. R. and Dowling, A. P., "Low-Order Modelling of Thermoacoustic Limit Cycles," *ASME Turbo Expo 2004; Power for Land, Sea, and Air*, ASME International, 2004, pp. 775–786, 10.1115/gt2004-54245.

[60] Noiray, N., Bothien, M., and Schuermans, B., "Investigation of azimuthal staging concepts in annular gas turbines," *Combustion Theory and Modelling* , 2011, pp. 585–606.

[61] Han, X., Li, J., and Morgans, A. S., "Prediction of combustion instability limit cycle oscillations by combining flame describing function simulations with a thermoacoustic network model," *Combustion and Flame*, Vol. 162, No. 10, oct 2015, pp. 3632–3647, 10.1016/j.combustflame.2015.06.020.

[62] Schuller, T., Ducruix, S., Durox, D., and Candel, S., "Modeling tools for the prediction of premixed flame transfer functions," *Proceedings of the Combustion Institute*, Vol. 29, No. 1, jan 2002, pp. 107–113, 10.1016/s1540-7489(02)80018-9.

[63] Schuller, T., Durox, D., and Candel, S., "A unified model for the prediction of laminar flame transfer functions," *Combustion and Flame*, Vol. 134, No. 1-2, jul 2003, pp. 21–34, 10.1016/s0010-2180(03)00042-7.

[64] Lieuwen, T., "Modeling premixed combustion-acoustic wave interactions: A review," *Journal of propulsion and power*, Vol. 19, No. 5, 2003, pp. 765–781.

[65] Schuller, T., "Self-induced combustion oscillations of laminar premixed flames stabilized on annular burners," *Combustion and Flame*, nov 2003, 10.1016/s0010-2180(03)00208-6.

[66] Gentemann, A., Hirsch, C., Kunze, K., Kiesewetter, F., Sattelmayer, T., and Polifke, W., "Validation of Flame Transfer Function Reconstruction for Perfectly Premixed Swirl Flames," *Volume 1: Turbo Expo 2004*, ASME International, 2004, 10.1115/gt2004-53776.

[67] Duchaine, F., Boudy, F., Durox, D., and Poinsot, T., "Sensitivity analysis of transfer functions of laminar flames," *Combustion and Flame*, Vol. 158, No. 12, dec 2011, pp. 2384–2394, 10.1016/j.combustflame.2011.05.013.

[68] Noiray, N., Durox, D., Schuller, T., and Candel, S., "A unified framework for nonlinear combustion instability analysis based on the flame describing function," *Journal of Fluid Mechanics* , Vol. 615, 2008, pp. 139–167.

[69] Schuermans, B. B. H., Polifke, W., and Paschereit, C. O., "Modeling Transfer Matrices of Premixed Flames and Comparison With Experimental Results," *Volume 2: Coal, Biomass and Alternative Fuels Combustion and Fuels Oil and Gas Applications Cycle Innovations*, ASME International, jun 1999, 10.1115/99-gt-132.

[70] Paschereit, C. O., Polifke, W., Schuermans, B., and Mattson, O., "Measurement of transfer matrices and source terms of premixed flames," *Journal of Engineering for Gas Turbines and Power*, Vol. 124, 2002, pp. 239–247, 10.1115/1.1383255.

[71] Alemela, P. R., Fanaca, D., Ettner, F., Hirsch, C., Sattelmayer, T., and Schuermans, B., "Flame Transfer Matrices of a Premixed Flame and a Global Check With Modelling and Experiments," *Volume 3: Combustion, Fuels and Emissions, Parts A and B*, ASME International, 2008, 10.1115/gt2008-50111.

[72] Truffin, K. and Poinsot, T., "Comparison and extension of methods for acoustic identification of burners," *Combustion and Flame* , Vol. 142, No. 4, Sept. 2005, pp. 388–400, 10.1016/j.combustflame.2005.04.001.

[73] Stokes, G. G., "On the effect of the inertial friction of fluids on the motions of pendulums," *Trans. Cambridge Phil. Soc.*, Vol. 9, 1851, pp. 8–23, 10.1017/cbo9780511702266.002.

[74] Kirchhoff, G., "Ueber den Einfluss der Wärmeleitung in einem Gase auf die Schallbewegung," *Annalen der Physik*, Vol. 210, No. 6, 1868, pp. 177–193, 10.1002/andp.18682100602.

[75] Nielsen, A. K., *Acoustic Resonators of circular cross-section and with axial symmetry*, Transactions of the Danish Academy of Technical Sciences, Akad. for de Tekniske Videnskaber : Gad [in Kommm.], 1949.

[76] Searby, G., Nicole, A., Habiballah, M., and Laroche, E., "Prediction of the Efficiency of Acoustic Damping Cavities," *Journal of Propulsion and Power*, Vol. 24, No. 3, may 2008, pp. 516–523, 10.2514/1.32325.

[77] Levine, H. and Schwinger, J., "On the radiation of sound from an unflanged circular pipe," *Physical Review*, Vol. 73, No. 4, Feb. 1948, pp. 383–406, 10.1103/physrev.73.383.

[78] Zinn, B., "Longitudinal mode acoustic losses in short nozzles," *Journal of Sound and Vibration* , Vol. 22, No. 1, 1972, pp. 93 – 105, 10.1016/0022-460X(72)90847-4.

[79] Duran, I. and Moreau, S., "Solution of the quasi one-dimensional linearized Euler equations using flow invariants and the Magnus expansion," *Journal of Fluid Mechanics*, Vol. 723, May 2013, pp. 190–231.

[80] Duran, I. and Morgans, A. S., "On the reflection and transmission of circumferential waves through nozzles," *Journal of Fluid Mechanics*, Vol. 773, 2015, pp. 137–153.

[81] Pierce, A. D., *Acoustics: an introduction to its physical principles and applications*, McGraw Hill, New York, 1981.

[82] Williams, F. A., *Combustion Theory*, Benjamin Cummings, Menlo Park, CA, 1985.

[83] Richard, J. and Nicoud, F., "Effect of the fluid structure coupling on the aeroacoustic instabilities of solid rocket motors," *17th AIAA/CEAS AeroAcoustics Conference*, Portland, Oregon, USA, 2011.

[84] Temkin, S. and Dobbins, R. A., "Attenuation and Dispersion of Sound by Particulate-Relaxation Processes," *Journal of the Acoustical Society of America*, Vol. 40, No. 2, 1966, pp. 317, 10.1121/1.1910073.

[85] DeSpirito, J. and Wang, L.-P., "Linear instability of two-way coupled particle-laden jet," *International Journal of Multiphase Flow*, Vol. 27, No. 7, jul 2001, pp. 1179–1198, 10.1016/s0301-9322(00)00067-7.

[86] Dowling, A. P. and Hughes, I. J., "Sound absorption by a screen with a regular array of slits," *Journal of Sound and Vibration*, Vol. 156, No. 3, 1992, pp. 387–405.

[87] Howe, M. S., *Theory of vortex sound*, Cambridge University Press, 2003.

[88] Rienstra, S. W. and Hirschberg, A., *An introduction to acoustics*, Eindhoven University of Technology, 2003.

[89] Tonon, D., Landry, B., Belfroid, S., Willems, J., Hofmans, G., and Hirschberg, A., "Whistling of a pipe system with multiple side branches: Comparison with corrugated pipes," *Journal of Sound and Vibration*, Vol. 329, No. 8, apr 2010, pp. 1007–1024, 10.1016/j.jsv.2009.10.020.

[90] Lacombe, R., Föller, S., Jasor, G., Polifke, W., Aurégan, Y., and Moussou, P., "Identification of aero-acoustic scattering matrices from large eddy simulation: Application to whistling orifices in duct," *Journal of Sound and Vibration*, Vol. 332, No. 20, 2013, pp. 5059–5067.

[91] Khor, M., Khor, M., Sheridan, J., Hourigan, K., Sheridan, J., and Hourigan, K., "The response of the separated shear layer from a cylinder to acoustic perturbations," *28th Fluid Dynamics Conference*, American Institute of Aeronautics and Astronautics (AIAA), jun 1997, 10.2514/6.1997-2003.

[92] Birbaud, A. L., Durox, D., Ducruix, S., and Candel, S., "Dynamics of confined premixed flames submitted to upstream acoustic modulations," *Proceedings of the Combustion Institute* , Vol. 31, 2007, pp. 1257–1265.

[93] Ho, C. M. and Huerre, P., "Perturbed free shear layers," *Annual Review of Fluid Mechanics* , Vol. 16, 1984, pp. 365.

[94] Bechert, D. W., "Sound absorption caused by vorticity shedding, demonstrated with a jet flow," *AIAA, Aeroacoustics Conference, 5th, Seattle, Wash., Mar. 12-14, 1979, 11 p.*, 1979.

[95] Hughes, I. and Dowling, A., "The absorption of sound by perforated linings," *Journal of Fluid Mechanics*, Vol. 218, No. 1, Sept. 1990, pp. 299–335, 10.1017/s002211209000101x.

[96] Dupère, I. D. J. and Dowling, A. P., "THE ABSORPTION OF SOUND NEAR ABRUPT AXISYMMETRIC AREA EXPANSIONS," *Journal of Sound and Vibration* , Vol. 239, No. 4, 2001, pp. 709 – 730, http://dx.doi.org/10.1006/jsvi.2000.3224.

[97] Eldredge, J. D. and Dowling, A. P., "The absorption of axial acoustic waves by a perforated liner with bias flow," *Journal of Fluid Mechanics* , Vol. 485, 2003, pp. 307–355.

[98] Tam, C. K. W., Ju, H., Jones, M. G., Watson, W. R., and Parrott, T. L., "A computational and experimental study of resonators in three dimensions," *Journal of Sound and Vibration*, Vol. 329, No. 24, Nov. 2010, pp. 5164–5193, 10.1016/j.jsv.2010.06.005.

[99] Ji, C. and Zhao, D., "Lattice Boltzmann investigation of acoustic damping mechanism and performance of an in-duct circular orifice," *The Journal of the Acoustical Society of America*, Vol. 135, No. 6, 2014, pp. 3243–3251.

[100] Tran, N., Ducruix, S., and Schuller, T., "Passive Control of the Inlet Acoustic Boundary of a Swirled Burner at High Amplitude Combustion Instabilities," *Journal of Engineering for Gas Turbines and Power*, Vol. 131, No. 5, 2009, pp. 051502, 10.1115/1.3078206.

[101] Zhao, D. and Li, X., "A review of acoustic dampers applied to combustion chambers in aerospace industry," *Progress in Aerospace Sciences*, Vol. 74, April 2015, pp. 114–130, 10.1016/j.paerosci.2014.12.003.

[102] Disselhorst, J. H. M. and Wijngaarden, L. V., "Flow in the exit of open pipes during acoustic resonance," *Journal of Fluid Mechanics*, Vol. 99, No. 02, 1980, pp. 293–319.

[103] Luong, T., Howe, M., and McGowan, R., "On the Rayleigh conductivity of a bias-flow aperture," *Journal of Fluids and Structures*, Vol. 21, No. 8, 2005, pp. 769–778.

[104] Scarpato, A., Ducruix, S., and Schuller, T., "A LES Based Sound Absorption Analysis of High-Amplitude Waves Through an Orifice With Bias Flow,"

Volume 2: Combustion, Fuels and Emissions, Parts A and B, ASME International, 2011, 10.1115/gt2011-45639.

[105] Rienstra, S. W., *Edge influence on the response of shear layers to acoustic forcing*, Ph.D. thesis, Technische Hogeschool Eindhoven, 1979.

[106] Noiray, N., Durox, D., Schuller, T., and Candel, S., "Mode Conversion in Acoustically Modulated Confined Jets," *AIAA Journal*, Vol. 47, No. 9, sep 2009, pp. 2053–2062, 10.2514/1.37734.

[107] Munjal, M. L., *Acoustics of Ducts and Mufflers*, John Wiley & Sons, 1986.

[108] Howe, M. S., "Contributions to the theory of aerodynamic sound, with application to excess jet noise and the theory of the flute," *Journal of Fluid Mechanics* , Vol. 71, No. 04, 1975, pp. 625–673.

[109] Richard, J., *Développement d'une chaîne de calcul pour les interactions fluide-structure et application aux instabilités aéro-acoustiques d'un moteur à propergol solide*, Ph.D. thesis, Montpellier 2, 2012.

[110] Boij, S. and Nilsson, B., "Scattering and absorption of sound at flow duct expansions," *Journal of sound and vibration*, Vol. 289, No. 3, 2006, pp. 577–594.

[111] Howe, M. S., "On the Theory of Unsteady High Reynolds Number Flow Through a Circular Aperture," *Proceedings of the Royal Society of London: Mathematical, Physical and Engineering Sciences*, Vol. 366, No. 1725, jun 1979, pp. 205–223, 10.1098/rspa.1979.0048.

[112] Jing, X. and Sun, X., "Effect of plate thickness on impedance of perforated plates with bias flow," *AIAA journal*, Vol. 38, No. 9, Jan. 2000, pp. 1573–1578, 10.2514/3.14583.

[113] Jing, X. and Sun, X., "Discrete vortex simulation on the acoustic nonlinearity of an orifice," *AIAA Journal*, Vol. 38, jan 2000, pp. 1565–1572, 10.2514/3.14582.

[114] Hofmans, G., Boot, R., Durrieu, P., Auregan, Y., and Hirschberg, A., "AEROACOUSTIC RESPONSE OF A SLIT-SHAPED DIAPHRAGM IN A PIPE AT LOW HELMHOLTZ NUMBER, 1: QUASI-STEADY RESULTS," *Journal of Sound and Vibration* , Vol. 244, No. 1, 2001, pp. 35 – 56, http://dx.doi.org/10.1006/jsvi.2000.3457.

[115] Dai, X., Jing, X., and Sun, X., "Acoustic-excited vortex shedding and acoustic nonlinearity at a rectangular slit with bias flow," *Journal of Sound and Vibration*, Vol. 333, No. 13, jun 2014, pp. 2713–2727, 10.1016/j.jsv.2014.02.029.

[116] Dequand, S., Hulshoff, S., and Hirschberg, A., "Self-sustained oscillations in a closed side branch system," *Journal of Sound and Vibration*, Vol. 265, No. 2, aug 2003, pp. 359–386, 10.1016/s0022-460x(02)01458-x.

[117] Jing, X. and Sun, X., "Sound-excited flow and acoustic nonlinearity at an orifice," *Physics of Fluids*, Vol. 14, No. 1, 2002, pp. 268, 10.1063/1.1423934.

[118] Cummings, A. and Eversman, W., "High amplitude acoustic transmission through duct terminations: Theory," *Journal of Sound and Vibration*, Vol. 91, No. 4, 1983, pp. 503 – 518, http://dx.doi.org/10.1016/0022-460X(83)90829-5.

[119] Cummings, A., "Acoustic nonlinearities and power losses at orifices," *AIAA Journal*, Vol. 22, No. 6, jun 1984, pp. 786–792, 10.2514/3.8680.

[120] Durrieu, P., Hofmans, G., Ajello, G., Boot, R., Auregan, Y., Hirschberg, A., and Peters, M. C. A. M., "Quasisteady aero-acoustic response of orifices," *Journal of the Acoustical Society of America* , Vol. 110, No. 4, 2001, pp. 1859–1872, 10.1121/1.1398058.

[121] Mendez, S. and Eldredge, J., "Acoustic modeling of perforated plates with bias flow for Large-Eddy Simulations," *Journal of Computational Physics* , Vol. 228, No. 13, July 2009, pp. 4757–4772, 10.1016/j.jcp.2009.03.026.

[122] Föller, S. and Polifke, W., "Identification of aero-acoustic scattering matrices from large eddy simulation. Application to a sudden area expansion of a duct," *Journal of Sound and Vibration*, Vol. 331, No. 13, June 2012, pp. 3096–3113, 10.1016/j.jsv.2012.01.004.

[123] Kierkegaard, A., Allam, S., Efraimsson, G., and Åbom, M., "Simulations of whistling and the whistling potentiality of an in-duct orifice with linear aeroacoustics," *Journal of Sound and Vibration*, Vol. 331, No. 5, feb 2012, pp. 1084–1096, 10.1016/j.jsv.2011.10.028.

[124] Yang, D. and Morgans, A., "Helmholtz resonators for damping thermoacoustics," *The 22nd International Congress on Sound and Vibration (ICSV) 2015*, 2015.

[125] Peters, M., Hirschberg, A., Reijnen, A. J., and Wijnands, A. P. J., "Damping and reflection coefficient measurements for an open pipe at low Mach and low Helmholtz numbers," *Journal of Fluid Mechanics* , Vol. 256, 1993, pp. 499–499.

[126] Fischer, A., Hirsch, C., and Sattelmayer, T., "Comparison of multi-microphone transfer matrix measurements with acoustic network models of swirl burners," *Journal of Sound and Vibration* , Vol. 298, No. 1-2, Nov. 2006, pp. 73–83, 10.1016/j.jsv.2006.04.040.

[127] Föller, S. and Polifke, W., "Determination of acoustic transfer matrices via Large Eddy Simulation and System Identification," *16th AIAA/CEAS Aeroacoustics Conference, Stockholm, Sweden, June*, 2010, pp. 7–9.

[128] Kierkegaard, A., Boij, S., and Efraimsson, G., "Simulations of the scattering of sound waves at a sudden area expansion," *Journal of Sound and Vibration*, Vol. 331, No. 5, 2012, pp. 1068–1083.

[129] Gentemann, A., Fischer, A., Evesque, S., and Polifke, W., "Acoustic transfer matrix reconstruction and analysis for ducts with sudden change of area," *9th AIAA/CEAS Aeroacoustics Conference*, Vol. 3142, American Institute of Aeronautics and Astronautics, may 2003, 10.2514/6.2003-3142.

[130] Föller, S., Polifke, W., and Tonon, D., "Aeroacoustic characterization of T-junctions based on Large Eddy Simulation and System Identification," *16th AIAA/CEAS Aeroacoustics Conference*, American Institute of Aeronautics and Astronautics, June 2010, 10.2514/6.2010-3985.

[131] Campa, G. and Camporeale, S. M., "Influence of flame and burner transfer matrix on thermoacoustic combustion instability modes and frequencies,"

ASME Turbo Expo 2010: Power for Land, Sea, and Air, American Society of Mechanical Engineers, 2010, pp. 907–918.

[132] Strobio Chen, L., Witte, A., and Polifke, W., "Thermo-acoustic characterization of a heat exchanger in cross flow using compressible and weakly compressible numerical simulation," *22nd International Congress on Sound and Vibration (ICSV22)*, ICSV, July 2015.

[133] Schmid, P. J., "Dynamic mode decomposition of numerical and experimental data," *Journal of Fluid Mechanics*, Vol. 656, July 2010, pp. 5–28, 10.1017/s0022112010001217.

[134] Poinsot, T., Chatelier, T. L., Candel, S., and Esposito, E., "Experimental determination of the reflection coefficient of a premixed flame in a duct," *Journal of Sound and Vibration* , Vol. 107, 1986, pp. 265–278.

[135] Kopitz, J., Bröcker, E., and Polifke, W., "Characteristics-based filter for identification of planar acoustic waves in numerical simulation of turbulent compressible flow," *12th International Congress on Sound and Vibration, Lisbon, Portugal, July*, 2005, pp. 11–14.

[136] Boden, H. and Åbom, M., "Modelling of fluid machines as sources of sound in duct and pipe systems," *ACTA ACUSTICA-LES ULIS-*, Vol. 3, 1995, pp. 549–560.

[137] Polifke, W., "Black-box system identification for reduced order model construction," *Annals of Nuclear Energy*, Vol. 67, may 2014, pp. 109–128, 10.1016/j.anucene.2013.10.037.

[138] Gullaud, E., *Impact des plaques multiperforées sur l'acoustique des chambres de combustion aéronautiques*, Ph.D. thesis, PhD thesis, Université Montpellier II-DOCTORALE ISS: Spécialité Mathématiques et Modélisation, 2010., 2010.

[139] Schmid, M., Blumenthal, R. S., Schulze, M., Polifke, W., and Sattelmayer, T., "Quantitative stability analysis using real-valued frequency response data," *Journal of Engineering for Gas Turbines and Power*, Vol. 135, No. 12, 2013, pp. 121601.

[140] Noiray, N. and Schuermans, B., "Deterministic quantities characterizing noise driven Hopf bifurcations in gas turbine combustors," *International Journal of Non-Linear Mechanics*, Vol. 50, April 2013, pp. 152–163, 10.1016/j.ijnonlinmec.2012.11.008.

[141] Palies, P., Durox, D., Schuller, T., and Candel, S., "Nonlinear combustion instability analysis based on the flame describing function applied to turbulent premixed swirling flames," *Combustion and Flame*, Vol. 158, No. 10, 2011, pp. 1980–1991.

[142] Holmberg, A., Åbom, M., and Bodén, H., "Accurate experimental two-port analysis of flow generated sound," *Journal of Sound and Vibration*, Vol. 330, No. 26, Dec. 2011, pp. 6336–6354, 10.1016/j.jsv.2011.07.041.

[143] Schönfeld, T., "Steady and Unsteady Flow Simulations Using the Hybrid Flow Solver AVBP," *AIAA Journal*, Vol. 37, Jan. 1999, pp. 1378–1385, 10.2514/3.14333.

[144] Selle, L., Lartigue, G., Poinsot, T., Koch, R., Schildmacher, K.-U., Krebs, W., Prade, B., Kaufmann, P., and Veynante, D., "Compressible large eddy simulation of turbulent combustion in complex geometry on unstructured meshes," *Combustion and Flame*, Vol. 137, No. 4, 2004, pp. 489 – 505, http://dx.doi.org/10.1016/j.combustflame.2004.03.008.

[145] Mendez, S. and Nicoud, F., "Large-eddy simulation of a bi-periodic turbulent flow with effusion," *Journal of Fluid Mechanics*, Vol. 598, 3 2008, pp. 27–65, 10.1017/S0022112007009664.

[146] Duran, I., Leyko, M., Moreau, S., Nicoud, F., and Poinsot, T., "Computing combustion noise by combining Large Eddy Simulations with analytical models for the propagation of waves through turbine blades," *Comptes Rendus de l'Académie des Sciences - Mécanique*, Vol. 341, No. 1-2, January 2013, pp. 131–140.

[147] Motheau, E., Nicoud, F., and Poinsot, T., "Mixed acoustic–entropy combustion instabilities in gas turbines," *Journal of Fluid Mechanics*, Vol. 749, 6 2014, pp. 542–576, 10.1017/jfm.2014.245.

[148] Colin, O. and Rudgyard, M., "Development of high-order Taylor-Galerkin schemes for unsteady calculations," *Journal of Computational Physics* , Vol. 162, No. 2, 2000, pp. 338–371.

[149] Nicoud, F., Baya Toda, H., Cabrit, O., Bose, S., and Lee, J., "Using singular values to build a subgrid-scale model for large eddy simulations," *Physics of Fluids* , Vol. 23, No. 8, 2011, pp. 085106, 10.1063/1.3623274.

[150] Baya Toda, H., Cabrit, O., Truffin, K., Bruneaux, G., and Nicoud, F., "Assessment of subgrid-scale models with a large-eddy simulation-dedicated experimental database: The pulsatile impinging jet in turbulent cross-flow," *Physics of Fluids*, Vol. 26, No. 7, July 2014, pp. 075108, 10.1063/1.4890855.

[151] Poinsot, T. and Lele, S., "Boundary conditions for direct simulations of compressible viscous flows," *Journal of Computational Physics* , Vol. 101, No. 1, 1992, pp. 104–129, 10.1016/0021-9991(92)90046-2.

[152] Paschereit, C. O. and Polifke, W., "Characterization of lean premixed gas-turbine burners as acoustic multi-ports," *Bulletin of the American Physical Society/ Division of Fluid Dynamics, Annual Meeting, San Francisco, California, USA*, 1997.

[153] Bauerheim, M., *Theoretical and numerical study of symmetry breaking effects on azimuthal thermoacoustic modes in annular combustors*, Ph.D. thesis, Institut National Polytechnique de Toulouse, 2014.

[154] Aurégan, Y. and Starobinski, R., "Determination of acoustical energy dissipation/production potentiality from the acoustical transfer functions of a multi-port," *Acta Acustica United with Acustica*, Vol. 85, No. 6, 1999, pp. 788–792.

[155] Wolf, P., Balakrishnan, R., Staffelbach, G., Gicquel, L. Y., and Poinsot, T., "Using LES to study reacting flows and instabilities in annular combustion chambers," *Flow, turbulence and combustion*, Vol. 88, No. 1-2, 2012, pp. 191–206.

[156] Silva, C. F., Leyko, M., Nicoud, F., and Moreau, S., "Assessment of combustion noise in a premixed swirled combustor via Large-Eddy Simulation," *Computers & Fluids*, Vol. 78, apr 2013, pp. 1–9, 10.1016/j.compfluid.2010.09.034.

[157] F.R.S., L. R., "XXXVII. On the passage of waves through apertures in Plane screens, and allied problems," *Philosophical Magazine Series 5*, Vol. 43, No. 263, 1897, pp. 259–272, 10.1080/14786449708620990.

[158] Bellucci, V., Flohr, P., and Paschereit, C. O., "Numerical and Experimental Study of Acoustic Damping Generated by Perforated Screens." *AIAA Journal*, Vol. 42, No. 8, aug 2004, pp. 1543–1549, 10.2514/1.9841.

[159] Kang, Z. and Ji, Z., "Acoustic length correction of duct extension into a cylindrical chamber," *Journal of Sound and Vibration*, Vol. 310, No. 4-5, mar 2008, pp. 782–791, 10.1016/j.jsv.2007.11.005.

[160] Komkin, A. I., Mironov, M. A., and Yudin, S. I., "On the attached length of orifices," *Acoustical Physics*, Vol. 58, No. 6, nov 2012, pp. 628–632, 10.1134/s1063771012050090.

[161] Ingard, U., "On the theory and design of acoustic resonators," *The Journal of the acoustical society of America*, Vol. 25, No. 6, 1953, pp. 1037–1061.

[162] Colin, O., Ducros, F., Veynante, D., and Poinsot, T., "A thickened flame model for large eddy simulations of turbulent premixed combustion," *Physics of Fluids* , Vol. 12, No. 7, 2000, pp. 1843–1863.

[163] Mendez, S. and Nicoud, F., "Adiabatic homogeneous model for flow around a multiperforated plate," *AIAA Journal*, Vol. 46, No. 10, Oct. 2008, pp. 2623–2633, 10.2514/1.37008.

[164] Franzelli, B., Riber, E., Sanjosé, M., and Poinsot, T., "A two-step chemical scheme for Large-Eddy Simulation of kerosene-air flames," *Combustion and Flame* , Vol. 157, No. 7, 2010, pp. 1364–1373.

[165] Sanjosé, M., Senoner, J., Jaegle, F., Cuenot, B., Moreau, S., and Poinsot, T., "Fuel injection model for Euler–Euler and Euler–Lagrange large-eddy simulations of an evaporating spray inside an aeronautical combustor," *International Journal of Multiphase Flow*, Vol. 37, No. 5, jun 2011, pp. 514–529, 10.1016/j.ijmultiphaseflow.2011.01.008.

[166] Smagorinsky, J., "General circulation experiments with the primitive equations: 1. The basic experiment." *Mon. Weather Rev.* , Vol. 91, 1963, pp. 99–164.

[167] Lu, T. and Law, C. K., "Toward accommodating realistic fuel chemistry in large-scale computations," *Progress in Energy and Combustion Science*, Vol. 35, No. 2, 2009, pp. 192–215.

[168] Salas, P., *Aspects numériques et physiques des instabilités de combustion dans les chambres de combustion annulaires*, Ph.D. thesis, Université Bordeaux - INRIA, 2013.

[169] Ingard, U. and Ising, H., "Acoustic nonlinearity of an orifice," *The journal of the Acoustical Society of America*, Vol. 42, No. 1, 1967, pp. 6–17.

[170] Melling, T., "The acoustic impendance of perforates at medium and high sound pressure levels," *Journal of Sound and Vibration*, Vol. 29, No. 1, jul 1973, pp. 1–65, 10.1016/s0022-460x(73)80125-7.

[171] Lee, S.-H., Ih, J.-G., and Peat, K. S., "A model of acoustic impedance of perforated plates with bias flow considering the interaction effect," *Journal of Sound and Vibration*, Vol. 303, No. 3-5, jun 2007, pp. 741–752, 10.1016/j.jsv.2007.02.001.

[172] Norris, A. N. and Sheng, C., "Acoustic Radiation From a Circular Pipe with an Infinite Flange," *Journal of Sound and Vibration*, Vol. 135, 1989, pp. 85–93.